EN ROUTE TO BETTER TREATMENT OF RHABDOMYOSARCOMA:
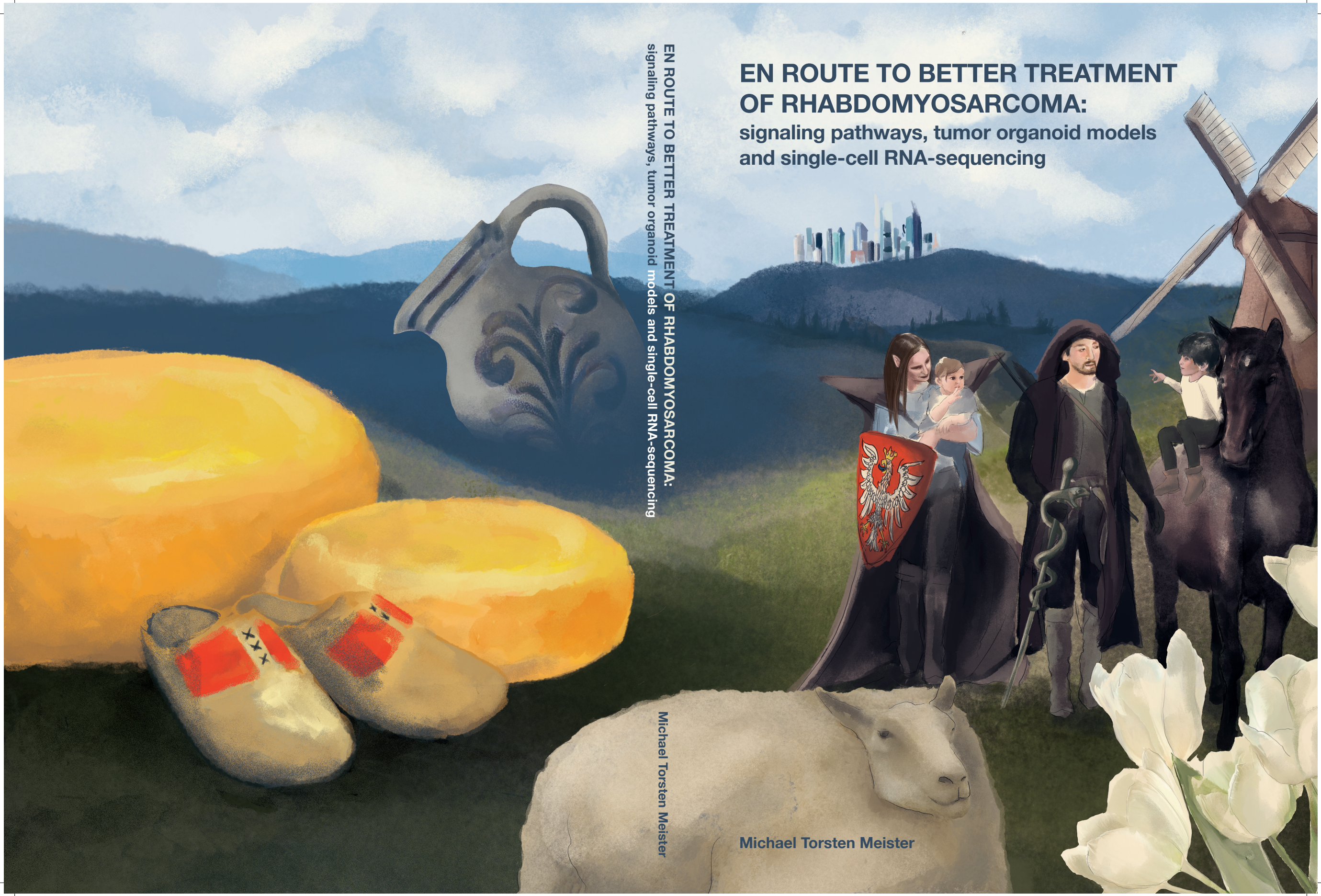## signaling pathways, tumor organoid models and single-cell RNA-sequencing

Michael Torsten Meister

EN ROUTE TO BETTER TREATMENT OF RHABDOMYOSARCOMA:
signaling pathways, tumor organoid models and single-cell RNA-sequencing

Michael Torsten Meister

En route to better treatment of rhabdomyosarcoma: signaling pathways, tumor organoid models and single-cell RNA-sequencing

En route naar een betere behandeling van rhabdomyosarcomen: signaal transductie, tumor organoïd modellen en single-cell RNA-sequencing

(met een samenvatting in het Nederlands)

Proefschrift

ter verkrijging van de graad van doctor aan de
Universiteit Utrecht op gezag van de rector magnificus,
prof. dr. H. R. B. M. Kummeling, ingevolge het besluit van het
college voor promoties in het openbaar te verdedigen op

woensdag 7 juni 2023 des middags te 2.15 uur

door

Michael Torsten Meister

geboren op 27 november 1985
te Bad Soden am Taunus, Duitsland

Table of contents

List of abbreviations

ANOVA	analysis of variance
aRMS	alveolar rhabdomyosarcoma
ATAC-seq	assay for transposase-accessible chromatin using sequencing
ATCC	American Type Culture Collection
ATO	arsenic trioxide
AUC	area under the curve
AYA	adolescents and young adults
B-H	Bonferroni-Holm
BCC	basal cell carcinoma
BME	basement membrane extract
BSA	bovine serum albumine
CBMC	cord blood mononuclear cell
CCC	comprehensive cancer center
CCRCC	clear cell renal cell carcinoma
cDC	conventional dendritic cell
cDNA	complementary deoxyribonucleic acid
CHAPS	3-((3-cholamidopropyl) dimethylammonio)-1-propanesulfonate
Chk1	checkpoint kinase 1
CI	combination index
CMN	congenital mesoblastic nephroma
CNA	copy number alteration
CNS	central nervous system
CNV	copy number variation
cor	correlation
CRISPR/Cas9	clustered regularly interspaced short palindromic repeats / CRISPR associated protein 9
CTG3D	CellTiter-Glo 3D®
ctr / ctrl	control
d	day
D. melanogaster	*Drosophila melanogaster* (fruit fly)

D. rerio	*Danio rerio* (zebrafish)
DAPI	4′,6-diamidino-2-phenylindole
DMEM	Dulbecco's Modified Eagle's Medium
DMP	dimetyl pimelimidate dihydrochloride
DMSO	dimethyl sulfoxide
DNA	deoxyribonucleic acid
DNA-meth	deoxyribonucleic acid methylation (analysis)
DP	depth
DPBS	Dulbecco's phosphate buffered saline
DSB	double-strand break
DSMZ	Deutsche Sammlung von Mikroorganismen und Zellkulturen
e.g.	exempli gratia (for example)
EBRT	external beam radiation therapy
ECL	enhanced chemiluminescence
ECM	extracellular matrix
EDTA	ethylenediaminetetraacetic acid
EGFR	epidermal growth factor receptor
EGR1	early growth response protein 1
Eri	eribulin
ERK	extracellular-signal regulated kinase
eRMS	embryonal rhabdomyosarcoma
etc.	et cetera
EtOH	ethanol
EV	empty vector
FACS	fluorescence activated cell sorting
FaR-RMS	Frontline and Relapse RMS (study)
FCS	fetal calf serum
FDA	Food and Drug Administration
FDR	false discovery rate
FFPE	formalin-fixed paraffin-embedded
FISH	fluorescence in situ hybridization
FN	fusion-negative

FP	fusion-positive
FSC	forward scatter
GATK	The Genome Analysis Toolkit
GEM	genetically engineered (animal) model
GFP	green fluorescent protein
GLI	glioma-associated oncogene
GSEA	geneset enrichment analysis
h	hour
H&E	hematoxylin and eosin (stain)
H3	histone 3
hEGF	human epidermal growth factor
HEPES	4-(2-hydroxyethyl)-1-piperazineethanesulfonic acid
hFGF	human fibroblast growth factor
Hh	hedgehog
hIGF	human insulin-like growth factor
HPI	hedgehog pathway inhibitor
HREF	human reference
HRP	horseradish peroxidase
HTS	high-throughput screening
i.e.	id est (that is to say)
IHC	immunohistochemistry
INFORM	INdividualized Therapy FOr Relapsed Malignancies in Childhood
IP	immunoprecipitation
IRCI	International Rare Cancers Initiative
ITCC	Innovative Therapies for Children with Cancer
iTHER	individualized THERapy
IVA	ifosfamide / vincristine / actinomycin-D
JCRB	Japanese Collection of Research Biosources Cell Bank
kD	kilodalton
KO	knockout
LOH	loss of heterozygosity

M. musculus	*Mus musculus* (mouse)
M/F	male / female
MAPK	mitogen-activated protein kinase
MAPPYACTS	MoleculAr Profiling for Pediatric and Young Adult Cancer Treatment Stratification
MB	medulloblastoma
MCL1i	MCL1 inhibitor
MDR-1	multidrug-resistance protein 1
MEK	dual specificity mitogen-activated protein kinase kinase
MEM	minimum essential medium
METC	Medisch Ethische Toetsingscommissie (Medical Research Ethics Committee)
min	minute
MoA	mechanism of action
mRNA	messenger ribonucleid acid
MTT	3-(4,5-dimethylthiazol-2-yl)-2,5-diphenyltetrazolium bromide
NES	normalized enrichment score
NF1	neurofibromatosis type 1
NK	natural killer
NMF	non-negative matrix factorization
ns	not significant
O	standard organoid line
O2	independently derived organoid line
OE	overexpression
OL	late passage organoid line
OS	overall survival
PAM	protospacer adjacent motif
PBS	phosphate buffered saline
PC	principal component
PCA	principal component analysis
PCD	programmed cell death
pDC	plasmacytoid dendritic cell

PFS	progression-free survival
PI	propidium iodide
PMC	Princess Máxima Center for Pediatric Oncology
PTCH	Patched
QC	quality control
QoL	quality of life
RAS	derived from "Rat sarcoma virus"
RBC	red blood cell
RKI	rho-kinase inhibitor
RMS	rhabdomyosarcoma
RNA-seq	mRNA sequencing
RPMI	Roswell Park Memorial Institute (medium)
RT	room temperature
RT-qPCR	real-time quantitative polymerase chain reaction
SBS	single-base substitution
SC-like	satellite-cell like
scRMS	sclerosing/spindle-cell rhabdomyosarcoma
scRNA-seq	single-cell mRNA sequencing
SD	standard deviation
SEER	Surveillance, Epidemiology, and End Results Program
SHH	sonic hedgehog
shRNA	short hairpin ribonucleic acid
siRNA	small interfering ribonucleic acid
SMO	Smoothened
SNP	single nucleotide polymorphism
SNV	single nucleotide variant
SSC	sideward scatter
STR profiling	short tandem repeat profiling
STS	soft tissue sarcoma
SUFU	Suppressor of Fused
t-SNE	t-distributed stochastic neighbor embedding
TBS	Tris-buffered saline

TIDE	Tracking of Indels by Decomposition (analysis)
TME	tumor microenvironment
TMZ	temozolomide
tumoroid	tumor organoid
UDS	undifferentiated sarcoma
UMAP	uniform manifold approximation and projection for dimension reduction
UMI	unique molecular identifier
US	United States
VAC	vincristine / actinomycin-D / cyclophosphamide
VAF	variant allele fraction
VCR	vincristine
VIT	vincristine / irinotecan / temozolomide
WGS	whole-genome sequencing
WHO	World Health Organization
WMA	World Medical Association
Wnt	wingless
WT	wildtype / Wilms tumor
zVAD.fmk	carbobenzoxy-valyl-alanyl-aspartyl-[O-methyl]-fluoromethylketone

1

General Introduction

Michael Torsten Meister

Pediatric Cancer

Cancer is a disease that is characterized by abnormal cellular growth resulting in the formation of tumors that infiltrate healthy tissue and spread to distant body sites (i.e., metastasize). It is one of the main causes of death among adults [1] and a major cause of disease-related death in children and adolescents after infancy in developed countries [2]. The most common cancer types in adults arise from epithelial tissues (i.e., carcinomas) usually from a well-defined cell of origin and their development can frequently be attributed to lifestyle or environmental risk factors [3]. The types of cancer encountered in childhood and adolescents are different, with a large proportion of hematological malignancies [4] and tumors displaying hallmarks of cells halted in their physiological differentiation trajectory with an often unknown cell of origin [5]. While lifestyle and environmental risk factors are thought to be less relevant for the development of pediatric cancer, for a subset of pediatric tumor entities a hereditary tumor disposition that contributes to tumorigenesis can be found [6].

Treatment of pediatric cancer is for most entities based on clinical trials and studies developed by multinational collaborative groups and just as diverse as the entities themselves. The last decades have seen major advances in the treatment of pediatric cancer resulting in an 5-year overall survival (5y-OS) rate of 85% for all children and adolescents with cancer [7]. However, survival across entities varies widely. While some confer an excellent prognosis (such as Hodgkin lymphoma with a 5y-OS of almost 100% [8]), the prognosis of patients suffering from others (e.g., diffuse intrinsic pontine glioma, malignant rhabdoid tumors, or high-risk neuroblastomas), as well as patients suffering from therapy-resistant progressive, relapsed, or metastatic disease often remains poor [9]. In addition, improved prognosis still comes at a high cost for patients given an immense treatment burden at a young age, resulting in potential long-term toxicities [10]. For most entities, treatment regimens are multimodal and consist of local therapy (surgery and/or radiotherapy) and systemic therapy (mostly conventional chemotherapy).

Compared to adult cancer, pediatric cancer is characterized by a vastly lower mutation frequency [11]. In fact, a high proportion of pediatric cancers are driven by a sole tumorigenic alteration, including aberrant fusion transcripts

resulting from genomic translocations [12] or homozygous loss of a crucial gene during development (e.g., *SMARCB1*, encoding a subunit of the SWI/ SNF chromatin remodeling complex, in malignant rhabdoid tumors [13] and epithelioid sarcomas [14] or *H3F3A*, encoding histone H3.3, in diffuse intrinsic pontine glioma [15]).

Targeted therapies aimed at tumor specific genetic alterations have revolutionized the treatment of adult cancer [16]. Although pediatric tumors are driven by highly specific genetic alterations, for only a handful of these have targeted drugs shown efficacy. Examples include drugs targeting the protein product of the *BCR-ABL1* fusion in acute lymphoblastic leukemia [17] and drugs targeting the protein product of *NTRK*-fusions in infantile fibrosarcoma [18].

Taken together, new therapeutic avenues with higher efficacy and lower toxicity are needed for children and adolescents suffering from high-risk cancer types such as rhabdomyosarcoma (RMS), the tumor type studied in this thesis. Key aspects of RMS, including the clinical characteristics, therapy, prognosis, molecular biology and preclinical model systems, will be introduced on the following pages. Moreover, single-cell RNA sequencing will be introduced, which is the technology used for the study presented in chapter 6. Lastly, the overall scope of this thesis is described.

Rhabdomyosarcomas (RMS)

General overview

Rhabdomyosarcomas (RMS) are the most common soft tissue sarcomas (STS) in children and adolescents, comprising 4% of all cancer in this age group and approximately one quarter of all pediatric sarcomas [19]. Sarcomas are malignant tumors arising from mesenchymal progenitors [20]. Depending on the specific cell of origin and/or differentiation, sarcomas display characteristics of different types of connective tissue (e.g., muscles, bones, adipose tissue *etc.*) that arises from the mesenchyme during embryogenesis [21]. RMS display characteristics of skeletal muscle with its defining cell type, the rhabdomyoblast, exhibiting cross-striations, reflective of those in mature myotubes in skeletal muscle [22]. In addition, core proteins of cells in the myogenic differentiation trajectory (i.e., Myogenin and MyoD1) are expressed

by RMS and are important in the histological diagnosis of RMS [23], further indicating the myogenic-lineage commitment of these tumors. RMS can occur in any age group (mostly, however, in children and adolescents) and throughout the body [24].

Subtypes: Histology *versus* fusion type

Historically, RMS have been classified by histological characteristics. In children and adolescents, the embryonal (eRMS, 60% of all cases), alveolar (aRMS, 30% of all cases), and sclerosing/spindle cell (scRMS, less than 10% of all cases) subtypes are the most commonly observed [24]. While eRMS display cellular heterogeneity and characteristics of skeletal muscle progenitor cells [25], aRMS cells are more homogeneous and form structures resembling pulmonary alveoli, hence the name [26]. scRMS were historically treated as a subgroup of eRMS that exhibits a more fascicular spindle cell and/or sclerosing morphology, and were only in 2013 recognized by the WHO as an independent RMS subtype [27]. Besides morphological differences, these subtypes differ in their clinical presentation, underlying molecular alterations and overall prognosis (summarized in Table 1).

Historically, the outcome for embryonal histology has been favorable compared to the outcome for alveolar histology, resulting in histology being a key risk stratification parameter for patients with RMS [34]. As depicted in Table 1, aRMS are usually characterized by the presence of a genomic translocation, resulting in an oncogenic fusion transcript of either *PAX3* or *PAX7* and *FOXO1* in most cases (fusion-positive aRMS, FP-aRMS) [29]. However, a subset of aRMS do not carry the prototypical *PAX3* or *PAX7* containing gene fusions and are therefore classified as fusion-negative aRMS (FN-aRMS). Interestingly, FN-aRMS appear to be indistinguishable from eRMS concerning their molecular make-up and clinical course, including a better prognosis than in patients with FP-aRMS [35,36]. Therefore, given its higher prognostic value, fusion status has replaced histology in the risk stratification systems of recent clinical RMS studies [34]. In fact, current studies differentiate only between fusion-positive and fusion-negative RMS (FP-RMS and FN-RMS, respectively) without taking histology into account (e.g., in the current European Frontline and Relapse RMS (FaR-RMS) study, NCT04625907).

Table 1: *Characteristics of the most common histological subtypes of RMS in children and adolescents. Adapted from* [28] *with added information from* [21,29-33]. *Abbreviations: IHC (immunohistochemistry), F (female), M (male), LOH (loss of heterozygosity).*

	eRMS	aRMS	scRMS
Histology	Small, round-to-elongated cells with interspersed loose myxoid stroma. Anaplasia associated with *TP53* mutations	Discohesive primitive round cells within interwoven fibrous septa	Spindle cell: Relatively differentiated spindle cells with features reminiscent of smooth muscle neoplasms. Sclerosing: Prominent sclerosis/hyalinization with tumor cells arranged in cords, nests, microalveoli, or trabeculae
IHC	Desmin, Myogenin (focal), MyoD1	Desmin, Myogenin (diffuse), MyoD1	Desmin, Myogenin (focal), MyoD1 (focal in spindle cell, diffuse in sclerosing subtype)
Location	Genitourinary tract, head and neck (including orbit), urinary bladder, prostate, biliary tract, abdomen, pelvis, retroperitoneum	Extremities, head and neck, chest, genital organs, abdomen, anal area	Paratesticular, head and neck
Age (years)	< 10	10 – 25	Group 1: congenital / infantile. Group 2: adolescents (with F > M)
Molecular alterations	Aneuploidy with polysomy 8 and other chromosomes; LOH chromosome 11p15.5 (*IGF2* locus); mutations in *RAS* pathway (*NRAS, KRAS, HRAS, NF1, FGFR4*), PI3K signaling (*PTEN, PIK3CA*), *TP53, FBXW7, CTNNB1* and *BCOR*	t(2;13)(q35;q14) → *PAX3-FOXO1*. t(1;13)(p36;q14) → *PAX7-FOXO1*. Additional amplifications of *CDK4* and *MYCN*. 15% are fusion-negative	Group 1: Gene fusions of *SRF-NCOA2, TEAD1-NCOA2, VGLL2-NCOA2, VGLL2-CITED2*. Group 2: *MYOD1* p.L122R mutation
Associated syndromes (mutated gene)	Costello syndrome (*HRAS*), Neurofibromatosis type I (*NF1*), Noonan syndrome (several), DICER1 syndrome (*DICER1*, uterine eRMS), Li-Fraumeni syndrome (*TP53*, often associated with anaplasia)	None reported	None reported
Prognosis	Overall favorable	Overall unfavorable	Group 1: Favorable. Group 2: Unfavorable

Therapy

The therapy of RMS is multi-modal consisting of systemic (i.e., chemotherapy) and local therapy (i.e., surgery and/or radiotherapy) [24]. Current therapeutic regimens have evolved over the last decades thanks to the efforts of multi-national collaborative study groups conducting large-scale clinical studies to optimize therapy. The key findings of these efforts include but are not limited to:

- All pediatric patients suffering from RMS need systemic therapy even in a clinically localized disease setting as the omission of systemic therapy results in a high proportion of relapses, likely due to microscopical metastases already present at diagnosis [37].

- The chemotherapeutic backbone of RMS therapy consists of vincristine and actinomycin-D with the addition of an alkylating agent in standard or (very) high-risk patients. Historically, US studies have used cyclophosphamide as an alkylating agent (courses therefore termed "VAC"), while European studies have used ifosfamide (courses therefore termed "IVA"). Importantly, no difference in efficacy between these alkylating agents has been observed [38].

- The addition of a metronomic maintenance therapy (i.e., oral cyclophosphamide and intravenous vinorelbine) after the intense induction therapy increases the survival of patients with high-risk RMS, resulting in maintenance therapy being the current standard of care [39]. Ongoing studies (such as the above-mentioned European FaR-RMS trial) are evaluating the necessary duration of such maintenance therapies.

- The combination therapy of vincristine, irinotecan, and temozolomide ("VIT" course) provides improved survival in patients with relapsed RMS compared to vincristine plus irinotecan alone, resulting in VIT being the current therapeutic standard for patients with relapsed RMS [40].

- Most patients suffering from RMS need radiotherapy as an additional local therapy modality besides surgery to decrease the risk of local relapses [41]. A therapeutic approach with surgery and adjuvant chemotherapy alone is only feasible in localized FN-RMS at certain body sites (e.g., paratesticular, vaginal).

- As mentioned above, FN-aRMS are clinically and molecularly indistinguishable from eRMS, which resulted in fusion status having replaced histology for risk stratification which in turn governs the treatment regimen used [35,36].

Prognosis

Across all subtypes and risk groups of RMS, 5-year overall survival (5y-OS) for children below the age of 15 is currently 70%, while it is 50% for teenagers from 15 to 19 [42]. Prognosis for patients with RMS has improved over the last decades with 5y-OS rates for patients with localized RMS increasing from 75% to 92% (treatment era 1975 to 1978 *versus* 1992 to 2000) [43]. Similar trends were observed over the same period for patients with RMS with regional spread (i.e., lymph node metastases, 5y-OS from 45% to 69%) and patients with metastatic RMS (5y-OS from 13% to 33%), respectively [43]. While these numbers are encouraging, they clearly illustrate that the prognosis for patients with metastatic RMS is still poor. Importantly, patients with metastatic RMS can be further sub-stratified according to certain additional risk factors like location and number of distant metastases (commonly referred to as "Oberlin risk factors" after the first author of the study evaluating these factors): Patients with zero or one Oberlin risk factor have a long-term survival of 40%, while patients with two or more Oberlin risk factors have a dismal prognosis with only 12% long-term survival, which has not improved over the last decades [44].

In summary, despite major improvements in risk stratification and treatment of RMS over the last decades, prognosis remains poor for patients with high-risk and metastatic disease. Therefore, novel therapeutic strategies are needed for these patients. Studies on the molecular biology of RMS have identified signaling pathways and mutations critical for tumor cell survival, which thus constitute attractive targets for such novel therapies.

The molecular biology of RMS

A block in myogenic differentiation characterizes some RMS

RMS display phenotypic features of cells at different stages of the physiological skeletal muscle differentiation trajectory [21]. This observation resulted in the

hypothesis that the cell of origin of RMS may be a progenitor cell of such muscle, e.g., a myoblast [45]. This, however, does not explain that RMS can arise at body sites devoid of skeletal muscle, e.g., the genitourinary tract. In fact, a recent study has shown that FN-RMS of the head and neck area can arise from endothelial progenitor cells [46]. Thus, it is prudent to assume that the cell of origin of RMS is still under debate with indications that it may be a mesenchymal progenitor cell [47].

As described above, FN-RMS display characteristics of immature skeletal progenitor cells with a varying degree of maturation from undifferentiated mesenchymal progenitor cells to cells resembling myotubes [21]. Interestingly, therapy induces maturation in FN-RMS cells, resulting in resection specimens after neoadjuvant therapy exhibiting areas of variably differentiated cells [48]. FP-RMS are more homogeneous with small cells with prominent nuclei and little cytoplasm [21]. Both subtypes express marker proteins characteristic for developing skeletal muscle, i.e., Desmin, MyoD1, and Myogenin, to a varying degree. While FP-RMS usually express all three of these, FN-RMS can be devoid of or only weakly express MyoD1 and Myogenin while still expressing Desmin [21]. This is in line with the notion that FN-RMS represent cells stuck at an early stage of myogenic development as Desmin precedes MyoD1 and Myogenin here [49], while FP-RMS may represent more mature myogenic progenitors due to their expression of MyoD1 and Myogenin.

Several mechanisms that impede terminal myogenic differentiation in RMS have been proposed [50]. A recent report suggested that in FN-RMS oncogenic *RAS* impedes the expression of *MYOG* (the gene encoding the Myogenin protein), thereby stalling myogenic differentiation at an early step of myogenic differentiation [51]. In FP-RMS, the prototypical *PAX3-FOXO1* fusion alters the epigenetic enhancer landscape to generate so-called "super enhancers" to not only facilitate its own expression but also to hyperactivate *MYCN* and *MYOD1* (the gene encoding MyoD1 protein) expression directly, which in turn promotes *MYOG* expression indirectly [52]. This concomitant constitutive expression of *MYOD1* and *MYOG* disrupts the normal sequential expression of these factors, resulting in impaired myogenic differentiation [52]. In summary, while RMS display hallmarks of developing skeletal muscle, their cell of origin is not necessarily a skeletal muscle progenitor cell.

1

The mutational landscape of RMS

Like most pediatric cancer entities, RMS are characterized by a relatively low mutational burden compared to cancer entities in adults [53], with FN-RMS usually harboring more mutations than FP-RMS [54]. An overview of commonly observed mutations can be found in Table 1.

FN-RMS are characterized by mutations resulting in hyperactivated mitogen-activated protein kinase (MAPK) signaling, i.e., activating mutations in the three main isoforms of *RAS* (*HRAS, KRAS, NRAS*) or *FGFR4,* or inactivating mutations of the tumor suppressor *NF1* [29]. Interestingly, RMS are among the few tumor entities in which mutations in all *RAS* isoforms can occur and there seems to be a correlation of patient-age and affected isoform (e.g., *HRAS* mutations appear to be more common in infants) [32]. Besides such single-gene mutations, chromosomal aberrations are common in FN-RMS including copy-number neutral loss of heterozygosity (LOH) of chromosome 11p15.5 and aneuploidy of chromosome 8 [29]. The proposed sequence of events concerning tumor evolution is that in FN-RMS, the first two hits are the afore-mentioned activating mutations in MAPK signaling and the LOH on chromosome 11p15.5, respectively, followed by aneuploidy on chromosome 8 and further mutations thereafter [55]. Contrary to FP-RMS and the rare scRMS subtype, FN-RMS can be associated with certain hereditary syndromes as shown in Table 1.

FP-RMS are characterized by a prototypical fusion transcript resulting from a balanced genomic translocation [56]. Commonly observed fusion transcripts are *PAX3-FOXO1* and *PAX7-FOXO1*, with the first being the most common [57]. This fusion results from a translocation between chromosome 2 and chromosome 13 (see Table 1) and fuses the first 7 exons of *PAX3* with exon 2 and 3 of *FOXO1* [58]. Several mechanisms of action (MoA) have been proposed for the *PAX3-FOXO1* fusion: Given that the resulting aberrant fusion protein contains the DNA binding domain of *PAX3* and the transactivation domain of *FOXO1*, studies have suggested that this leads to a constitutively high expression of *bona fide PAX3* target genes as the fusion protein can bind to PAX3 DNA binding sites without the physiological cues that are usually necessary to activate its transcription factor activity [59]. In fact, *PAX3* activity is crucial during normal skeletal muscle development as it drives, among

others, the expression of *MYOD1* [60], which is also highly expressed in FP-RMS as discussed above. Besides this proposed function, a recent study suggested that the *PAX3-FOXO1* fusion can also work on an epigenetic level by altering the enhancer landscape of cells as discussed in the section above [52].

Lastly, the rare sclerosing/spindle cell subtype (scRMS) can be subdivided in two types: The congenital type occurring in infants is like the "classical" FP-RMS characterized by a genomic translocation resulting in the presence of an aberrant fusion gene transcript that frequently involves *VGLL2* and *NCOA2* [33]. Prognosis for these patients is favorable [61]. Contrary to this, the second type, which mainly occurs in adolescents, confers a dismal prognosis, and is characterized by a recurring *MYOD1* p.L122R mutation [32]. Interestingly, the resulting mutant MyoD1 protein exhibits a dominant negative effect on physiological MyoD1 DNA binding sites (thus abrogating normal MyoD1 target gene expression) while also aberrantly binding to MYC DNA binding sites, thereby activating the expression of numerous oncogenes under the control of MYC [62].

The role of embryonic signalling pathways in RMS tumorigenesis

Signaling pathways active during embryonic development are silenced in most mature tissues [63]. Physiological exceptions from this are tissue stem cells that regenerate lost or damaged tissue such as in the case of the intestinal epithelial layer which is constantly renewed throughout adult life [64].

A prominent example of such a pathway is the highly-conserved Hedgehog (Hh) signaling pathway [65]. Hh signaling governs various aspects of embryonic development including cell differentiation, tissue polarity, and cell proliferation, and it is furthermore critical for stem cell maintenance in mature tissue [66]. The crucial role of Hh signaling for embryonic development is illustrated by diseases associated with germline mutations in Hh signaling such as holoprosencephaly [67], Gorlin syndrome [68] and Greig cephalopolysyndactyly syndrome [69].

Aberrant activity of Hh signaling has been reported for various cancer such as basal cell carcinomas (BCC), a type of semi-malignant skin cancer, which is

1

often driven by inactivating mutations of *PTCH*, resulting in hyperactivated Hh signaling [70]. Downstream inhibitors of Hh signaling, i.e., Smoothened (SMO) inhibitors, show single-agent efficacy in unresectable BCC [71]. In children, so-called Sonic Hedgehog-Subgroup medulloblastomas (SHH-MB) are driven by hyperactivated Hh signaling [72] and also respond to SMO inhibitors [73].

Aberrant Hh signaling activity has been reported both in FN-RMS [74] and FP-RMS [75]. While one study found that aberrant Hh signaling activity is associated with poor prognosis in FN-RMS [74], another study did not find such an association [76]. Nevertheless, the importance of Hh signaling for RMS tumorigenesis has been illustrated in several studies, to-date [46,77]. Intriguingly, Hh signaling is critical for normal muscle and limb development [78] as well as the maintenance of satellite cells (the tissue stem cells of mature muscle tissue) [79], forming a link to the observation that RMS exhibit features of non-terminally differentiated muscle cells. Consequently, targeting HH signaling via so-called Hh signaling pathway inhibitors (HPIs) became an interesting prospect for the treatment of RMS and was evaluated in several preclinical studies [80–82]. However, no successful single-agent HPI clinical trials have been reported for patients with RMS to-date. Moreover, HPI can lead to irreversible growth plate fusions in young children, impeding height growth [83]. Combination therapies may be able to reduce HPI toxicity while increasing treatment efficacy [84] as targeting relevant signaling pathways is an important area of research to find new treatment possibilities for RMS.

Programmed cell death mechanisms in RMS

Other important signaling pathways in RMS include those regulating programmed cell death (PCD). PCD is vital for the homeostasis of an organism: It preserves the integrity of tissues by maintaining cell populations, removes cells infected by viruses or damaged by other noxious agents, and eradicates dysfunctional cells, including those with mutations that may give rise to malignant tumors [85].

Various mechanisms of PCD have been described to date [85] with apoptosis being by far the most widely studied form [86]. A myriad of factors have been described that initiate and regulate apoptosis with the most important effectors being proteins of the so-called BCL-2 family. The BCL-2 protein

family includes members with pro-apoptotic function (e.g., all so-called BH3-only proteins like NOXA and PUMA, but also downstream effectors like BAK and BAX) as well as members with anti-apoptotic function (e.g., BCL-2 and MCL-1). The fate of a cell is ultimately determined by the balance of pro- and anti-apoptotic BCL-2 family proteins, with apoptosis being undergone if the pro-apoptotic factors predominate [87].

Evasion of apoptosis is key to cancer cell survival and has been appreciated by D. Hanahan and R.A. Weinberg already in the first iteration of "The Hallmarks of Cancer" [88]. Cancer cells achieve this by, among other mechanisms, overexpressing anti-apoptotic BCL-2 family protein members such as the afore-mentioned BCL-2 [89] or MCL-1 [90], thereby shifting the balance towards cell survival. Drugs specifically targeting anti-apoptotic BCL-2 family protein members (so-called BH3-mimetics as they mimic the function of the above-mentioned pro-apoptotic BH3-only proteins) have first been developed and tested in hematological malignancies [91], resulting in the approval of drugs like venetoclax (an orally available, BCL-2 selective BH3-mimetic) for multiple hematological malignancies in adults [92].

High expression of anti-apoptotic BCL-2 family protein members has also been reported for RMS [93–95] and preclinical testing of BH3-mimetics as single-agents or in combination with other drugs has shown efficacy in RMS [96–98]. There is currently one ongoing trial (clinicaltrials.gov identifier NCT03236857) evaluating the safety and efficacy of venetoclax in pediatric hematological and solid tumors (including RMS) for which, however, no definitive study data are available [99].

Model systems of RMS

Cell lines

Preclinical models are required to understand the molecular mechanisms by which signaling pathways such as Hh and PCD drive RMS tumorigenesis. As for most tumor entities to date, the most commonly used preclinical model system for RMS are conventional cell lines given their availability, convenience in use, maintenance, scalability, and overall costs involved [100]. The first RMS cell lines were established more than 30 years ago and are still used today,

with the two most common ones being RD cells for FN-RMS and RH30 cells for FP-RMS [101]. While RD cells harbor mutations common for FN-RMS [29] (e.g., in *NRAS* [102] and *TP53* [103]), RH30 cells carry besides the prototypical *PAX3-FOXO1* fusion gene also an inactivating *TP53* mutation [103], which is usually not observed in FP-RMS in patients [29]. Such uncommon mutations, which may have been acquired during the establishment and/or extensive culturing of cell lines, can potentially reduce the predictive value of cell lines when being used to evaluate the efficacy of therapeutic strategies [104]. Nevertheless, *in vitro* and *in vivo* (when transplanted onto mice, for example) experiments with RMS cell lines have shaped our understanding of RMS tumor biology and have been a cornerstone of preclinical RMS research.

Genetically engineered animal models

Genetically engineered animal models (GEMs) allow for the study of the onset and development of cancer in an organism by introducing mutations of interest into the germline (resulting in the mutation being present in all cells of the organism if not mosaic) or into specific cell lineages at defined time points during development [105,106]. Thus, GEMs proved to be excellent models to study the cell of origin and the specific time window in and during which cancer develops [106], which is particularly interesting in pediatric cancer given that these tumors arise early during human development [107].

A multitude of GEMs exist for RMS spanning mouse but also zebrafish and drosophila models [28]. As discussed above, the cell of origin of RMS is still under debate, which is illustrated by GEM studies showing that RMS can arise from cells from the myogenic lineage (as summarized in [28]), but also endothelial cells in the head and neck region [46]. Interestingly, while the *PAX3-FOXO1* fusion gene is a strong transforming alteration when ectopically expressed in healthy cells *in vitro* [108], it only rarely induces tumors on its own when expressed in a mouse GEM *in vivo* [109]. To increase the penetrance of *PAX3-FOXO1* driven tumors in mice, additional mutations including a mutation in *Trp53* (the mouse equivalent of the human *TP53*, which often has to be mutated in GEMs [110]) were necessary [109], illustrating the limitation of this model as *TP53* mutations are uncommon in FP-RMS. In summary, GEMs have significantly contributed to our understanding of the initiation and

progression of RMS but have not yet resulted in the identification of the cell of origin of RMS.

Patient-derived xenograft models

A recent addition to the repertoire of available preclinical models of RMS are patient-derived xenograft (PDX) models. The principle of PDX models is that when transplanted onto immunodeficient animal hosts, human tumors can engraft and expand with low selective pressure as the host environment supports the normal evolution of the patient tumor, resulting in a preclinical model that closely resembles the patient tumor it was derived from with potential predictive value for treatment efficacy [111]. Disadvantages include the necessary use of animals as hosts and the tumor-entity specific engraftment time which can take up to several months [112]. Furthermore, given that host animals must be immunodeficient to not reject the human tumor tissue, studies on the involvement of the immune system in cancer are challenging and usually require specialized animal model systems [113]. Lastly, there is evidence that not all PDX models are genetically stable [114].

For RMS, such models were first described in immunodeficient mice as so-called orthotopic PDX (O-PDX), meaning that tumors were transplanted at a body site where they have arisen in patients or which resembles the tumor phenotypically (i.e., the musculature of the upper thigh of the mouse in the case of RMS) [115]. The establishment efficacy for O-PDX models of RMS has been reported to be 65%, with engraftment (i.e., the first signs of tumor growth observed in the mice) ranging from 1 to 5.5 months [115]. This means that the time from sample acquisition to performing first experiments in these models usually takes at least two months, limiting this model system's usability in a personalized medicine approach where the time from acquisition to readout (e.g., for drug screening) is critical. Tumor cells derived from established pre-grown mouse RMS O-PDX tumors can be expanded *in vitro* to a limited extent to facilitate high-throughput *in vitro* readouts [116]. Lastly, the RMS PDX approach can be implemented in immunodeficient zebrafish which allows for high throughput, but also results in new challenges (e.g., the lower body temperature of zebrafish which may influence the metabolic activity of the human tumor growing in the fish) [117].

1

In summary, RMS O-PDX possess the highest degree of resemblance to patient tumors and are currently viewed as the gold standard of preclinical models of RMS with the limitations described above.

Introduction to the tumor organoid technology and its prospects for RMS research

The principle of the organoid technology is that tissue stem cells can self-renew and produce their natural progeny if supplied with an adequate *in vitro* culturing environment. Cells then organize in structures most suitable for their growth. The technology was first established in healthy epithelium from mouse small intestine [118] and soon adapted to various other healthy and diseased epithelial tissues, including cancer, resulting in tumor organoid (tumoroid) systems [119]. These systems retain the molecular characteristics of the tumor tissue they were derived from over extended culture periods, indicating their predictive potential for cancer research. Tumoroid models can efficiently be expanded, thereby facilitating high-throughput screening approaches such as small molecule or CRISPR/Cas9-knockout screening [120]. The majority of available systems today consist purely of tumor cells, but recent studies showed efficient co-culturing of tumoroid cells with non-tumor cells (e.g., immune cells) [121].

While the tumoroid technology has been primarily applied to carcinomas, recent studies demonstrated that deriving tumoroid models from non-epithelial cancer is feasible [122–126]. However, applying the tumoroid technology to purely mesenchymal cancers (i.e., sarcomas) has not yet been achieved. Tumoroid models of pediatric nephroblastoma (Wilms tumors) have been described, which, depending on the subtype, can contain mesenchymal cells (i.e., stromal cells) [127]. Studies on synovial sarcoma and other adult soft tissue sarcomas further indicate feasibility as cells derived from these cancers can grow to a limited extent on fetal calf serum, which is, however, undefined in terms of the required essential growth factors [128,129].

Considering the advantages provided by tumoroid systems compared to other preclinical systems, it seemed reasonable to invest in this technology to generate novel preclinical models of RMS. Specifically, tumoroid models of

RMS could combine advantages from conventional cell lines (e.g., scalability) and PDX models (e.g., retention of patient tumor characteristics) and thereby fill a niche currently unoccupied in preclinical RMS research.

Single-cell RNA-sequencing

Available technologies

The most commonly used technologies to sequence RNA today are so-called "bulk" transcriptomic techniques, which refers to the fact that gene expression data obtained from these assays reflect the average of the whole population of cells in the sample analyzed. Bulk transcriptomic techniques such as microarray- or mRNA-sequencing based approaches have vastly improved our understanding of biological processes in cancer cells. Furthermore, by linking these bulk transcriptomic sequencing data to clinical parameters, for various cancer entities risk stratification systems could be refined [130] and predictive models could be proposed [131]. However, these always also reflect the transcriptome of non-malignant cells such as immune or stromal cells. Moreover, while bulk transcriptomic techniques are useful to assess inter-tumoral differences, intra-tumoral transcriptional heterogeneity cannot be faithfully detected. Approaches to deconvolute bulk transcriptomic data to infer cellular heterogeneity have been established [132], but they often lack the ability to detect small but potentially biologically meaningful differences between cells.

To overcome these limitations, sequencing of single-cell transcriptomes has been developed, commonly referred to as single-cell RNA sequencing (scRNA-seq). While the first techniques that enabled the sequencing of the whole transcriptome of a single cell were limited to a handful of cells [133], recent years have seen a steady improvement of this technology with exponential scaling of numbers that can simultaneously be analyzed [134]. Currently, the most used techniques are either plate- or nanodroplet-based. For plate-based sequencing techniques (e.g., SORT-seq [135]), single cells are sorted into the wells of microwell plates (e.g., 384-wells) containing reagents to tag cells ("barcoding") to make a cell identifiable later. Thereafter, cells can be pooled, further processed, and sequenced as a bulk population. During

the downstream bioinformatic analysis, detected mRNA molecules can be assigned to individual cells via the barcode introduced in the first steps. Besides the barcoding of cells, every mRNA molecule is tagged with a so-called unique molecular identifier (UMI), ensuring that it is counted only once in the final analysis, thereby enabling a quantitative analysis [136]. The principle of first barcoding cells and tagging individual mRNA molecules to allow for a pooled analysis later is similar for nanodroplet-based techniques [137,138], which, however, enable an even higher throughput. Here, cells are isolated in a droplet with the necessary reagents (including the cell barcodes and UMIs) by merging two liquid flows (one carrying the cells, one the reagents) in a way that per droplet on average only one cell is captured. While plate-based techniques possess a lower throughput, they result in less sample loss and are therefore suitable for small samples, whereas nanodroplet-based techniques permit a high-throughput analysis in larger samples that allow for losing cells during the processing [139].

Single-cell techniques require that the cells of a tumor sample have been processed to a single cell suspension. Therefore, information on spatial relationships of cells is not captured. While certain bioinformatic algorithms can infer signaling between cells from such samples (e.g., CellChat [140]), true spatial information require other available technologies, which are also computationally and technically more intricate [141].

Opportunities and limitations

The increased resolution of transcriptomic data provided by scRNA-seq to investigate intra-tumoral cell heterogeneity as well as the tumor microenvironment has fundamentally improved our understanding of key hallmarks of cancer such as resistance to treatment [142] or a tumor's propensity to relapse [143]. Thus, scRNA-seq will likely be useful to further refine risk stratification systems or to identify novel predictive biomarkers. This can potentially be even further improved by integrating scRNA-seq with other single-cell genomic technologies (such as single-cell DNA genome sequencing, DNA methylation and chromatin status as reviewed in [144]). scRNA-seq cannot yet be considered standard of care for the analysis of a patient's tumor in a clinical setting in all treatment centers as the technology

is limited by (a) the high-costs involved, (b) the technical and bioinformatic expertise necessary to generate and evaluate scRNA-seq data and (c) by the fact that scRNA-seq as a platform has not yet stabilized. While the first two aspects may not be a limitation in large comprehensive cancer centers, they are in smaller centers. The third aspect (platform stabilization) refers to the fact that scRNA-seq is a technology which still experiences major assay improvements and updates. This means that scRNA-seq data generated at different centers can be difficult to compare as these centers may use different scRNA-seq platforms or versions of the same platform [145]. Lastly, small sample size and low cell viability and, thus, a low number of viable cells can be problematic [146].

Taken together, scRNA-seq and other single-cell genomic technologies offer an unprecedented resolution of intra-tumoral cell heterogeneity, resulting in exciting new studies on the molecular biology of tumors. Prospectively, scRNA-seq can become a cornerstone in the standard of care diagnostics of cancer.

Scope of this thesis

Treatment of patients suffering from RMS is a challenge. While our understanding of the molecular biology of and treatment options for RMS have steadily increased over the last decades, some key questions and problems have not yet been addressed. These include, among others, the lack of effective treatment regimens in high-risk RMS patients, preclinical model systems that can be used to inform treatment decisions in a personalized medicine approach and the lack of understanding of the cellular composition of RMS, which may be indicative for treatment resistance and/or propensity to relapse. The studies described in this thesis address a number of these questions and problems.

In **chapters 2 to 4**, we explore the relationship between aberrant Hh signaling pathway activity and PCD in RMS cell lines. We propose mechanisms by which RMS cells evade apoptosis induction and study how to overcome this by using combination treatments.

As these studies were limited to RMS cell lines, we sought to generate novel preclinical models of RMS which more closely resemble patient tumors. The establishment and characterization of the resulting RMS tumor organoid (tumoroid) models is described in **chapter 5**.

Intrigued by indications of retained cellular heterogeneity of RMS tumors *in vitro* in our tumoroid models, we lastly sought to analyze the cellular composition of primary RMS tumors using scRNA-seq. We describe this study in **chapter 6**.

In **chapter 7**, we summarize and discuss the findings of the previous chapters considering recent studies. We furthermore discuss general aspects and developments in the clinical care of pediatric soft tissue sarcoma patients such as potential benefits of precision medicine programs as well as advantages and disadvantages of centralizing pediatric oncology care and research in large comprehensive cancer centers.

References

1. Centers for Disease Control and Prevention. Deaths and Mortality - Data for the U.S. - 2020.

2. Cunningham, R. M., Walton, M. A. & Carter, P. M. The Major Causes of Death in Children and Adolescents in the United States. *N. Engl. J. Med.* (2018).

3. Weinberg, A. *The Biology of Cancer*. (2013).

4. Pritchard-Jones, K. *et al.* Cancer in children and adolescents in Europe: Developments over 20 years and future challenges. *Eur. J. Cancer* **42**, 2183–2190 (2006).

5. Filbin, M. & Monje, M. Developmental origins and emerging therapeutic opportunities for childhood cancer. *Nature Medicine* vol. 25 367–376 (2019).

6. Akhavanfard, S., Padmanabhan, R., Yehia, L., Cheng, F. & Eng, C. Comprehensive germline genomic profiles of children, adolescents and young adults with solid tumors. *Nat. Commun.* **11**, (2020).

7. Howlander, N. *et al.* SEER Cancer Statistics Review, 1975-2018, National Cancer Institute. Bethesda, MD, https://seer.cancer.gov/csr/1975_2018/, based on November 2020 SEER data submission, posted to the SEER web site, April 2021.

8. Connors, J. M. *et al.* Hodgkin lymphoma. *Nat. Rev. Dis. Prim.* **6**, 61 (2020).

9. Perkins, S. M., Shinohara, E. T., DeWees, T. & Frangoul, H. Outcome for children with metastatic solid tumors over the last four decades. *PLoS One* **9**, (2014).

10. Pui, C.-H. *et al.* Extended Follow-up of Long-Term Survivors of Childhood Acute Lymphoblastic Leukemia. *N. Engl. J. Med.* **349**, 640–649 (2003).

11. Lawrence, M. S. *et al.* Mutational heterogeneity in cancer and the search for new cancer-associated genes. *Nature* **499**, 214–218 (2013).

12. Hehir-Kwa, J. Y. *et al.* Improved Gene Fusion Detection in Childhood Cancer Diagnostics Using RNA Sequencing. *JCO Precis. Oncol.* (2022) doi:10.1200/po.20.00504.

13. Versteege, I. *et al.* Truncating mutations of hSNF5/INI1 in aggressive paediatric cancer. *Nature* **394**, 203–206 (1998).

14. Sullivan, L. M., Folpe, A. L., Pawel, B. R., Judkins, A. R. & Biegel, J. A. Epithelioid sarcoma is associated with a high percentage of SMARCB1 deletions. *Mod. Pathol.* **26**, 385–392 (2013).

15. Khuong-Quang, D.-A. *et al.* K27M mutation in histone H3.3 defines clinically and biologically distinct subgroups of pediatric diffuse intrinsic pontine gliomas. *Acta Neuropathol.* **124**, 439–447 (2012).

16. National Cancer Institute: List of Targeted Therapy Drugs Approved for Specific Types of Cancer.

17. Cario, G. *et al.* BCR-ABL1-like acute lymphoblastic leukemia in childhood and targeted therapy. *Haematologica* vol. 105 2200–2204 (2020).

18. Laetsch, T. W. *et al.* Larotrectinib for paediatric solid tumours harbouring NTRK gene fusions: phase 1 results from a multicentre, open-label, phase 1/2 study. *Lancet Oncol* **19**, 705–714 (2018).

19. Li, J., Thompson, T. D., Miller, J. W., Pollack, L. A. & Stewart, S. L. Cancer incidence among children and adolescents in the United States, 2001-2003. *Pediatrics* **121**, (2008).

20. Yang, J., Ren, Z., Du, X., Hao, M. & Zhou, W. The role of mesenchymal stem/progenitor cells in sarcoma: update and dispute. *Stem cell Investig.* **1**, 18–18 (2014).

21. WHO. WHO Classification of Tumors: Soft Tissue and Bone Tumors. 5th Edition. (2020).

22. Stiller, D. & Holzhausen, H. J. Ultrastructural organization of cell characteristics relevant to diagnosis in rhabdomyosarcomas. *Zentralbl. Allg. Pathol.* **134**, 449–466 (1988).

23. Sebire, N. J. & Malone, M. Myogenin and MyoD1 expression in paediatric rhabdomyosarcomas. *Journal of Clinical Pathology* vol. 56 412–416 (2003).

24. Skapek, S. X. *et al.* Rhabdomyosarcoma. *Nat Rev Dis Prim.* **5**, 1 (2019).

25. Patton, R. B. & Horn, R. G. Rhabdomyosarcoma: Clinical and pathological features and comparison with human fetal and embryonal skeletal muscle. *Surgery* **52**, 572–584 (1962).

26. Enterline, H. T. & Horn, R. C. Alveolar rhabdomyosarcoma; a distinctive tumor type. *Am. J. Clin. Pathol.* **29**, 356–366 (1958).

27. WHO. WHO Classification of Tumours: Soft Tissue and Bone Tumors. 4th Edition. (2013).

28. Kashi, V. P., Hatley, M. E. & Galindo, R. L. Probing for a deeper understanding of rhabdomyosarcoma: insights from complementary model systems. *Nat Rev Cancer* **15**, 426–439 (2015).

29. Shern, J. F. *et al.* Comprehensive genomic analysis of rhabdomyosarcoma reveals a landscape of alterations affecting a common genetic axis in fusion-positive and fusion-negative tumors. *Cancer Discov* **4**, 216–231 (2014).

30. Shenoy, A. *et al.* The prognostic significance of anaplasia in childhood rhabdomyosarcoma: A report from the Children's Oncology Group. *Eur. J. Cancer* **143**, 127–133 (2021).

31. Hettmer, S. *et al.* Anaplastic rhabdomyosarcoma in TP53 germline mutation carriers. *Cancer* **120**, 1068–1075 (2014).

32. Shern, J. F. *et al.* Genomic Classification and Clinical Outcome in Rhabdomyosarcoma: A Report From an International Consortium. *J. Clin. Oncol.* **39**, 2859–2871 (2021).

33. Alaggio, R. *et al.* A Molecular Study of Pediatric Spindle and Sclerosing Rhabdomyosarcoma. *Am. J. Surg. Pathol.* **40**, 224–235 (2016).

34. Rudzinski, E. R. Histology and Fusion Status in Rhabdomyosarcoma. *Am. Soc. Clin. Oncol. Educ. B.* 425–428 (2013) doi:10.14694/edbook_am.2013.33.425.

35. Williamson, D. *et al.* Fusion gene-negative alveolar rhabdomyosarcoma is clinically and molecularly indistinguishable from embryonal rhabdomyosarcoma. *J Clin Oncol* **28**, 2151–2158 (2010).

36. Missiaglia, E. *et al.* PAX3/FOXO1 fusion gene status is the key prognostic molecular marker in rhabdomyosarcoma and significantly improves current risk stratification. *J. Clin. Oncol.* **30**, 1670–1677 (2012).

37. Heyn, R. M. *et al.* The role of combined chemotherapy in the treatment of rhabdomyosarcoma in children. *Cancer* **34**, 2128–2145 (1974).

38. Crist, W. M. *et al.* Intergroup Rhabdomyosarcoma Study-IV: Results for Patients With Nonmetastatic Disease. *J. Clin. Oncol.* **19**, 3091–3102 (2001).

39. Bisogno, G. *et al.* Vinorelbine and continuous low-dose cyclophosphamide as maintenance chemotherapy in patients with high-risk rhabdomyosarcoma (RMS 2005): a multicentre, open-label, randomised, phase 3 trial. *Lancet Oncol.* (2019) doi:10.1016/s1470-2045(19)30617-5.

40. Defachelles, A.-S. *et al.* Randomized Phase II Trial of Vincristine-Irinotecan With or Without Temozolomide, in Children and Adults With Relapsed or Refractory Rhabdomyosarcoma: A European Paediatric Soft Tissue Sarcoma Study Group and Innovative Therapies for Children With Cancer . *J. Clin. Oncol.* **39**, 2979–2990 (2021).

41. Wolden, S. L. *et al.* Indications for Radiotherapy and Chemotherapy After Complete Resection in Rhabdomyosarcoma: A Report From the Intergroup Rhabdomyosarcoma Studies I to III. *J. Clin. Oncol.* **17**, 3468–3475 (1999).

42. Siegel, R. L., Miller, K. D., Fuchs, H. E. & Jemal, A. Cancer statistics, 2022. *CA. Cancer J. Clin.* **72**, 7–33 (2022).

43. Punyko, J. A. *et al.* Long-term survival probabilities for childhood rhabdomyosarcoma: A population-based evaluation. *Cancer* **103**, 1475–1483 (2005).

44. Oberlin, O. *et al.* Prognostic factors in metastatic rhabdomyosarcomas: results of a pooled analysis from United States and European cooperative groups. *J Clin Oncol* **26**, 2384–2389 (2008).

45. Abraham, J. *et al.* Lineage of origin in rhabdomyosarcoma informs pharmacological response. *Genes Dev.* **28**, 1578–1591 (2014).

46. Drummond, C. J. *et al.* Hedgehog Pathway Drives Fusion-Negative Rhabdomyosarcoma Initiated From Non-myogenic Endothelial Progenitors. *Cancer Cell* **33**, 108-124.e5 (2018).

47. Hettmer, S. & Wagers, A. J. Muscling in: Uncovering the origins of rhabdomyosarcoma. *Nature Medicine* vol. 16 171–173 (2010).

48. Arndt, C. A. S., Hammond, S., Rodeberg, D. & Qualman, S. Significance of persistent mature rhabdomyoblasts in bladder/prostate rhabdomyosarcoma: Results from IRS IV. *J. Pediatr. Hematol. Oncol.* **28**, 563–567 (2006).

49. Capetanaki, Y., Milner, D. J. & Weitzer, G. Desmin in muscle formation and maintenance: Knockouts and consequences. in *Cell Structure and Function* vol. 22 103–116 (Japan Society for Cell Biology, 1997).

50. Keller, C. & Guttridge, D. C. Mechanisms of impaired differentiation in rhabdomyosarcoma. *FEBS Journal* vol. 280 4323–4334 (2013).

51. Yohe, M. E. *et al.* MEK inhibition induces MYOG and remodels super-enhancers in RAS-driven rhabdomyosarcoma. *Sci Transl Med* **10**, (2018).

52. Gryder, B. E. *et al.* PAX3-FOXO1 Establishes Myogenic Super Enhancers and Confers BET Bromodomain Vulnerability. *Cancer Discov* **7**, 884–899 (2017).

53. Gröbner, S. N. *et al.* The landscape of genomic alterations across childhood cancers. *Nature* **555**, 321–327 (2018).

54. Casey, D. L. *et al.* Genomic determinants of clinical outcomes in rhabdomyosarcoma. *Clin. Cancer Res.* **26**, 1135–1140 (2020).

55. Chen, L. *et al.* Clonality and Evolutionary History of Rhabdomyosarcoma. *PLOS Genet.* **11**, e1005075 (2015).

56. Turc-Carel, C. *et al.* Consistent chromosomal translocation in alveolar rhabdomyosarcoma. *Cancer Genetics and Cytogenetics* vol. 19 361–362 (1986).

57. Sorensen, P. H. *et al.* PAX3-FKHR and PAX7-FKHR gene fusions are prognostic indicators in alveolar rhabdomyosarcoma: a report from the children's oncology group. *J Clin Oncol* **20**, 2672–2679 (2002).

58. Barr, F. G. Gene fusions involving PAX and FOX family members in alveolar rhabdomyosarcoma. *Oncogene* vol. 20 5736–5746 (2001).

59. Cao, L. *et al.* Genome-wide identification of PAX3-FKHR binding sites in rhabdomyosarcoma reveals candidate target genes important for development and cancer. *Cancer Res* **70**, 6497–6508 (2010).

60. Maroto, M. *et al.* Ectopic Pax-3 activates MyoD and Myf-5 expression in embryonic mesoderm and neural tissue. *Cell* **89**, 139–148 (1997).

61. Whittle, S. *et al.* Congenital spindle cell rhabdomyosarcoma: An international cooperative analysis. *Eur. J. Cancer* **168**, 56–64 (2022).

62. Kohsaka, S. *et al.* A recurrent neomorphic mutation in MYOD1 defines a clinically aggressive subset of embryonal rhabdomyosarcoma associated with PI3K-AKT pathway mutations. *Nat. Genet.* **46**, 595–600 (2014).

63. Perrimon, N., Pitsouli, C. & Shilo, B. Z. Signaling mechanisms controlling cell fate and embryonic patterning. *Cold Spring Harb. Perspect. Biol.* **4**, (2012).

64. Barker, N. Adult intestinal stem cells: Critical drivers of epithelial homeostasis and regeneration. *Nature Reviews Molecular Cell Biology* vol. 15 19–33 (2014).

65. Nüsslein-Volhard, C. & Wieschaus, E. Mutations affecting segment number and polarity in Drosophila. *Nature* **287**, 795–801 (1980).

66. Briscoe, J. & Thérond, P. P. The mechanisms of Hedgehog signalling and its roles in development and disease. *Nat. Rev. Mol. Cell Biol.* **14**, 416–429 (2013).

67. Ming, J. E. *et al.* Mutations in PATCHED-1, the receptor for SONIC HEDGEHOG, are associated with holoprosencephaly. *Hum. Genet.* **110**, 297–301 (2002).

68. Gorlin, R. J. & Goltz, R. W. Multiple Nevoid Basal-Cell Epithelioma, Jaw Cysts and Bifid Rib. *N. Engl. J. Med.* **262**, 908–912 (1960).

69. Kalff-Suske, M. *et al.* Point Mutations Throughout the GLI3 Gene Cause Greig Cephalopolysyndactyly Syndrome. *Hum. Mol. Genet.* **8**, 1769–1777 (1999).

70. Zhang, H. *et al.* Role of PTCH and p53 genes in early-onset basal cell carcinoma. *Am. J. Pathol.* **158**, 381–385 (2001).

71. Danhof, R., Lewis, K. & Brown, M. Small Molecule Inhibitors of the Hedgehog Pathway in the Treatment of Basal Cell Carcinoma of the Skin. *Am J Clin Dermatol* **19**, 195–207 (2018).

72. Taylor, M. D. *et al.* Molecular subgroups of medulloblastoma: the current consensus. *Acta Neuropathol* **123**, 465–472 (2012).

73. Robinson, G. W. *et al.* Vismodegib Exerts Targeted Efficacy Against Recurrent Sonic Hedgehog-Subgroup Medulloblastoma: Results From Phase II Pediatric Brain Tumor Consortium Studies PBTC-025B and PBTC-032. *J Clin Oncol* **33**, 2646–2654 (2015).

74. Zibat, A. *et al.* Activation of the hedgehog pathway confers a poor prognosis in embryonal and fusion gene-negative alveolar rhabdomyosarcoma. *Oncogene* **29**, 6323–6330 (2010).

75. Roberts, W. M., Douglass, E. C., Peiper, S. C., Houghton, P. J. & Look, A. T. Amplification of the gli gene in childhood sarcomas. *Cancer Res* **49**, 5407–5413 (1989).

76. Pressey, J. G., Anderson, J. R., Crossman, D. K., Lynch, J. C. & Barr, F. G. Hedgehog pathway activity in pediatric embryonal rhabdomyosarcoma and undifferentiated sarcoma: a report from the Children's Oncology Group. *Pediatr Blood Cancer* **57**, 930–938 (2011).

77. Almazan-Moga, A. *et al.* Ligand-dependent Hedgehog pathway activation in Rhabdomyosarcoma: the oncogenic role of the ligands. *Br J Cancer* **117**, 1314–1325 (2017).

78. Hu, J. K. H., Mcglinn, E., Harfe, B. D., Kardon, G. & Tabin, C. J. Autonomous and nonautonomous roles of hedgehog signaling in regulating limb muscle formation. *Genes Dev.* **26**, 2088–2102 (2012).

79. Koleva, M. *et al.* Pleiotropic effects of sonic hedgehog on muscle satellite cells. *Cell Mol Life Sci* **62**, 1863–1870 (2005).

80. Ridzewski, R. *et al.* Hedgehog inhibitors in rhabdomyosarcoma: A comparison of four compounds and responsiveness of four cell lines. *Front. Oncol.* **5**, (2015).

81. Satheesha, S. *et al.* Targeting hedgehog signaling reduces self-renewal in embryonal rhabdomyosarcoma. *Oncogene* **35**, 2020–2030 (2016).

82. Tostar, U., Toftgård, R., Zaphiropoulos, P. G. & Shimokawa, T. Reduction of human embryonal rhabdomyosarcoma tumor growth by inhibition of the hedgehog signaling pathway. *Genes and Cancer* **1**, 941–951 (2010).

83. Robinson, G. W. *et al.* Irreversible growth plate fusions in children with medulloblastoma treated with a targeted hedgehog pathway inhibitor. *Oncotarget* **8**, 69295–69302 (2017).

84. Graab, U., Hahn, H. & Fulda, S. Identification of a novel synthetic lethality of combined inhibition of hedgehog and PI3K signaling in rhabdomyosarcoma. *Oncotarget* **6**, 8722–8735 (2015).

85. Galluzzi, L. *et al.* Molecular mechanisms of cell death: recommendations of the Nomenclature Committee on Cell Death 2018. *Cell Death Differ* **25**, 486–541 (2018).

86. Elmore, S. Apoptosis: A Review of Programmed Cell Death. *Toxicologic Pathology* vol. 35 495–516 (2007).

87. Walensky, L. D. BCL-2 in the crosshairs: tipping the balance of life and death. *Cell Death Differ* **13**, 1339–1350 (2006).

88. Hanahan, D. & Weinberg, R. A. The Hallmarks of Cancer. *Cell* **100**, 57–70 (2000).

89. Roberts, A. W. Therapeutic development and current uses of BCL-2 inhibition. *Hematology* **2020**, 1–9 (2020).

90. Wang, H., Guo, M., Wei, H. & Chen, Y. Targeting MCL-1 in cancer: current status and perspectives. *J. Hematol. Oncol.* **14**, 67 (2021).

91. Merino, D. *et al.* BH3-Mimetic Drugs: Blazing the Trail for New Cancer Medicines. *Cancer Cell* **34**, 879–891 (2018).

92. Deeks, E. D. Venetoclax: First Global Approval. *Drugs* **76**, 979–987 (2016).

93. Armistead, P. M. *et al.* Expression of receptor tyrosine kinases and apoptotic molecules in rhabdomyosarcoma: correlation with overall survival in 105 patients. *Cancer* **110**, 2293–2303 (2007).

94. Pazzaglia, L. *et al.* Genetic and molecular alterations in rhabdomyosarcoma: mRNA overexpression of MCL1 and MAP2K4 genes. *Histol Histopathol* **24**, 61–67 (2009).

95. Margue, C. M., Bernasconi, M., Barr, F. G. & Schafer, B. W. Transcriptional modulation of the anti-apoptotic protein BCL-XL by the paired box transcription factors PAX3 and PAX3/FKHR. *Oncogene* **19**, 2921–2929 (2000).

96. Preuss, E., Hugle, M., Reimann, R., Schlecht, M. & Fulda, S. Pan-mammalian target of rapamycin (mTOR) inhibitor AZD8055 primes rhabdomyosarcoma cells for ABT-737-induced apoptosis by down-regulating Mcl-1 protein. *J Biol Chem* **288**, 35287–35296 (2013).

97. Alcon, C. *et al.* Sequential combinations of chemotherapeutic agents with BH3 mimetics to treat rhabdomyosarcoma and avoid resistance. *Cell Death Dis.* **11**, 1–13 (2020).

98. Manzella, G. *et al.* A combinatorial drug screen in PDX-derived primary rhabdomyosarcoma cells identifies the NOXA - BCL-XL/MCL-1 balance as target for re-sensitization to first-line therapy in recurrent tumors. *Neoplasia* **23**, 929–938 (2021).

99. Goldsmith, K. C. *et al.* The first report of pediatric patients with solid tumors treated with venetoclax. *J. Clin. Oncol.* **38**, 10524–10524 (2020).

100. Mirabelli, P., Coppola, L. & Salvatore, M. Cancer cell lines are useful model systems for medical research. *Cancers* vol. 11 (2019).

101. Hinson, A. R. P. *et al.* Human rhabdomyosarcoma cell lines for rhabdomyosarcoma research: Utility and pitfalls. *Front. Oncol.* **3 JUL**, (2013).

102. Schaaf, G. *et al.* Silencing of SPRY1 Triggers Complete Regression of Rhabdomyosarcoma Tumors Carrying a Mutated RAS Gene. *Cancer Res.* **70**, 762–771 (2010).

103. Felix, C. A., Winick, N. J., Crouch, G. D. & Helman, L. J. Frequency and Diversity of p53 Mutations in Childhood Rhabdomyosarcoma. *Cancer Res.* **52**, 2243–2247 (1992).

104. Borrell, B. How accurate are cancer cell lines? *Nature* **463**, 858–858 (2010).

105. Heyer, J., Kwong, L. N., Lowe, S. W. & Chin, L. Non-germline genetically engineered mouse models for translational cancer research. *Nature Reviews Cancer* vol. 10 470–480 (2010).

106. Kersten, K., Visser, K. E., Miltenburg, M. H. & Jonkers, J. Genetically engineered mouse models in oncology research and cancer medicine. *EMBO Mol. Med.* **9**, 137–153 (2017).

107. Chesler, L. & Weiss, W. A. Genetically engineered murine models - Contribution to our understanding of the genetics, molecular pathology and therapeutic targeting of neuroblastoma. *Seminars in Cancer Biology* vol. 21 245–255 (2011).

108. Scheidler, S., Fredericks, W. J., Rauscher, F. J., Barr, F. G. & Vogt, P. K. The hybrid PAX3-FKHR fusion protein of alveolar rhabdomyosarcoma transforms fibroblasts in culture. *Proc. Natl. Acad. Sci. U. S. A.* **93**, 9805–9809 (1996).

109. Keller, C. *et al.* Alveolar rhabdomyosarcomas in conditional Pax3:Fkhr mice: cooperativity of Ink4a/ARF and Trp53 loss of function. *Genes Dev* **18**, 2614–2626 (2004).

110. Jackson, J. G. & Lozano, G. The mutant p53 mouse as a pre-clinical model. *Oncogene* **32**, 4325–4330 (2013).

111. Gao, H. *et al.* High-throughput screening using patient-derived tumor xenografts to predict clinical trial drug response. *Nat. Med.* **21**, 1318–1325 (2015).

112. Pompili, L., Porru, M., Caruso, C., Biroccio, A. & Leonetti, C. Patient-derived xenografts: A relevant preclinical model for drug development. *Journal of Experimental and Clinical Cancer Research* vol. 35 (2016).

113. Shultz, L. D., Brehm, M. A., Garcia-Martinez, J. V. & Greiner, D. L. Humanized mice for immune system investigation: progress, promise and challenges. *Nat. Rev. Immunol.* **12**, 786–798 (2012).

114. Petljak, M. *et al.* Characterizing Mutational Signatures in Human Cancer Cell Lines Reveals Episodic APOBEC Mutagenesis. *Cell* **176**, 1282-1294.e20 (2019).

115. Stewart, E. *et al.* Orthotopic patient-derived xenografts of paediatric solid tumours. *Nature* **549**, 96–100 (2017).

116. Manzella, G. *et al.* Phenotypic profiling with a living biobank of primary rhabdomyosarcoma unravels disease heterogeneity and AKT sensitivity. *Nat. Commun.* **11**, 1–15 (2020).

117. Yan, C. *et al.* Visualizing Engrafted Human Cancer and Therapy Responses in Immunodeficient Zebrafish. *Cell* **177**, 1903-1914.e14 (2019).

118. Sato, T. *et al.* Single Lgr5 stem cells build crypt-villus structures in vitro without a mesenchymal niche. *Nature* **459**, 262–265 (2009).

119. Clevers, H. Modeling Development and Disease with Organoids. *Cell* vol. 165 1586–1597 (2016).

120. Bleijs, M., Wetering, M., Clevers, H. & Drost, J. Xenograft and organoid model systems in cancer research. *EMBO J.* **38**, e101654 (2019).

121. Yuki, K., Cheng, N., Nakano, M. & Kuo, C. J. Organoid Models of Tumor Immunology. *Trends Immunol.* **41**, 652–664 (2020).

122. Abdullah, K. G. *et al.* Establishment of patient-derived organoid models of lower grade glioma. *Neuro. Oncol.* (2021) doi:10.1093/neuonc/noab273.

123. Jacob, F. *et al.* A Patient-Derived Glioblastoma Organoid Model and Biobank Recapitulates Inter- and Intra-tumoral Heterogeneity. *Cell* **180**, 188-204.e22 (2020).

124. Fusco, P. *et al.* Patient-derived organoids (PDOs) as a novel in vitro model for neuroblastoma tumours. *BMC Cancer* **19**, 1–11 (2019).

125. Saltsman, J. A. *et al.* A human organoid model of aggressive hepatoblastoma for disease modeling and drug testing. *Cancers (Basel).* **12**, 1–18 (2020).

126. Yamazaki, S. *et al.* Newly established patient-derived organoid model of intracranial meningioma. *Neuro. Oncol.* **23**, 1936–1948 (2021).

127. Calandrini, C. *et al.* An organoid biobank for childhood kidney cancers that captures disease and tissue heterogeneity. *Nat. Commun.* **11**, (2020).

128. Boulay, G. *et al.* The chromatin landscape of primary synovial sarcoma organoids is linked to specific epigenetic mechanisms and dependencies. *Life Sci. Alliance* **4**, (2021).

129. Brodin, B. A. *et al.* Drug sensitivity testing on patient-derived sarcoma cells predicts patient response to treatment and identifies c-Sarc inhibitors as active drugs for translocation sarcomas. *Br. J. Cancer* **120**, 435–443 (2019).

130. Wang, M. *et al.* Validation of risk stratification models in acute myeloid leukemia using sequencing-based molecular profiling. *Leukemia* **31**, 2029–2036 (2017).

131. van de Vijver, M. J. *et al.* A Gene-Expression Signature as a Predictor of Survival in Breast Cancer. *N. Engl. J. Med.* **347**, 1999–2009 (2002).

132. Avila Cobos, F., Alquicira-Hernandez, J., Powell, J. E., Mestdagh, P. & De Preter, K. Benchmarking of cell type deconvolution pipelines for transcriptomics data. *Nat. Commun. 2020 111* **11**, 1–14 (2020).

133. Tang, F. *et al.* mRNA-Seq whole-transcriptome analysis of a single cell. *Nat. Methods* **6**, 377–382 (2009).

134. Aldridge, S. & Teichmann, S. A. Single cell transcriptomics comes of age. *Nature Communications* vol. 11 (2020).

135. Muraro, M. J. *et al.* A Single-Cell Transcriptome Atlas of the Human Pancreas. *Cell Syst.* **3**, 385-394.e3 (2016).

136. Islam, S. *et al.* Quantitative single-cell RNA-seq with unique molecular identifiers. *Nat. Methods* **11**, 163–166 (2014).

137. Klein, A. M. *et al.* Droplet Barcoding for Single-Cell Transcriptomics Applied to Embryonic Stem Cells. *Cell* **161**, 1187–1201 (2015).

138. Macosko, E. Z. *et al.* Highly Parallel Genome-wide Expression Profiling of Individual Cells Using Nanoliter Droplets. *Cell* **161**, 1202–1214 (2015).

139. Svensson, V., Vento-Tormo, R. & Teichmann, S. A. Exponential scaling of single-cell RNA-seq in the past decade. *Nature Protocols* vol. 13 599–604 (2018).

140. Jin, S. *et al.* Inference and analysis of cell-cell communication using CellChat. *Nat. Commun.* **12**, 1–20 (2021).

141. Ståhl, P. L. *et al.* Visualization and analysis of gene expression in tissue sections by spatial transcriptomics. *Science (80-.).* **353**, 78–82 (2016).

142. Aissa, A. F. *et al.* Single-cell transcriptional changes associated with drug tolerance and response to combination therapies in cancer. *Nat. Commun.* **12**, (2021).

143. Candelli, T. *et al.* Identification and characterization of relapse-initiating cells in MLL-rearranged infant ALL by single-cell transcriptomics. *Leukemia* **36**, 58–67 (2022).

144. Stuart, T. & Satija, R. Integrative single-cell analysis. *Nature Reviews Genetics* vol. 20 257–272 (2019).

145. Chen, W. *et al.* A multicenter study benchmarking single-cell RNA sequencing technologies using reference samples. *Nat. Biotechnol.* **39**, 1103–1114 (2021).

146. Nguyen, Q. H., Pervolarakis, N., Nee, K. & Kessenbrock, K. Experimental considerations for single-cell RNA sequencing approaches. *Frontiers in Cell and Developmental Biology* vol. 6 (2018).
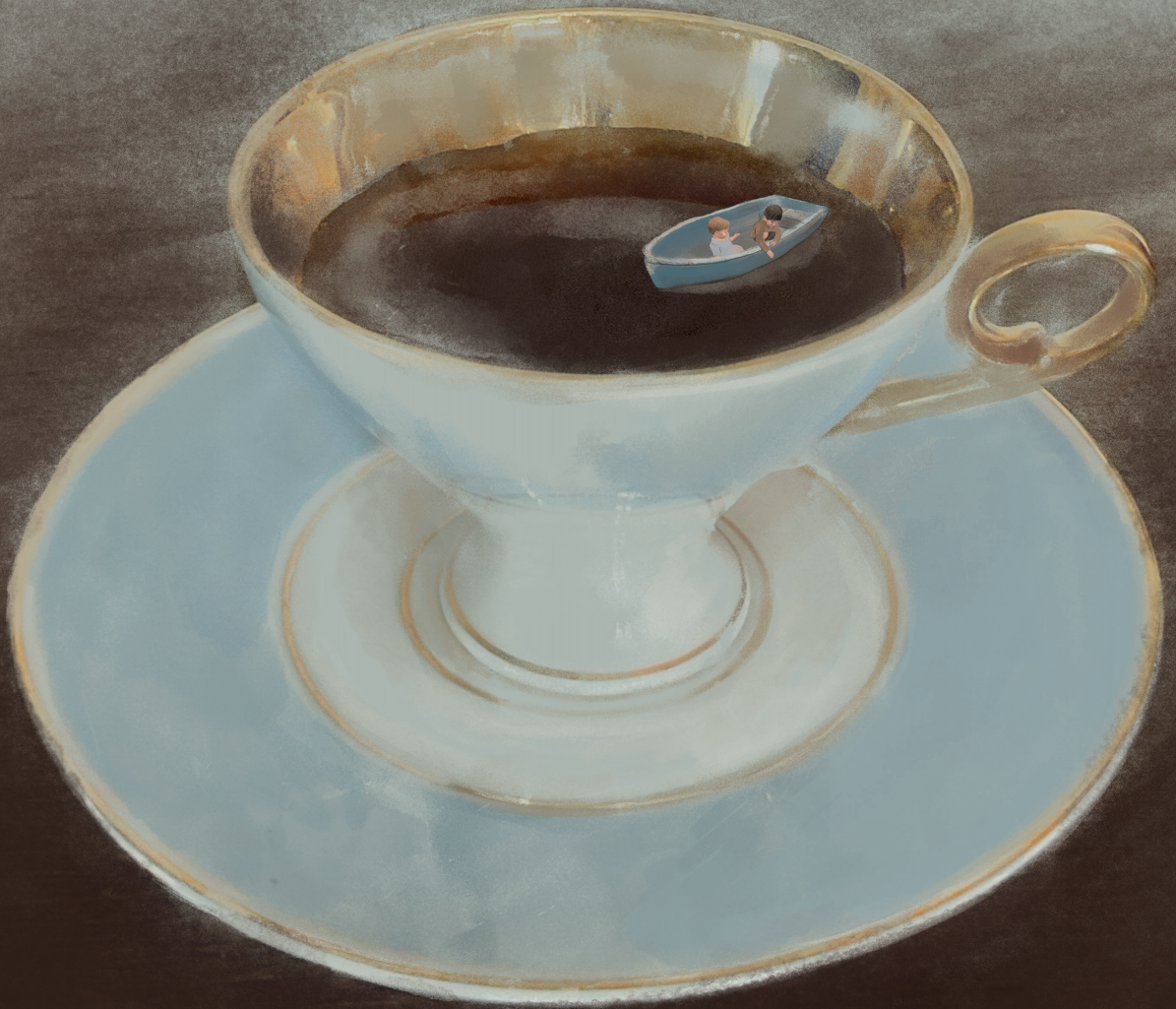
1

Arsenic trioxide induces NOXA-dependent apoptosis in rhabdomyosarcoma cells and synergizes with antimicrotubule drugs

Michael Torsten Meister[1-4], Cathinka Boedicker[1-3], Ulrike Graab[1], Manuela Hugle[1],
Heidi Hahn[5], Thomas Klingebiel[2-4], Simone Fulda[1-3]

[1] Institute for Experimental Cancer Research in Pediatrics, Goethe-University Frankfurt, Komturstr. 3a, 60528, Frankfurt, Germany
[2] German Cancer Consortium (DKTK), Partner Site Frankfurt, Germany
[3] German Cancer Research Center (DKFZ), Heidelberg, Germany
[4] Division of Pediatric Hematology and Oncology, Hospital for Children and Adolescents, Goethe-University, Frankfurt, Germany
[5] Department of Human Genetics, University Medical Center Göttingen, Göttingen, Germany

Abstract

The prognosis of metastatic or relapsed rhabdomyosarcoma (RMS) is poor, highlighting the need of new treatment options. In the present study, we evaluated the *in vitro* efficacy of arsenic trioxide (ATO) in RMS, an FDA-approved drug used in pediatric leukemia. Here, we report that ATO exerts antitumor activity against RMS cells both as single agent and in combination with microtubule-targeting drugs. Monotherapy with ATO reduces cell viability, triggers apoptosis, and suppresses clonogenic survival of RMS cells, at least in part, by transcriptional induction of the proapoptotic BH3-only protein NOXA. siRNA-mediated knockdown of NOXA significantly rescues ATO-mediated cell death, demonstrating that NOXA is required for cell death. Also, ATO suppresses endogenous Hedgehog (Hh) signaling, as it significantly reduces GLI1 transcriptional activity and expression levels of several Hh target genes. Furthermore, we identify synergistic induction of apoptosis by ATO together with several antimicrotubule agents including vincristine (VCR), vinblastine and eribulin. The addition of the broad-range caspase inhibitor zVAD.fmk or overexpression of the antiapoptotic protein BCL-2 significantly reduce ATO/VCR-induced cell death, indicating that the ATO/VCR combination triggers caspase-dependent apoptosis via the mitochondrial pathway. In summary, ATO exerts antitumor activity against RMS, especially in combination with antimicrotubule drugs. These findings have important implications for the development of novel therapeutic strategies for RMS.

Introduction

RMS is the most common soft-tissue sarcoma in children and adolescents and, after brain tumors and neuroblastoma, the third most common solid tumor in these patients [1]. The two main subtypes exhibit characteristic genetic aberrations: while alveolar RMS is characterized by a fusion protein (*PAX3/7-FOXO1*), embryonal RMS typically harbors copy-number neutral loss of heterozygosity on chromosome 11p [2]. Current therapeutic strategies include intense chemotherapy (including VCR, actinomycin-D and others) and irradiation as well as surgery, if applicable. Despite major advances made in the field of pediatric cancer therapy in general, patients with RMS still suffer from poor prognosis, especially in primary metastatic, refractory or relapsed disease [3].

The Hh pathway is an evolutionarily highly conserved signaling cascade with major functions during embryonal development [4]. Postnatally, the Hh pathway is deactivated in most tissues of the body while retaining regenerative functions in others [5]. However, reactivation of the Hh pathway has been reported for a variety of cancer entities [6]. To block aberrant Hh pathway activation in cancer, Hh pathway inhibitors have been developed that target different elements of canonical as well as non-canonical Hh signaling [7]. Canonical Hh signaling is conducted at the so-called primary cilium and activated via binding of one of the three known ligands to the transmembrane receptor Patched (PTCH). This results in an inactivation of PTCH and subsequently in the release of the second transmembrane receptor, Smoothened (SMO). SMO governs expression and/or post-translational processing of the three GLI transcription factors by interacting with and inhibiting Suppressor of Fused (SUFU), which forms complexes with GLI proteins when the pathway is not activated. GLI1 and GLI2 are reported to act mainly as transcriptional activators, while GLI3 functions as a transcriptional repressor [8,9]. GLI proteins can also be activated in a non-canonical and SMO-independent manner via phosphorylation by PI3K/AKT and RAS [10], mTOR/S6 [11], MAPK/ERK [12] or c-MYC [13]. Hh has been shown to be activated in a portion of RMS, especially in embryonal RMS [14]. While one study showed that reactivation of the Hh pathway in RMS is associated with poor survival [14], another study found no such an association [15].

ATO is an FDA-approved drug that is mainly used in the treatment of pediatric and adult patients with acute promyelocytic leukemia [16]. In sarcoma, *in vitro* antitumor activity of ATO treatment has been reported in Ewing sarcoma [17,18], osteosarcoma [19,20] and chondrosarcoma [21]. Recent screening approaches identified ATO, amongst its other functions, as an Hh pathway inhibitor that binds to GLI1 and GLI2, thereby abrogating DNA-binding capacities of these transcription factors [17]. Therefore, ATO diminishes canonical as well as non-canonical Hh signaling [17].

Apoptosis is by far the most extensively studied form of cell death, mediated by effector proteins called caspases [22]. Evasion of apoptosis is a hallmark of cancers and can be mediated by overexpression of antiapoptotic or downregulation of proapoptotic proteins [23]. High expression levels of the antiapoptotic BCL-2 family proteins BCL-2, BCL-x$_L$ and MCL-1 have been reported in RMS [24–26].

In search of novel therapeutic drugs for the treatment of RMS which are already in clinical trials, we investigated the potential of ATO to regulate proapoptotic proteins and to synergize with standard drugs in RMS therapy.

Results

ATO reduces cell viability and clonogenic survival and induces apoptosis in RMS cells

To investigate the therapeutic potential of ATO in RMS we used an embryonal (RD) and an alveolar (RH30) RMS cell line as cellular models. Initially, we determined the effect of ATO on cell viability, cell death and colony formation. ATO reduced cell viability and triggered DNA fragmentation, used as an indicator of apoptotic cell death, in a time- and dose-dependent manner in both cell lines (Fig. 1A and B). Also, ATO significantly suppressed clonogenic survival of RD and RH30 cells, demonstrating its effect on long-term survival (Fig. 1C). These findings demonstrate that ATO exerts antitumor activity against RMS cells.

ATO inhibits endogenous Hh signaling in RD and RH30 cells

ATO was described to act as a Hh pathway inhibitor by binding the transcription factor GLI1, thereby reducing its transcriptional activity [17].
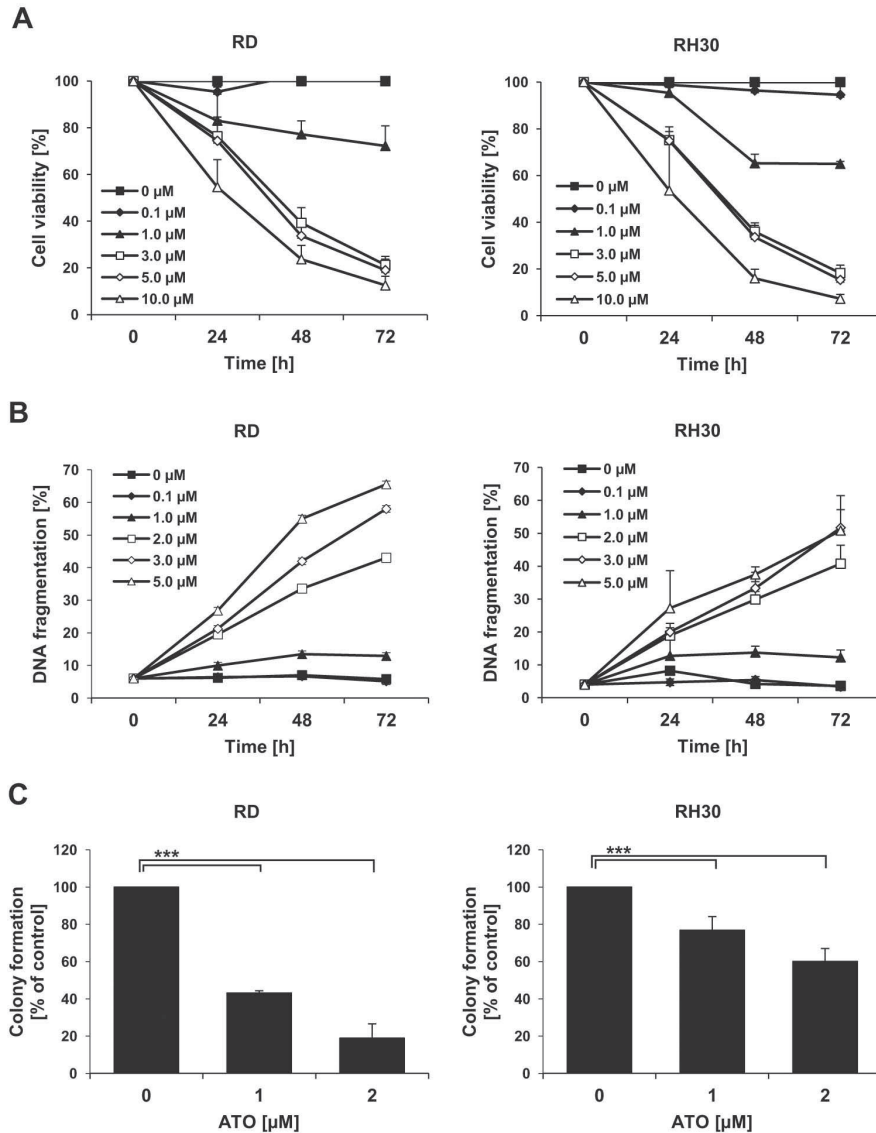
Fig. 1. ATO reduces cell viability and clonogenic survival and induces apoptosis in RMS cells. (**A** and **B**) RD and RH30 cells were treated with indicated concentrations of ATO for 24, 48 or 72 h. Cell viability was measured by MTT assay (**A**) and cell death by analysis of DNA fragmentation of PI-stained nuclei using flow cytometry (**B**). (**C**) RD and RH30 cells were treated with indicated concentrations of ATO for 10 h and colony formation was assessed after 12–15 d as described in the Material and methods section. The number of colonies is expressed as percentage of solvent-treated controls. Mean and SD of three independent experiments performed in triplicate are shown. ***$p < 0.001$.

To evaluate whether ATO also suppresses Hh activity in RMS cells, we determined GLI1 transcriptional activity using luciferase reporter assay. ATO treatment significantly reduced transcriptional activity of GLI1 in both RD and RH30 cells (Fig. 2A). This ATO-imposed suppression of GLI1 transcriptional activity was associated with a significant decrease of several Hh target genes, i.e., *GLI1*, *GLI2*, *PTCH*, *GAS1*, and *HHIP* in RH30 cells and *GAS1* and *HHIP* in RD cells (Fig. 2B). These results show that ATO inhibits Hh pathway activity in RMS cells.

ATO induces NOXA expression and NOXA-dependent cell death

Since we recently reported that the GLI1/2-specific inhibitor GANT-61 induces expression of the proapoptotic BH3-only protein NOXA in RMS cells [27], we hypothesized that ATO-mediated inhibition of Hh signaling might lead to increased expression of NOXA. To test this hypothesis, we monitored *NOXA* mRNA levels by RT-qPCR upon treatment with ATO. Indeed, ATO treatment upregulated *NOXA* mRNA expression (Fig. 3A). To verify that this increase in *NOXA* mRNA levels leads to increased protein levels of NOXA, we performed Western Blot analysis. This showed that ATO caused a significant increase in NOXA protein expression levels in both cell lines (Fig. 3B). To investigate whether the ATO-stimulated induction of NOXA is required for ATO-mediated cell death, we knocked down NOXA by siRNA (Fig. 3C). Importantly, NOXA silencing significantly rescued RMS cells from ATO-triggered apoptosis (Fig. 3D) and increased the percentage of surviving cells (Suppl. Fig. S1). Together, these results show that ATO induces NOXA expression and NOXA-dependent cell death in RMS cells.

ATO synergizes with the antimicrotubule agent VCR to reduce cell viability and clonogenic survival and to induce apoptosis in RMS cells

VCR forms the basis of the majority of chemotherapeutic regimens currently used in the treatment of RMS [28]. Therefore, we tested ATO in combination with VCR against RMS cells. Importantly, we found that VCR synergized with ATO to induce apoptosis in both RMS cell lines (Fig. 4A). The synergism was confirmed by calculation of combination index (CI) values (Table 1A). Furthermore, the combination therapy of ATO and VCR resulted in a more pronounced reduction of cell viability as well as clonogenic survival compared to either drug alone (Fig. 4B and C).
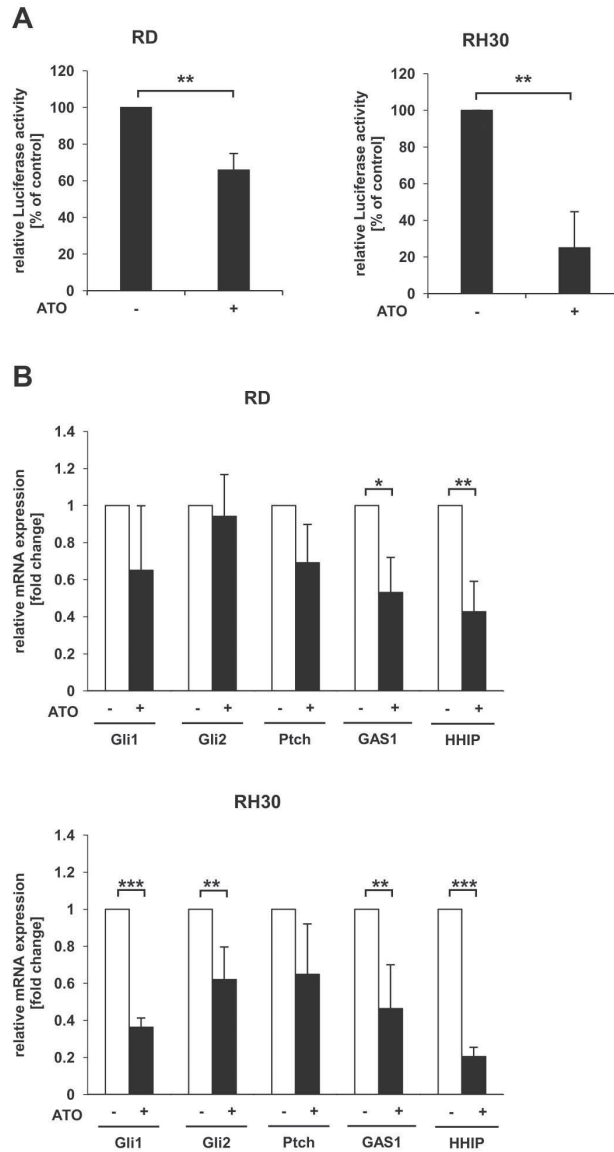
Fig. 2. ATO inhibits endogenous Hh signaling in RD and RH30 cells. (**A**) RD and RH30 cells were transfected with GLI1 luciferase reporter plasmids and treated with 1 μM of ATO for 24 h. GLI1 transcriptional activity was determined using dual-luciferase reporter assay. (**B**) RD and RH30 cells were treated with 1 μM of ATO for 24 h. mRNA expression levels of Hh target genes were determined by RT-qPCR, normalized to *28S* expression and are shown as x-fold change compared to untreated control. Mean and SD of three independent experiments performed in triplicate are shown. *$p < 0.05$; **$p < 0.01$; ***$p < 0.001$.
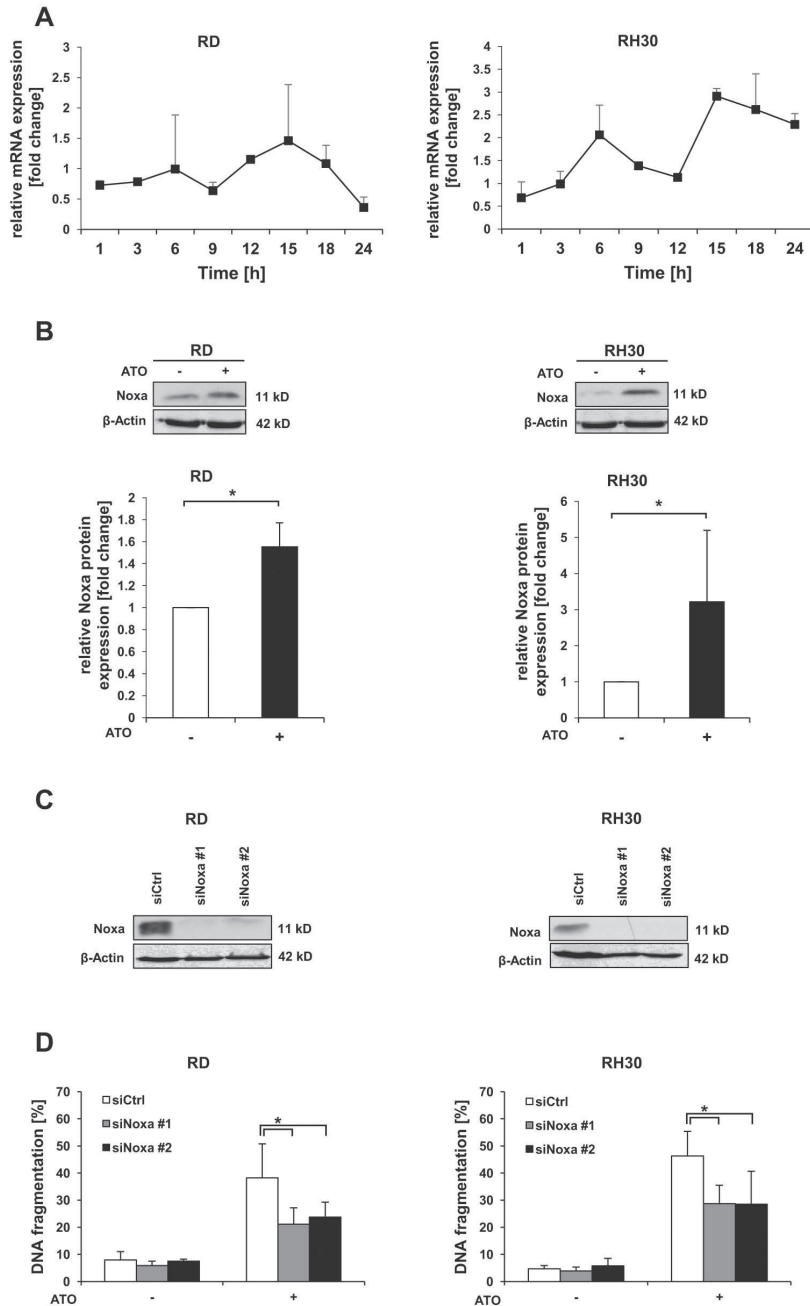
Fig. 3. ATO induces NOXA expression and NOXA-dependent cell death. (**A**) RD and RH30 cells were treated with 2 µM of ATO for indicated h. mRNA expression levels of Hh target genes were determined by RT-qPCR, normalized to *28S* expression and

Fig. 3. Continued

are shown as x-fold change compared to untreated control. Mean and SD of two independent experiments performed in triplicate are shown. (**B**) RD and RH30 cells were treated with 2 µM of ATO for 15 h. Protein expression of NOXA was determined by Western blot analysis, β-ACTIN served as loading control (upper panels). NOXA protein expression was quantified by densitometry and is shown as relative expression compared to untreated control (lower panels). (**C** and **D**) RD and RH30 cells were transiently transfected with two distinct siRNAs targeting NOXA or control siRNA. Protein expression of NOXA was analyzed by Western blotting (**C**). Cells were treated for 72 h with 2 µM ATO and cell death was determined by analysis of DNA fragmentation of PI-stained nuclei using flow cytometry (**D**). Mean and SD of three independent experiments performed in triplicate are shown. *$p < 0.05$.

Previous studies identified antimicrotubule agents such as VCR as inhibitors of canonical Hh signaling, which might be mediated via truncation of the primary cilium where canonical Hh signaling is transmitted [29,30]. Since RH30 cells were reported to form primary cilia that can respond to Hh ligand [31], we hypothesized that VCR and ATO might cooperate to inhibit endogenous Hh signaling. However, VCR neither decreased endogenous GLI1 transcriptional activity nor further reduced ATO-mediated reduction of GLI1 transcriptional activity in RH30 cells (Suppl. Fig. S2A). In addition, VCR neither reduced Hh target genes nor further decreased ATO-mediated transcriptional reduction of these genes (Suppl. Fig. S2B). In summary, ATO and VCR act in concert to inhibit cell proliferation and clonogenic growth and to induce cell death in RMS cell lines. However, this combinatory effect seems to occur regardless of inhibition of Hh signaling by VCR.

ATO synergizes with several antimicrotubule agents to induce apoptosis in RMS cells

To explore whether the synergistic interaction that we found for ATO and VCR also applies to other antimicrotubule agents, we extended our experiments to vinblastine and eribulin. Eribulin is a synthetic analogue of the chemically complex marine natural compound halichondrin B that binds to tubulin and inhibits the assembly and lengthening of fully functional microtubules [32]. Similarly to VCR, ATO acted in concert with vinblastine or eribulin to synergistically trigger cell death in RMS cells (Fig. 5A and B, Table 1B and C). This indicates a class-specific effect of antimicrotubule agents in combination with ATO.
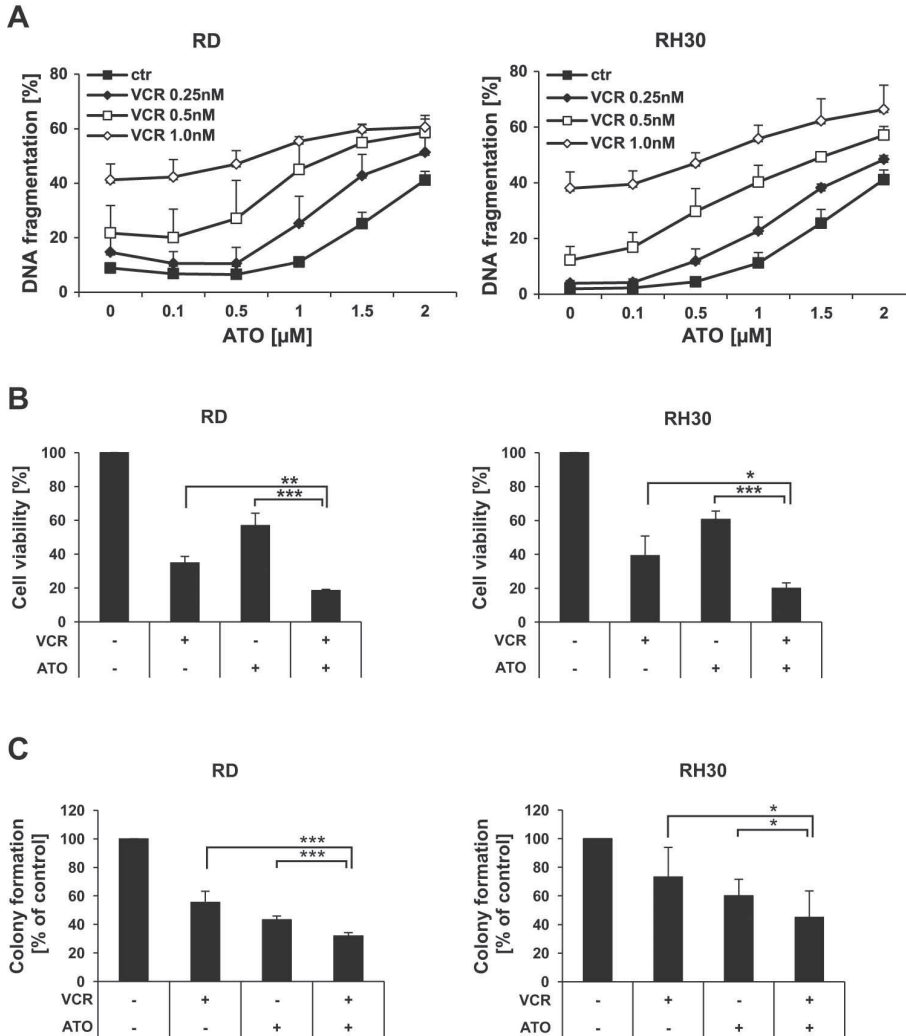
A

B

C

Fig. 4. ATO synergizes with VCR to reduce cell viability and clonogenic survival and to induce apoptosis in RMS cells. (**A**) RD and RH30 cells were treated with indicated concentrations of ATO and VCR for 72 h. Cell death was measured by analysis of DNA fragmentation of PI-stained nuclei using flow cytometry. (**B**) RD and RH30 cells were treated with 1 µM of ATO and/or 0.5 nM VCR for 72 h. Cell viability was measured by MTT assay. (**C**) RD and RH30 cells were treated with 1 µM of ATO and/or 0.5 nM VCR for 10 h and colony formation was assessed after 12–15 d as described in the Material and methods section. The number of colonies is expressed as percentage of solvent-treated controls. Mean and SD of three independent experiments performed in triplicate are shown. *$p < 0.05$; **$p < 0.01$; ***$p < 0.001$.
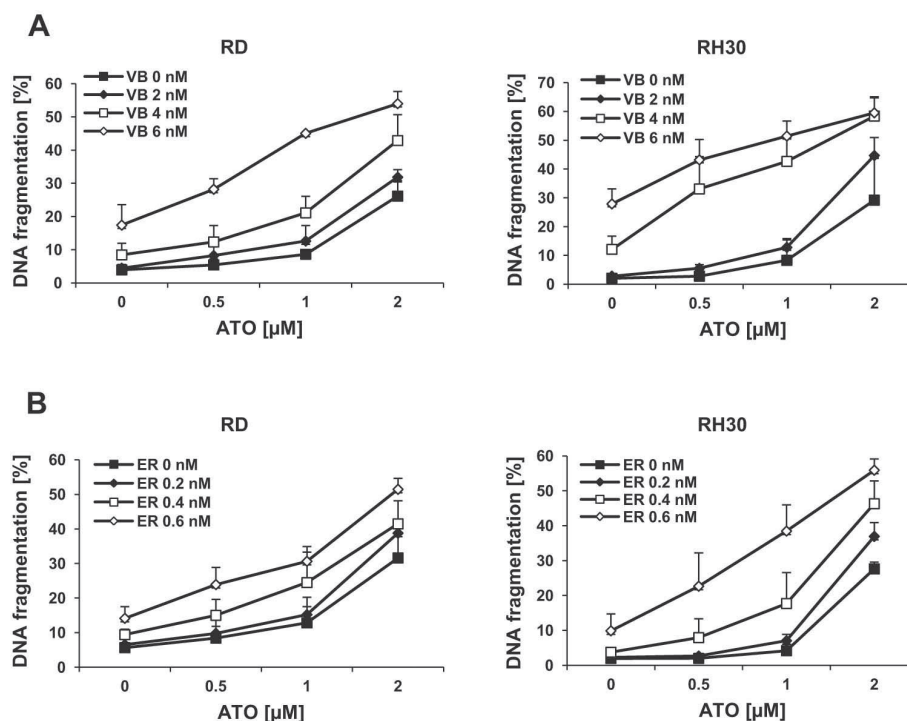
Fig. 5. ATO synergizes with several antimicrotubule agents to induce apoptosis in RMS cells. RD and RH30 cells were treated with different concentrations of ATO and/or vinblastine (**A**) or eribulin (**B**) for 72 h. Cell death was measured by analysis of DNA fragmentation of PI-stained nuclei using flow cytometry. Mean and SD of three independent experiments performed in triplicate are shown.

Overexpression of BCL-2 or inhibition of caspases block ATO/VCR-induced apoptosis

Finally, we investigated the mechanism of cell death induced by the combination treatment with ATO and VCR. To this end, we engineered RMS cells with overexpression of BCL-2 (Fig. 6A), which is known to inhibit proapoptotic proteins such as BAX and BAK that engage mitochondrial apoptosis [33–35]. Ectopic expression of murine BCL-2 (mBcl-2) was confirmed by Western Blotting (Fig. 6A). Of note, BCL-2 overexpression significantly rescued RMS cells from ATO/VCR-mediated cell death compared to the empty vector control (Fig. 6B) and increased the percentage of surviving cells (Suppl. Fig. S3). Furthermore, we examined the requirement of caspases for

ATO/VCR-induced apoptosis by using the pan-caspase inhibitor zVAD.fmk. Importantly, the addition of zVAD.fmk significantly protected RMS cells from ATO/VCR-triggered apoptosis (Fig. 6C). These findings show that BCL-2 overexpression or caspase inhibition block ATO/VCR-induced apoptosis.

Table 1. Synergistic induction of apoptosis by ATO and antimicrotubule drugs. Combination index (CI) was calculated as described in the Materials and methods section for cell death induced by combined treatment for 72 hours with indicated concentrations of ATO and VCR (**A**), vinblastine (**B**) or eribulin (**C**). CI < 0.9 indicates synergism, 0.9–1.1 additivity and > 1.1 antagonism.

A

RD	Vincristine [nM]			RH30	Vincristine [nM]		
ATO [µM]	0.25	0.5	1	ATO [µM]	0.25	0.5	1
0.1	1.398	1.281	0.889	0.1	1.29	0.901	0.954
0.5	1.614	0.871	0.735	0.5	0.859	0.654	0.829
1	0.48	0.398	0.528	1	0.566	0.527	0.699

B

RD	Vinblastine [nM]			RH30	Vinblastine [nM]		
ATO [µM]	2	4	6	ATO [µM]	2	4	6
0.5	1.230	1.278	0.773	0.5	1.395	0.813	0.916
1	1.298	1.063	0.557	1	1.326	0.853	0.940
2	0.894	0.736	0.604	2	0.922	0.892	1.059

C

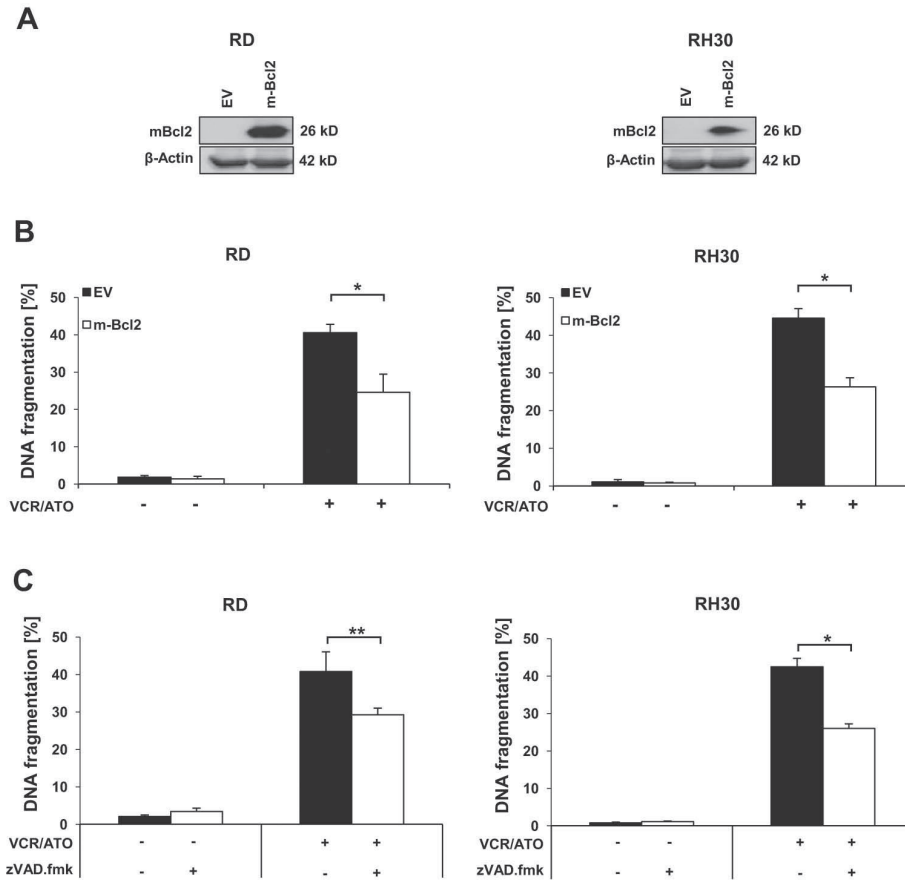| RD	Eribulin [nM]			RH30	Eribulin [nM]		
ATO [µM]	0.2	0.4	0.6	ATO [µM]	0.2	0.4	0.6
0.5	1.310	0.943	0.557	0.5	1.607	1.141	0.664
1	1.020	0.546	0.450	1	1.336	0.932	0.590
2	0.284	0.286	0.188	2	0.817	0.736	0.650

Fig. 6. Overexpression of BCL-2 or inhibition of caspases block ATO/VCR-induced apoptosis. (**A** and **B**) RD and RH30 cells were transduced with murine BCL-2 (mBcl-2) or empty vector (EV) and expression of BCL-2 was assessed by Western blot analysis. β-ACTIN served as loading control (**A**). Cells were treated with 2 µM ATO and 1 nM VCR for 72 h and cell death was measured by analysis of DNA fragmentation of PI-stained nuclei using flow cytometry (**B**). Mean and SD of three independent experiments performed in triplicate are shown. $*p < 0.05$. (**C**) RD and RH30 cells were treated with 2 µM ATO and 1 nM VCR in the presence of 20 µM zVAD.fmk for 72 h. Cell death was measured by analysis of DNA fragmentation of PI-stained nuclei using flow cytometry (**C**). Mean and SD of three independent experiments performed in triplicate are shown. $*p < 0.05$; $**p < 0.01$.

Discussion

In the present study, we found that ATO exerts antitumor activity against RMS cells both as a single agent and in combination therapies. Monotherapy with ATO triggers apoptosis in RMS cells, at least in part, by transcriptional induction of the proapoptotic BH3-only protein Noxa, since ATO upregulates NOXA mRNA and protein levels and since genetic silencing of NOXA knockdown rescues cells from cell death. In addition, ATO inhibits endogenous Hh signaling in RMS cells. We recently reported that the GLI1/2 inhibitor GANT-61 upregulates NOXA expression [27]. Together with our present study showing that ATO inhibits Hh pathway activity and upregulates NOXA expression, these findings point to a link between ATO-mediated inhibition of Hh signaling and upregulation of NOXA. However, further studies are required to explore whether ATO-mediated inhibition of Hh signaling leads to increased NOXA expression and cell death in RMS cells. While ATO has previously been reported to induce NOXA-dependent cell death in multiple myeloma [36], the involvement of Hh signaling has not been addressed in that study.

Furthermore, we show that ATO synergizes with several antimicrotubule agents to induce cell death in RMS cells as confirmed by calculation of CI values. Synergistic induction of cell death was not only found for VCR, a key component of most RMS treatment regimens, but also for vinblastine and eribulin, indicating that ATO broadly acts together with antimicrotubule agents. Mechanistic studies revealed that ATO/VCR co-treatment triggers apoptosis via the mitochondrial pathway and caspase activation, since overexpression of BCL-2, which is known to block mitochondrial outer membrane permeabilization [37], protects cells from ATO/VCR-mediated DNA fragmentation, a hallmark of apoptotic cell death [38]. In addition, rescue experiments using the pan-caspase inhibitor zVAD.fmk demonstrate that cell death induced by ATO and VCR depends on the activation of caspases, key effector molecules of apoptotic cell death [39].

Furthermore, we tested the hypothesis that the observed synergism of ATO and VCR to induce apoptosis is due to their cooperative abrogation of Hh signaling. This hypothesis was based on our current findings showing that ATO inhibits endogenous Hh signaling in RMS cell lines. VCR has previously

been reported to suppress canonical Hh signaling via truncation of the primary cilium, which is critical for canonical Hh signaling [29,30], and RH30 cells have been described to form partially active primary cilia that respond to Hh ligand [31]. However, our data showing that VCR exerts no additional effect on ATO-imposed suppression of GLI1 transcriptional activity or on Hh target gene expression do not support this hypothesis. An explanation for this might be that constitutive Hh activity in RH30 cells is primarily caused by their reported *GLI1* amplification [40] rather than by canonical stimulation of the Hh pathway.

Our study has several important implications. First, there is a clear perspective that the ATO/VCR combination therapy can in principle be translated into clinical use, since VCR is one of the standard-of-care agents in the treatment of RMS patients [28] and since ATO is used in pediatric oncology for acute promyelocytic leukemia [16]. Second, the combination of ATO with antimicrotubule drugs could also be of use in VCR-resistant cases, as we observed a similar synergism for the combination of ATO and other antimicrotubule drugs such as vinblastine and eribulin. Resistance against microtubule targeting agents in RMS has been shown to be mediated not only by drug efflux pumps such as MDR-1 [41], but may also involve additional mechanisms such as mutations in tubulin proteins which lead to impaired binding of these compounds to their target [42]. Since eribulin has been described to bind to tubulin in a different manner than vinca alkaloids [43], it might still be active in VCR-resistant cases where resistance is mediated by mutation of tubulin proteins. Eribulin has been shown to exhibit a high level of activity in preclinical models of different pediatric cancers [44], indicating that it represents a promising drug candidate for childhood cancers. In addition, clinical studies with eribulin have shown a low frequency of treatment discontinuation due to peripheral neuropathy, a typical side effect of antimicrotubule drugs [45]. Third, monotherapeutic ATO might only have limited efficacy *in vivo*, emphasizing the need for ATO-based combination therapies. While ATO as single agent showed broad antitumor efficacy in several *in vitro* models of sarcoma [18,19,21], Smith et al. found no significant *in vivo* activity of ATO against Ewing sarcoma xenografts [46]. Beauchamp et al. observed a significant reduction of tumor growth in ATO-treated mice that was, however, of limited extent [17]. Of note, we identified a synergistic antitumor activity of ATO and antimicrotubule

agents at ATO concentrations that might be clinically achievable, as peak plasma levels up to 0.5 µM ATO were reported in children and adolescents with acute promyelocytic leukemia [47].

In conclusion, our study provides novel insights into the antitumor activity of ATO against RMS and identifies a synergistic combination of ATO and antimicrotubule drugs. These findings have important implications for the development of novel therapeutic strategies for RMS.

Acknowledgements

Materials & Methods

Cell culture and chemicals

RMS cell lines were obtained from the American Type Culture Collection (ATCC) (Manassas, VA, USA). RD cells were maintained in DMEM GlutaMAX™-I medium and RH30 in RPMI 1640 GlutaMAX™-I (Life Technologies, Inc., Carlsbad, CA), both supplemented with 10% fetal calf serum (FCS) (Life Technologies, Inc.), 1% penicillin/streptomycin (Life Technologies, Inc.), and 1 mM sodium pyruvate (Life Technologies, Inc.). Stable overexpression of murine BCL-2 was performed by lentiviral vectors according to protocols previously described [48]. ATO and VCR were purchased from Sigma-Aldrich (Taufkirchen, Germany), and zVAD.fmk from Bachem (Heidelberg, Germany). If not indicated differently, chemicals were purchased from Sigma-Aldrich or Carl Roth (Karlsruhe, Germany).

Determination of cell viability, cell survival, cell death or colony formation

Cell viability was determined by 3-(4,5-dimethylthiazol-2-yl)-2,5-diphenyltetrazolium bromide (MTT) assay according to the manufacturer's instructions (Roche Diagnostics, Mannheim, Germany). Cell death was

determined by flow cytometric analysis (FACSCanto II, BD Biosciences, Heidelberg, Germany) of DNA fragmentation of propidium iodide (PI)-stained nuclei as described previously [49]. For determination of colony formation, cells were seeded (200 cells/well for RD cells, 100 cells/well for RH30 cells) in six-well plates, allowed to settle overnight and treated with ATO for 10 hours. Then, medium was exchanged and colonies were stained after 12–15 days with crystal violet solution (0.5% crystal violet, 30% ethanol, 3% formaldehyde). Colonies were counted and the percentage of colonies relative to solvent-treated controls was calculated.

GLI1 luciferase reporter assay

Cells were transfected with either pGL3-promoter vector (Promega, Mannheim) harboring the *GLI1* promoter or pGL3-control vector as well as renilla luciferase DNA using Lipofectamine 2000 (Invitrogen) and OptiMEM (Life Technologies Inc.) according to the manufacturer's protocol. Six hours after transfection, the medium was changed to regular culture medium. Treatment for 24 h was started 18 h after medium change. Firefly and renilla luciferase activity were measured by microplate reader (Infinite M200, Tecan, Crailsheim, Germany) using the Dual-Luciferase® Reporter Assay System (Promega) according to the manufacturer's protocol.

Quantitative real-time PCR

mRNA levels were determined by quantitative RT-PCR analysis as previously described [50] using peqGOLD Total RNA kit from Peqlab Biotechnologie GmbH (Erlangen, Germany), RevertAid H Minus First Strand cDNA Synthesis Kit (MBI Fermentas GmbH, St. Leon-Rot, Germany) and 7900HT fast real-time PCR system from Applied Biosystems (Darmstadt, Germany). Primers are listed in Supplemental Table S1. At least three independent experiments were performed for each gene.

Transient RNA interference

For transient knockdown of NOXA by siRNA, cells were reversely transfected with 10 nM SilencerSelect siRNA (Invitrogen) for control siRNA (4390843)

or NOXA targeting siRNAs (s10708 and s10710) using Lipofectamine RNAi Max (Invitrogen) and OptiMEM (Life Technologies, Inc.) according to the manufacturer's protocol.

Western blot analysis

Western blot analysis was performed as described previously [51] using the following antibodies: NOXA (Enzo Life Sciences, Farmingdale, NY, USA), murine BCL-2 (10C4, Invitrogen), and β-ACTIN (Sigma-Aldrich). Goat anti-mouse IgG conjugated to horseradish peroxidase (Santa Cruz Biotechnology, Santa Cruz, CA) and enhanced chemiluminescence (Amersham Bioscience, Freiburg, Germany) or infrared dye-labeled secondary antibodies and infrared imaging (Odyssey Imaging System, LI-COR Bioscience, Bad Homburg, Germany) were used for detection. Representative blots of at least two independent experiments are shown. Quantification of blots was performed using ImageJ software (version 1.51a, Wayne Rasband, open source).

Statistical analysis

Statistical significance was assessed by Student's t-Test (two-tailed distribution, two-sample, equal variance). Drug interactions were analyzed by the combination index (CI) method based on that described by Chou [52] using CalcuSyn software (Biosoft, Cambridge, UK). CI < 0.9 indicates synergism, 0.9–1.1 additivity and >1.1 antagonism.

References

1.   Kramer, S., Meadows, A. T., Jarrett, P. & Evans, A. E. Incidence of childhood cancer: experience of a decade in a population-based registry. *J Natl Cancer Inst* **70**, 49–55 (1983).

2.   Merlino, G. & Helman, L. J. Rhabdomyosarcoma--working out the pathways. *Oncogene* **18**, 5340–5348 (1999).

3.   Malempati, S. & Hawkins, D. S. Rhabdomyosarcoma: review of the Children's Oncology Group (COG) Soft-Tissue Sarcoma Committee experience and rationale for current COG studies. *Pediatr Blood Cancer* **59**, 5–10 (2012).

4.   Varjosalo, M. & Taipale, J. Hedgehog: functions and mechanisms. *Genes Dev* **22**, 2454–2472 (2008).

5.   Beachy, P. A., Karhadkar, S. S. & Berman, D. M. Tissue repair and stem cell renewal in carcinogenesis. *Nature* **432**, 324–331 (2004).

6.   Kelleher, F. C., Cain, J. E., Healy, J. M., Watkins, D. N. & Thomas, D. M. Prevailing importance of the hedgehog signaling pathway and the potential for treatment advancement in sarcoma. *Pharmacol. Ther.* **136**, 153–168 (2012).

7.   Low, J. A. & de Sauvage, F. J. Clinical experience with Hedgehog pathway inhibitors. *J Clin Oncol* **28**, 5321–5326 (2010).

8.   Eichberger, T. *et al.* Overlapping and distinct transcriptional regulator properties of the GLI1 and GLI2 oncogenes. *Genomics* **87**, 616–632 (2006).

9.   Ryan, K. E. & Chiang, C. Hedgehog secretion and signal transduction in vertebrates. *J Biol Chem* **287**, 17905–17913 (2012).

10. Stecca, B. *et al.* Melanomas require HEDGEHOG-GLI signaling regulated by interactions between GLI1 and the RAS-MEK/AKT pathways. *Proc. Natl. Acad. Sci.* **104**, 5895–5900 (2007).

11. Wang, Y. *et al.* The Crosstalk of mTOR/S6K1 and Hedgehog Pathways. *Cancer Cell* **21**, 374–387 (2012).

12. Seto, M. *et al.* Regulation of the hedgehog signaling by the mitogen-activated protein kinase cascade in gastric cancer. *Mol. Carcinog.* **48**, 703–712 (2009).

13. Yoon, J. W. *et al.* Noncanonical Regulation of the Hedgehog Mediator GLI1 by c-MYC in Burkitt Lymphoma. *Mol. Cancer Res.* **11**, 604–615 (2013).

14. Zibat, A. *et al.* Activation of the hedgehog pathway confers a poor prognosis in embryonal and fusion gene-negative alveolar rhabdomyosarcoma. *Oncogene* **29**, 6323–6330 (2010).

15. Pressey, J. G., Anderson, J. R., Crossman, D. K., Lynch, J. C. & Barr, F. G. Hedgehog pathway activity in pediatric embryonal rhabdomyosarcoma and undifferentiated sarcoma: a report from the Children's Oncology Group. *Pediatr Blood Cancer* **57**, 930–938 (2011).

16. Stein, E. M. & Tallman, M. S. Acute Promyelocytic Leukemia in Children and Adolescents. *Acta Haematol.* **132**, 307–312 (2014).

17. Beauchamp, E. M. *et al.* Arsenic trioxide inhibits human cancer cell growth and tumor development in mice by blocking Hedgehog/GLI pathway. *J Clin Invest* **121**, 148–160 (2011).

18. Mathieu, J. & Besançon, F. Clinically tolerable concentrations of arsenic trioxide induce p53-independent cell death and repress NF-κB activation in Ewing sarcoma cells. *Int. J. Cancer* **119**, 1723–1727 (2006).

19. Nakamura, S. *et al.* Arsenic Trioxide Prevents Osteosarcoma Growth by Inhibition of GLI Transcription via DNA Damage Accumulation. *PLoS One* **8**, e69466 (2013).

20. Nagao-Kitamoto, H. *et al.* GLI2 is a novel therapeutic target for metastasis of osteosarcoma. *Int. J. Cancer* **136**, 1276–1284 (2015).

21. Jiao, G., Ren, T., Guo, W., Ren, C. & Yang, K. Arsenic trioxide inhibits growth of human chondrosarcoma cells through G2/M arrest and apoptosis as well as autophagy. *Tumor Biol.* **36**, 3969–3977 (2015).

22. Fulda, S. & Debatin, K. M. Extrinsic versus intrinsic apoptosis pathways in anticancer chemotherapy. *Oncogene* **25**, 4798–4811 (2006).

23. Fulda, S. Tumor resistance to apoptosis. *Int J Cancer* **124**, 511–515 (2009).

24. Armistead, P. M. *et al.* Expression of receptor tyrosine kinases and apoptotic molecules in rhabdomyosarcoma: correlation with overall survival in 105 patients. *Cancer* **110**, 2293–2303 (2007).

25. Pazzaglia, L. *et al.* Genetic and molecular alterations in rhabdomyosarcoma: mRNA overexpression of MCL1 and MAP2K4 genes. *Histol Histopathol* **24**, 61–67 (2009).

26. Margue, C. M., Bernasconi, M., Barr, F. G. & Schafer, B. W. Transcriptional modulation of the anti-apoptotic protein BCL-XL by the paired box transcription factors PAX3 and PAX3/FKHR. *Oncogene* **19**, 2921–2929 (2000).

27. Graab, U., Hahn, H. & Fulda, S. Identification of a novel synthetic lethality of combined inhibition of hedgehog and PI3K signaling in rhabdomyosarcoma. *Oncotarget* **6**, 8722–8735 (2015).

28. Weigel, B. J. *et al.* Intensive Multiagent Therapy, Including Dose-Compressed Cycles of Ifosfamide/Etoposide and Vincristine/Doxorubicin/Cyclophosphamide, Irinotecan, and Radiation, in Patients With High-Risk Rhabdomyosarcoma: A Report From the Children's Oncology Group. *J. Clin. Oncol.* **34**, 117–122 (2016).

29. Wang, Y. *et al.* Selective Identification of Hedgehog Pathway Antagonists By Direct Analysis of Smoothened Ciliary Translocation. *ACS Chem. Biol.* **7**, 1040–1048 (2012).

30. Kim, J. *et al.* Itraconazole and Arsenic Trioxide Inhibit Hedgehog Pathway Activation and Tumor Growth Associated with Acquired Resistance to Smoothened Antagonists. *Cancer Cell* **23**, 23–34 (2013).

31. Fu, W., Asp, P., Canter, B. & Dynlacht, B. D. Primary cilia control hedgehog signaling during muscle differentiation and are deregulated in rhabdomyosarcoma. *Proc. Natl. Acad. Sci.* **111**, 9151–9156 (2014).

32. Jain, S. & Vahdat, L. T. Eribulin Mesylate. *Clin. Cancer Res.* **17**, 6615–6622 (2011).

33. Dai, H. *et al.* Contribution of Bcl-2 Phosphorylation to Bak Binding and Drug Resistance. *Cancer Res.* **73**, 6998–7008 (2013).

34. Dlugosz, P. J. *et al.* Bcl-2 changes conformation to inhibit Bax oligomerization. *EMBO J.* **25**, 2287–2296 (2006).

35. Murphy, K. M., Ranganathan, V., Farnsworth, M. L., Kavallaris, M. & Lock, R. B. Bcl-2 inhibits Bax translocation from cytosol to mitochondria during drug-induced apoptosis of human tumor cells. *Cell Death Differ.* **7**, 102–111 (2000).

36. Morales, A. A., Gutman, D., Lee, K. P. & Boise, L. H. BH3-only proteins Noxa, Bmf, and Bim are necessary for arsenic trioxide–induced cell death in myeloma. *Blood* **111**, 5152–5162 (2008).

37. Chipuk, J. E. & Green, D. R. How do BCL-2 proteins induce mitochondrial outer membrane permeabilization? *Trends Cell Biol.* **18**, 157–164 (2008).

38. Galluzzi, L. *et al.* Molecular definitions of cell death subroutines: recommendations of the Nomenclature Committee on Cell Death 2012. *Cell Death Differ.* **19**, 107–120 (2012).

39. Kurokawa, M. & Kornbluth, S. Caspases and Kinases in a Death Grip. *Cell* **138**, 838–854 (2009).

40. Sokolowski, E., Turina, C. B., Kikuchi, K., Langenau, D. M. & Keller, C. Proof-of-concept rare cancers in drug development: the case for rhabdomyosarcoma. *Oncogene* **33**, 1877–1889 (2014).

41. Seitz, G. *et al.* Effects of standard chemotherapy on tumor growth and regulation of multidrug resistance genes and proteins in childhood rhabdomyosarcoma. *Pediatr. Surg. Int.* **23**, 431–439 (2007).

42. Kavallaris, M. *et al.* Multiple microtubule alterations are associated with Vinca alkaloid resistance in human leukemia cells. *Cancer Res.* **61**, 5803–5809 (2001).

43. Bai, R. *et al.* Interactions of Halichondrin B and Eribulin with Tubulin. *J. Chem. Inf. Model.* **51**, 1393–1404 (2011).

44. Kolb, E. A. *et al.* Initial testing (stage 1) of eribulin, a novel tubulin binding agent, by the pediatric preclinical testing program. *Pediatr. Blood Cancer* **60**, 1325–1332 (2013).

45. Dybdal-Hargreaves, N. F., Risinger, A. L. & Mooberry, S. L. Eribulin Mesylate: Mechanism of Action of a Unique Microtubule-Targeting Agent. *Clin. Cancer Res.* **21**, 2445–2452 (2015).

46. Smith, M. A. *et al.* Evaluation of arsenic trioxide by the pediatric preclinical testing program with a focus on Ewing sarcoma. *Pediatr. Blood Cancer* **59**, 753–755 (2012).

2

47. Fox, E. *et al.* Phase 1 trial and pharmacokinetic study of arsenic trioxide in children and adolescents with refractory or relapsed acute leukemia, including acute promyelocytic leukemia or lymphoma. *Blood* **111**, 566–573 (2008).

48. Naumann, I., Kappler, R., von Schweinitz, D., Debatin, K.-M. & Fulda, S. Bortezomib Primes Neuroblastoma Cells for TRAIL-Induced Apoptosis by Linking the Death Receptor to the Mitochondrial Pathway. *Clin. Cancer Res.* **17**, 3204–3218 (2011).

49. Preuss, E., Hugle, M., Reimann, R., Schlecht, M. & Fulda, S. Pan-mammalian target of rapamycin (mTOR) inhibitor AZD8055 primes rhabdomyosarcoma cells for ABT-737-induced apoptosis by down-regulating Mcl-1 protein. *J Biol Chem* **288**, 35287–35296 (2013).

50. Heinicke, U., Kupka, J., Fichter, I. & Fulda, S. Critical role of mitochondria-mediated apoptosis for JNJ-26481585-induced antitumor activity in rhabdomyosarcoma. *Oncogene* **35**, 3729–3741 (2016).

51. Fulda, S., Sieverts, H., Friesen, C., Herr, I. & Debatin, K. M. The CD95 (APO-1/Fas) system mediates drug-induced apoptosis in neuroblastoma cells. *Cancer Res* **57**, 3823–3829 (1997).

52. Chou, T. C. Drug combination studies and their synergy quantification using the Chou-Talalay method. *Cancer Res* **70**, 440–446 (2010).

Supplementary data
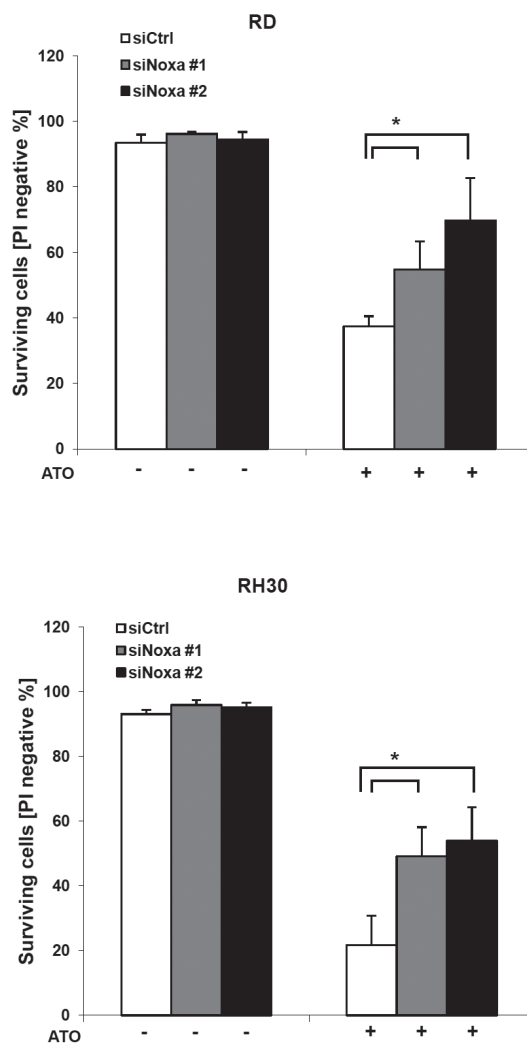
Suppl. Fig. 1. Knockdown of NOXA increases cell survival upon ATO treatment.
RD and RH30 cells were transiently transfected with two distinct siRNAs targeting
NOXA and control siRNA. Cells were treated for 72 h with 2 µM ATO and cell survival
was determined by fluorescence-based microscopic analysis of PI exclusion using
Hoechst 33342 and PI double-staining and ImageXpress Micro XLS Widefield High-
Content Analysis System. PI-negative/Hoechst-positive nuclei were counted as
surviving cells. Mean and SD of at least three independent experiments performed in
triplicate are shown. *$p < 0.05$.

A

B
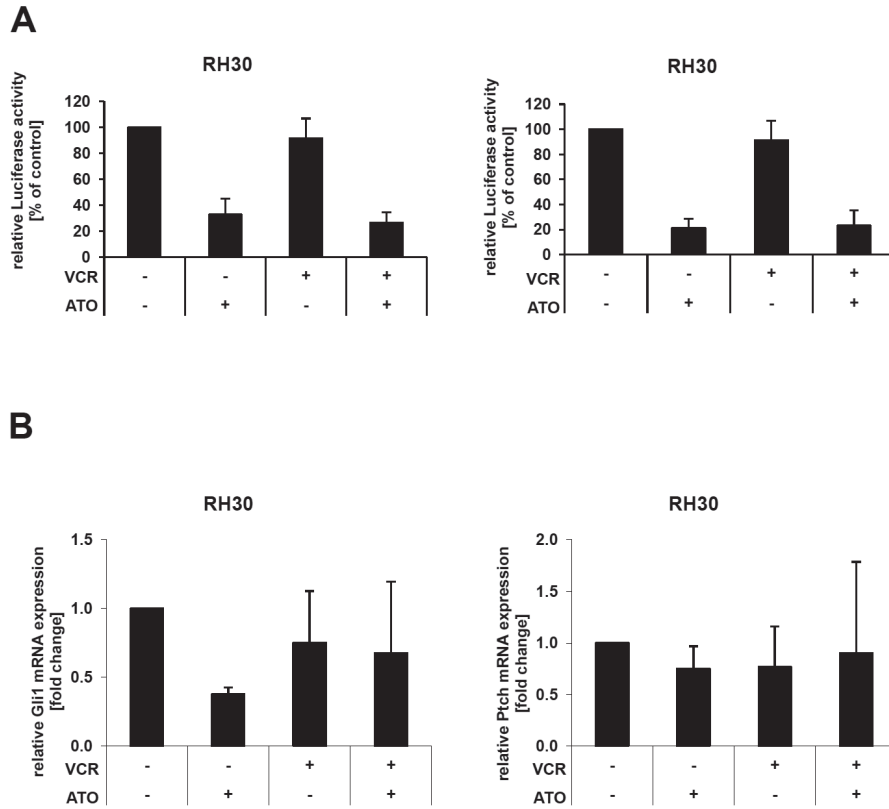
Suppl. Fig. 2. VCR shows no effect on endogenous Hh in RH30 cells. After transfection with the GLI1 luciferase reporter plasmids, RH30 cells were treated with 1 µM of ATO and/or 0.5 nM of VCR for 24 h. Thereafter, *GLI1* transcriptional activity was calculated using a dual-luciferase reporter assay system (**A**). RH30 cells were treated with 1 µM of ATO and/or 0.5 nM of VCR for 24 h, after which relative decrease of *GLI1* and PTCH mRNA was calculated (**B**). Mean plus SD of three independent experiments performed in triplicate are shown.

2
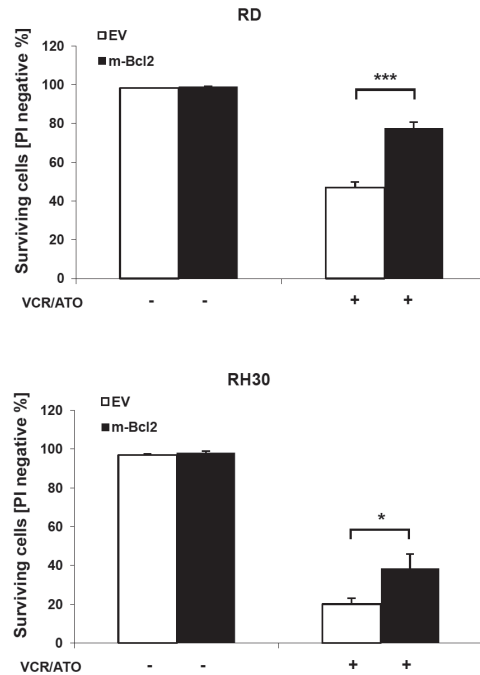
Suppl. Fig. 3. Overexpression of BCL-2 increases cell survival upon ATO treatment. RD and RH30 cells transduced with murine BCL-2 or empty vector (EV) were treated with 2 µM ATO and 1 nM VCR for 72 h. Cell survival was determined by fluorescence-based microscopic analysis of PI exclusion using Hoechst 33342 and PI double-staining and imageXpress Micro XLS Widefield High-Content Analysis System. PI-negative/Hoechst-positive nuclei were counted as surviving cells. Mean and SD of three independent experiments performed in triplicate are shown. *$p < 0.05$.

Suppl. Table 1. Primer sequences. Listed are all primer sequences used for RT-qPCR experiments.

Primer	Sequence
h28S_for	5'-TTGAAAATCCGGGGGAGAG-3'
h28S_rev	5'-ACATTGTTCCAACATGCCAG-3'
hNoxa_for	5'-GGAGATGCCTGGGAAGAAG-3'
hNoxa_rev	5'-CCTGAGTTGAGTAGCACACTCG-3'
hGli1_for	5'-CAGGGAGGAAAGCAGACTGA-3'
hGli1_rev	5'-ACTGCTGCAGGATGACTGG-3'
hGli2_for	5'-CACGCTCTCCATGATCTCTG-3'
hGli2_rev	5'-CCCCTCTCCTTAAGGTGCTC-3'
hPtch_for	5'-GAGGTTGGTCATGGTTACATGGA-3'
hPtch_rev	5'-TGCTGTTCTTGACTGTGCCACC-3'
hGAS1_for	5'-TCTCGACAGCTGTTCATTTCC-3'
hGAS1_rev	5'-GCAGAAGGTCCCCTTTCG-3'
hHHIP_for	5'-TTCACAAACTTGTTCAAAGTGGA-3'
hHHIP_rev	5'-ATGCGAGGCTTAGCAGTCC-3'

2

Hedgehog signaling negatively co-regulates BH3-only protein NOXA and TAp73 in *TP53*-mutated cells

Michael Torsten Meister[1-4], Cathinka Boedicker[1-3], Thomas Klingebiel[2-4], Simone Fulda[1-3]

[1] Institute for Experimental Cancer Research in Pediatrics, Goethe-University, Frankfurt, Komturstr. 3a, 60528, Frankfurt, Germany
[2] German Cancer Consortium (DKTK), Partner Site Frankfurt, Germany
[3] German Cancer Research Center (DKFZ), Heidelberg, Germany
[4] Division of Pediatric Hematology and Oncology, Hospital for Children and Adolescents, Goethe-University, Frankfurt, Germany

Abstract

In the present study, we show that pharmacological repression by the Hedgehog (Hh) pathway inhibitor (HPI) GANT61 induces expression of the proapoptotic protein NOXA in *TP53*-mutated embryonal pediatric tumor cells driven by Hh signaling (i.e., rhabdomyosarcoma (RMS) and medulloblastoma (MB)). Similarly, genetic silencing of GLI1 by siRNA causes increased NOXA mRNA and protein levels, while overexpression of GLI1 results in decreased NOXA expression. Furthermore, TAp73 mRNA and protein levels are increased upon GLI1 knockdown, while GLI1 overexpression reduces TAp73 mRNA and protein levels. However, knockdown of TAp73 fails to block NOXA induction in GANT61-treated cells, suggesting that NOXA is not primarily regulated by TAp73. Interestingly, mRNA levels of the transcription factor *EGR1* correlate with those of *NOXA* and *TAp73*. Silencing of EGR1 results in decreased *NOXA* and *TAp73* mRNA levels, indicating that EGR1 is involved in regulating transcriptional activity of NOXA and TAp73. These findings suggest that GLI1 represses NOXA and TAp73, possibly via EGR1. These findings could be exploited for the treatment of Hh-driven tumors, e.g., for their sensitization to chemotherapeutic agents.

Introduction

RMS is the most common soft-tissue sarcoma in pediatric patients and, after brain tumors and neuroblastoma, the third most common solid tumor entity in this patient cohort [1]. RMS comprise two major subtypes: While alveolar RMS (aRMS) are characterized by a fusion gene (*PAX3-* or *PAX7-FOXO1*), embryonal RMS (eRMS) commonly harbor a copy-number neutral loss of heterozygosity (LOH) on chromosome 11p [2]. Recent sequencing studies suggest a low mutational burden for aRMS, while eRMS typically harbor alterations in the *TP53* tumor suppressor gene (including LOH on chromosome 17p13.1, which harbors the *TP53* gene) and in the *RAS* (i.e., *HRAS*, *KRAS* and *NRA*S) oncogenes [3]. MB is the most common malignant tumor in the central nervous system (CNS) of children and adolescents [1]. In recent years, MB classification has been revised based on molecular features rather than histological features of the tumor with now four distinct subgroups: Wingless (Wnt) driven MB, Sonic Hh (SHH) driven MB, group 3 MB and group 4 MB [4].

The Hh pathway is an evolutionarily highly conserved signaling cascade with major functions during embryonal development [5]. After birth, Hh signaling is commonly deactivated in most body tissues while retaining regenerative functions in others (e.g., in muscle or hair follicle cells) [6]. Canonical Hh signaling is conducted at the so-called primary cilium and activated after binding of one of the three known ligands to the transmembrane receptor Patched (PTCH). This leads to the inactivation of PTCH and subsequently to the release of the second transmembrane receptor Smoothened (SMO). SMO governs expression and/or post-translational processing of the three GLI transcription factors by interacting with and inhibiting Suppressor of Fused (SUFU), which forms complexes with GLI proteins when the pathway is not activated. GLI1 and GLI2 have been reported to act mainly as transcriptional activators, while GLI3 functions as a transcriptional repressor [7,8]. Aberrant reactivation of Hh signaling has been observed in a variety of tumor entities and has been linked to tumorigenesis. Here, Hh signaling facilitates transcription of factors promoting cell cycle progression, proliferation and evasion of cell death such as apoptosis (i.e., BCL-2) [9,10]. Apoptosis is by far the most extensively studied form of cell death [11]. Evasion of apoptosis is a hallmark of human cancers and can be mediated by overexpression of antiapoptotic or by downregulation of proapoptotic proteins [12]. High expression

levels of the antiapoptotic BCL-2 family proteins BCL-2, BCL-x$_L$ and MCL-1 have been reported in RMS [13–15] as well as MB [16,17]. Importantly, switching the balance of pro- and antiapoptotic BCL-2 proteins towards proapoptotic BCL-2 proteins is regarded as a key to overcome tumor resistance [18].

Hh signaling has been shown to be activated in childhood cancers at different levels of the pathway such as PTCH or SUFU, but also often downstream on the level of the GLI proteins, in particular in a portion of embryonal pediatric tumors (i.e., eRMS and fusion gene-negative aRMS (with occasional *GLI1* amplifications) [19,20] and SHH MB [4]). In eRMS and fusion gene-negative aRMS, a study showed that reactivation of the Hh pathway is associated with poor survival [19], while another study did not find any such association [21]. In SHH MB, germline mutations of *PTCH* (resulting in Gorlin syndrome) [22] and *SUFU* [23] as well as somatic mutations in *PTCH*, *SMO*, *SUFU* and amplifications in *GLI1* and *GLI2* have been observed [24–26]. Importantly, patients with SHH MB harboring *TP53* mutations (21% of SHH MB, in 56% of the cases germline mutation of *TP53* resulting in Li-Fraumeni syndrome) show a much poorer prognosis than patients with functional *TP53* [27].

To target aberrant Hh signaling activity HPIs have been developed that target different proteins in the Hh pathway signaling cascade [28]. Vismodegib and sonidegib target Hh signaling on the level of SMO. Both compounds have been evaluated in patients with advanced MB [29]. Here, tumor responses have only been observed in tumors with Hh signaling activation on the upstream level of SMO [29].

We recently reported that pharmacological inhibition of GLI1 increases mRNA and protein expression of proapoptotic BH3-only proteins including NOXA [30]. In the present study, we investigated the mechanism by which inhibition of Hh signaling may induce NOXA in embryonal pediatric tumors harboring inactivating *TP53* mutations.

Results

Pharmacological inhibition of GLI1 results in NOXA upregulation

To investigate whether inhibition of Hh signaling leads to an upregulation of the proapoptotic BH3-only protein NOXA in embryonal pediatric tumor cells

harboring a *TP53* mutation, we selected several *TP53*-mutated cancer cell lines. Abrogation of Hh signaling activity was confirmed by decreased GLI1 target gene expression (Suppl. Fig. 1) with no alterations of GLI1 protein levels (Suppl. Fig. 2). Of note, treatment with the GLI1 inhibitor GANT61 increased expression of NOXA protein in the aRMS cell line RH30, the eRMS cell line RD and the MB cell line DAOY (Fig. 1A–C), which are all *TP53*-mutated. This suggests that Hh signaling suppresses NOXA expression.
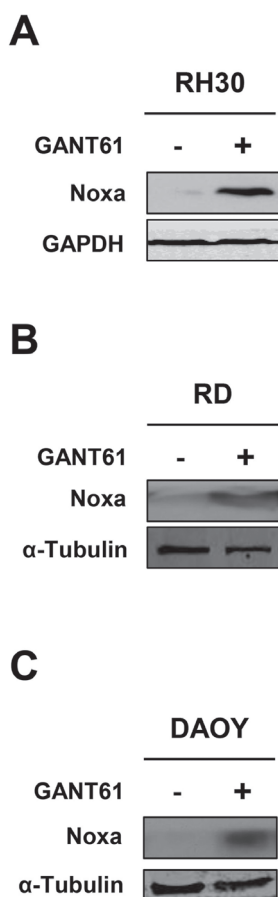

Fig. 1. Pharmacological inhibition of GLI1 results in NOXA upregulation. (**A** to **C**), RH30, RD and DAOY cells were treated with GANT61 (RH30 8 µM (**A**), RD 6 µM (**B**), DAOY 10 µM (**C**)) for 6 h (RD, DAOY) or 24 h (RH30). Protein expression of NOXA was determined by Western blot analysis, GAPDH and α-TUBULIN served as loading controls.

siRNA-mediated knockdown of GLI1 causes transcriptional upregulation of NOXA

To further evaluate NOXA regulation by Hh signaling, we also investigated whether silencing of GLI1 causes upregulation of NOXA. To this end, we knocked down GLI1 in RH30 cells which harbor high GLI1 levels due to amplification [21]. Control experiments confirmed that GLI1 silencing by two distinct siRNA targeting constructs significantly decreased mRNA levels of the GLI1 target genes *GLI1* and *HHIP* compared to cells transfected with control, non-silencing siRNA (Fig. 2A and B). Of note, knockdown of GLI1 resulted in elevated NOXA protein levels (Fig. 2C). To test if decreased NOXA protein levels were due to inhibition of transcriptional activity of NOXA, we assessed *NOXA* mRNA levels by RT-qPCR. Here, knockdown of GLI1 resulted in an increase of *NOXA* mRNA levels (Fig. 2D). These findings emphasize that GLI1 represses transcription of *NOXA*.

Overexpression of GLI1 leads to transcriptional downregulation of NOXA

To directly test if Hh signaling negatively regulates NOXA expression we created RD cells overexpressing GLI1 (Fig. 3A). To confirm activation of the Hh pathway, we performed a GLI1 luciferase reporter assay which showed a significant increase in GLI1 transcriptional activity in GLI1-overexpressing RD cells compared to empty vector (EV) control cells (Fig. 3B). Also, expression of the Hh pathway target gene *HHIP* was significantly elevated in RD cells overexpressing GLI1 compared to EV control cells (Fig. 3C). Importantly, overexpression of GLI1 resulted in reduced NOXA protein levels (Fig. 3A). In addition, *NOXA* mRNA levels were decreased in RD cells with GLI1 overexpression compared to EV cells (Fig. 3D).

Since NOXA is a short-lived protein that is regulated also posttranslationally [31–33], we investigated whether decreased basal protein levels of NOXA in RD cells overexpressing GLI1 were mediated by increased proteasomal degradation. To this end, we used the proteasome inhibitor bortezomib. While addition of bortezomib caused accumulation of NOXA protein levels in both GLI1-overexpressing and the corresponding EV cells, RD cells overexpressing GLI1 showed significantly lower NOXA protein levels upon

bortezomib treatment than EV cells (Fig. 3E). This underscores that, besides the proteasome, also transcriptional mechanisms are involved in regulating NOXA levels.
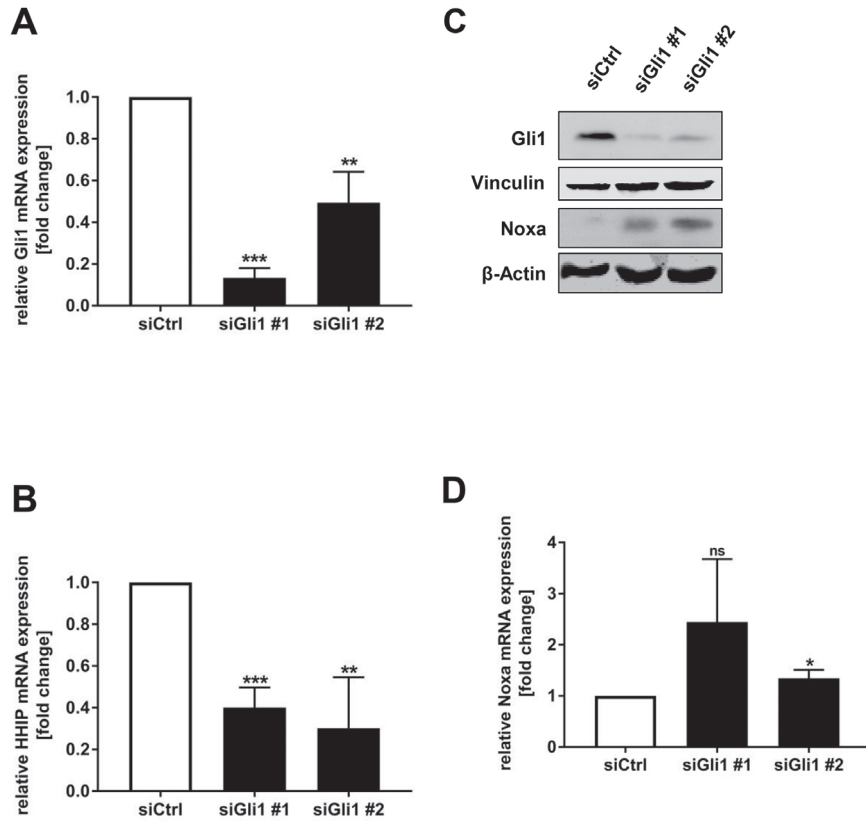
Fig. 2. siRNA-mediated knockdown of GLI1 causes transcriptional upregulation of NOXA. RH30 cells were transiently transfected with two distinct siRNAs targeting *GLI1* or control siRNA. In **A**, **B** and **D**, mRNA levels of *GLI1* 24 h (**A**), of *HHIP* 30 h (**B**) and of *NOXA* 36 h (**D**) after reverse transfection were determined by RT-qPCR, normalized to *28S* expression and are shown as x-fold change compared to siRNA control. Mean and SD of three independent experiments performed in duplicate are shown. *$p < 0.05$, **$p < 0.01$, ***$p < 0.001$. In C, protein expression of GLI1 and NOXA 36 h after reverse transfection was analyzed by Western blot analysis. VINCULIN and β-ACTIN served as loading controls.
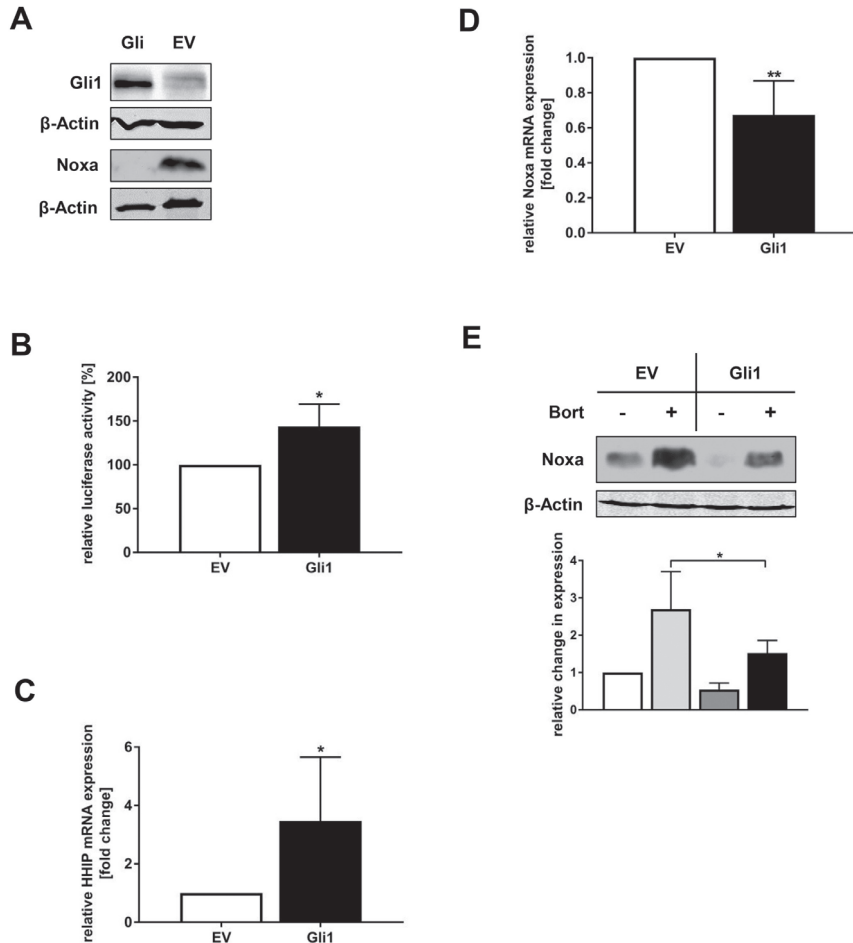
Fig. 3. Overexpression of GLI1 leads to transcriptional downregulation of NOXA.
(**A**) Protein expression of NOXA and GLI1 in RD cells was determined by Western blot analysis, β-ACTIN served as loading control. (**B**) RD cells overexpressing GLI1 were transfected with GLI1 luciferase reporter plasmids. GLI1 transcriptional activity was determined 24 h after transfection using dual-luciferase reporter assay. Mean and SD of three independent experiments performed in duplicate are shown. *$p < 0.05$. (**C** and **D**) Basal *HHIP* (**C**) and NOXA (**D**) mRNA levels were determined in RD cells overexpressing GLI1 by RT-qPCR, normalized to *28S* expression and are shown as x-fold change compared to EV control. Mean and SD of three independent experiments performed in duplicate are shown. *$p < 0.05$, **$p < 0.01$. (**E**) RD cells overexpressing GLI1 were treated with 50 nM bortezomib for 6 h. Protein expression of NOXA was determined by Western blot analysis, β-ACTIN served as loading control (upper panel). NOXA and β-ACTIN protein levels were quantified by densitometry. NOXA expression normalized to β-ACTIN is shown as relative expression compared to untreated control (lower panels). Mean and SD of four independent experiments are shown. *$p < 0.05$.

3

Hh signaling negatively regulates TAp73

Next, we addressed the question of how the *bona fide* P53 target *NOXA* [34] is transcriptionally regulated in *TP53*-mutated cancer cells, since transcriptional activity of P53 is rendered non-functional in all three cell lines [35,36]. We therefore investigated the involvement of other P53 family proteins, i.e., the TA-isoform of P73 which has been reported to be able to compensate the loss of P53 transcriptional activity [37–39]. To this end, we used an TA-specific antibody for detection of TAp73. Importantly, protein expression levels of TAp73 were decreased in RD cells with GLI1 overexpression compared to EV control cells (Fig. 4A). Consistently, GLI1 overexpression in RD cells caused a significant decrease of *TAp73* mRNA levels (Fig. 4B). *Vice versa*, protein levels of TAp73 were elevated in RH30 cells in which GLI1 was knocked down compared to cells transfected with control siRNA (Fig. 4C). In addition to TAp73 protein expression, *TAp73* mRNA levels were increased in RH30 cells with GLI1 knockdown (Fig. 4D). These findings suggest that Hh signaling negatively regulates TAp73 transcription and thereby protein expression.

TAp73 is dispensable for GLI1-imposed suppression of NOXA

To investigate whether TAp73 mediates the GLI1-imposed suppression of NOXA, we designed two distinct siRNA constructs targeting the TA-domain of TAp73, thereby silencing all transcriptionally active TA-isoforms. Knockdown efficiency was evaluated by assessing TAp73 protein as well as mRNA levels (Fig. 5A and B). However, under basal conditions siRNA-mediated knockdown of TAp73 did not result in decreased NOXA protein or mRNA levels (Fig. 5A and C). Also, knockdown of TAp73 failed to block NOXA induction upon inhibition of the Hh pathway by GANT61 (Fig. 5D).

We hypothesized that altered TAp73 protein levels may have no effect on NOXA expression due to the expression of dominant-negative repressors of TAp73 function. Since deltaNp63 has been reported to exhibit dominant-negative effects on TAp73 transcriptional ability [40], we investigated mRNA expression of *deltaNp63* in RH30, RD and DAOY cells. However, under basal conditions none of the three tested cell lines exhibited relevant mRNA levels of *deltaNp63* compared to two breast cancer cell lines (Fig. 5E), which served as positive controls due to their reported high levels of deltaNp63 [41]. In summary, these findings suggest that TAp73 is dispensable for GLI1-imposed suppression of NOXA.
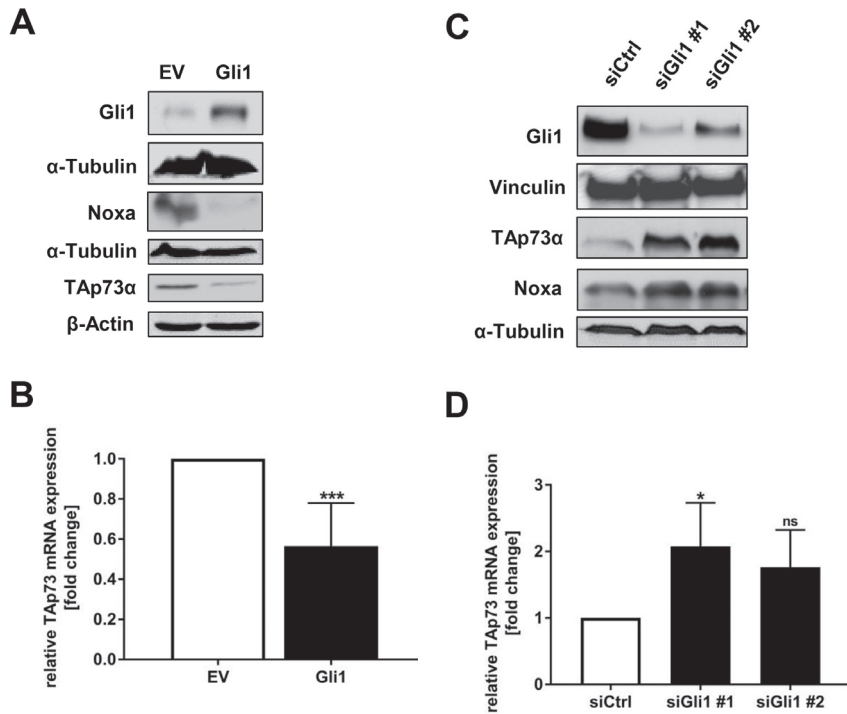
Fig. 4. Hh signaling negatively regulates TAp73. (**A**) Basal protein expression levels of GLI1, NOXA and TAp73 were determined in RD cells overexpressing GLI1 by Western blot analysis, α-TUBULIN and β-ACTIN served as loading control. (**B**) Basal *TAp73* mRNA levels in RD cells overexpressing GLI1 were determined by RT-qPCR, normalized to *28S* expression, and are shown as x-fold change compared to EV control. Mean and SD of three independent experiments performed in duplicate are shown. ****p* < 0.001. (**C** and **D**) RH30 cells were transiently transfected with two distinct siRNAs targeting GLI1 or control siRNA. Protein expression of GLI1, NOXA and TAp73 36 h after reverse transfection was analyzed by Western blot analysis, VINCULIN and α-TUBULIN served as loading controls (**C**). mRNA levels of *TAp73* 36 h after reverse transfection were determined by RT-qPCR, normalized to *28S* expression and shown as x-fold change compared to siRNA control (**D**). Mean and SD of three independent experiments performed in duplicate are shown. **p* < 0.05.

EGR1 transcriptionally activates NOXA and TAp73 expression

Since we found that TAp73 was not the major regulator of NOXA, we hypothesized that GLI1 may repress NOXA and TAp73 concomitantly rather than sequentially. Therefore, we searched for transcription factors that have been described to regulate transcriptional activity of both NOXA and TAp73. Since E2F1 was reported to transcriptionally activate NOXA [42] and TAp73 [43],

we investigated whether *E2F1* mRNA levels correlated with those of *NOXA* or *TAp73*. However, we found no correlation of *E2F1* mRNA levels with *NOXA* or *TAp73* mRNA levels in RD cells overexpressing GLI1 (Fig. 6A) or in RH30 GLI1 knockdown cells (Fig. 6B).
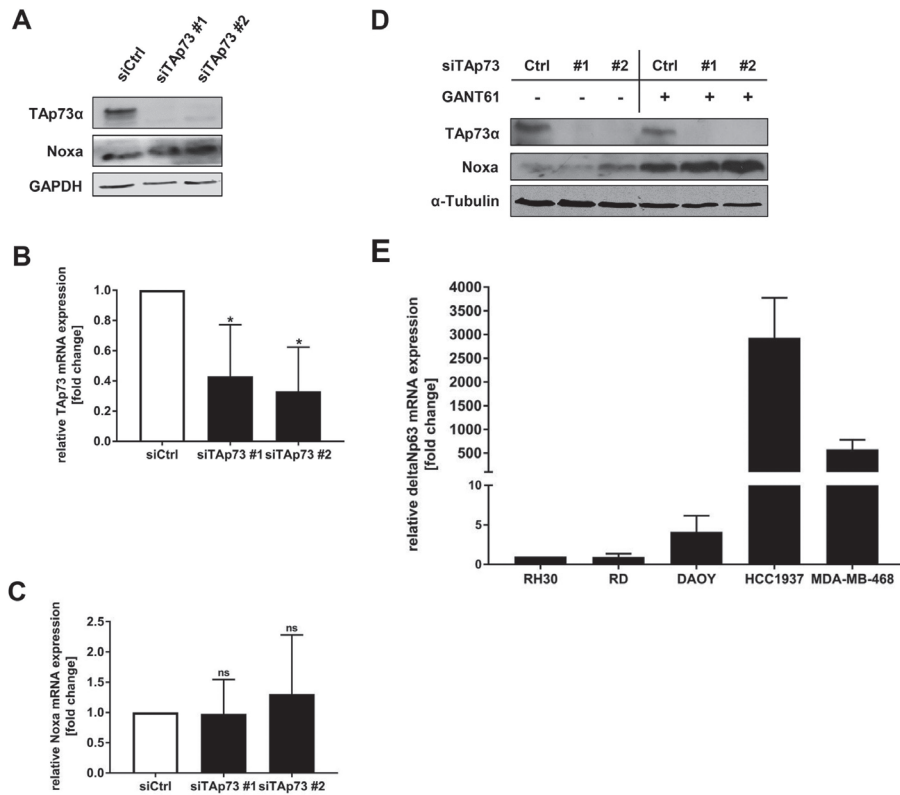
3

Fig. 5. TAp73 is dispensable for GLI1-imposed suppression of NOXA. (**A** to **D**), RH30 cells were transiently transfected with two distinct siRNAs targeting TAp73 or control siRNA. Protein expression of TAp73 and NOXA 24 h after reverse transfection was analyzed by Western blot analysis, GAPDH served as loading control (**A**). mRNA levels of *TAp73* (**B**) and *NOXA* (**C**) 24 h after reverse transfection were determined by RT-qPCR, normalized to *28S* expression, and shown as x-fold change compared to siRNA control. Mean and SD of three independent experiments performed in duplicate are shown. *$p < 0.05$. 24 h after reverse transfection cells were treated with 8 µM GANT61 for 24 h and protein expression of TAp73 and NOXA were analyzed by Western blot analysis, α-TUBULIN served as loading control (**D**). (**E**) Basal *deltaNp63* mRNA levels were determined in RH30, RD, DAOY, HCC1937 and MDA-MB-468 cells by RT-qPCR, normalized to *28S* expression and are shown as x-fold change compared to expression in RH30 cells. Mean and SD of three independent experiments performed in duplicate are shown.

Besides E2F1, also EGR1 has been reported to activate *TAp73* transcription [44] and to bind to the *NOXA* promotor [45]. To investigate if EGR1 regulates transcriptional activity of TAp73 or NOXA we correlated *EGR1* with *TAp73* and *NOXA* mRNA levels. Of note, mRNA levels of *EGR1* were significantly decreased in RD cells overexpressing GLI1 compared to the corresponding EV cells (Fig. 6C). Consistently, knockdown of GLI1 in RH30 cells resulted in increased *EGR1* mRNA levels (Fig. 6D). Thus, mRNA levels of *EGR1* showed a similar regulation by Hh signaling as mRNA levels of *NOXA* (Fig. 2, Fig. 3D) and *TAp73* (Fig. 4B and 4D). To further test if EGR1 regulates NOXA and TAp73, we silenced EGR1 by siRNA (Fig. 6E). Importantly, knockdown of EGR1 resulted in a significant decrease of *NOXA* and *TAp73* mRNA levels (Fig. 6F and 6G). In summary, these findings indicate that GLI1 represses EGR1 expression which in turn functions as a transcriptional repressor of NOXA and TAp73.
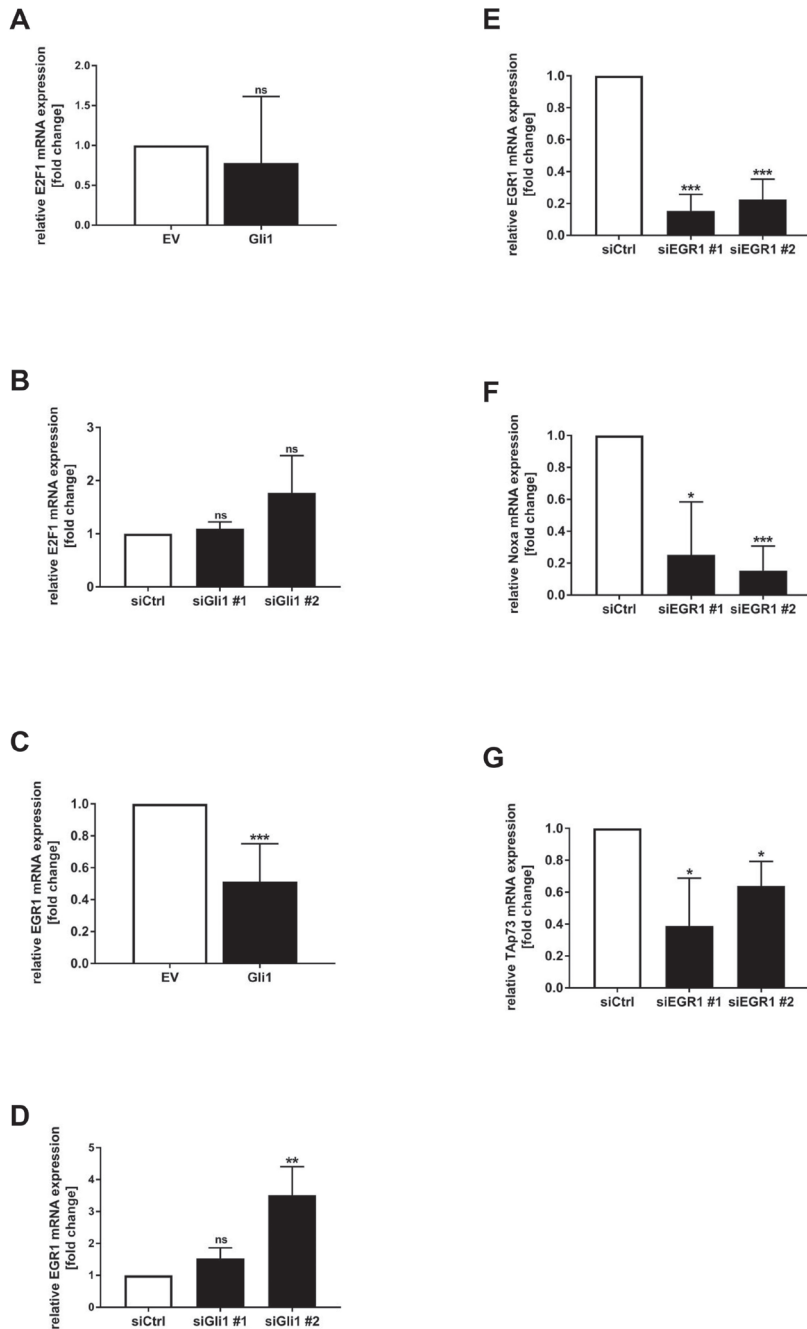
3

Fig. 6. EGR1 transcriptionally activates NOXA and TAp73 expression. (**A** and **C**) Basal E2F1 (**A**) and EGR1 (**C**) mRNA levels in RD cells overexpressing GLI1 were

Fig. 6. Continued

determined by RT-qPCR, normalized to 28S expression, and are shown as x-fold change compared to EV control. Mean and SD of three independent experiments performed in duplicate are shown. ***$p < 0.001$. (**B** and **D**) RH30 cells were transiently transfected with two distinct siRNAs targeting GLI1 or control siRNA. mRNA levels of *E2F1* (**B**) and *EGR1* (**D**) 24 h after reverse transfection were determined by RT-qPCR, normalized to 28S expression and shown as x-fold change compared to siRNA control. Mean and SD of three independent experiments performed in duplicate are shown. **$p < 0.01$. (**E** to **G**), RH30 cells were transiently transfected with two distinct siRNAs targeting EGR1 or control siRNA. mRNA levels of *EGR1* (**E**), *NOXA* (**F**) and *TAp73* (**G**) 24 h after reverse transfection were determined by RT-qPCR, normalized to 28S expression and shown as x-fold change compared to siRNA control. Mean and SD of three independent experiments performed in duplicate are shown. *$p < 0.05$, ***$p < 0.001$.

Discussion

The results obtained by the present study show that Hh signaling on the level of GLI1 represses transcriptional activity of the proapoptotic BH3-only protein NOXA (Fig. 7A). Pharmacological as well as genetic evidence supports this conclusion, as suppression of Hh signaling by GANT61 treatment or genetic silencing resulted in the induction of NOXA protein and mRNA (Fig. 7C). *Vice versa*, overexpression of GLI1 resulted in transcriptional repression of NOXA (Fig. 7B).
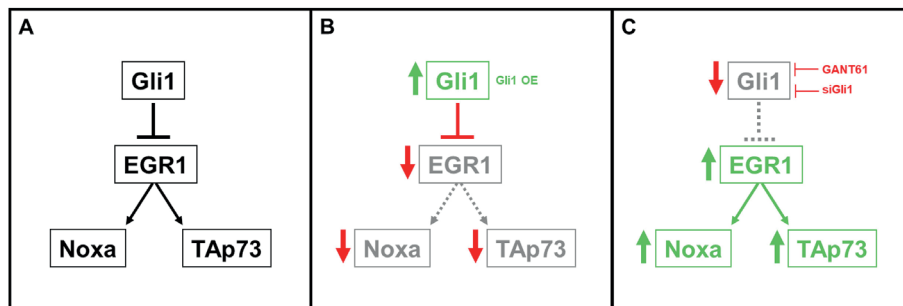

Fig. 7. Proposed mechanism of action. (**A**) GLI1 suppresses EGR1 transcriptional activity which governs expression of NOXA and TAp73. (**B**) Upon overexpression of GLI1, suppression of EGR1 results in reduced NOXA and TAp73 expression. (**C**) Upon genetic inhibition of Hh signaling by GLI1 silencing, increased EGR1 expression results in increased NOXA and TAp73 expression. Hypothetically, the same may be true for pharmacological inhibition of Hh signaling by GANT61.

Importantly, NOXA is a *bona fide* transcriptional target of P53 [34] and *TP53* is mutated and thus rendered non-functional in the tested cell lines [35,36]. While TAp73 is known as a transcriptional regulator of NOXA [37–39], our findings are consistent with a model showing that EGR1 co-regulates transcriptional activity of NOXA and TAp73 (Fig. 7A). This conclusion is supported by our data showing that silencing of EGR1 resulted in decreased *NOXA* and *TAp73* mRNA levels and that mRNA levels of *EGR1* correlated to those of *NOXA* and *TAp73*.

Our findings indicate that TAp73 is not the primary regulator of NOXA expression upon Hh pathway inhibition in embryonal pediatric tumor cells, as transient knockdown of TAp73 could not block NOXA induction in RH30 cells upon GLI1 knockdown. Thus, in the context of mutated *TP53*, inhibition of Hh signaling can activate in parallel the proapoptotic and the DNA damage response machinery at different levels (NOXA and TAp73).

Our findings are in line with a previous study showing the induction of EGR1 upon HPI treatment (with the SMO inhibitor cyclopamine) [46]. Also, EGR1 has been shown to be involved in transcriptional activation of NOXA in *TP53*-deficient tumor cells [45]. In the context of RMS, *PAX3-FOXO1* as the hallmark fusion gene of aRMS has been reported to interfere with EGR1 promotor binding and to bind to and destabilize EGR1 protein resulting in impaired p57Kip2 expression, thus highlighting its relevance as a tumor suppressor in RMS [47]. Although no data for the expression or the role of EGR1 in MB have been published so far, the crucial role of EGR1 in brain development has been studied extensively [48]. Furthermore, high EGR1 expression levels are associated with a better prognosis in high-grade astrocytomas, showing its relevance as a tumor suppressor in these brain tumors [49]. Taken together, our findings suggest that the suppression of Hh signaling may induce EGR1 as a tumor suppressor in RMS which in turn facilitates transcriptional induction of NOXA (Fig. 7C).

Importantly, the balance of pro- and antiapoptotic proteins ultimately determines whether or not a cell undergoes cell death or survives [18]. The results of the present study indicate that suppression of Hh signaling may shift this balance towards cell death by inducing NOXA and TAp73. This goes

in line with a previous study showing that GANT61 sensitizes DAOY cells to mitochondrial apoptosis [50]. In addition, NOXA has been described to function as a crucial cell death inducer in a *TP53*-mutated, SHH-driven MB mouse model treated with the proteasome inhibitor bortezomib [51]. Of note, high deltaNp73 expression as another (besides deltaNp63) repressor of TAp73 function has been reported to be associated with decreased overall survival in MB patients [52], whereas MB patients with high *TAp73* mRNA expression showed a trend towards better overall and progression-free survival [53]. Also, the latter study showed apoptosis induction and sensitization towards chemotherapeutics upon ectopic overexpression of TAp73 in MB cell lines [53]. Since overexpression of both TAp73 and its negative regulator deltaNp73 has been reported in RMS [46], upregulation of TAp73 upon inhibition of Hh signaling may change the balance of those two P73 isoforms towards the pro-cell death TA-isoform. In summary, induction of NOXA and TAp73 by HPI may be a crucial step in *TP53*-mutated, Hh-driven tumors to shift cell fate towards cell death. These findings could be exploited for the treatment of Hh-driven tumors, e.g., for their sensitization to chemotherapeutic agents.

Taken together, our study elucidates the regulatory mechanisms of Hh signaling with respect to the apoptotic machinery in embryonal pediatric tumors driven by Hh signaling (i.e., RMS and MB) and may therefore provide a rationale for novel combinatory anticancer drug treatments in these pediatric cancer entities.

Acknowledgements

Materials & Methods

Cell culture and chemicals

RMS cell line RH30 was obtained from Deutsche Sammlung von Mikroorganismen und Zellkulturen (DSMZ, Braunschweig, Germany) and

RMS cell line RD was obtained from American Type Culture Collection (Manassas, VA, USA). The MB cell line DAOY was kindly provided by Marc Remke (Duesseldorf, Germany). The breast carcinoma cell lines HCC1937 and MDA-MB-468 were kindly provided by Jindrich Cinatl (Frankfurt, Germany). Cell lines were authenticated by STR profiles and negatively tested for mycoplasma contamination. RD, DAOY, HCC1937 and MDA-MB-468 cells were maintained in DMEM GlutaMAX™-I medium, RH30 in RPMI 1640 GlutaMAX™-I (Life Technologies, Inc., Carlsbad, CA), both supplemented with 10% fetal calf serum (FCS) (Life Technologies, Inc.), 1% penicillin/streptomycin (Life Technologies, Inc.), 1 mM sodium pyruvate (Life Technologies, Inc.). If not indicated differently, chemicals were purchased from Sigma-Aldrich (Taufkirchen, Germany) or Carl Roth (Karlsruhe, Germany).

Western blot analysis

Western blot analysis was performed as described previously [54] using the following antibodies: NOXA (ALX-804-408-C100, Enzo Life Sciences), GLI1 (2643S, Cell Signaling), β-ACTIN (A5441, Sigma-Aldrich), GAPDH (5G4-6C5, Hytest), α-TUBULIN (CP06, Calbiochem), VINCULIN (V9131, Sigma-Aldrich). TAp73-specific antibody was kindly provided by Volker Dötsch (Frankfurt, Germany). Goat anti-mouse IgG conjugated to horseradish peroxidase (Santa Cruz Biotechnology, Santa Cruz, CA) and enhanced chemiluminescence (Amersham Bioscience, Freiburg, Germany) or infrared dye-labeled secondary antibodies and infrared imaging (Odyssey Imaging System, LI-COR Bioscience, Bad Homburg, Germany) were used for detection. Representative blots of at least two independent experiments are shown. Quantification of blots was performed using ImageJ software (version 1.51a, Wayne Rasband, open source).

Overexpression of GLI1

Cells were transfected with pCR3.1 expression vector containing murine *GLI1* gene (pCR3.1-mGLI1) or control vector (both kindly provided by Heidi Hahn (Göttingen, Germany)) using Lipofectamine 2000 (Invitrogen) and OptiMEM (Life Technologies Inc.) according to the manufacturer's protocol. Six hours after transfection, the medium was changed to regular culture medium.

Selection for transfected cells was started 42 h after medium change using G418 (geneticin). Overexpression was confirmed by Western blot analysis.

GLI1 luciferase reporter assay

Cells were transfected with either pGL3-promoter vector (Promega, Mannheim) harboring the *GLI1* promoter or pGL3-control vector as well as renilla luciferase DNA using Lipofectamine 2000 (Invitrogen) and OptiMEM (Life Technologies Inc.) according to the manufacturer's protocol. Six hours after transfection, the medium was changed to regular culture medium. Firefly and renilla luciferase activity were measured 18 h after medium change by microplate reader (Infinite M200, Tecan, Crailsheim, Germany) using the Dual-Luciferase® Reporter Assay System (Promega) according to the manufacturer's protocol.

Quantitative real-time PCR

mRNA levels were determined by quantitative RT-PCR analysis as previously described [55] using peqGOLD Total RNA kit from Peqlab Biotechnologie GmbH (Erlangen, Germany), RevertAid H Minus First Strand cDNA Synthesis Kit (MBI Fermentas GmbH, St. Leon-Rot, Germany) and 7900HT fast real-time PCR system from Applied Biosystems (Darmstadt, Germany) as well as QuantStudio 7 Flex Real-Time PCR System from Applied Biosystems (Darmstadt, Germany). Primers are listed in Supplemental Table 1. At least three independent experiments were performed for each gene.

Transient RNA interference

For transient knockdown by siRNA, cells were reversely transfected with 10 nM SilencerSelect siRNA (Invitrogen) for control siRNA (4390843), GLI1 targeting siRNAs (s5815 and s5816), early growth response protein 1 (EGR1) targeting siRNAs (s4537 and s4538) or TAp73 targeting siRNAs (designed with Invitrogen Support, sequences #1 sense GCAUGGACGUCUUCCACCUtt, antisense AGGUGGAAGACGUCCAUGCtg; #2 sense GCACCUACUUCGACCUUCCtt, antisense GGAAGGUCGAAGUAGGUGCtg) using Lipofectamine RNAi Max (Invitrogen) and OptiMEM (Life Technologies, Inc.) according to the manufacturer's protocol.

Statistical analysis

Statistical significance was assessed by Student's t-Test (two-tailed distribution, two-sample, equal variance) or one-way ANOVA via GraphPad Prism software (version 7, GraphPad Software, CA, USA).

3

References

1.   Kramer, S., Meadows, A. T., Jarrett, P. & Evans, A. E. Incidence of childhood cancer: experience of a decade in a population-based registry. *J Natl Cancer Inst* **70**, 49–55 (1983).

2.   Merlino, G. & Helman, L. J. Rhabdomyosarcoma--working out the pathways. *Oncogene* **18**, 5340–5348 (1999).

3.   Shern, J. F. *et al.* Comprehensive genomic analysis of rhabdomyosarcoma reveals a landscape of alterations affecting a common genetic axis in fusion-positive and fusion-negative tumors. *Cancer Discov* **4**, 216–231 (2014).

4.   Taylor, M. D. *et al.* Molecular subgroups of medulloblastoma: the current consensus. *Acta Neuropathol* **123**, 465–472 (2012).

5.   Varjosalo, M. & Taipale, J. Hedgehog: functions and mechanisms. *Genes Dev* **22**, 2454–2472 (2008).

6.   Beachy, P. A., Karhadkar, S. S. & Berman, D. M. Tissue repair and stem cell renewal in carcinogenesis. *Nature* **432**, 324–331 (2004).

7.   Eichberger, T. *et al.* Overlapping and distinct transcriptional regulator properties of the GLI1 and GLI2 oncogenes. *Genomics* **87**, 616–632 (2006).

8.   Ryan, K. E. & Chiang, C. Hedgehog secretion and signal transduction in vertebrates. *J Biol Chem* **287**, 17905–17913 (2012).

9.   Scales, S. J. & de Sauvage, F. J. Mechanisms of Hedgehog pathway activation in cancer and implications for therapy. *Trends Pharmacol Sci* **30**, 303–312 (2009).

10. Stecca, B. & Ruiz, I. A. A. Context-dependent regulation of the GLI code in cancer by HEDGEHOG and non-HEDGEHOG signals. *J Mol Cell Biol* **2**, 84–95 (2010).

11. Fulda, S. & Debatin, K. M. Extrinsic versus intrinsic apoptosis pathways in anticancer chemotherapy. *Oncogene* **25**, 4798–4811 (2006).

12. Fulda, S. Tumor resistance to apoptosis. *Int J Cancer* **124**, 511–515 (2009).

13. Armistead, P. M. *et al.* Expression of receptor tyrosine kinases and apoptotic molecules in rhabdomyosarcoma: correlation with overall survival in 105 patients. *Cancer* **110**, 2293–2303 (2007).

14. Pazzaglia, L. *et al.* Genetic and molecular alterations in rhabdomyosarcoma: mRNA overexpression of MCL1 and MAP2K4 genes. *Histol Histopathol* **24**, 61–67 (2009).

15. Margue, C. M., Bernasconi, M., Barr, F. G. & Schafer, B. W. Transcriptional modulation of the anti-apoptotic protein BCL-XL by the paired box transcription factors PAX3 and PAX3/FKHR. *Oncogene* **19**, 2921–2929 (2000).

16. Krajewski, S. *et al.* Immunohistochemical analysis of Bcl-2, Bcl-X, Mcl-1, and Bax in tumors of central and peripheral nervous system origin. *Am J Pathol* **150**, 805–814 (1997).

17. Schiffer, D., Cavalla, P., Migheli, A., Giordana, M. T. & Chiad-Piat, L. Bcl-2 distribution in neuroepithelial tumors: an immunohistochemical study. *J. Neurooncol.* **27**, (1996).

18. Walensky, L. D. BCL-2 in the crosshairs: tipping the balance of life and death. *Cell Death Differ* **13**, 1339–1350 (2006).

19. Zibat, A. *et al.* Activation of the hedgehog pathway confers a poor prognosis in embryonal and fusion gene-negative alveolar rhabdomyosarcoma. *Oncogene* **29**, 6323–6330 (2010).

20. Roberts, W. M., Douglass, E. C., Peiper, S. C., Houghton, P. J. & Look, A. T. Amplification of the gli gene in childhood sarcomas. *Cancer Res* **49**, 5407–5413 (1989).

21. Pressey, J. G., Anderson, J. R., Crossman, D. K., Lynch, J. C. & Barr, F. G. Hedgehog pathway activity in pediatric embryonal rhabdomyosarcoma and undifferentiated sarcoma: a report from the Children's Oncology Group. *Pediatr Blood Cancer* **57**, 930–938 (2011).

22. Taylor, M. D., Mainprize, T. G. & Rutka, J. T. Molecular Insight into Medulloblastoma and Central Nervous System Primitive Neuroectodermal Tumor Biology from Hereditary Syndromes: A Review. *Neurosurgery* **47**, 888–901 (2000).

23. Brugieres, L. *et al.* Incomplete penetrance of the predisposition to medulloblastoma associated with germ-line SUFU mutations. *J. Med. Genet.* **47**, 142–144 (2010).

24. Northcott, P. A. *et al.* Pediatric and adult sonic hedgehog medulloblastomas are clinically and molecularly distinct. *Acta Neuropathol.* **122**, 231–240 (2011).

25. Taylor, M. D. *et al.* Mutations in SUFU predispose to medulloblastoma. *Nat. Genet.* **31**, 306–310 (2002).

26. Northcott, P. A. *et al.* Multiple recurrent genetic events converge on control of histone lysine methylation in medulloblastoma. *Nat. Genet.* **41**, 465–472 (2009).

27. Zhukova, N. *et al.* Subgroup-specific prognostic implications of TP53 mutation in medulloblastoma. *J Clin Oncol* **31**, 2927–2935 (2013).

28. Low, J. A. & de Sauvage, F. J. Clinical experience with Hedgehog pathway inhibitors. *J Clin Oncol* **28**, 5321–5326 (2010).

29. Robinson, G. W. *et al.* Vismodegib Exerts Targeted Efficacy Against Recurrent Sonic Hedgehog-Subgroup Medulloblastoma: Results From Phase II Pediatric Brain Tumor Consortium Studies PBTC-025B and PBTC-032. *J Clin Oncol* **33**, 2646–2654 (2015).

30. Graab, U., Hahn, H. & Fulda, S. Identification of a novel synthetic lethality of combined inhibition of hedgehog and PI3K signaling in rhabdomyosarcoma. *Oncotarget* **6**, 8722–8735 (2015).

31. Ploner, C., Kofler, R. & Villunger, A. Noxa: at the tip of the balance between life and death. *Oncogene* **27 Suppl 1**, S84-92 (2008).

32. Baou, M. *et al.* Role of NOXA and its ubiquitination in proteasome inhibitor-induced apoptosis in chronic lymphocytic leukemia cells. *Haematologica* **95**, 1510–1518 (2010).

33. Brinkmann, K. *et al.* Ubiquitin C-Terminal Hydrolase-L1 Potentiates Cancer Chemosensitivity by Stabilizing NOXA. *Cell Rep.* **3**, 881–891 (2013).

34. Oda, E. *et al.* Noxa, a BH3-only member of the Bcl-2 family and candidate mediator of p53-induced apoptosis. *Science (80-.).* **288**, 1053–1058 (2000).

35. Felix, C. A., Winick, N. J., Crouch, G. D. & Helman, L. J. Frequency and Diversity of p53 Mutations in Childhood Rhabdomyosarcoma. *Cancer Res.* **52**, 2243–2247 (1992).

36. Saylors 3rd, R. L. *et al.* Infrequent p53 gene mutations in medulloblastomas. *Cancer Res* **51**, 4721–4723 (1991).

37. Dabiri, Y. *et al.* The essential role of TAp73 in bortezomib-induced apoptosis in p53-deficient colorectal cancer cells. *Sci. Rep.* **7**, 5423 (2017).

38. Engelmann, D., Meier, C., Alla, V. & Pützer, B. M. A balancing act: orchestrating amino-truncated and full-length p73 variants as decisive factors in cancer progression. *Oncogene* **34**, 4287–4299 (2015).

39. Murray-Zmijewski, F., Lane, D. P. & Bourdon, J.-C. p53/p63/p73 isoforms: an orchestra of isoforms to harmonise cell differentiation and response to stress. *Cell Death Differ.* **13**, 962–972 (2006).

40. Gebel, J. *et al.* Mechanism of TAp73 inhibition by ΔNp63 and structural basis of p63/p73 hetero-tetramerization. *Cell Death Differ.* **23**, 1930–1940 (2016).

41. Buckley, N. E. *et al.* The ΔNp63 Proteins Are Key Allies of BRCA1 in the Prevention of Basal-Like Breast Cancer. *Cancer Res.* **71**, 1933–1944 (2011).

42. Hershko, T. & Ginsberg, D. Up-regulation of Bcl-2 Homology 3 (BH3)-only Proteins by E2F1 Mediates Apoptosis. *J. Biol. Chem.* **279**, 8627–8634 (2004).

43. Zaika, A., Irwin, M., Sansome, C. & Moll, U. M. Oncogenes Induce and Activate Endogenous p73 Protein. *J. Biol. Chem.* **276**, 11310–11316 (2001).

44. Yu, J., Baron, V., Mercola, D., Mustelin, T. & Adamson, E. D. A network of p73, p53 and Egr1 is required for efficient apoptosis in tumor cells. *Cell Death Differ.* **14**, 436–446 (2007).

45. Wirth, M. *et al.* MYC and EGR1 synergize to trigger tumor cell death by controlling NOXA and BIM transcription upon treatment with the proteasome inhibitor bortezomib. *Nucleic Acids Res.* **42**, 10433–10447 (2014).

46. Bai, L.-Y. *et al.* Inhibition of Hedgehog signaling induces monocytic differentiation of HL-60 cells. *Leuk. Lymphoma* **53**, 1196–1202 (2012).

47. Roeb, W., Boyer, A., Cavenee, W. K. & Arden, K. C. PAX3-FOXO1 controls expression of the p57Kip2 cell-cycle regulator through degradation of EGR1. *Proc. Natl. Acad. Sci.* **104**, 18085–18090 (2007).

48. Duclot, F. & Kabbaj, M. The Role of Early Growth Response 1 (EGR1) in Brain Plasticity and Neuropsychiatric Disorders. *Front. Behav. Neurosci.* **11**, (2017).

49. Mittelbronn, M. *et al.* EGR-1 is Regulated by N-Methyl-D-Aspartate-Receptor Stimulation and Associated with Patient Survival in Human High Grade Astrocytomas. *Brain Pathol.* **19**, 195–204 (2009).

50. Lin, Z. *et al.* Suppression of GLI sensitizes medulloblastoma cells to mitochondria-mediated apoptosis. *J. Cancer Res. Clin. Oncol.* **142**, 2469–2478 (2016).

51. Ohshima-Hosoyama, S., Davare, M. A., Hosoyama, T., Nelon, L. D. & Keller, C. Bortezomib stabilizes NOXA and triggers ROS-associated apoptosis in medulloblastoma. *J. Neurooncol.* **105**, 475–483 (2011).

52. Zitterbart, K. *et al.* p73 expression in medulloblastoma: TAp73/ΔNp73 transcript detection and possible association of p73α/ΔNp73 immunoreactivity with survival. *Acta Neuropathol.* **114**, 641–650 (2007).

53. Castellino, R. C. *et al.* Overexpressed TP73 induces apoptosis in medulloblastoma. *BMC Cancer* **7**, 127 (2007).

54. Fulda, S., Sieverts, H., Friesen, C., Herr, I. & Debatin, K. M. The CD95 (APO-1/Fas) system mediates drug-induced apoptosis in neuroblastoma cells. *Cancer Res* **57**, 3823–3829 (1997).

55. Heinicke, U., Kupka, J., Fichter, I. & Fulda, S. Critical role of mitochondria-mediated apoptosis for JNJ-26481585-induced antitumor activity in rhabdomyosarcoma. *Oncogene* **35**, 3729–3741 (2016).

3

Supplementary data
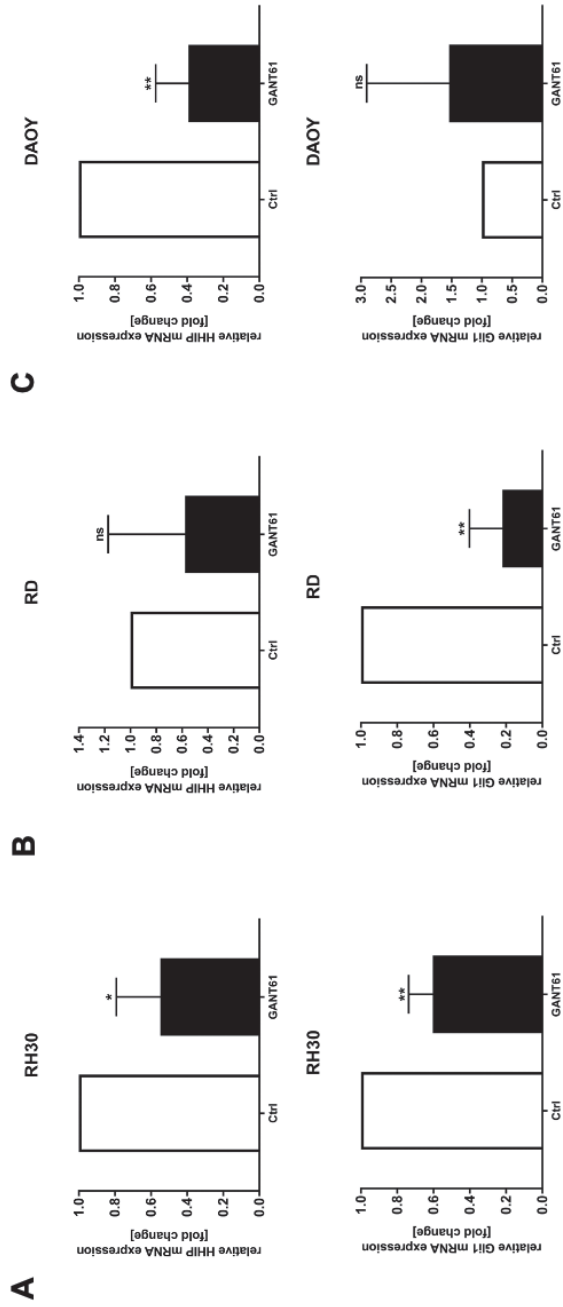
Suppl. Fig. 1. Pharmacological inhibition of GLI1 results in decreased GLI1 target gene expression. (A to **C)** RH30 (**A**), RD (**B**) and DAOY (**C**) cells were treated with GANT61 (RH30 8 µM, RD 6 µM, DAOY 10 µM) for 24 h. mRNA levels of GLI1 target genes *HHIP* and *GLI1* were determined by RT-qPCR, normalized to 28S expression and shown as x-fold change compared to untreated control. Mean and SD of three independent experiments performed in duplicate are shown. * $p < 0.05$, ** $p < 0.01$.
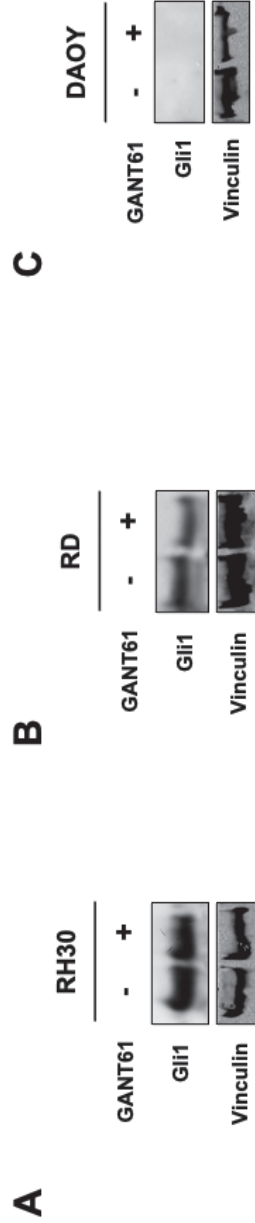
Suppl. Fig. 2. Pharmacological inhibition of GLI1 does not result in decreased GLI1 protein levels. (A to **C)**, RH30, RD and DAOY cells were treated with GANT61 (RH30 8 µM (**A**), RD 6 µM (**B**), DAOY 10 µM (**C**)) for 24 h. Protein expression of GLI1 was determined by Western blot analysis, VINCULIN served as loading control.

Concomitant targeting of Hedgehog signaling and MCL-1 synergistically induces cell death in Hedgehog-driven cancer cells

Michael Torsten Meister[1-4], Cathinka Boedicker[1-3], Benedikt Linder[5], Donat Kögel[2,5], Thomas Klingebiel[2-4], Simone Fulda[1-3]

[1] Institute for Experimental Cancer Research in Pediatrics, Goethe-University Frankfurt, Komturstr. 3a, 60528, Frankfurt, Germany
[2] German Cancer Consortium (DKTK), Partner Site Frankfurt, Germany
[3] German Cancer Research Center (DKFZ), Heidelberg, Germany
[4] Division of Pediatric Hematology and Oncology, Hospital for Children and Adolescents, Goethe-University, Frankfurt, Germany
[5] Experimental Neurosurgery, Neuroscience Center, Goethe-University Hospital, Frankfurt, Germany

Abstract

In the present study, we show that concomitant inhibition of Hedgehog (Hh) signaling by the glioma-associated oncogene homolog1 (GLI1)-targeting agent GANT61 and the antiapoptotic BCL-2 protein family member MCL-1 by A-1210477 synergistically induces cell death in Hh-driven cancers, i.e., rhabdomyosarcoma (RMS) and medulloblastoma (MB) cells. Combined genetic and pharmacological inhibition emphasized that co-treatment of GANT61 and A-1210477 indeed relies on inhibition of GLI1 (by GANT61) and MCL-1 (by A-1210477). Mechanistic studies revealed that A-1210477 triggers the release of BIM from MCL-1 and its shuttling to BCL-x$_L$ and BCL-2. Indeed, BIM proved to be required for GANT61/A-1210477-induced cell death, as genetic silencing of BIM using siRNA significantly rescues cell death upon GANT61/A-1210477 co-treatment. Similarly, genetic silencing of NOXA results in a significant reduction of GANT61/A-1210477-mediated cell death. Also, overexpression of MCL-1 or BCL-2 significantly protects RMS cells from GANT61/A-1210477-triggered cell death. Addition of the pan-caspase inhibitor zVAD.fmk significantly decreases GANT61/A-1210477-stimulated cell demise, indicating apoptotic cell death. In conclusion, GANT61 and A-1210477 synergize to engage mitochondrial apoptosis. These findings provide the rationale for further evaluation of dual inhibition of Hh signaling and MCL-1 in Hh-driven cancers.

Introduction

RMS, the most common soft-tissue sarcoma in children and adolescents, is the third most frequently occurring solid tumor in this patient cohort [1] and comprises two major histological subtypes: Embryonal RMS (eRMS) predominantly occurs in smaller children, while alveolar RMS (aRMS) primarily affects older children and adolescents. Overall, eRMS shows better prognosis than aRMS which may be attributed to the fact that aRMS more often display metastases upon diagnosis [2,3]. While the cell of origin of different RMS subtypes is still under debate [4], multiple studies on the biological features of RMS cells have already been conducted: While aRMS are characterized by a fusion gene (predominantly *PAX3-* or *PAX7-FOXO1*, more infrequently *PAX3-NCOA1* or *-NCOA2* and others) and infrequent activations of the *MYC* or *CDK4* oncogene [5–7], eRMS commonly harbor a copy-number neutral loss of heterozygosity (LOH) on chromosome 11p [8]. Recent studies employing whole-genome sequencing and other next-generation sequencing techniques suggest a low mutational burden for aRMS, while eRMS typically harbor alterations in the *TP53* tumor suppressor gene (including LOH on chromosome 17p13.1, which harbors the *TP53* gene, and activating mutations of *MDM2*, a suppressor of *TP53* function) and in *RAS* signaling (i.e., activating alterations of *FGFR4*, *HRAS*, *KRAS* and *NRAS* or inactivating alterations of *NF1*) [9]. Therapeutic regimens for RMS consist of chemotherapy (including compounds such as vincristine, actinomycin-D and ifosfamide), radiation therapy and, if feasible, surgery. Despite major advances made in the field of pediatric tumor therapy in general, patients with RMS still suffer from only mediocre to dismal prognosis, which is especially poor in primary metastatic, refractory or relapsed disease [10].

The Hh signaling pathway plays a fundamental role in embryonal development [11] and is deactivated in most body tissues after birth (with remaining regenerative functions in some) [12]. Signal transduction of canonical Hh signaling occurs at the so-called primary cilium: After binding of one of the three known Hh ligands (Sonic, Desert, Indian) to the transmembrane receptor Patched (PTCH), PTCH is inactivated. This inactivation results in the release of the second transmembrane receptor Smoothened (SMO). SMO governs the release of the glioma-associated oncogene (GLI) transcription factors by releasing GLI from their inhibiting factor Suppressor of Fused (SUFU). The released GLI transcription factors exhibit

differential roles in Hh signaling: While GLI1 and GLI2 mainly act as transcriptional activators, GLI3 acts as a transcriptional repressor [13,14].

Importantly, aberrant reactivation of Hh signaling has been reported for a variety of tumor entities including RMS and MB, where it facilitates transcription of factors promoting cell cycle progression, proliferation and evasion of cell death such as apoptosis (i.e., by transcriptional activation of antiapoptotic BCL-2) [15,16]. Apoptosis is a form of programmed cell death [17] and evasion of apoptosis is a hallmark of human cancers that can be mediated by overexpression of antiapoptotic or by downregulation/inactivation of proapoptotic proteins [18]. Several studies found high expression levels of the antiapoptotic BCL-2 family proteins BCL-2, BCL-x_L and MCL-1 in RMS specimens [19–21]. Of note, switching the balance of pro- and antiapoptotic BCL-2 proteins towards proapoptotic BCL-2 proteins is regarded as a crucial step in overcoming tumor drug resistance [22]. Importantly, besides overexpressing antiapoptotic BCL-2 proteins, RMS have been reported to exhibit activated Hh signaling on different levels of the pathway (i.e., canonically by ligand expression, non-canonically or by amplification of *GLI1*), in particular in a portion of eRMS and fusion-negative aRMS [23–25]. However, the prognostic impact of Hh signaling activation in RMS remains unclear: While one study found that reactivation of the Hh pathway is associated with poor survival in RMS [24], another study did not find any such association [26].

In an effort to target aberrant Hh signaling in cancer, so-called Hh pathway inhibitors (HPIs) have been developed that target different proteins in the signaling cascade [27]: vismodegib and sonidegib target Hh signaling on the level of SMO and have been approved for metastasized or otherwise untreatable basal cell carcinoma, which often harbors deactivating *PTCH* mutations, thereby resulting in an activation of Hh signaling [28]. Furthermore, both compounds were evaluated in patients with advanced childhood MB. Here, tumor responses were only observed in tumors with Hh signaling activation upstream of SMO [29,30]. Lastly, the Food & Drug Administration (FDA)-approved drug arsenic trioxide targets Hh signaling at the level of GLI1 by directly binding this protein and inhibiting its transcriptional activity [31].

We recently reported that Hh signaling suppresses the transcription of the proapoptotic BH3-only protein NOXA and that pharmacological or genetic

abrogation of Hh signaling reconstitutes NOXA expression in *TP53*-mutated RMS and MB cell lines [32]. However, we also found that NOXA induction in RMS cells treated with HPIs as a single agent is not sufficient to induce cell death on its own [33]. Since NOXA binds and thereby neutralizes the antiapoptotic protein MCL-1 [34] and RMS show high intrinsic MCL-1 levels [21], we hypothesized that transcriptional induction of NOXA by HPIs is insufficient to effectively neutralize MCL-1. Importantly, a novel BH3-mimetic named A-1210477 that specifically targets MCL-1 without increasing NOXA levels has been described recently [35]. In the present study, we tested the hypothesis that the combination treatment of A-1210477 and an HPI (that induces NOXA) may fully block MCL-1 function and thereby overcome intrinsic resistance of Hh-driven cancers to HPIs.

Results

Concomitant targeting of Hh signaling and MCL-1 synergistically induces cell death in RMS cells

To test our hypothesis that concomitant inhibition of Hh signaling and MCL-1 overcomes intrinsic resistance to HPIs and results in synergistic induction of cell death we treated two representative RMS cell lines (i.e., RH30 as a fusion gene positive aRMS and RD as a fusion gene negative eRMS) with the GLI1-targeting HPI GANT61 and the BH3-mimetic A-1210477 inhibiting MCL-1 (MCL-1i). Of note, combination treatment with GANT61 and A-1210477 cooperated to trigger cell death in both RH30 and RD cells, as determined by PI uptake (Fig. 1A). In contrast, single treatment with either GANT61 or A-1210477 resulted only in a minor increase in cell death (Fig. 1A). Calculation of combination indices (CI) revealed a synergistic interaction of the two compounds (Suppl. Tab. 1A). We verified these findings by employing another cell death assay. Similarly, GANT61 and A-1210477 synergized to induce DNA fragmentation used as a typical marker of cell death (Fig. 1B and Suppl. Tab. 1B). A kinetic analysis revealed that the GANT61/A-1210477 combination triggered cell death in a time-dependent manner with the onset of cell death occurring after 24 h (Fig. 1C). To study the long-term efficacy of the combination treatment we performed colony formation assays. Importantly, GANT61/A-1210477 co-treatment resulted in a significant decrease in colony numbers in both RH30 and RD cells when compared to the untreated control or either single agent

(Fig. 1D). We did not observe any significant changes in the distribution of cell cycle phases upon treatment in RH30 cells (Suppl. Fig. 2).

Since both RH30 and RD cell lines harbor an inactivating *TP53* mutation [36], we extended our study to the *TP53* wildtype RMS cell line Kym-1 [37] to test if the *TP53* status influences the susceptibility to the GANT61/A-1210477 combination. However, GANT61 and A-1210477 similarly cooperated to engage cell death in *TP53* wildtype Kym-1 cells (Suppl. Fig. 1A). To explore the translational relevance of our findings we extended our study to a primary RMS cell culture (i.e., aRMS-CP cells). Of note, GANT61/A-1210477 co-treatment was significantly more effective to induce cell death compared to either treatment alone (Suppl. Fig. 1B).

To test if this synergism of GLI1 and MCL-1 inhibitors is tumor entity-specific we extended our experiments to the *TP53*-mutated MB cell line DAOY [38]. MB are known to exhibit hyperactivation of Hh signaling in a subgroup of cases (the so-called sonic Hh (SHH) subgroup) [39]. Of note, GANT61 and A-1210477 acted in concert to synergistically cause cell death in DAOY cells as well (Suppl. Fig. 1C and 1D). In addition, GANT61/A-1210477 co-treatment significantly suppressed colony formation in DAOY cells (Suppl. Fig. 1E).

Taken together, this set of experiments shows that GANT61 and A-1210477 synergistically induce cell death in RMS cells regardless of their *TP53* status.

Pharmacological and genetic blockade of GLI1 and MCL-1 act in concert to induce cell death

To further test our hypothesis that parallel inhibition of Hh signaling and MCL-1 causes synergistic induction of cell death we combined genetic and pharmacological abrogation of either GLI1 or MCL-1 protein. To this end, we silenced GLI1 by shRNA-mediated knockdown in RH30 cells which harbor a *GLI1* amplification [26] (Fig. 2A). Importantly, GLI1 silencing significantly increased cell death when combined with pharmacological inhibition of MCL-1, compared to control cells expressing a non-targeting shRNA (Fig. 2B). *Vice versa*, siRNA-mediated genetic silencing of MCL-1 in RH30 and RD cells (Fig. 2C) in combination with pharmacological inhibition of GLI1 resulted in significantly increased cell death compared to control cells (Fig. 2D).
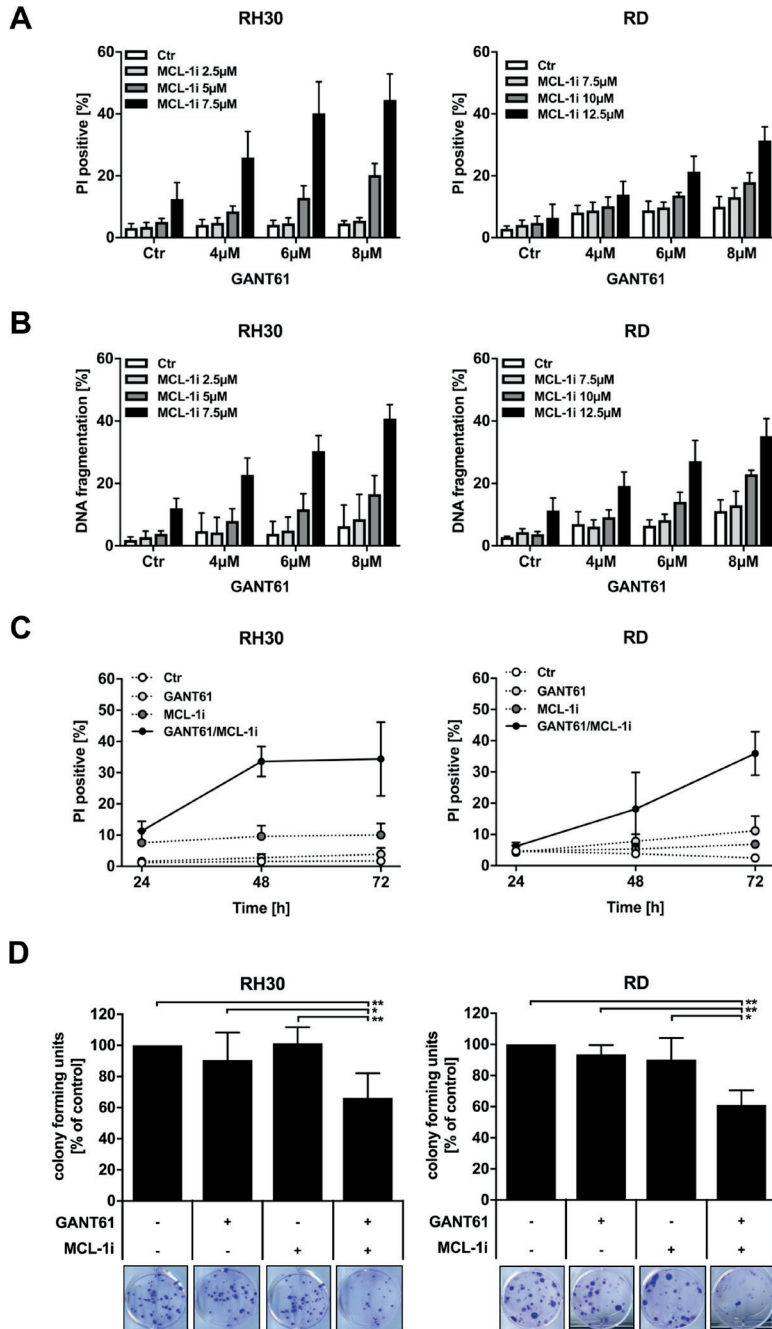
Fig. 1. Concomitant targeting of Hh signaling and MCL-1 synergistically induces cell death in RMS cells. (**A** and **B**) RH30 and RD cells were treated with indicated

Fig. 1. Continued

concentrations of GANT61 and/or A-1210477 (MCL-1i) for 72 h. Cell death was determined by PI-stained nuclei using microscopy (**A**) or flow cytometry (**B**). Mean and SD of at least three independent experiments performed in triplicate are shown. (**C**) Cells were treated with 8 µM (RH30) or 6 µM (RD) GANT61 and/or 7.5 µM (RH30) or 12.5 µM (RD) A-1210477 (MCL-1i) for indicated time points. Cell death was determined by PI-stained nuclei using microscopy. Mean and SD of three in-dependent experiments performed in triplicate are shown. (**D**) Cells were treated with 8 µM (RH30) or 6 µM (RD) GANT61 and/or 7.5 µM (RH30) or 12.5 µM (RD) A-1210477 (MCL-1i) for 10 h. Colony formation was assessed after 12–15 days. The number of colonies expressed as percentage of solvent-treated controls (top) and representative images (bottom) are shown. Mean and SD of at least three in-dependent experiments performed in duplicate are shown. *$p < 0.05$, ** $p < 0.01$.

Taken together, these findings show that pharmacological and genetic inhibition of GLI1 and MCL-1 act in concert to induce cell death. These findings provide evidence showing that GANT61/A-1210477-induced cell death indeed results from specific inhibition of GLI1 and MCL-1 rather than from off-target effects of these compounds.

MCL-1i triggers BIM translocating from MCL-1 to BCL-x$_L$ and BCL-2

Since RMS have been reported to express high levels of MCL-1 [21], we hypothesized that GANT61/A-1210477-induced cell death is mediated by a combined blockade of MCL-1 by pharmacological inhibition (by A-1210477) and NOXA induction (by GANT61, as previously reported by our group [32,33]) which binds to and thereby neutralizes MCL-1 [34], resulting in increased release of BIM from MCL-1. To test this hypothesis, we performed co-immunoprecipitation experiments of the antiapoptotic proteins MCL-1, BCL-2 and BCL-x$_L$ and analyzed their binding to BIM. Interestingly, A-1210477 decreased the binding of BIM to MCL-1 accompanied by increased binding of BIM to BCL-x$_L$ and also to BCL-2, in particular upon co-treatment of GANT61 and A-1210477, in both cell lines (Fig. 3A and B). This indicates that A-1210477 releases BIM from MCL-1 which then shuttles to BCL-x$_L$ and also to BCL-2. We also observed that treatment with A-1210477 caused an accumulation of MCL-1 which is in line with a previous report [35].
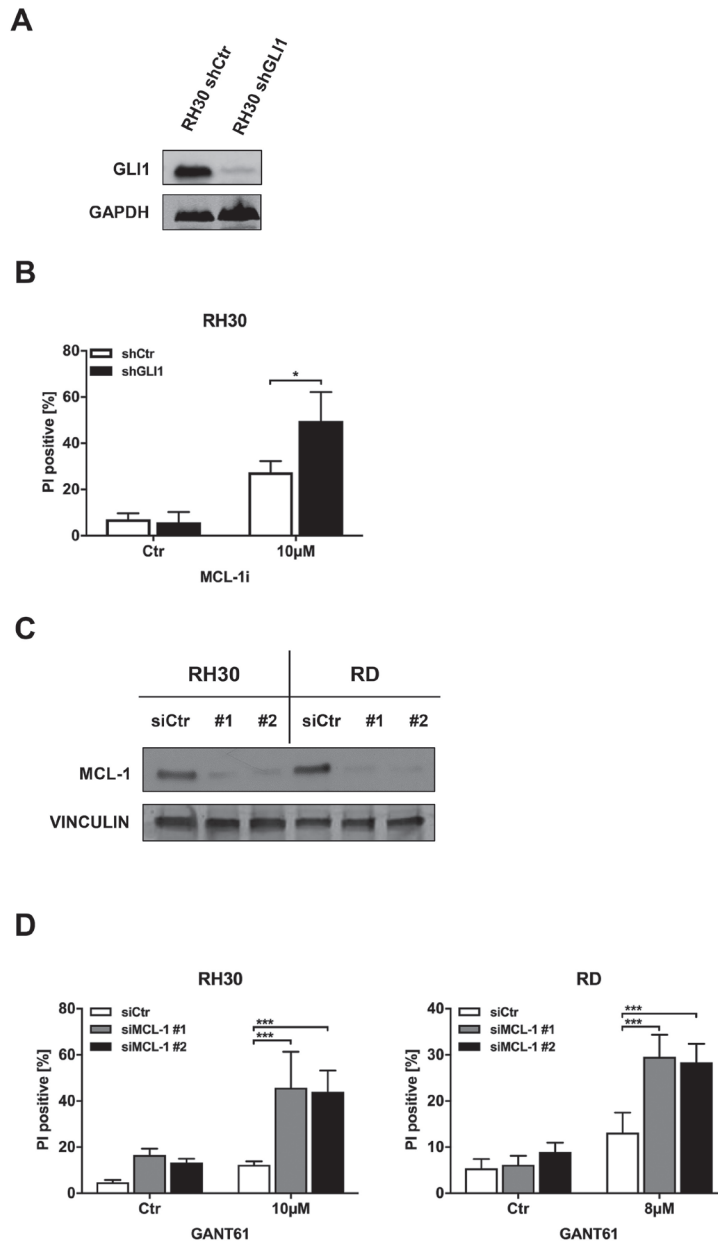
Fig. 2. Pharmacological and genetic blockade of GLI1 and MCL-1 act in concert to induce cell death. (**A** and **B**) RH30 cells were lentivirally transduced to knock down GLI1. GLI1 expression was assessed by Western blot analysis, GAPDH served as loading control (**A**). Transduced RH30 cells were treated with 10 µM A-1210477

Fig. 2. Continued

(MCL-1i) for 72 h. Cell death was determined by PI-stained nuclei using microscopy. Mean and SD of three independent experiments performed in triplicate are shown (**B**). *$p < 0.05$. (**C** and **D**) RH30 and RD cells were transiently transfected with siRNA against MCL-1 or non-targeting control siRNA. Expression of MCL-1 was assessed by Western blot analysis, VINCULIN served as loading control (**C**). 24 h after reverse transfection, cells were treated with 10 µM (RH30) or 8 µM (RD) GANT61 for 48 h. Cell death was determined by PI-stained nuclei using microscopy. Mean and SD of three independent experiments performed in triplicate are shown (**D**). ***$p < 0.001$.

BIM and NOXA contribute to GANT61/A-1210477-induced cell death

To test if the BH3-only proteins BIM and NOXA are crucial for cell death induced by the combination of GANT61 and A-1210477 we silenced BIM (Fig. 4A) and NOXA (Fig. 4C) by siRNA. Of note, silencing of BIM (Fig. 4B) as well as silencing of NOXA (Fig. 4D) significantly decreased GANT61/A-1210477-induced cell death in both RH30 and RD cells. These findings show that BIM and NOXA both contribute to GANT61/A-1210477-induced cell death and suggest that the translocation of BIM from MCL-1 to BCL-x_L and BCL-2 is indeed crucial for mediating cell death.

Overexpression of BCL-2 or MCL-1 rescues cells from GANT61/A-1210477-induced cell death

Since our co-immunoprecipitation experiments suggested that blockade of antiapoptotic proteins occurs upon combination treatment of GANT61/A-1210477, we asked whether this blockade is indeed crucial for cell death induction. We therefore overexpressed BCL-2 and MCL-1 in RH30 and RD cells. Importantly, BCL-2 overexpression significantly rescued both RH30 and RD cells from GANT61/A-1210477-triggered cell death (Fig. 5A and B). Also, we observed a significant rescue from cell death in RH30 cells treated with A-1210477 alone and in RD cells treated with GANT61 alone upon ectopic BCL-2 expression (data not shown). Similarly, ectopic expression of MCL-1 provided significant protection against cell death upon GANT61/A-1210477 cotreatment in both cell lines (Fig. 5C and D). Also, we observed a significant rescue from cell death in RD cells treated with GANT61 alone upon ectopic MCL-1 expression (data not shown). This suggests that the blockade of antiapoptotic BCL-2 and MCL-1 is crucial for cell death induction by GANT61/A-1210477.

A (RH30)
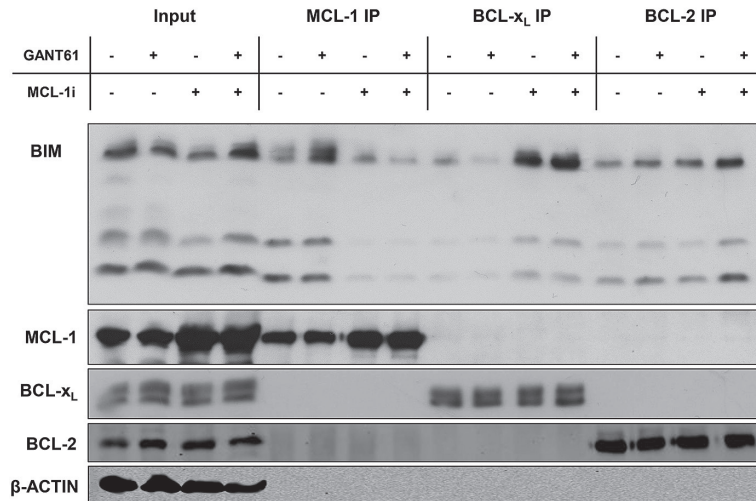
B (RD)
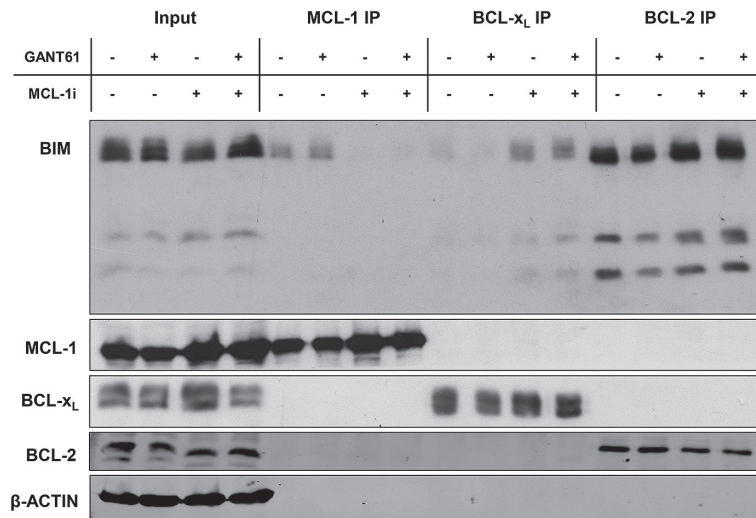
Fig. 3. MCL-1i triggers BIM translocating from MCL-1 to BCL-xL and BCL-2. (**A** and **B**) RH30 (**A**) and RD (**B**) cells were treated with 8 μM (RH30) or 6 μM (RD) GANT61 and/or 7.5 μM (RH30) or 12.5 μM (RD) A-1210477 (MCL-1i) for 20 h and MCL-1, BCL-xL and BCL-2 were immunoprecipitated. The precipitate was analyzed for BIM, MCL-1, BCL-xL and BCL-2 expression by Western blot analysis. β-ACTIN served as loading control.
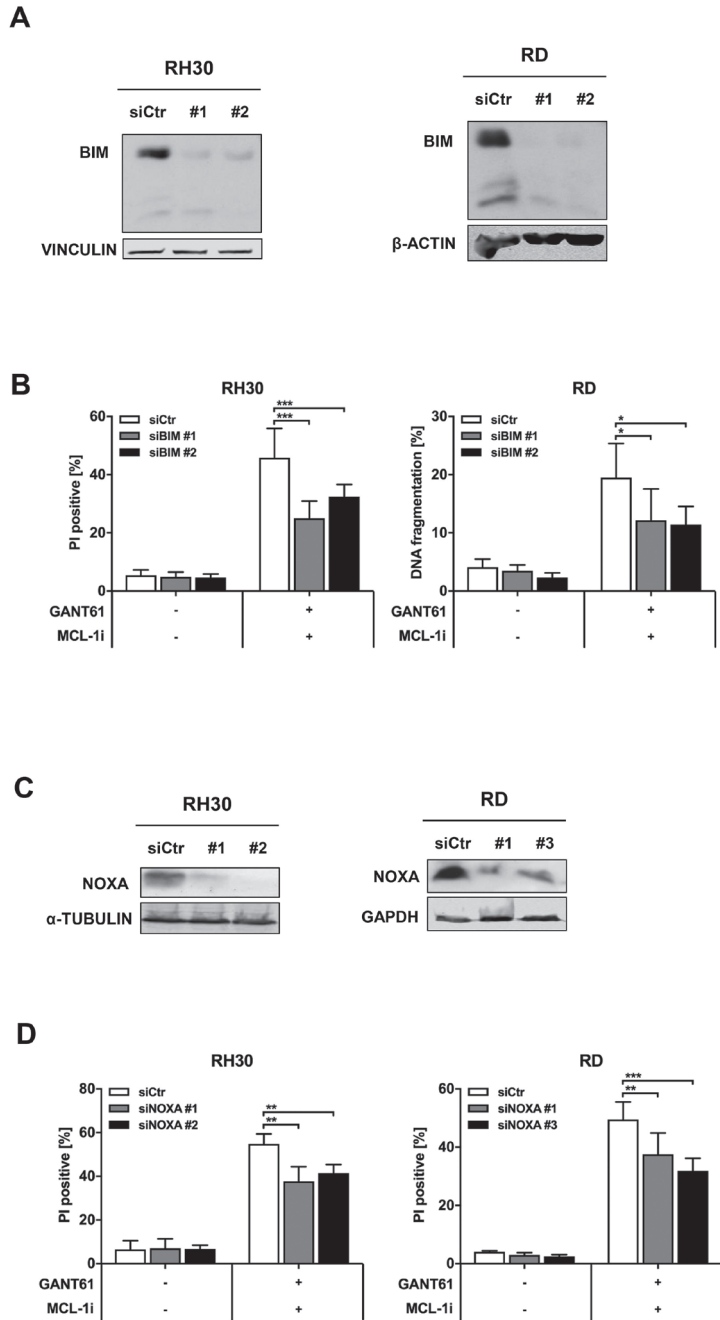
A

B

C

D

Fig. 4. BIM and NOXA contribute to GANT61/A-1210477-induced cell death.
(**A**) RH30 and RD cells were transiently transfected with siRNA against BIM or non-

Fig. 4. Continued

targeting control siRNA. Expression of BIM was assessed by Western blot analysis, VINCULIN or β-ACTIN served as loading control. (**B**) Cells were treated with 6 µM (RH30 and RD) GANT61 and 6 µM (RH30) or 12.5 µM (RD) A-1210477 (MCL-1i) for 48 h (RD) or 72 h (RH30). Cell death was determined by PI-stained nuclei using microscopy (RH30) or flow cytometry (RD). Mean and SD of at least three independent experiments performed in triplicate are shown. $*p < 0.05$, $***p < 0.001$. (**C**) RH30 and RD cells were transiently transfected with siRNA against NOXA or non-targeting control siRNA. Expression of NOXA was assessed by Western blot analysis, α-TUBULIN or GAPDH served as loading control. (**D**) Cells were treated with 6 µM (RH30 and RD) GANT61 and 6 µM (RH30) or 12.5 µM (RD) A-1210477 (MCL-1i) for 72 h. Cell death was determined by PI-stained nuclei using microscopy (RH30) or flow cytometry (RD). Mean and SD of three independent experiments performed in triplicate are shown. $**p < 0.01$, $***p < 0.001$.

Caspase activity contributes to GANT61/A-1210477-induced cell death

To test if cells undergo caspase-dependent apoptosis upon co-treatment of GANT61 and A-1210477 as a consequence of an altered balance of pro- and antiapoptotic BCL-2 protein family members we blocked caspase function by adding the pan-caspase inhibitor zVAD.fmk. Of note, zVAD.fmk significantly reduced GANT61/A-1210477-stimulated cell death in RH30 and also in RD cells (although to a lesser extent) (Fig. 6A and B). Furthermore, we observed a minor albeit significant rescue from cell death induced by A-1210477 alone in RH30 cells upon zVAD.fmk addition (data not shown). This finding indicates that caspase activity contributes to GANT61/A-1210477-induced cell death.
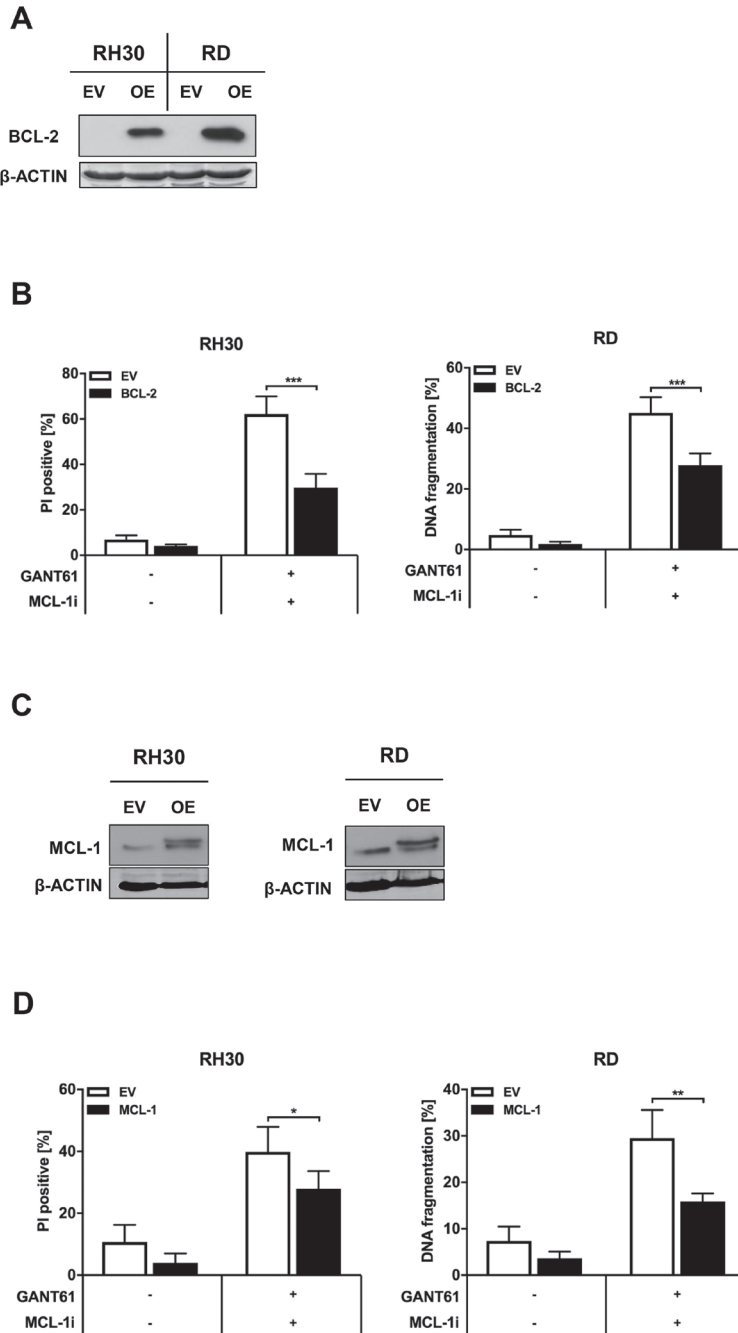
A

B

C

D

Fig. 5. Overexpression of BCL-2 or MCL-1 rescues cells from GANT61/A-1210477-induced cell death. (**A** and **B**) RH30 and RD cells were lentivirally transduced to over-

Fig. 5. Continued

express murine BCL-2 or EV and expression of BCL-2 was assessed by Western blot analysis. β-ACTIN served as loading control (**A**). Transduced cells were treated with 8 µM (RH30) or 6 µM (RD) GANT61 and 7.5 µM (RH30) or 12.5 µM (RD) A-1210477 (MCL-1i) for 72 h. Cell death was determined by PI-stained nuclei using microscopy (RH30) or flow cytometry (RD). Mean and SD of three independent experiments performed in triplicate are shown. ***$p < 0.001$ (**B**). (**C** and **D**) RH30 and RD cells were transfected to overexpress MCL-1 or EV and expression of MCL-1 was assessed by Western blot analysis. β-ACTIN served as loading control (**C**). Transfected cells were treated with 8 µM (RH30) or 6 µM (RD) GANT61 and 7.5 µM (RH30) or 12.5 µM (RD) A-1210477 (MCL-1i) for 72 h. Cell death was determined by PI-stained nuclei using microscopy. Mean and SD of at least three independent experiments performed in triplicate are shown. *$p < 0.05$, **$p < 0.01$ (**D**).

4

A

B

C

Fig. 6. Caspase activity contributes to GANT61/A-1210477-induced cell death.
(**A** and **B**) Cells were treated with 8 µM (RH30) (**A**) or 6 µM (RD) (**B**) GANT61 and 7.5 µM (RH30) or 12.5 µM (RD) A-1210477 (MCL-1i) for 48 h (RH30) or 72 h (RD). Cell death was determined by PI-stained nuclei using microscopy. Mean and SD of three independent experiments performed in triplicate are shown. **p < 0.01, ***p < 0.001. (**C**) Schematic representation of the results.
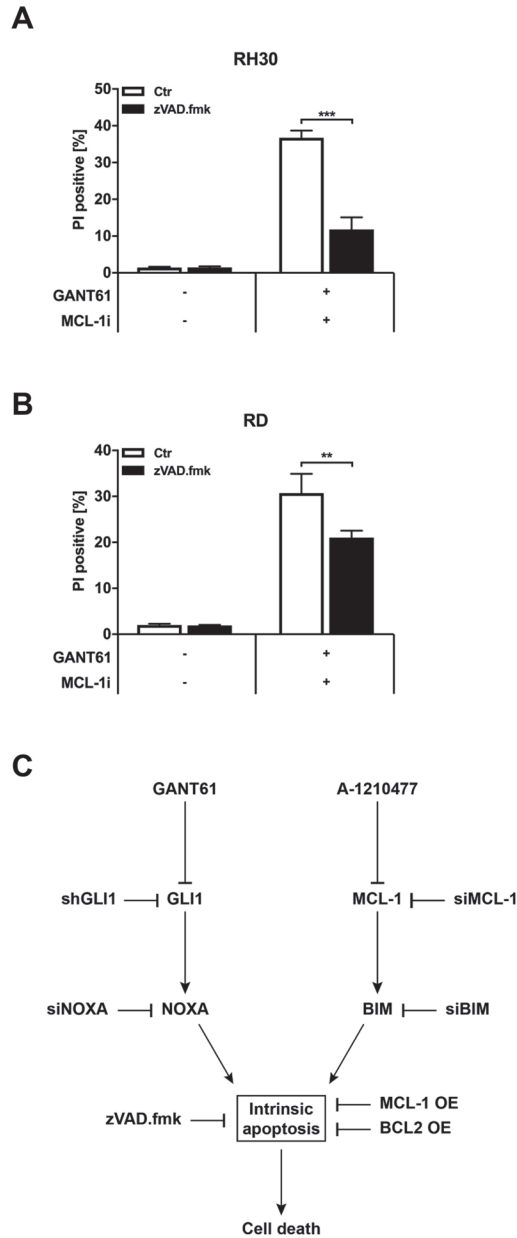
Discussion

In the present study, we show that concomitant pharmacological targeting of Hh signaling and MCL-1 synergistically induces cell death in RMS cells, whereas either compound alone exerts minimal or moderate effects. This conclusion is further supported by combined genetic and pharmacological inhibition, demonstrating that co-treatment of GANT61 and A-1210477 indeed relies on inhibition of GLI1 (by GANT61) and MCL-1 (by A-1210477).

Mechanistically, we show that A-1210477 triggers the release of BIM from MCL-1 and its re-shuttling to BCL-x_L and BCL-2, while GANT61 results in NOXA induction as previously reported by our group [32,33]. Thereby, A-1210477 and GANT61 act in concert to shift the balance of pro- and antiapoptotic BCL-2 family proteins in favor of apoptosis, facilitating the induction of cell death. In support of this model, genetic silencing of proapoptotic BIM or NOXA rescued cells from GANT61/A-1210477-induced cell death. *Vice versa*, overexpression of antiapoptotic BCL-2 or MCL-1 protected cells from GANT61/A-1210477-triggered cell death. These findings highlight that the shift in the balance of pro- and antiapoptotic BCL-2 family proteins is critical to ultimately engage cell death.

Of note, BIM has been implicated in the execution of cell death for a subset of RMS tumors [40], further highlighting the rationale to employ drugs in RMS therapy that may result in an increase of unbound BIM (such as MCL-1 inhibitors). Notably, abrogation of caspase function by addition of the pan-caspase inhibitor zVAD.fmk resulted in a significant rescue from cell death conferred by combination treatment, indicating that cells ultimately undergo cell death that largely depends on caspases. However, as zVAD.fmk was unable to completely block cell death, caspase-independent forms of cell death may also contribute to cell death upon the combination treatment of GANT61 and A-1210477.

In line with previous studies, we observed an increase of MCL-1 protein levels upon treatment with A-1210477 [35]. Besides neutralizing MCL-1, A-1210477 may potentially also stabilize MCL-1 due to conformational changes in its protein structure, rendering it less prone to degradation.

4

Taken together, the results of the present study show that single agent blockade of Hh signaling is not sufficient to induce cell death in RMS, which goes in line with our previous studies [33,41]. Intriguingly, the combination treatment including the GLI1 targeting agent GANT61 proved to be more efficacious in RH30 than in RD cells, although RH30 cells harbor a *GLI1* amplification, resulting in higher GLI1 protein levels than in RD cells [23]. We hypothesize that RH30 cells may be more dependent on the transcriptional activity of GLI1 and are therefore more sensitive to the combination therapy. Hence, we limited our efforts in combining genetic abrogation of Hh signaling (by shRNA mediated knockdown) and pharmacological abrogation of MCL-1 (by A-1210477) to this cell line. However, future studies could employ cell lines derived from other tumor entities that show elevated GLI1 expression as a result of an amplification to further investigate this putative dependency. Furthermore, it may be of interest to determine if the combination treatment with GANT-61/A-1210477 shows increased potential to induce myogenic differentiation in RMS cells compared to single-agent Hh pathway inhibitors [42,43].

Moreover, the combination treatment showed efficacy in RMS cells regardless of embryonal or alveolar histology or *TP53* status (RH30 and RD with defective *TP53* [36], Kym-1 with functional *TP53* [37]). Of note, *NOXA* is a *bona fide* target gene of P53 [44] and cell death induction by GANT61 and A-1210477 partially depended on NOXA. Of note, TAp73 might substitute for the lost *TP53* function to induce NOXA upon GANT61/A-1210477 co-treatment, in line with our recent report [32]. These findings support the notion that the combination treatment of GANT61/A-1210477 may be employed for the treatment of patients with RMS, since aRMS usually do not display *TP53* mutations (contrary to the aRMS cell line RH30), while eRMS commonly harbor mutations in this gene or other inactivating alterations in its regulation (i.e., amplification of P53 inactivator *MDM2*) [9].

Besides RMS, a combination therapy using HPI and MCL-1 inhibitors could also prove to be a promising therapeutic avenue for high risk MB patients, as the combination of GANT61 and A-1210477 also potently triggered cell death in *TP53*-mutated MB cells. A subgroup of MB exhibits Hh activation (the so-called SHH subgroup [39]) and patients in the SHH group MB who

also carry a *TP53* germline mutation (resulting in Li-Fraumeni syndrome) face a particularly poor prognosis [45]. Considering further clinical translation, it has to be stated that in the present study relatively high concentrations of A-1210477 (up to 20 μM) were necessary to induce cell death upon combination treatment. Interestingly, Leverson et al. described inhibitory concentrations for A-1210477 in the micromolar range in other cell lines with high MCL-1 levels, potentially indicating a limited efficacy if this compound [35]. Importantly, novel MCL-1 inhibitors have recently been described (e.g. AZD5991 [46] and S63845 [47]) which showed a higher efficacy in blocking MCL-1 function. Furthermore, the study by Kotschy et al. also illustrated the limited toxicity of S63845 in mice, highlighting the potential this compound might have in treating patients with cancer [47].

In conclusion, our study identifies a synergistic antitumor activity of GLI1- and MCL-1-targeting agents. These findings may have important implications for the development of novel therapeutic strategies for patients suffering from Hh-driven cancers.

Acknowledgements

Materials & Methods

Cell culture and chemicals

The RMS cell line RH30 was obtained from Deutsche Sammlung von Mikroorganismen und Zellkulturen (DSMZ, Braunschweig, Germany), the RMS cell line RD was obtained from American Type Culture Collection (ATCC, Manassas, VA, USA) and the RMS cell line Kym-1 was obtained from Japanese Cancer Research Resources Bank (JCRB, Ibaraki, Osaka, Japan). The RMS cell line aRMS-CP was established from a patient with a *PAX7-FOXO1-*positive, pre-treated (carboplatin, epirubicin, vincristine, actinomycin-D, ifosfamide, etoposide) aRMS. The MB cell line DAOY was kindly provided by Marc Remke (Düsseldorf, Germany). Cell lines were authenticated by

short tandem repeats (STR) profiles and negatively tested for mycoplasma contamination. RD, aRMS-CP and DAOY cells were maintained in DMEM GlutaMAX-I medium, RH30 and Kym-1 cells in RPMI 1640 GlutaMAX-I, both supplemented with 10% fetal calf serum (FCS), 1% penicillin/streptomycin and 1 mM sodium pyruvate (all Life Technologies, Inc., Darmstadt, Germany). RPMI 1640 medium was further supplemented with 25 mM HEPES for Kym-1 cells (Life Technologies, Inc., Darmstadt, Germany). GANT61 was purchased from Sigma-Aldrich (Taufkirchen, Germany), A-1210477 (MCL-1 inhibitor) was purchased from Active Biochem (Hongkong, China) and zVAD. fmk from Bachem (Heidelberg, Germany). If not indicated differently, all other chemicals were purchased from Sigma-Aldrich (Taufkirchen, Germany) or Carl Roth (Karlsruhe, Germany).

Determination of cell death and colony formation

Cell death was determined by fluorescence microscopy of propidium iodide (PI)-stained nuclei using ImageXpress Micro XLS system (Molecular Devices, Biberach an der Riss, Germany) or by flow cytometric analysis (FACSCanto II, BD Biosciences, Heidelberg, Germany) of DNA fragmentation of PI-stained nuclei as described previously [48]. For determination of colony formation, cells were seeded (200 cells/well for RD cells, 100 cells/well for RH30 and DAOY cells) in six-well plates, allowed to settle overnight and treated with the according substances for 10 h. Thereafter, medium was changed, and colonies were stained after 12–15 days of growth with crystal violet solution (0.5% crystal violet, 30% ethanol, 3% formaldehyde). Colonies were counted and the percentage of colonies relative to solvent-treated controls was calculated.

Transient RNA interference

For transient knockdown of BIM, MCL-1 and NOXA by siRNA, cells were reversely transfected with 10 nM SilencerSelect siRNA (Invitrogen, Carlsbad, CA, USA) for control siRNA (4390843), BIM targeting siRNAs (s195011 (#1) and s195012 (#2)), MCL-1 targeting siRNAs (s8583 (#1) and s8584 (#2)) or NOXA targeting siRNAs (s10708 (#1), s10709 (#2) and s10710 (#3)), using Lipofectamine RNAi Max (Invitrogen, Carlsbad, CA, USA) and OptiMEM (Life

Technologies, Inc., Darmstadt, Germany) according to the manufacturer's
protocol. Knockdown efficiency was determined by Western blot analysis 24
h after reverse transfection.

Western blot analysis

Western blot analysis was performed as described previously [49] using the
following antibodies: α-TUBULIN (CP06, Calbiochem), BCL-x$_L$ (2762S, Cell
Signaling), BCL-2 (610539, BD Bioscience), mBcl-2 (antimouse) (33–6100,
Invitrogen), β-ACTIN (A5441, Sigma-Aldrich), BIM (2819S, Cell Signaling),
GAPDH (5G4-6C5, Hytest), GLI1 (2643S, Cell Signaling), MCL-1 (ADI-AAP-
240F, Enzo Life Sciences), NOXA (ALX-804-408-C100, Enzo Life Sciences),
VINCULIN (V9131, Sigma-Aldrich). Goat anti-mouse IgG conjugated to
horseradish peroxidase (Santa Cruz Biotechnology, Santa Cruz, CA, USA) and
enhanced chemiluminescence (Amersham Bioscience, Freiburg, Germany)
or infrared dye-labeled secondary antibodies and infrared imaging (Odyssey
Imaging System, LI-COR Bioscience, Bad Homburg, Germany) were used
for detection. Representative blots of at least two independent experiments
are shown.

Stable GLI knockdown

Generation of plasmids

The plasmids for stable lentiviral knockdown of GLI1 were generated by
cloning the respective sequences into pLKO.1puro-TRC cloning vector
(addgene #10878; [50]) according to the Addgene Protocol (Plasmid 10878.
Protocol 1.0; http://www.addgene.org/tools/protocols/plko/#A). Briefly,
suitable oligonucleotides were annealed and ligated into pLKO.1-TRC
cloning cut with AgeI and EcoRI. Successful insertion was verified by Sanger
sequencing of shRNA sequences. The shRNA sequences were retrieved from
the RNAi consortium homepage (now Genetic Perturbation Platform; https://
portals.broadinstitute.org/gpp/public/; [51]). The oligonucleotides sequences
used for cloning are: CC GGCGTGAGCCTGAATCTGTGTATCTCGAGATACA
CAGATTCAGGCTCACGTTTTTG(GLI1_f);ATTCAAAAACGTGAGCCTGAATCT
GTGTATCTCGAG ATACACAGATTCAGGCTCACG (GLI1_r).

Production of lentiviral supernatant and transduction of RH30

Lentiviral supernatant was in principle generated according to the Addgene Protocol (Plasmid 10878. Protocol 1.0; http://www.addgene.org/tools/protocols/plko/#A). Briefly, HEK293T cells (70% confluent in six-well-plates) were transfected with the respective pLKO.1-shGLI plasmid or a scrambled pLKO.1-shCtrl (Sigma) together with the helper plasmids psPAX2 (Addgene plasmid 12260) and pMD.2G (Addgene plasmid 12259) using Fugene HD (Promega, Madison, WI, USA) according to the manufacturer's protocol. After 16 h of incubation, medium was changed to fresh medium and 24 h and 48 h later supernatant was collected, pooled and filtered through a 0.45 μm pore strainer to remove detached cells. The supernatant was used within one week of collection. For transduction, RH30 cells were grown to 70% confluency in a T25 flask. After removal of the culture medium, the viral supernatant was mixed 1:1 with fresh medium and added to the cells. To facilitate viral infection 8 μg/ml polybrene was added to the viral supernatant. After 24 h, the supernatant was removed and cells were supplied with fresh medium. After additional 24 h, cells were kept in medium containing 1 μg/ml puromycin for selection. Successful knockdown was validated using Western blot analysis.

Overexpression of BCL-2 and MCL-1

For BCL-2 overexpression, Phoenix packaging cells were transfected with 20 μg of murine stem cell virus (pMSCV, Clontech, Mountain View, CA, USA) vector containing murine BCL-2 or empty vector (EV) using calcium phosphate transfection as described previously [52]. Stable cell lines were generated by lentiviral transduction and selected with 10 μg/ ml Blasticidin (Invitrogen, Carlsbad, CA, USA). For stable expression of MCL-1, cells were transfected with 20 μg of pCMV-Tag3B plasmid containing MCL-1 or EV (kindly provided by Genentech (South San Francisco, CA, USA)) supplied with Lipofectamine 2000 (Life Technologies, Inc., Darmstadt, Germany) and selected with 0.5 mg/ml G418 as described previously [53]. Transfection efficiency was confirmed by Western blot analysis.

Co-immunoprecipitation of BCL-2, BCL-x$_L$ and MCL-1

Co-Immunoprecipitation of BCL-2, BCL-x$_L$ and MCL-1 was performed in 400 µl lysates (using CHAPS lysis buffer (10 mM HEPES (pH 7.4); 150 mM NaCl; 1% CHAPS) supplemented with 1 mM protease inhibitor cocktail (Sigma-Aldrich, Taufkirchen, Germany) according to the manufacturer's protocol) containing 1 mg protein, which was incubated overnight at 4 °C with 1.25 µg hamster anti-BCL-2 antibody (551051, clone 6C8, BD Biosciences), 1 µg mouse anti-BCL-x$_L$ antibody (MAB3121, clone 7B2.5, Millipore) or 2.5 µg rabbit anti-MCL-1 antibody (559027, clone 22, BD Biosciences). Antibodies were crosslinked to 30 µl pan-mouse IgG Dynabeads or Protein G Dynabeads (Life Technologies, Inc., Darmstadt, Germany) using 20 mM DMP prior to incubation. After incubation, samples were washed with CHAPS lysis buffer. Thereafter, the precipitate was analyzed for interaction with BCL-2, BCL-x$_L$, BIM, and MCL-1 by Western blot analysis.

Statistical analysis

Statistical significance was assessed by one-way or two-way ANOVA via GraphPad Prism software (version 7, GraphPad Software, CA, USA). Drug interactions were analyzed by the combination index (CI) method based on that described by Chou [54] using CalcuSyn software (Biosoft, Cambridge, UK). CI < 0.9 indicates synergism, 0.9–1.1 additivity and > 1.1 antagonism.

References

1. Kramer, S., Meadows, A. T., Jarrett, P. & Evans, A. E. Incidence of childhood cancer: experience of a decade in a population-based registry. *J Natl Cancer Inst* **70**, 49–55 (1983).

2. Newton Jr., W. A. *et al.* Histopathology of childhood sarcomas, Intergroup Rhabdomyosarcoma Studies I and II: clinicopathologic correlation. *J Clin Oncol* **6**, 67–75 (1988).

3. Oberlin, O. *et al.* Prognostic factors in metastatic rhabdomyosarcomas: results of a pooled analysis from United States and European cooperative groups. *J Clin Oncol* **26**, 2384–2389 (2008).

4. Abraham, J. *et al.* Lineage of origin in rhabdomyosarcoma informs pharmacological response. *Genes Dev.* **28**, 1578–1591 (2014).

5. Driman, D., Thorner, P. S., Greenberg, M. L., Chilton-MacNeill, S. & Squire, J. MYCN gene amplification in rhabdomyosarcoma. *Cancer* **73**, 2231–2237 (1994).

6. Toffolatti, L. *et al.* MYCN expression in human rhabdomyosarcoma cell lines and tumour samples. *J Pathol* **196**, 450–458 (2002).

7. Barr, F. G. *et al.* Genomic and clinical analyses of 2p24 and 12q13-q14 amplification in alveolar rhabdomyosarcoma: a report from the Children's Oncology Group. *Genes Chromosom. Cancer* **48**, 661–672 (2009).

8. Merlino, G. & Helman, L. J. Rhabdomyosarcoma--working out the pathways. *Oncogene* **18**, 5340–5348 (1999).

9. Shern, J. F. *et al.* Comprehensive genomic analysis of rhabdomyosarcoma reveals a landscape of alterations affecting a common genetic axis in fusion-positive and fusion-negative tumors. *Cancer Discov* **4**, 216–231 (2014).

10. Malempati, S. & Hawkins, D. S. Rhabdomyosarcoma: review of the Children's Oncology Group (COG) Soft-Tissue Sarcoma Committee experience and rationale for current COG studies. *Pediatr Blood Cancer* **59**, 5–10 (2012).

11. Varjosalo, M. & Taipale, J. Hedgehog: functions and mechanisms. *Genes Dev* **22**, 2454–2472 (2008).

12. Beachy, P. A., Karhadkar, S. S. & Berman, D. M. Tissue repair and stem cell renewal in carcinogenesis. *Nature* **432**, 324–331 (2004).

13. Eichberger, T. *et al.* Overlapping and distinct transcriptional regulator properties of the GLI1 and GLI2 oncogenes. *Genomics* **87**, 616–632 (2006).

14. Ryan, K. E. & Chiang, C. Hedgehog secretion and signal transduction in vertebrates. *J Biol Chem* **287**, 17905–17913 (2012).

15. Scales, S. J. & de Sauvage, F. J. Mechanisms of Hedgehog pathway activation in cancer and implications for therapy. *Trends Pharmacol Sci* **30**, 303–312 (2009).

16. Stecca, B. & Ruiz, I. A. A. Context-dependent regulation of the GLI code in cancer by HEDGEHOG and non-HEDGEHOG signals. *J Mol Cell Biol* **2**, 84–95 (2010).

17. Fulda, S. & Debatin, K. M. Extrinsic versus intrinsic apoptosis pathways in anticancer chemotherapy. *Oncogene* **25**, 4798–4811 (2006).

18. Fulda, S. Tumor resistance to apoptosis. *Int J Cancer* **124**, 511–515 (2009).

19. Armistead, P. M. *et al.* Expression of receptor tyrosine kinases and apoptotic molecules in rhabdomyosarcoma: correlation with overall survival in 105 patients. *Cancer* **110**, 2293–2303 (2007).

20. Margue, C. M., Bernasconi, M., Barr, F. G. & Schafer, B. W. Transcriptional modulation of the anti-apoptotic protein BCL-XL by the paired box transcription factors PAX3 and PAX3/FKHR. *Oncogene* **19**, 2921–2929 (2000).

21. Pazzaglia, L. *et al.* Genetic and molecular alterations in rhabdomyosarcoma: mRNA overexpression of MCL1 and MAP2K4 genes. *Histol Histopathol* **24**, 61–67 (2009).

22. Walensky, L. D. BCL-2 in the crosshairs: tipping the balance of life and death. *Cell Death Differ* **13**, 1339–1350 (2006).

23. Roberts, W. M., Douglass, E. C., Peiper, S. C., Houghton, P. J. & Look, A. T. Amplification of the gli gene in childhood sarcomas. *Cancer Res* **49**, 5407–5413 (1989).

24. Zibat, A. *et al.* Activation of the hedgehog pathway confers a poor prognosis in embryonal and fusion gene-negative alveolar rhabdomyosarcoma. *Oncogene* **29**, 6323–6330 (2010).

25. Almazan-Moga, A. *et al.* Ligand-dependent Hedgehog pathway activation in Rhabdomyosarcoma: the oncogenic role of the ligands. *Br J Cancer* **117**, 1314–1325 (2017).

26. Pressey, J. G., Anderson, J. R., Crossman, D. K., Lynch, J. C. & Barr, F. G. Hedgehog pathway activity in pediatric embryonal rhabdomyosarcoma and undifferentiated sarcoma: a report from the Children's Oncology Group. *Pediatr Blood Cancer* **57**, 930–938 (2011).

27. Low, J. A. & de Sauvage, F. J. Clinical experience with Hedgehog pathway inhibitors. *J Clin Oncol* **28**, 5321–5326 (2010).

28. Danhof, R., Lewis, K. & Brown, M. Small Molecule Inhibitors of the Hedgehog Pathway in the Treatment of Basal Cell Carcinoma of the Skin. *Am J Clin Dermatol* **19**, 195–207 (2018).

29. Kieran, M. W. *et al.* Phase I study of oral sonidegib (LDE225) in pediatric brain and solid tumors and a phase II study in children and adults with relapsed medulloblastoma. *Neuro Oncol* **19**, 1542–1552 (2017).

30. Robinson, G. W. *et al.* Vismodegib Exerts Targeted Efficacy Against Recurrent Sonic Hedgehog-Subgroup Medulloblastoma: Results From Phase II Pediatric Brain Tumor Consortium Studies PBTC-025B and PBTC-032. *J Clin Oncol* **33**, 2646–2654 (2015).

31. Beauchamp, E. M. *et al.* Arsenic trioxide inhibits human cancer cell growth and tumor development in mice by blocking Hedgehog/GLI pathway. *J Clin Invest* **121**, 148–160 (2011).

32. Meister, M. T., Boedicker, C., Klingebiel, T. & Fulda, S. Hedgehog signaling negatively co-regulates BH3-only protein Noxa and TAp73 in TP53-mutated cells. *Cancer Lett* **429**, 19–28 (2018).

33. Graab, U., Hahn, H. & Fulda, S. Identification of a novel synthetic lethality of combined inhibition of hedgehog and PI3K signaling in rhabdomyosarcoma. *Oncotarget* **6**, 8722–8735 (2015).

34. Ploner, C., Kofler, R. & Villunger, A. Noxa: at the tip of the balance between life and death. *Oncogene* **27 Suppl 1**, S84-92 (2008).

35. Leverson, J. D. *et al.* Potent and selective small-molecule MCL-1 inhibitors demonstrate on-target cancer cell killing activity as single agents and in combination with ABT-263 (navitoclax). *Cell Death Dis* **6**, e1590 (2015).

36. Felix, C. A., Winick, N. J., Crouch, G. D. & Helman, L. J. Frequency and Diversity of p53 Mutations in Childhood Rhabdomyosarcoma. *Cancer Res.* **52**, 2243–2247 (1992).

37. Muret, J. *et al.* Attenuation of soft-tissue sarcomas resistance to the cytotoxic action of TNF-alpha by restoring p53 function. *PLoS One* **7**, e38808 (2012).

38. Saylors 3rd, R. L. *et al.* Infrequent p53 gene mutations in medulloblastomas. *Cancer Res* **51**, 4721–4723 (1991).

39. Taylor, M. D. *et al.* Molecular subgroups of medulloblastoma: the current consensus. *Acta Neuropathol* **123**, 465–472 (2012).

40. Wachtel, M. *et al.* FGFR4 signaling couples to Bim and not Bmf to discriminate subsets of alveolar rhabdomyosarcoma cells. *Int J Cancer* **135**, 1543–1552 (2014).

41. Meister, M. T. *et al.* Arsenic trioxide induces Noxa-dependent apoptosis in rhabdomyosarcoma cells and synergizes with antimicrotubule drugs. *Cancer Lett* **381**, 287–295 (2016).

42. Satheesha, S. *et al.* Targeting hedgehog signaling reduces self-renewal in embryonal rhabdomyosarcoma. *Oncogene* **35**, 2020–2030 (2016).

43. Koleva, M. *et al.* Pleiotropic effects of sonic hedgehog on muscle satellite cells. *Cell Mol Life Sci* **62**, 1863–1870 (2005).

44. Oda, E. *et al.* Noxa, a BH3-only member of the Bcl-2 family and candidate mediator of p53-induced apoptosis. *Science (80-.).* **288**, 1053–1058 (2000).

45. Zhukova, N. *et al.* Subgroup-specific prognostic implications of TP53 mutation in medulloblastoma. *J Clin Oncol* **31**, 2927–2935 (2013).

46. Tron, A. E. *et al.* Discovery of Mcl-1-specific inhibitor AZD5991 and preclinical activity in multiple myeloma and acute myeloid leukemia. *Nat Commun* **9**, 5341 (2018).

47. Kotschy, A. *et al.* The MCL1 inhibitor S63845 is tolerable and effective in diverse cancer models. *Nature* **538**, 477–482 (2016).

48. Preuss, E., Hugle, M., Reimann, R., Schlecht, M. & Fulda, S. Pan-mammalian target of rapamycin (mTOR) inhibitor AZD8055 primes rhabdomyosarcoma cells for ABT-737-induced apoptosis by down-regulating Mcl-1 protein. *J Biol Chem* **288**, 35287–35296 (2013).

49. Fulda, S., Sieverts, H., Friesen, C., Herr, I. & Debatin, K. M. The CD95 (APO-1/ Fas) system mediates drug-induced apoptosis in neuroblastoma cells. *Cancer Res* **57**, 3823–3829 (1997).

50. Moffat, J. *et al.* A lentiviral RNAi library for human and mouse genes applied to an arrayed viral high-content screen. *Cell* **124**, 1283–1298 (2006).

51. Yang, X. *et al.* A public genome-scale lentiviral expression library of human ORFs. *Nat Methods* **8**, 659–661 (2011).

52. Heinicke, U. & Fulda, S. Chemosensitization of rhabdomyosarcoma cells by the histone deacetylase inhibitor SAHA. *Cancer Lett* **351**, 50–58 (2014).

53. Hugle, M., Belz, K. & Fulda, S. Identification of synthetic lethality of PLK1 inhibition and microtubule-destabilizing drugs. *Cell Death Differ* **22**, 1946–1956 (2015).

54. Chou, T. C. Drug combination studies and their synergy quantification using the Chou-Talalay method. *Cancer Res* **70**, 440–446 (2010).

4

Supplementary data
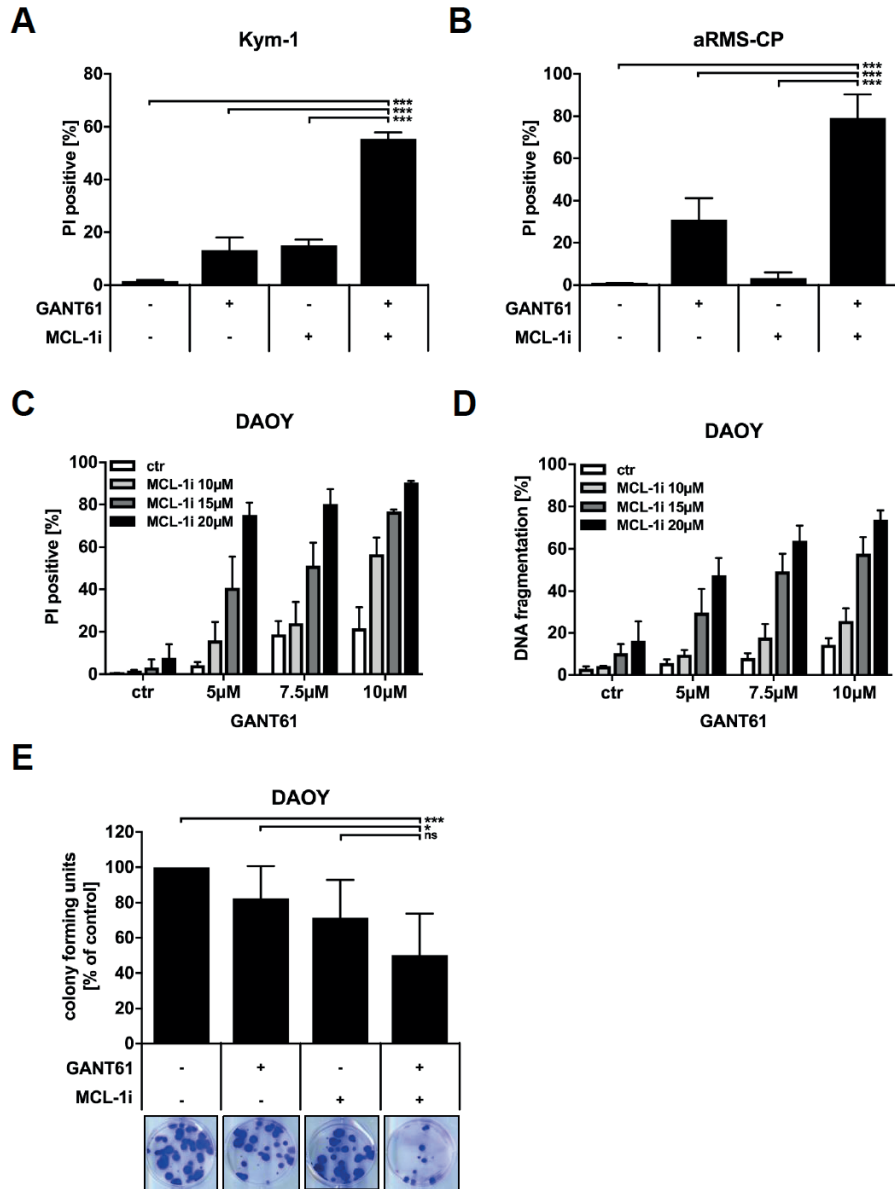
Suppl. Fig. 1. (**A** and **B**) Kym-1 (A) and aRMS-CP (**B**) cells were treated with 10 μM (Kym-1) or 5 μM (aRMS-CP) GANT61 and/or 10 μM (Kym-1) or 20 μM (aRMS-CP)

Suppl. Fig. 1. Continued

A-1210477 (MCL-1i) for 48 h. Cell death was determined by PI-stained nuclei using microscopy. Mean and SD of three independent experiments performed in triplicate are shown. In all cell lines, combination treatment showed significantly higher efficacy than control cells or cells treated with either compound alone. However, single compounds showed significant efficacy in some cells when compared to control cells. ***$p < 0.001$. (**C** and **D**) DAOY cells were treated with indicated concentrations of GANT61 and/or A-1210477 (MCL-1i) for 72 h. Cell death was determined by PI-stained nuclei using microscopy (C) or flow cytometry (**D**). (**E**) DAOY cells were treated with 5 µM GANT61 and/or 17 µM A-1210477 (MCL-1i) for 10 h. Colony formation was assessed after 12 to 15 d. The number of colonies expressed as percentage of solvent-treated controls (top) and representative images (bottom) are shown. Mean and SD of three independent experiments performed in duplicate are shown. ns = not significant, *$p < 0.05$ (combination relative to control and single compound-treated samples with combination not showing a significantly better decrease in colony number than MCL-1 treated cells).
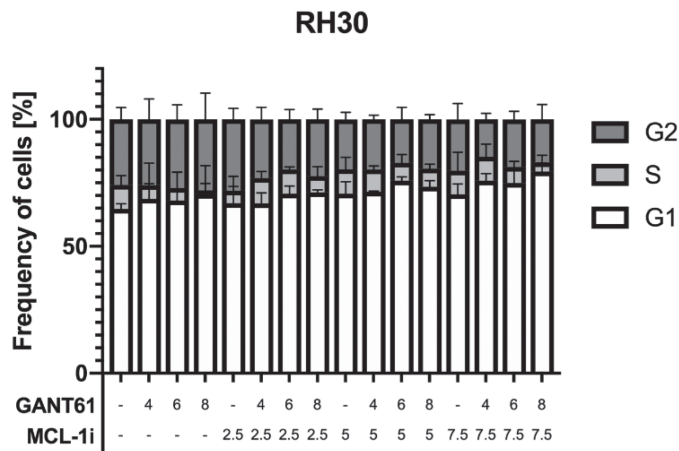
Suppl. Fig. 2. RH30 cells were treated with the indicated concentrations of GANT61 and/or A-1210477 (MCL1i) for 72 h. Frequency of cells per cell cycle phase was analyzed in PI-stained nuclei using flow cytometry and FlowJo software (version 7.6.5) after gating on living cells. Results showed no statistically significant difference. Parts of the shown data were used for Figure 1B.

Suppl. Table 1. CI was calculated as described in the Materials & Methods section for cell death induced by combination treatment (Fig. 1A and B) with indicated concentrations of GANT61 and A-1210477 (MCL-1i) for PI-stained nuclei analyzed by microscopy (**A**) or flow cytometry (**B**). CI < 0.9 indicates synergism, 0.9-1.1 additivity and > 1.1 antagonism.

A

RH30		MCL-1i		
		2.5µM	5µM	7.5µM
GANT61	4µM	1.292	0.994	0.452
	6µM	1.631	0731	0.272
	8µM	1.518	0.473	0.234

RD		MCL-1i		
		7.5µM	10µM	12.5µM
GANT61	4µM	1.159	1.074	0.677
	5µM	1.138	0.700	0.376
	6µM	0.826	0.504	0.194

B

RH30		MCL-1i		
		2.5µM	5µM	7.5µM
GANT61	4µM	2.564	0.843	0.434
	6µM	1.557	0.554	0.325
	8µM	0.426	0.393	0.221

RD		MCL-1i		
		7.5µM	10µM	12.5µM
GANT61	4µM	1.779	1.494	0.965
	5µM	1.635	1.192	0.786
	6µM	1.241	0.866	0.664

4

5

Mesenchymal tumor organoid models recapitulate rhabdomyosarcoma subtypes

Michael T. Meister[1,2], Marian J. A. Groot Koerkamp[1,2], Terezinha de Souza[1,2], Willemijn B. Breunis[1,3], Ewa Frazer-Mendelewska[1,2], Mariël Brok[1,2], Jeff DeMartino[1,2], Freek Manders[1,2], Camilla Calandrini[1,2], Hinri H. D. Kerstens[1], Alex Janse[1], M. Emmy M. Dolman[1,4,5], Selma Eising[1], Karin P. S. Langenberg[1], Marc van Tuil[1], Rutger R. G. Knops[1], Sheila Terwisscha van Scheltinga[1], Laura S. Hiemcke-Jiwa[1], Uta Flucke[1], Johannes H. M. Merks[1], Max M. van Noesel[1], Bastiaan B. J. Tops[1], Jayne Y. Hehir-Kwa[1], Patrick Kemmeren[1,6], Jan J. Molenaar[1], Marc van de Wetering[1,2], Ruben van Boxtel[1,2], Jarno Drost[1,2,#], Frank C. P. Holstege[1,6,#]

[1] Princess Máxima Center for Pediatric Oncology, Heidelberglaan 25, 3584 CS Utrecht, The Netherlands.
[2] Oncode Institute, Heidelberglaan 25, 3584 CS Utrecht, The Netherlands.
[3] Department of Oncology and Children's Research Center, University Children's Hospital Zürich, 8032 Zürich, Switzerland.
[4] Children's Cancer Institute, Lowy Cancer Centre, UNSW Sydney, Kensington, NSW, Australia.
[5] School of Women's and Children's Health, Faculty of Medicine, UNSW Sydney, Kensington, NSW, Australia.
[6] Center for Molecular Medicine, UMC Utrecht and Utrecht University, Utrecht, The Netherlands.
Co-correspondence

Abstract

Rhabdomyosarcomas (RMS) are mesenchyme-derived tumors and the most common childhood soft tissue sarcomas. Treatment is intense, with a nevertheless poor prognosis for high-risk patients. Discovery of new therapies would benefit from additional preclinical models. Here we describe the generation of a collection of 19 pediatric RMS tumor organoid (tumoroid) models (success rate of 41%) comprising all major subtypes. For aggressive tumors, tumoroid models can often be established within four to eight weeks, indicating the feasibility of personalized drug screening. Molecular, genetic, and histological characterization show that the models closely resemble the original tumors, with genetic stability over extended culture periods of up to six months. Importantly, drug screening reflects established sensitivities and the models can be modified by CRISPR/Cas9 with *TP53* knockout in an embryonal RMS model resulting in replicative stress drug sensitivity. Tumors of mesenchymal origin can therefore be used to generate organoid models, relevant for a variety of preclinical and clinical research questions.

Introduction

Rhabdomyosarcoma (RMS) is a type of malignant tumor of mesenchymal origin [1] and forms the most common soft tissue sarcoma in children and adolescents [2]. Historically, RMS has been divided into two main subtypes based on histology. Whereas embryonal RMS (eRMS) displays cellular heterogeneity and hallmarks of immature skeletal myoblasts [3], alveolar RMS (aRMS) cells are distributed around an open central space, thereby resembling pulmonary alveoli [4]. eRMS is more frequently observed in children under ten, accounting for two-thirds of all RMS cases, and generally has a better prognosis than aRMS, which is more common in adolescents and young adults [5]. In aRMS, a sole genetic driver alteration is usually observed, caused by a chromosomal translocation resulting in a fusion gene between either *PAX3* or *PAX7* and *FOXO1*. In contrast, eRMS is genetically more heterogeneous, harboring mutations in several common oncogenes or tumor suppressor genes [6]. Other subtypes of RMS have recently been recognized [7]. RMS treatment is guided by protocols developed by multi-national collaborative groups and includes systemic chemotherapy in addition to local therapy (radiotherapy and/or surgery) [8]. The prognosis of RMS has improved over the last decades [9]. For patients with high-risk, refractory or relapsed disease, prognosis remains poor however, despite an immense treatment burden [10,11]. Thus, development of new therapeutic options is of critical importance for these patients.

Development of such treatment options requires *in vitro* models and may therefore benefit from application of organoid technology. The basis of this technology is that given a suitable growth environment, tissue stem cells self-renew as well as give rise to natural progeny which organize according to their preferred growth modality without the need for artificial cell immortalization. The technology was first established in healthy epithelial tissue from mouse small intestine [12] and soon adapted to various other healthy and diseased epithelial tissues, including cancer [13]. Tumor organoid (tumoroid) systems are proving useful in cancer research as they display genetic stability over extended culture periods, retaining the molecular characteristics of the tumor they are derived from. While dedicated co-culturing tumoroid systems of tumor and non-tumor cells are starting to be developed [14], the majority of tumoroid systems consist only of tumor cells. Tumoroid models can be

5

expanded, facilitating high-throughput screening approaches such as small molecule or CRISPR/Cas9-knockout screening [15].

To date, tumoroid approaches have been primarily applied to cancers derived from epithelial cells (i.e., carcinomas). Recent studies demonstrate that deriving tumoroid models from non-epithelial cancer is feasible but this has as yet not been achieved for pure mesenchymal cancers [16–20]. Application to tumors of mesenchymal origin such as RMS would be of obvious benefit. Tumoroid models of pediatric nephroblastoma (Wilms tumors) have been described, which, depending on the subtype, can contain stromal cells [21]. In addition, cells derived from synovial sarcoma and other adult soft tissue sarcomas can grow to a limited extent on fetal calf serum, which, although undefined in terms of the required essential growth factors, also indicates feasibility [22,23]. Furthermore, *in vitro* propagation of RMS tumor cells derived from patient-derived xenograft (PDX) mouse models has recently been shown [24]. Although these results are encouraging, no directly patient-derived collection of tumoroid models of malignant tumors of pure mesenchymal origin (i.e., sarcomas) has been generated and studied after growth for extensive periods in well-defined media components. In this study, we therefore set out to develop and apply approaches for generating a collection of tumoroid models that covers the major RMS subtypes, a pediatric cancer of mesenchymal origin with poor outcome for high-risk patients. Besides generating and extensively characterizing the tumoroid collection, we also investigated applicability for drug screening and genetic modification (Fig. 1A).

Results

A protocol to collect and process RMS tumor samples for tumoroid model establishment and propagation

Before starting to generate a collection of RMS tumoroid models, we first optimized sample acquisition and logistics between surgery, pathology and organoid culture labs (Materials & Methods). In parallel to optimizing sample acquisition, we also optimized sample processing, including testing different formulations of growth media by a combination of systematic and trial and error approaches (Discussion). RMS tumor samples are diverse. Most samples are small needle biopsies (i.e, 16-gauge tru-cut), as large resection specimens

are mostly restricted to pre-treated RMS or to treatment-naïve paratesticular fusion-negative eRMS (FN-eRMS). In addition, a subset of samples (4% here) are not solid, being acquired as bone marrow aspirates of infiltrating tumor cells (Fig. 1B). Samples are plated as minced pieces embedded in a droplet of extracellular matrix (ECM) substitute (Basement-Membrane Extract, BME) and as single-cell suspensions in BME-supplemented medium. Outgrowth of tumor cells to tumoroid models can occur from both modalities. In the case of successful outgrowth of initially plated cells, cells organize as two-dimensional monolayers (Fig. 1C). This appears to be the cells' preferred growth modality, as plating them as single-cell suspensions in BME droplets results in cells escaping the surrounding matrix and sinking to the bottom of the culture plate from which they continue to grow in a monolayer. Therefore, cells are further propagated and expanded in this way. We considered an RMS tumoroid model to be successfully established if, over the course of culturing, the expression of specific tumor markers is retained and the culture expansion is at least sufficient for drug screening, all as described below (Table 1).

Early detection of tumor cells during culturing

Tumors consist of a variety of different cell types. These include normal cell types that can grow as well or even better in the provided culture conditions, possibly outcompeting tumor cells [25]. It would therefore be useful to test for the presence of tumor cells early during culturing to omit the unnecessary propagation of cultures lacking any. At early time points, material is limited, impacting the range of applicable assays. The establishment protocol therefore utilizes an RT-qPCR assay after the first or second passage of cells with probes for standard RMS histopathology markers, i.e., *DES, MYOG, MYOD1* [7], and the fusion transcript in fusion-positive RMS (FP-RMS) [26]. We considered a sample positive for tumor cells if at least one of the three genes, plus for FP-RMS the fusion transcript, test positive. All samples that successfully yield tumoroid models, show positivity for at least one marker gene at this stage, while most models (17 out of 19) are positive for all three marker genes and the fusion transcript if applicable (Fig. 2A and B). The RT-qPCR-based approach is therefore a useful tool to determine feasibility at an early stage.
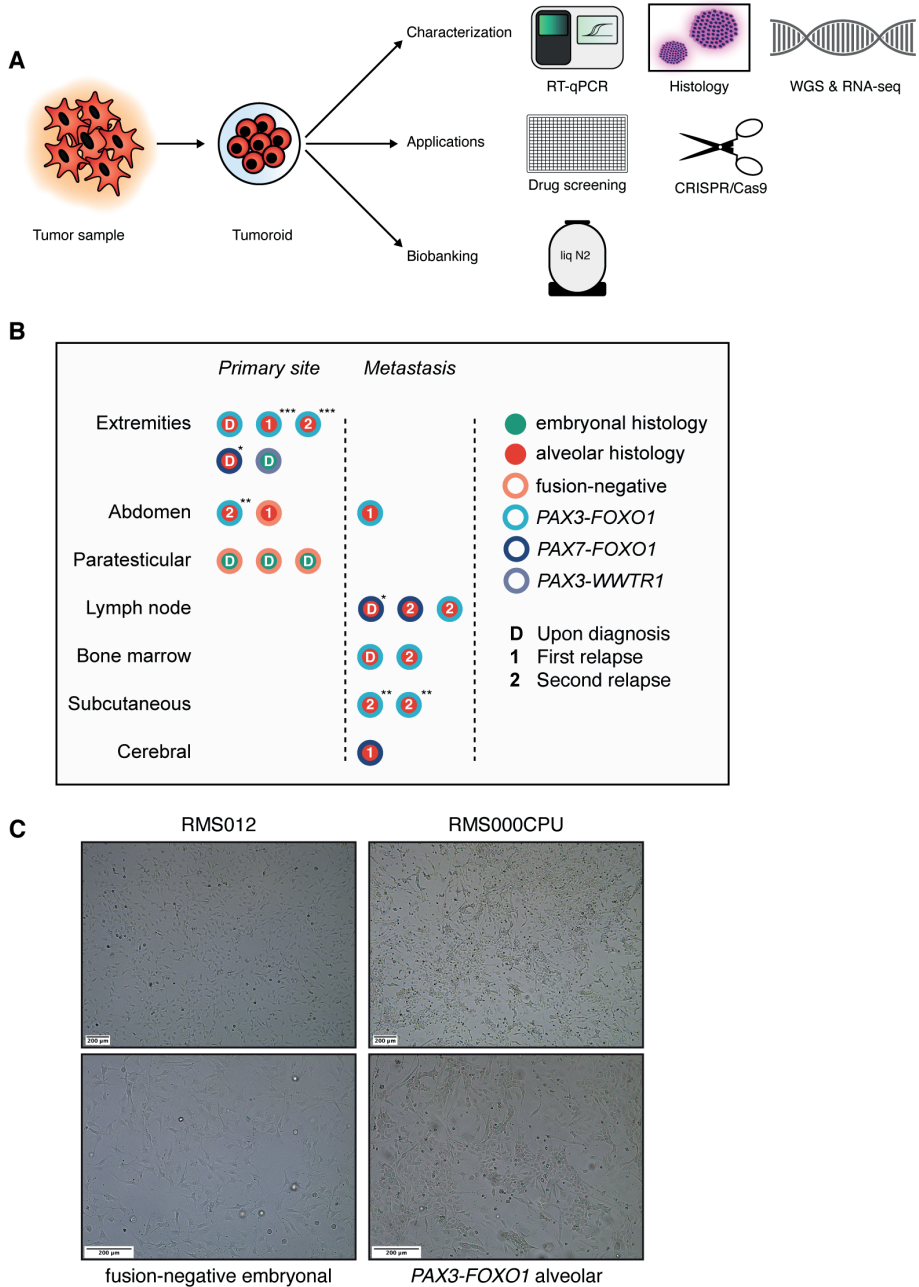
Fig. 1. A collection of RMS tumoroid models that represent the diverse clinical presentation of RMS: (**A**) Tumor organoid (tumoroid) pipeline. WGS = whole-genome sequencing, RNA-seq = mRNA sequencing, liq N2 = liquid nitrogen. (**B**) Overview

Fig. 1. Continued

of available RMS tumoroid models in the collection separated by primary versus metastatic site and exact tumor location. The color of the inner circle indicates the histological subtype while the color of the outer circle indicates the presence or absence of a fusion transcript. Letters within the circle indicate disease instance. Asterisks mark tumoroid models derived from the same patient but from distinct tumor samples. (**C**) Brightfield microscopy images of two representative RMS tumoroid models from a fusion-negative embryonal and a *PAX3-FOXO1* fusion-positive alveolar tumoroid model grown in a two-dimensional monolayer in two magnifications as indicated by the scale bars.

RMS tumoroid models retain marker protein expression and display heterogeneity in gene expression

A hallmark of RMS tumors is the expression of proteins associated with non-terminally differentiated muscle (i.e., Desmin, Myogenin and MYOD1). Expression of these proteins differs between RMS subtypes [27] and can be associated with prognosis [28]. To properly reflect the original tumors, RMS tumoroid models should therefore retain the expression patterns of these proteins. The RMS tumoroid establishment protocol therefore includes a morphological (H&E) and immunohistochemical (IHC) assessment at the time of successful establishment (i.e., drug screening). To enable comparison between tumoroid models and the tumors they were derived from, models are grown as three-dimensional spheres to mimic the three-dimensional architecture of tumors (Fig. 2C). When evaluated in this manner, RMS tumoroid models show retained expression patterns of Desmin, Myogenin and MYOD1 at the time of successful establishment (i.e., drug screening), comparable to parental tissue. Cellular morphology is also retained, with aRMS models displaying homogeneous, primitive cells, with large nuclei and minimal cytoplasm, and eRMS models displaying more heterogeneous tumor cells with variable maturation (Fig. 2C and Figure EV1A), as in the tumors [7]. Lastly, additional H&E and IHC stainings performed on two different passages of two tumoroid models (i.e., after the acquisition of the tumor sample and before the drug screening was performed) (Figure EV2A) show a high concordance concerning the heterogeneity of marker protein expression when compared to the primary tumor and the tumoroid model at the time of drug screening (Fig. 2C). This indicates that there are no major changes concerning the composition of tumor cells acquired over the course of expanding the culture for drug screening.

Table 1. Overview of available RMS tumoroid models in the collection. Patients are numbered to allow identification of RMS tumoroid models derived from the same patient. For additional clinical parameters see Dataset EV1.

Tumoroid model	Patient	Patient birth year	Histology	Fusion transcript	Patient sex	Disease instance of tumoroid establishment	Body site of sample used for tumoroid establishment
RMS007	1	2011	alveolar	negative	male	First relapse	Abdomen
RMS102	2	2000	alveolar	PAX3-FOXO1	male	Second relapse	Lymph node metastasis (clavicle)
RMS410	3	2001	alveolar	PAX3-FOXO1	male	Second relapse	Bone marrow metastasis
RMS000CPU	4	2001	alveolar	PAX3-FOXO1	male	First relapse	Kidney
RMS127	5	2003	alveolar	PAX3-FOXO1	male	Primary disease	Bone marrow metastasis
RMS006	6	2004	alveolar	PAX3-FOXO1	male	First relapse	Calf
RMS013	6	2004	alveolar	PAX3-FOXO1	male	Second relapse	Calf
RMS108	7	2004	alveolar	PAX3-FOXO1	female	Second relapse	Bladder
RMS109	7	2004	alveolar	PAX3-FOXO1	female	Second relapse	Subcutaneous metastasis
RMS110	7	2004	alveolar	PAX3-FOXO1	female	Second relapse	Subcutaneous metastasis
RMS000FLV	8	2018	alveolar	PAX3-FOXO1	female	Primary disease	Arm
RMS335	9	2010	alveolar	PAX7-FOXO1	female	Second relapse	Lymph node metastasis (groin)
RMS000HQC	10	2011	alveolar	PAX7-FOXO1	male	First relapse	Cerebral metastasis
RMS000HWO	11	2014	alveolar	PAX7-FOXO1	female	Primary disease	Leg

Table 1. Continued

Tumoroid model	Patient	Patient birth year	Histology	Fusion transcript	Patient sex	Disease instance of tumoroid establishment	Body site of sample used for tumoroid establishment
RMS000HWQ	11	2014	alveolar	*PAX7-FOXO1*	female	Primary disease	Lymph node metastasis (groin)
RMS444	12	2003	embryonal	negative	male	Primary disease	Paratesticular
RMS012	13	2013	embryonal	negative	male	Primary disease	Paratesticular
RMS000ETY	14	2014	embryonal	negative	male	Primary disease	Paratesticular
RMS000EEC	15	2005	embryonal	*PAX3-WWTR1*	male	Primary disease	Shoulder

5

In line with the heterogeneous expression of these marker proteins, single-cell RNA sequencing (scRNA-seq) shows that RMS tumoroid models retain heterogeneity in the expression of the corresponding genes (i.e., *MYOG*, *MYOD1*, and *DES*) (Fig. 2D). Importantly, this heterogeneity is not due to differences in cell cycle activity as differential gene expression patterns do not correspond with the expression of the cell cycle marker *MKI67* (Fig. 2D). Single cell RNA-seq inferred per cell copy-number plots also suggest genomic heterogeneity, and furthermore show that RMS tumoroid models consist only of tumor cells as all analyzed cells in the samples show copy-number alterations in agreement with whole-genome sequencing inferred copy-number plots (Figure EV2B). In summary, RMS tumoroid models retain histopathological hallmarks of RMS tumors as well as display transcriptional heterogeneity in line with heterogeneous protein expression at the time of drug screening, giving a first indication that they reflect the tumors they were derived from to a high extent.

A collection of RMS tumoroid models that represent the diverse clinical presentation of RMS

Having established protocols for the acquisition, processing, initial growth, and characterization of RMS tumoroid models, we applied this to 46 consecutive samples from pediatric RMS patients treated in the Netherlands, resulting in a collection of 19 RMS tumoroid models (41% efficiency). These models are derived from tumors comprising both main histological subtypes (embryonal and alveolar), different fusion types (fusion positive *PAX3-FOXO1, PAX7-FOXO1*, a novel fusion *PAX3-WWTR1*, as well as fusion negative), various risk groups, locations, and are derived from primary as well as relapsed disease (Fig. 1B, Table 1 and Dataset EV1). Outgrowth of cells from highly aggressive RMS subtypes shows a higher success rate, as indicated by 83% successful establishment for FP-RMS versus 16% for FN-RMS, and 61% success in relapsed, versus 30% in primary RMS tumors, respectively. There was no statistically significant difference in the success rate between recently treated and untreated tumors (33% versus 43%, respectively, $p = 0.59$, chi-square test). Similar differences between relapsed and primary tumors in establishment rates have been observed for orthotopic PDX models (O-PDX) of RMS [29].
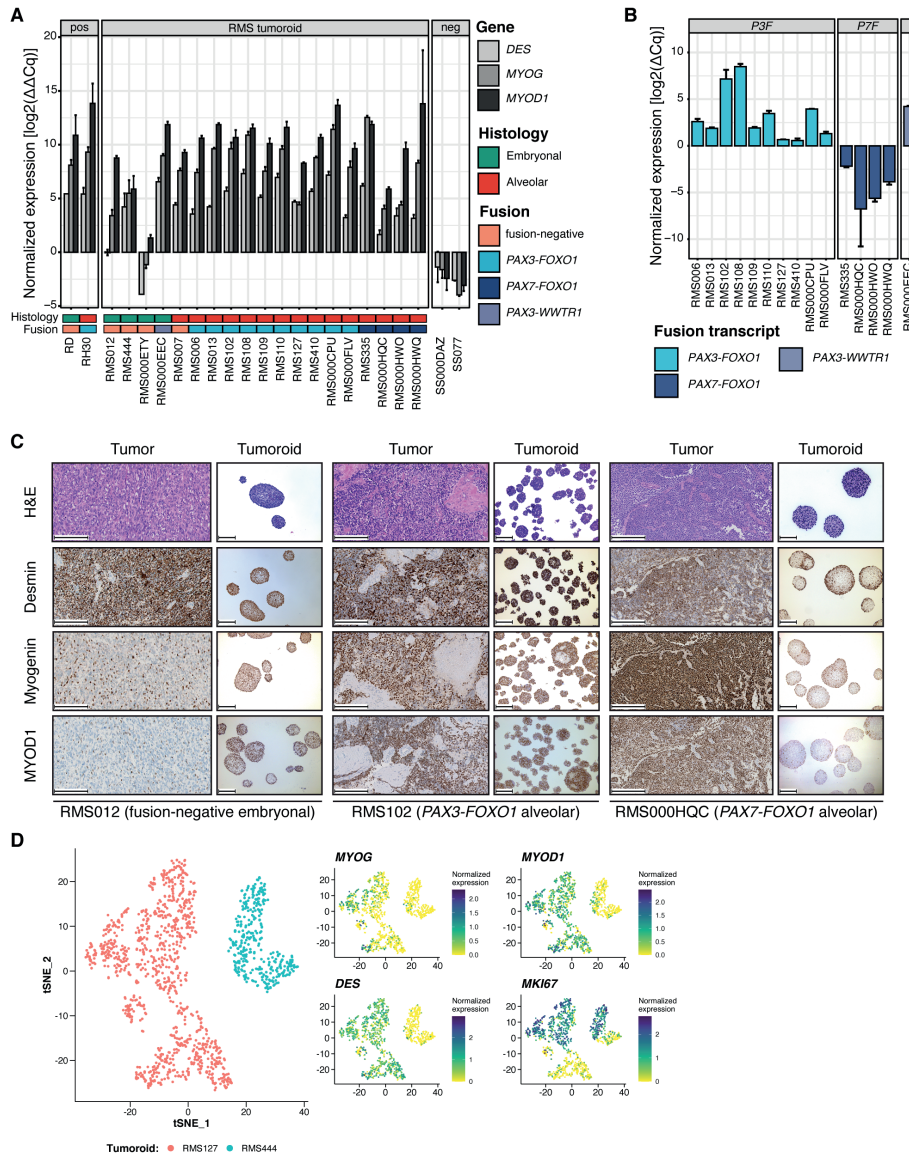
Fig. 2. Early detection of tumor cells during culturing, retained marker protein expression and heterogeneity in gene expression: (**A**) RT-qPCR of early passage RMS tumoroid models shows positivity for at least one gene used in standard-of-care pathology analysis (*DES*, *MYOG*, or *MYOD1*). Conventional RMS cell lines (RD and RH30) were used as positive controls, while two Synovial Sarcoma (SS000DAZ and SS077) tumoroid models were used as negative controls. Gene expression was normalized to the expression of a house-keeping gene and human reference RNA (HREF) via the ΔΔCq method. Each tumoroid line was measured once with four

Fig. 2. Continued

technical replicates with the error bars representing the standard deviation of said technical replicates. (**B**) RT-qPCR of early passage RMS tumoroid models reliably detects the aberrant fusion transcripts. Fusion gene expression was normalized to the expression of a house-keeping gene via the ΔCq method. Each tumoroid line was measured once with four technical replicates with the error bars representing the standard deviation of said technical replicates. (**C**) Morphological (via H&E) and immunohistochemical (IHC) comparison of RMS tumors and derived RMS tumoroid models shows retained marker protein (Desmin, Myogenin and MYOD1) expression and cellular morphology. Scale bars equal 200 μm (RMS012, RMS102) or 100 μm (RMS000HQC). (**D**) t-SNE projection of single-cell transcriptomes from the RMS127 and RMS444 tumoroid models. Plots on the right show the normalized expression values, per single cell, of *MYOG*, *MYOD1*, *DES* and *MKI67*, respectively.

Compared to O-PDX models of RMS, the overall success rate is lower for establishing RMS tumoroid models (41% versus 65%, respectively). While the success rate is lower, RMS tumoroid models can be more rapidly established. Engraftment of O-PDX RMS models takes 1 to 5.5 months before tumor growth is first observed in mice, while RMS tumoroid models can be fully established, i.e., characterized and subjected to drug screening, in as little as 27 days for highly aggressive tumors. Overall, the median time from acquisition of the tumor sample to successful drug screening was 81 days (with 7 models being screened in less than 2 months). This indicates that our approach could potentially be applied in a personalized medicine setting where it is crucial to obtain results as fast as possible to provide information on treatment options.

A subset of the tumoroid models were derived from the same patient, but at different points during treatment and/or from different body sites (marked with one or more asterisks in Fig. 1B). This potentially facilitates studies of tumor evolution or acquired treatment resistance. Furthermore, the collection contains a model of an eRMS with a fusion between *PAX3* and *WWTR1* which has not previously been described in RMS. Such fusions have been reported as rare events in biphenotypic sinonasal sarcomas, which usually harbor *PAX3-MAML3* fusions [30]. Taken together, the protocol efficiently yields tumoroid models from highly aggressive as well as from extremely rare RMS subtypes, resulting in an initial collection covering a broad spectrum of subtypes.

RMS tumoroid models molecularly resemble the tumor they are derived from

Given that the present tumoroid collection is the first to be established from tumors of purely mesenchymal origin, we asked to what extent the models further resemble the tumors they were derived from besides the retained hallmark protein expression levels and patterns described above. To this end, whole-genome sequencing (WGS) and bulk mRNA sequencing (RNA-seq) of the tumor and tumoroid model at the time of drug screening (i.e., successful establishment), were performed.

Copy number profiles were first compared between tumors and tumoroid models showing that profiles are indeed highly concordant (Fig. 3A). The detected copy number alterations included those commonly observed in RMS, with genomic gains in chromosome 8 in FN-RMS and gains in chromosome 1 and 12 in FP-RMS [6,31]. In addition, copy number profiles of individual RMS tumors and derived tumoroid models show a high concordance (Figure EV3A and B). This indicates that the established models resemble the tumors they were derived from on a more global genomic level.

Various mutational processes are active in cells, which cause distinct somatic mutational signatures. These signatures are characterized by specific patterns of single base substitutions (SBS) in the context of their two flanking bases [32]. The presence of certain somatic mutational signatures in a cell can be associated with the underlying mutational processes. These processes are not restricted to *in vivo* systems, but can also occur during culture [33], forming a potential source of genomic destabilization. To test whether the somatic mutational signatures and thus the underlying mutational processes present in the tumors ("T") are concordant with those in the derived tumoroid models ("O"), we first measured the relative contributions of different signatures per sample. The main signatures observed are signatures associated with cellular aging (SBS1 and SBS5), a signature associated with increased oxidative stress (SBS18) [32] and a signature associated with exposure to the chemotherapeutic temozolomide (TMZ) [34] used in the treatment of RMS [35] (Fig. 3B). Signatures associated with cellular aging (SBS1 and SBS5) show a significant correlation with patient age only for SBS1 and only in RMS tumoroid models ($p = 0.02$) but not tumors ($p = 0.17$). Furthermore, FP-RMS tumors and tumoroid models show a significantly higher contribution of SBS1 (but

not SBS5) to their overall somatic mutation frequency compared to FN-RMS tumors and tumoroid models ($p = 0.02$ and $p = 0.006$, respectively). However, patients with FP-RMS were older than patients with FN-RMS (median 14 years versus median 6 years, respectively), which may have influenced this. Importantly, the signatures detected in the tumoroid models are highly concordant with those detected in the original tumors (Fig. 3B). In line with this, no global differences in SBS profiles between RMS tumors and derived tumoroid models are detected when analyzed collectively (Figure EV3C). Lastly, we calculated the similarities of the individual SBS profiles of all tested tumor and tumoroid model samples. Tumoroid models cluster with the tumors they are derived from, indicating that the mutational landscape is retained in the models (Figure EV3D). Only the tumor and tumoroid model of RMS127 do not cluster closely, likely due to derivation from a bone marrow aspirate with low tumor cell infiltration (5-10% as estimated by pathology). Overall, there is a high concordance between the somatic mutational signatures of RMS tumors and the derived tumoroid models, again illustrating that the established models resemble the patient tumors.

While FP-RMS are driven by the prototypical fusion genes, FN-RMS are characterized by SNVs in known oncogenes such as *TP53* or *RAS* family members [6]. Currently available preclinical models of RMS do not cover the full spectrum of these SNVs, thus limiting the applicability to test novel targeted drugs in RMS. To investigate whether the established RMS tumoroid models harbor any of these SNVs and whether these were already present in the tumor, all SNVs predicted to be pathogenic for protein function and with a variant allele fraction (VAF) of above 0.3 in either tumor and/or tumoroid were evaluated. As already indicated by the mutational signature analyses, RMS tumoroid models retain SNVs present in the tumor to a high degree (Fig. 3C). Similarly, samples from the same patient but from different sites or acquired from different relapses also show a high overlap in SNVs (Fig. 3C). In agreement with a recent study investigating mutational frequency in different tumor types [36], the FN-RMS tumoroid models show a higher somatic mutation frequency than the FP-RMS tumoroid models ($p = 0.02$) (Figure EV3E) indicating that the models are representative for this characteristic, as well.

Two of the FN-eRMS tumoroid models harbor previously described oncogenic mutations for FN-eRMS, i.e., *CTNNB1* (p.T41A) in RMS012 and *FGFR4* (p.V550L) in RMS444 [6]. To our knowledge, RMS012 is the first preclinical RMS model harboring this specific mutation. Moreover, one *PAX3-FOXO1* FP-aRMS (RMS410) displays an oncogenic mutation in *KRAS* (p.G12A), which is uncommon in FP-RMS [6]. Lastly, two FN-RMS tumoroid models (RMS007 and RMS012) display non-annotated frameshift mutations in the *BCOR* gene with a high VAF of above 0.9. Mutations in *BCOR* have been reported in RMS with a higher prevalence in FN-RMS compared to FP-RMS [6]. The mutation analysis shows that RMS tumoroid models not only retain specific SNVs already present in the tumor but that these models also contain mutations for which no preclinical model was previously available.

Tumors are composed of different tumor cell clones that can undergo processes such as clonal expansion, genetic diversification as well as clonal selection [37]. To assess to what degree established RMS tumoroid models reflect the clonal composition of the tumor they were derived from, we performed two analyses on the matching WGS data.

First, we compared the VAFs of SNVs in coding regions which showed no copy-number alterations or loss of heterozygosity (LOH) (Figure EV4A). For the majority of samples, SNVs with a VAF of around 0.5 (indicating a major clone in the population given the filtering criteria for SNVs described above) can be detected in tumor and tumoroid, indicating that major clones are retained. Furthermore, the presence of SNVs with VAFs of below 0.5 indicate subclonal populations. Again, such SNVs with matching VAFs in tumor and tumoroid samples can be detected, indicating that subclonal populations are also largely retained in the established RMS tumoroid models. In addition, a subset of SNVs present in the tumoroid with a high VAF is not present in the tumor with the chosen cut-offs, indicating that our method may enrich for such clones. Importantly, none of these SNVs are found in reported oncogenic driver genes, indicating that these are likely passenger mutations.

In the second analysis performed on the matching WGS data, fractions of alternate alleles (B-alleles) were compared between matching tumors and tumoroid models (Figure EV4B). Importantly, patterns present in the tumor are retained in the derived tumoroid, indicating that the relative

contributions of clones with varying B-allele fractions is retained in the established models. Minor shifts between the peaks are likely the result of the tumor sample being impure, i.e., containing normal cells, whereas the tumoroid models consist purely of tumor cells.

Taken together, these analyses indicate that established RMS tumoroid models maintain the genetic characteristics including the clonal composition of the RMS tumor they were derived from to a large extent.

mRNA expression profiles of FN- and FP-RMS are fundamentally different, mainly due to the transcriptome-wide impact of the fusion transcript in FP-RMS [38]. Additionally, the transcriptional program of *in vitro* cultured organoids is influenced by the culture conditions and can deviate from the transcriptional program of the parent tissue [39]. Given that FN-RMS and FP-RMS tumoroid models are cultured in the same medium, we asked whether the transcriptional differences observed between the original tumors are retained in the models. Analysis of RNA-seq shows a high correlation between the expression profiles of RMS tumoroid models with the same fusion status (i.e., FP-RMS versus FN-RMS, Fig. 3D), as has previously been shown for primary RMS tumor samples [38]. Furthermore, correlation between the expression profiles of RMS tumor and tumoroid models of the same fusion-type is high, while correlation with control kidney tumors is low, showing that the fundamental differences in the expression profiles of FN- and FP-RMS are retained in culture (Fig. 3D). In summary, the early tumor cell detection by RT-qPCR, the morphological and marker protein analyses, WGS for copy number profiles, for somatic mutational signatures, for individual SNVs, and for assessing the clonal composition, as well as the comparative transcriptomic analyses, indicate that the RMS tumoroid models resemble the original RMS tumor they are derived from.

Genetic and transcriptional stability of tumoroid models over time

We next asked whether the models remain genetically and transcriptionally stable after culture over extended periods. To investigate stability, a subset of RMS tumoroid models were kept in culture over three to six months until they reached passage 40 ("OL" for late passage, as compared to "O", the standard passage analyzed here and sufficient for drug screening) and characterized again by WGS and RNA-seq. Furthermore, two independently derived

tumoroid models (i.e., established from the same tumor piece of which a part was cryo-preserved after the first tumoroid establishment) were included in this comparison ("O2") to assess the robustness of the establishment protocol.
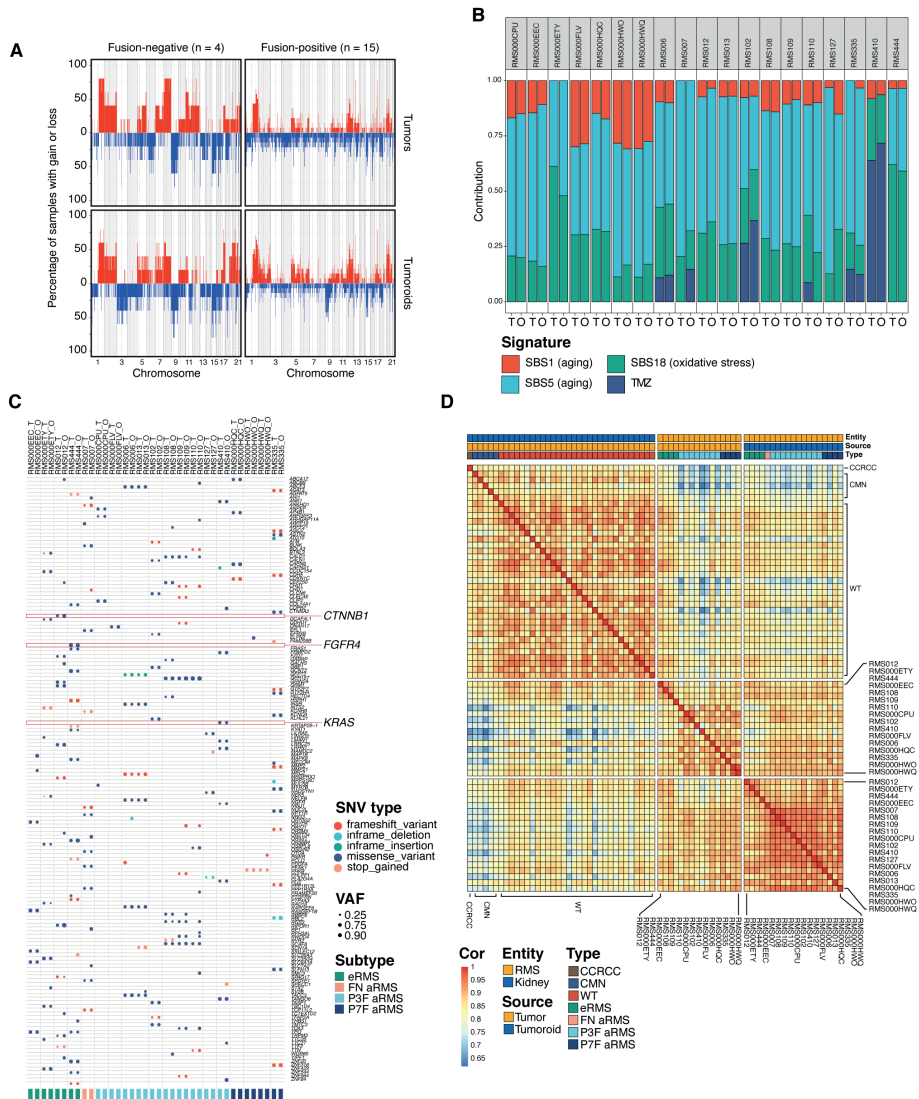

Fig. 3. RMS tumoroid models molecularly resemble the tumor they are derived from: (**A**) Copy number frequency plots of RMS tumors (upper row) and derived RMS tumoroid models (lower row) divided by fusion-status (columns). Chromosomes are annotated on the x-axis from left to right while the y-axis shows the percentage

Fig. 3. Continued

of samples in this group carrying a gain (red) or loss (blue) in this genomic region. (**B**) Contribution of somatic mutational signatures per tumor and tumoroid model. SBS = single base substitution, TMZ = temozolomide, T = tumor, O = tumoroid. (**C**) Table depicting pathogenic single-nucleotide variants (SNVs) in RMS tumors (T) and tumoroid models (O). Circle color indicates SNV type while circle size indicates variant allele fraction (VAF). Vertical dotted lines separate samples derived from individual patients. Highlighted are genes previously reported for this RMS subtype. (**D**) Correlogram of bulk mRNA sequencing expression profiles of pediatric kidney tumors (controls) as well as RMS tumoroid models and RMS tumors. CCRCC = Clear Cell Renal Cell Carcinoma, CMN = Congenital Mesoblastic Nephroma, WT = Wilms Tumor, Cor = correlation.

RMS tumoroid models show long-term propagation potential with five out of seven lines tested reaching passage 40 and two lines dropping out at passage 17 and 20, respectively. As drug screening is usually performed between passage 6 to 12, this shows that models can be readily used after such an initial screening. Comparison of individual copy number profiles of standard and late passage (Figure EV5A), as well as independently derived paired tumoroid models (Figure EV5B) shows no major copy number differences between the respective models. Furthermore, analysis of somatic mutational signatures shows that the contributions of identified somatic mutational signatures (Fig. 4A) as well as the contributions of individual SBSs between models (Figure EV5C) are highly similar. Lastly, analysis based on SBS profiles shows clustering of models derived from individual patients (Figure EV5D). The exception to this is RMS335 "OL" which may be due to a mutation in the DNA damage response gene *ATR* in both the tumor and the tumoroid sample, potentially resulting in the gain of new mutations during culturing. The similarity between SBS profiles of RMS335 "O" and "OL" was nevertheless high. Taken together, these analyses show that RMS tumoroid models generally remain stable, even over extended periods of culturing and that the establishment protocol is robust, yielding highly similar models when independently derived from a single tumor sample.

As before (see Fig. 3C), individual pathogenic SNVs were also evaluated. Importantly, the majority of SNVs are retained after long-term culturing, with the models acquiring only a few additional SNVs (Fig. 4B). In addition, the models independently derived from the same tumor show a high overlap of pathogenic

SNVs (Fig. 4B). Notably, the afore-mentioned oncogenic mutations in *CTNNB1* and *FGFR4* are detected in all related samples (Fig. 4B). This further indicates that the models do not lose key mutations and that the establishment protocol results in the outgrowth of representative tumor cells harboring these mutations. RNA-seq expression profiles from the standard passage, late passage, as well as the independently derived tumoroid models were compared to test whether the core transcriptional program of RMS is retained. Principal component analysis shows that global expression profiles of tumoroid models derived from the same patient cluster together (Fig. 4C). This suggests that our models are not only genetically, but also transcriptionally stable over time.

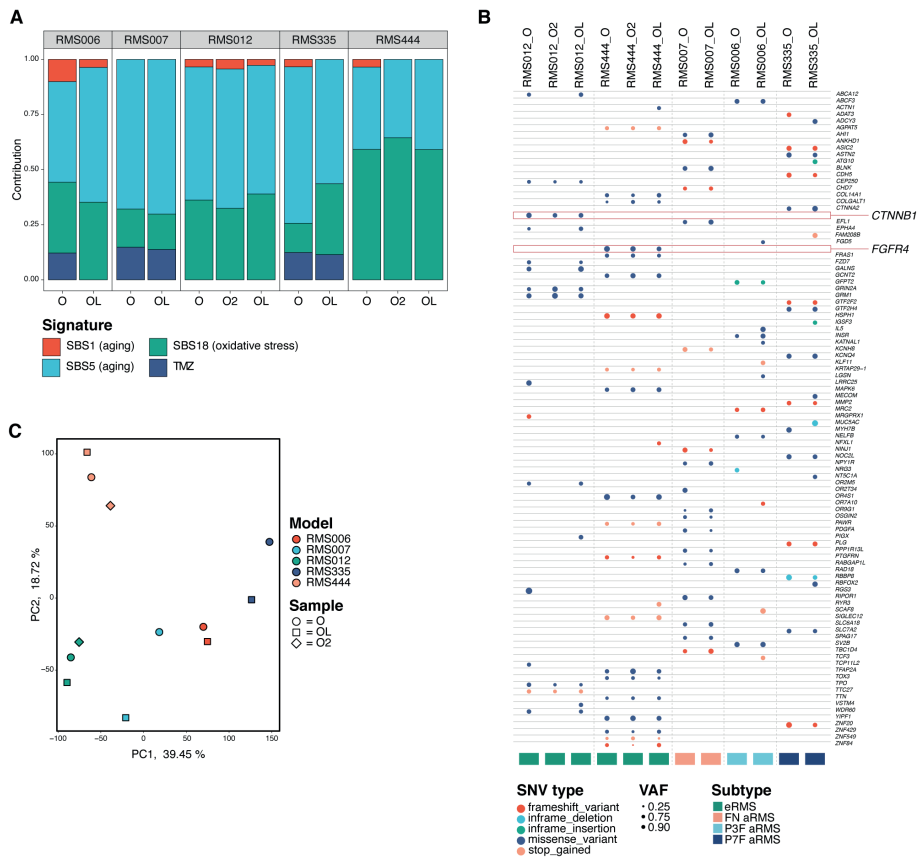
Fig. 4. Genetic and transcriptional stability of tumoroid models over time: (A) Contribution of somatic mutational signatures per tumor and tumoroid model. SBS = single base substitution, TMZ = temozolomide, T = tumor, O = standard passage

Fig. 4. Continued

tumoroid model, OL = late passage tumoroid model, O2 = independently derived tumoroid model. (**B**) Table depicting pathogenic single-nucleotide variants (SNVs) in different RMS tumoroid models derived from the same tumor sample. Circle color indicates SNV type while circle size indicates variant allele fraction (VAF). Highlighted are genes previously reported for this RMS subtype. (**C**) Principal component analysis on bulk mRNA sequencing derived global gene expression. Color indicates the RMS tumoroid model while the symbol indicates the sample. O = standard passage tumoroid model, OL = late passage tumoroid model, O2 = independently derived tumoroid model.

RMS tumoroid drug screening reflects established drug sensitivities

Having established that the RMS tumoroid models resemble the tumors they are derived from with stability during prolonged culturing, their suitability for research was further investigated in two specific ways, i.e., via drug screening and CRISPR/Cas9 genome editing. Development of novel RMS treatments has been hampered by a lack of preclinical models that can efficiently be subjected to drug screening. To be of use for such screening approaches, it is imperative that new models reflect drug sensitivities already known for these tumors. This was investigated with a custom pediatric cancer library of 165 compounds, comprising standard of care chemotherapeutics as well as early-phase clinical trial targeted compounds. To mimic the three-dimensional configuration of tumors, cell plating was optimized so that tumoroid cells form homogeneous 3D spheres in 384-well plates. The protocol also included prior growth curve determination of the number of cells that must be plated for each individual tumoroid model to prevent overgrowth during screening (Materials & Methods).

Vincristine and actinomycin D are routinely used in RMS treatment and indeed show broad efficacy in all models tested (Fig. 5A, bottom highlighted box). Furthermore, the proteasome inhibitor bortezomib shows a similarly high efficacy in all tested models. This is in line with previous studies showing that both major histological RMS subtypes are susceptible to bortezomib treatment *in vitro* [40] and *in vivo* [24], suggesting that RMS tumoroid models indeed reflect drug sensitivities known for RMS tumors.

Clustering of RMS tumoroid models based on drug efficacy shows two main groups, comprising 12 and 4 models, respectively, with one unclustered model (RMS000FLV). This model nevertheless shows high sensitivity to the afore-mentioned drugs (bottom of Fig. 5A). The outlier behavior is not caused by differences in growth during the experiment (see Table EV1) and may be explained by the fact that this is the only treatment-naïve FP-aRMS model in the collection (Fig. 1B). The group of 4 models, that contains all successfully screened FN-RMS tumoroid models, is more sensitive to all tested inhibitors of MEK/ERK (MAPK signaling pathway) as well as the two inhibitors of γ-secretase (NOTCH signaling pathway) in the drug panel, when compared to the other group containing only FP-RMS tumoroid models (Fig. 5A, top highlighted box, and Fig. 5B and C). Importantly, sensitivity of FN-RMS against inhibitors of MAPK and NOTCH signaling has previously been reported [41,42]. This group also contains the FP-aRMS tumoroid model RMS000HQC which shows a very low expression of its fusion transcript (Fig. 2B), which potentially resulted in it displaying sensitivities more commonly observed in FN-RMS. Taken together, our results indicate that drug sensitivities observed in RMS tumoroid models reflect those known in primary RMS tumors. This shows the potential these models hold for testing novel drugs. As drug screening could be performed as early as 27 days after sample acquisition, with a median time to drug screening of 81 days, this highlights their relevance for personalized approaches.

RMS tumoroid models can be molecularly edited using CRISPR/Cas9

The applicability of preclinical models would be further enhanced by the possibility of genetic modification. To test this, we used CRISPR/Cas9 [43] to knock out the well-known tumor suppressor gene *TP53*. This choice is based on the recent report that loss of functional P53 protein confers a worse prognosis in RMS [44]. RMS012 FN-eRMS tumoroid cells, with wildtype *TP53* as determined by WGS, were transfected with a plasmid harboring a *TP53* targeting sgRNA as well as Cas9. Successfully edited cells were selected with nutlin-3 [45] (Fig. 6A), resulting in cells with complete loss of P53 protein as confirmed by Western Blot (Fig. 6B). Sanger sequencing shows a spectrum of Indels consistent with a polyclonal population of P53 deficient cells (Figure EV6A).
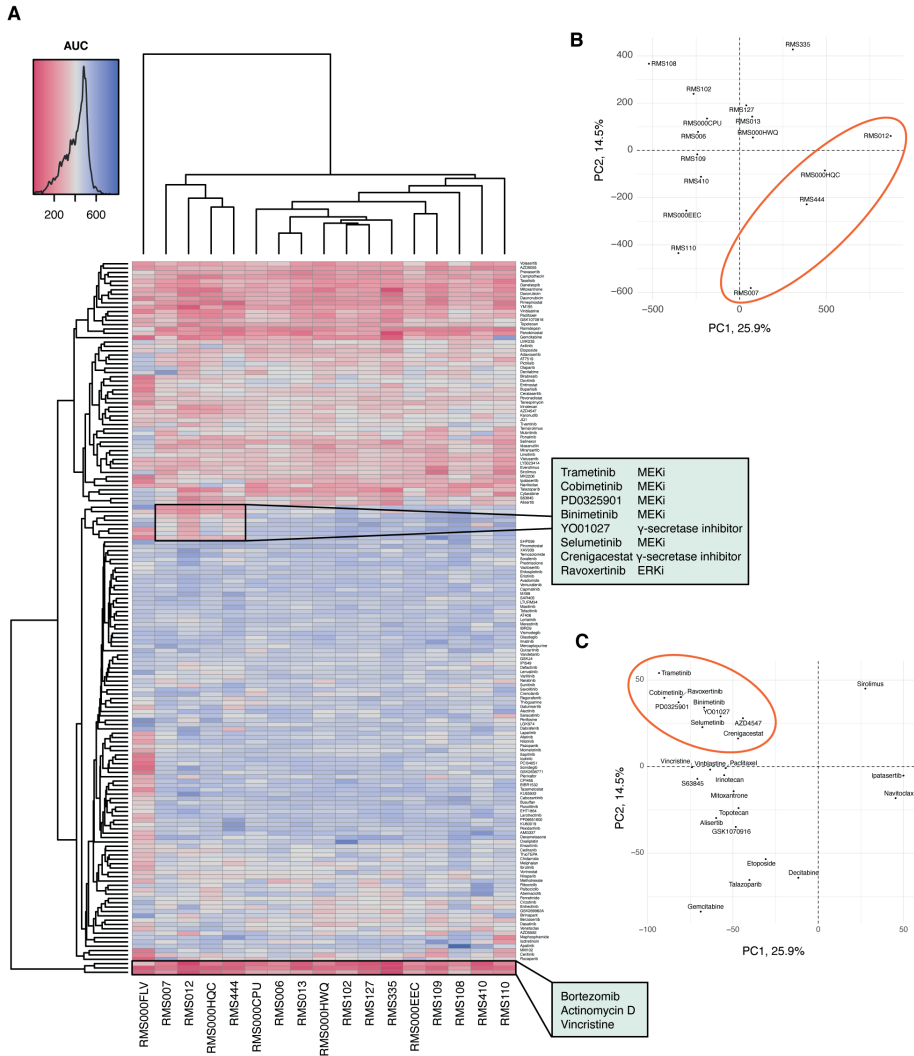
Fig. 5. RMS tumoroid drug screening reflects established drug sensitivities:
(**A**) Clustered heatmap of viability measurements per RMS tumoroid model (x axis)
and drug (y axis), showing the Area Under the Curve (AUC) after treatment of the
cells for 120 h with a dose-range of 0.1 nM to 10 μM. Low AUC (red) indicates high
drug efficacy while high AUC (blue) indicates low drug efficacy. Annotated clusters of
(1) MEK/ERK and γ-secretase inhibitors showing specific efficacy in RMS tumoroid
models without (RMS007, RMS012, RMS444) or low (RMS000HQC) fusion transcript
expression, and (2) drugs that show broad efficacy across RMS tumoroid models.
(**B**) Principal component analysis of drug screening AUC values of the RMS tumoroid
models (RMS000FLV omitted due to outlier behavior as discussed in the main text).
The ellipse indicates the cluster that shows specific sensitivity against MEK/ERK and

Fig. 5. Continued

γ-secretase inhibitors. (**C**) Principal component analysis of the top 25 contributing drugs that influence variance. The ellipse indicates the MEK/ERK and γ-secretase inhibitors as well as AZD4547 (RMS000FLV omitted as described above).

P53 deficient eRMS tumoroid cells are more sensitive to the checkpoint kinase inhibitor prexasertib

In light of the recently reported prognostic significance of P53 loss in RMS [44], we investigated what implications loss of P53 might have. P53 governs various cellular functions, including response to DNA damage through control of the G1/S checkpoint during cell cycle progression by halting the proliferative machinery to give cells time to repair DNA damage [46]. The rate of DNA double-strand breaks (DSBs) was therefore first examined in the P53 deficient RMS tumoroid cells by measuring phosphorylation of histone H2AX serine 139, a proxy for DNA DSBs [47]. No difference in the amount of DNA DSBs was observed between *TP53* wildtype and knockout cells however (Figure EV6B). To avoid catastrophic failure of the proliferative machinery and avoid cell death, P53 deficient cells are dependent on the G2/M checkpoint to repair DNA DSBs [48]. Inhibitors of the checkpoint kinase 1 (Chk1), which controls the G2/M checkpoint, have therefore been suggested as a treatment for P53 deficient tumors, such as in certain ovarian and breast cancer subtypes [49,50]. This hypothesis was tested, resulting in the observation that *TP53* knockout RMS tumoroid cells are significantly ($p = 0.008$) more sensitive to the Chk1 inhibitor prexasertib, compared to their wildtype counterpart (Fig. 6C). The absolute difference between IC_{50} values is not extreme (18.5 nM for *TP53* wildtype versus 12.9 nM for *TP53* knockout cells), likely reflecting the fact that RMS012 *TP53* wildtype cells are already sensitive to prexasertib. These results indicate that exploiting replicative stress in P53 deficient RMS is indeed an interesting therapeutic avenue to pursue. Moreover, the results demonstrate that it is possible to perform gene editing in these novel RMS tumoroid models, thereby further increasing their utility.
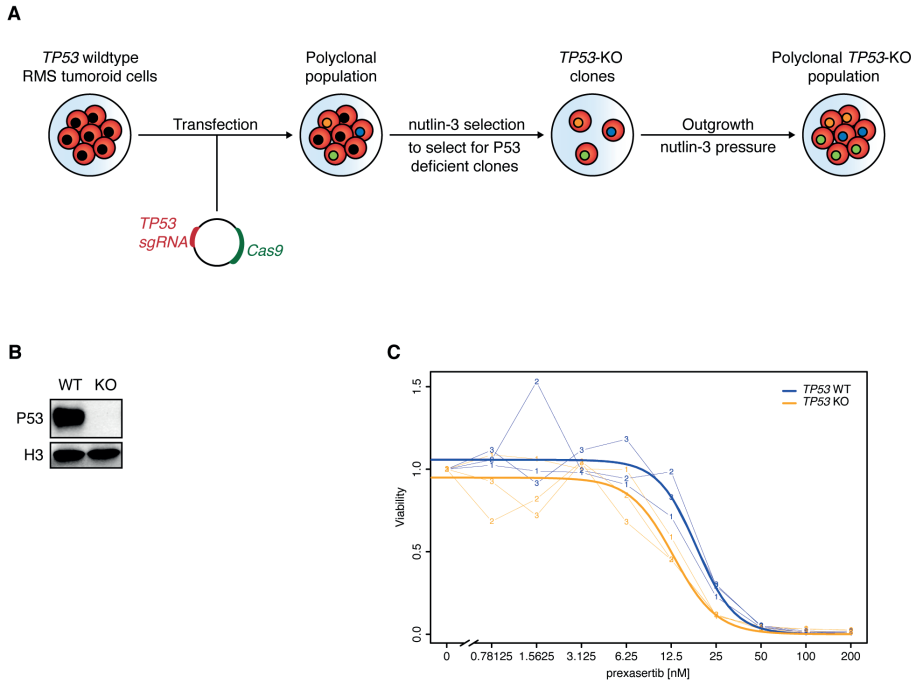
A

B

C

Fig. 6. RMS tumoroid models can be molecularly edited using CRISPR/Cas9 with P53 deficient eRMS being more sensitive to the checkpoint kinase inhibitor prexasertib: (**A**) Transfection and selection strategy to achieve *TP53* knockout in a *TP53* wildtype tumoroid model. (**B**) Western Blot analysis of *TP53* wildtype (WT) and knockout (KO) RMS tumoroid line RMS012. Histone 3 (H3) served as loading control. (**C**) Dose-response curve of *TP53* WT and KO cells treated with the Chk-1 inhibitor prexasertib. Thin lines with numbers indicate individual biological replicates (n = 3) while thick lines indicate fitted lines over all replicates. The statistical significance of the differences in fitted IC$_{50}$ values between WT and KO were obtained using a two-sided t-test (*p* = 0.008).

Discussion

A tumoroid collection of purely mesenchymal origin

To date, organoid technology has primarily been employed to generate models of malignant tumors of epithelial origin (i.e., carcinomas) [15]. Feasibility to use this technology on non-epithelial cancer has only recently been shown [16–20]. Here we extend the tumor organoid approach, demonstrating applicability to tumors of entirely mesenchymal origin (i.e., sarcomas), resulting in only the second thoroughly characterized tumoroid collection specific for pediatric cancer.

Two factors likely contributed to the delayed adaptation of organoid technology to sarcomas. First, the technology was developed for healthy epithelial tissue, followed later by translation to the corresponding cancer entity, as in the case of colorectal carcinoma [12,51,52]. The cell of origin of RMS is still not fully characterized [53]. Therefore, extensive culture optimization of healthy tissue first, with translation to cancerous tissue later, has not been feasible for RMS. Consequently, optimization had to be conducted on tumor samples, which are not readily available. Secondly, and related to the issue of tissue availability, sarcomas are far less common than carcinomas, accounting for less than 1% of all solid adult malignancies [54]. In pediatric cancer however, sarcomas are much more common, encompassing 21% of all solid tumors in children [54]. This further highlights the importance of the currently described approach and collection.

Representation of a broad spectrum of RMS subtypes

The tumoroid models include representatives of both major histological subtypes, all major fusion types, different age groups, both sexes, treatment-naïve as well as pre-treated, primary as well as metastatic tumors (Fig. 1B and Dataset EV1). Rarer subtypes such as sclerosing/spindle-cell RMS [55] will be exciting to include, as also indicated by a recent case report [56]. Compared to patient incidence rates [57], the collection has an underrepresentation of head and neck RMS. Although RMS tumor samples from this region were acquired, models from such samples failed, regardless of subtype, clinical stage, sample quantity or quality. Interestingly, this indicates that RMS arising in the head and neck may depend on specific factors that have not yet been identified. Studies in genetically engineered mice indicate that aberrant Hedgehog signaling can give rise to FN-RMS from non-myogenic endothelial progenitors in the head and neck [58]. Here, activation of Hedgehog signaling by Smoothened agonists did not facilitate establishment of head and neck RMS tumoroid models, indicating that additional factors may be necessary. Regardless of such future developments, the protocol described here yields models that can be rapidly established from a broad range of quite different RMS subtypes.

New models for RMS research

Currently available preclinical models of RMS include conventional cell lines, various genetically engineered animal models (GEMs), as well as patient-

derived xenograft models (PDX or O-PDX when transplanted orthotopically) [59,60]. Each of these systems possesses specific benefits and drawbacks, resulting in suitabilities for different research questions or stages in drug development [61]. While conventional cell lines are easy to use, with low costs, large-scale screening potential and ease of genetic modification, due to prolonged culturing they often do not recapitulate many basic features of the genetic and molecular background of the tumor they were derived from, thus possessing only limited predictive value [62]. GEMs, on the other hand, are well-suited for cell of origin studies and can provide valuable insights into cancer onset mechanisms. GEMs are usually not suitable for high-throughput screening, mostly due to the low tumor penetrance or the intricacies of animal studies [63]. In contrast to GEMs, in O-PDX models, tumor samples are transplanted onto immune-deficient animals (usually mice, although a study on zebrafish has recently been reported [64]). This allows for engraftment, growth, and later propagation of the tumor tissue from animal to animal. Tumors propagated in this manner are thought to be genetically stable over time and to reflect the patient tumor they were derived from, giving them predictive value concerning preclinical drug testing [65]. Disadvantages include the necessary use of animals as hosts and the tumor-entity specific engraftment time which can take up to several months [66]. Furthermore, there is evidence that not all PDX models are genetically stable [33].

The RMS tumoroid models combine several of the above-mentioned benefits. They can be rapidly established and expanded like conventional cell lines, enabling drug screening. Importantly, established drug sensitivities of RMS in general and of RMS subtypes specifically (i.e., inhibitors of MAPK and NOTCH signaling in FN-RMS), are retained in tumoroid models, showing their applicability as models in translational RMS research. In addition, tumoroid models in general are suitable for transplantation into mice [67–69], which enables pharmacokinetic studies, further broadening their use in translational research. As with cell lines, molecular editing to mimic certain disease backgrounds is possible using CRISPR/Cas9. Unlike cell lines however, tumoroid models depend on defined media including recombinant growth factors as well as an ECM substitute, resulting in higher costs. RMS tumoroid models molecularly resemble the patient tumor they are derived from, with tumor sample-specific SNV patterns being retained in matching tumoroid models, thereby also recapitulating differences

between tumor samples derived from the same patient (e.g., RMS108, RMS109, and RMS110 showing overlap but also differences in SNVs in the tumor samples which are retained in the corresponding tumoroid models). A subset of SNVs present in the tumor are not detected in the established RMS tumoroid which can be due to (i) this clone not being present in the tissue piece that was used for the establishment of the tumoroid, and/or (ii) the respective clone was present in the piece but got lost over the course of culturing and/or (iii) the sequencing depth for the tumoroid model was not sufficient to pick up this mutation (30X coverage in the tumoroid model versus 90X coverage in the tumor, respectively). RMS tumoroid models share this resemblance with the patient tumor they were derived from with O-PDX mouse models, while possessing the above-mentioned advantages of rapid establishment and expansion. Compared to O-PDX mouse models, establishment success is lower in RMS tumoroid models, indicating that niche factors in the host mice are important for facilitating establishment. This may be especially important in particular subtypes such as RMS from the head and neck region. On the other hand, RMS tumoroid models are less intricate in their propagation. Lastly, while GEMs are considered essential for cell of origin studies, recent advances have shown that by genetic editing, such studies can now also be performed in tumoroid models [70]. Lastly, the scRNA-seq based analysis of two RMS tumoroid models indicates that tumor cell heterogeneity, an important hallmark of plasticity, are maintained *in vitro*. To fully assess to what extent this heterogeneity reflects the heterogeneity in the tumor the models were derived from, an extensive analysis of matching primary RMS tumor samples would be necessary, which will be exciting to explore in future studies.

In conclusion, we established a well-characterized, well-annotated collection of RMS tumoroid models, being the first such collection of tumoroid models derived from purely mesenchymal malignant tumors (i.e., sarcomas) and only the second comprehensive tumoroid model collection derived from pediatric cancer [21]. This collection contains all major subtypes of RMS and the models can be used for drug screening as well as molecular editing. An interactive, browser-based companion Shiny app (https://rmsdata.rms-biobank.eu/) that makes all the described data easily accessible, accompanies this paper. The RMS tumoroid models will be a useful complementary system to study the biology of RMS and to improve treatment.

Materials & Methods

Tumor sample acquisition

Tumor samples of RMS were obtained via an established tumor sample acquisition route from patients treated at the Emma Children's Hospital Amsterdam (Amsterdam UMC) (RMS006, RMS007, RMS013) or as part of the biobank initiative of the Princess Máxima Center for Pediatric Oncology, Utrecht, Netherlands (PMC) (remaining tumor samples). Ethics approval was granted for the biobanking initiative, and the PMC biobank committee granted approval for the present project. All patients and/or their legal representatives signed informed consent to have tumor samples taken for biobank usage. Experiments conformed to the principles set out in the WMA Declaration of Helsinki and the Department of Health and Human Services Belmont Report.

A subset of patients was furthermore enrolled in a local personalized medicine trial (i.e., iTHER study) through which a subset of DNA and RNA specimens from RMS tumors were obtained.

Tumor sample preparation for establishment of RMS tumoroid models

Solid tumor samples (i.e., needle biopsies or resection specimens) were transferred to collection medium (see below) to retain viability of cells. After pathological examination, suitable samples (i.e., containing tumor cells) were processed in a sterile work environment as follows: the sample was transferred to a sterile dish and covered with a droplet of BM1* culture medium (see below) before being minced to fine pieces using scalpels. If the tumor sample was of sufficient size, a portion of this minced mixture was stored viably (see below). The remainder of the mixture was put on a pre-wet 70 µM strainer, scrapped with a cell scraper to obtain a single-cell suspension and collected in a tube (A, single-cell fraction, cultured in 2D). Tissue fragments left on the strainer were collected in another tube (B, strainer fraction, cultured in 3D).

A: The single-cell fraction was now spun down (300 g, 5 min, 4 °C) and the supernatant was removed from the resulting pellet. If the pellet was of grey color (i.e., not containing a high percentage of red blood cells, RBCs), the pellet was resuspended in 1 ml of BM1* medium. If the pellet contained a high percentage of RBCs (i.e., by displaying a red stain), the cell pellet was

resuspended in red blood cell lysis buffer (Roche) and incubated at room temperature for 5 min. Thereafter, the reaction was stopped by adding collection medium and the mixture was spun down again (as above). Again, supernatant was removed and now the pellet was resuspended in 1 ml of BM1* medium (without Basement Membrane Extract, BME, see below). In each case, cells were now counted using a TC20 Automated Cell Counter (BioRad) to get a rough estimate on viability and cell numbers. Cells were plated with a sufficient density (at least 10.000 viable cells per 1 cm^2 of surface area), supplemented with 0.3 to 0.5% cold BME (see below).

B: The strainer fraction was dissolved in pure cold BME (roughly one-third volume strainer fraction and two-third volume BME) and mixed thoroughly. Droplets of 5 to 10 µl of this mixture were formed on 24- or 48-well pre-warmed cell culture plates and incubated for 5 min at room temperature to allow the BME to solidify. Thereafter, the cell culture plates were incubated upside-down for another 25 min at 37 °C to allow the material to "sink" to the top of the droplet. Upon completed solidification, BM1* medium (at room temperature (RT) and without BME) was added to the wells so that droplets were very fully submerged in medium.

In the case of bone marrow aspirates as tumor samples (RMS410 and RMS127), sample tubes were spun down (300 g, 5 min, 4 °C, slow break) to separate RBCs and nucleated cells (white clot at the bottom of the tube). In the case of RMS410, the normal hematopoietic system was almost entirely superseded by infiltrating tumor cells so that the clot consisted mainly of tumor cells which could directly be plated (in BM1* with BME) which resulted in rapid outgrowth of the model. In the case of RMS127, the percentage of infiltrating tumor cells was estimated by pathology to be low at circa 5 to 10%. Therefore, initial cultures (plated in BM1* and BME) from the white clot also contained normal nucleated bone marrow cells which, however, were eventually outcompeted by the rapidly growing tumor cells which overtook the culture.

Tumoroid model culturing and propagation

Growing RMS tumoroid models were inspected regularly and showed adequate growth behavior under conventional cell culture conditions (i.e.,

37 °C, 5% CO_2). All models were regularly tested negative for mycoplasma contamination. Estimated division times ranged from 24 to 72 hours for most models. Models were passaged once or twice per week at a confluency of 70 to 80%. For passaging, old culture medium was aspirated and cells were briefly washed with sterile DPBS (Gibco, cat no. 14190144). Cell detachment was performed using TrypLE Express Enzyme (1X, phenol red, Gibco, cat no. 12605010). Depending on the model and the BME percentage, detachment took between 3 and 10 minutes (higher BME concentrations resulting in longer detachment time). Cells were collected by flushing the well or flask with collection medium and the resulting mixture was spun down (300 g, 5 min, 4 °C). Thereafter, the supernatant was removed, and the pellet was resuspended in 1 ml of BM1* and cells were counted using a TC20 Automated Cell Counter (BioRad). Single-cell suspensions were mostly re-seeded at the same density as their parental/previous generation/passage.

Cell culture media

Base medium (BM)

To prepare a 500 ml bottle of BM, Glutamax (5 ml, Gibco, cat no. 35050061), Penicillin/Streptomycin (10,000 U/ml, 5 ml, Gibco, cat no. 15140122), and B27 (without vitamin A, 10 ml, Gibco, cat no. 12587010) were added to a full bottle of advanced DMEM/F12 (500 ml, Gibco, cat no. 12634010). BM was stored at 4 °C and was used within two months.

Complete culture medium (BM1)*

To prepare the complete culture medium BM1*, 47.5 ml of the above-mentioned base medium (BM) was taken and pipetted into 50 ml tube. Thereafter, the components below were added (no specific order). BM1* was stored at 4 °C and was used within 7 to 10 days (thereafter, the stability of the growth factors may be compromised).

Collection medium

To prepare a 500 ml bottle of collection medium, Glutamax (5 ml, Gibco, cat no. 35050061), Penicillin/Streptomycin (10,000 U/ml, 5 ml, Gibco, cat no. 15140122), and HEPES (1 M, 5 ml, Gibco, cat no. 15630049) were added

to a full bottle of advanced DMEM/F12 (500 ml, Gibco, cat no. 12634010). Collection medium was stored at 4 °C and was used within two months.

Components:

N2	500 µl	Gibco, cat no. 17502048
N-acetylcysteine (500 mM)	125 µl	Sigma, cat no. A9165
MEM non-essential amino acids	500 µl	Gibco, cat no. 11140035
Sodium pyruvate (100 mM)	500 µl	Gibco, cat no. 11360070
Heparin (5,000 U/ml)	5 µl	Sigma, cat no. H3149-10KU
hEGF (2 µg/ml)	500 µl	Peprotech, cat no. AF-100-15
hFGF-basic (40 µg/ml)	50 µl	Peprotech, cat no. 100-18B
hIGF1 (100 µg/ml)	10 µl	Peprotech, cat no. 100-11
RKi (Y-27632, 100 mM)	5 µl	AbMole Bioscience, cat no. M1817
A83-01 (5 mM)	50 µl	Tocris Bioscience, cat no. 2939

Basement Membrane Extract type 2 (BME)

To facilitate attachment of cells, culture medium was supplemented with 0.1 to 0.5% BME (Cultrex Reduced Growth Factor Basement Membrane Extract, type 2, Pathclear, R&D Systems, 3533-005-02). We observed batch-to-batch variations of this product, resulting occasionally in suboptimal attachment of cells when the BME concentration was too low. On average, 0.2 to 0.3% BME supplementation was sufficient for stably established RMS tumoroid models. However, upon encountering suboptimal cell attachment, BME concentrations were raised to 0.5% in established cultures. During the initial establishment process, higher concentrations of BME (0.3% to 0.5%) showed increased attachment rates of cells.

Freezing and storing procedure

RMS tumor samples as well as established RMS tumoroid cultures were viably frozen as follows: a sufficient number of viable cells (at least 0.5x10E6, mostly 1x10E6) were diluted in 0.5 ml BM1* medium in a cryo tube. Then, an equal volume of freeze-mixture consisting of 80% fetal calf serum (FCS) and 20% DMSO was added dropwise, resulting in final concentrations of

5

50% BM1* medium, 40% FCS, and 10% DMSO. Samples were frozen slowly using a freezing container in a minus 80 °C freezer. For long term storage, frozen vials were transferred to liquid nitrogen.

Thawing procedure

Cryo-preserved RMS tumoroid cell suspensions were quickly defrosted in a water bath at 37 °C and then immediately dissolved in washing medium (to at least 5 ml of total volume to dilute the DMSO). Samples were then spun down (300 g, 5 min, 4 °C), supernatant was removed, and the cell pellet was resuspended in 1 ml of BM1* medium. Thereafter, cells were counted using a TC20 Automated Cell Counter (BioRad). Cell viability was on average 20 to 50% lower compared to viability at the time of freezing. Cells were then plated at a proper density in BME-supplemented BM1* medium and needed one to two weeks to recover before being stable enough for further experiments. Restarting tumoroid cultures from cryo vials was possible for all tumoroid models.

Early tumor validation by RT-qPCR

Early during tumoroid establishment (upon first or second passaging), a portion of cells was set aside for evaluation of marker gene expression. For this, cells were spun down (500 g, 5 min, 4 °C), the supernatant was removed from the pellet, the pellet was dissolved in Trizol (10 minutes incubation at RT) and was immediately processed or snap-frozen and stored at minus 80 °C until further processing. Upon processing, first the organic and aqueous phases were separated by addition of 20% chloroform, followed by spinning down (maximum centrifugation speed, 15 min, 4 °C). The (upper) aqueous phase was further processed using the Direct-zol RNA MiniPrep Kit (Zymo Research) according to the manufacturer's protocol, including the recommended DNAse I treatment. Quality and quantity of isolated RNA were measured using a NanoDrop OneC (Thermo Fisher Scientific). Synthesis of cDNA from isolated RNA as well as a Universal Human Reference RNA that was used as negative control or for normalization (HREF, Stratagene/Agilent # 740000) was performed using an oligo-dT primed SuperScript III Reverse Transcriptase (Invitrogen) based reaction according to the manufacturer's

protocol. RT-qPCR was performed with the obtained cDNAs testing for expression levels of *G6PD* (forward: 5'-ACGGCAACAGATACAAGAAC-3', reverse: 5'-CGAAGTGCATCTGGCTCC-3'; product size: 86 bp) [71], *DES* (forward: 5'-CCGTGGTCTCTTACTTTCCTTT-3', reverse: 5'-CCCACTTTCT CTCCTTCTCAATC-3'; product size: 119 bp), *MYOG* (forward: 5'-TGCCC AACTGAGATTGTCTTC-3', reverse: 5'-CTGCTACAGAAGTAGTGGCATC-3', product size: 81 bp), *MYOD1* (forward: 5'-GTAGCAGGTGTAACCGTAACC-3', reverse: 5'-CACACCATGCCTCAGAGATAAA-3', product size: 148 bp), the *PAX-FOXO1* fusion transcript (forward: 5'-CCGACAGCAGCTCTGCCTAC-3', reverse: 5'-TGAACTTGCTGTGTAGGGACAG-3', product size: 171 bp for *PAX3-FOXO1* and 159 bp for *PAX7-FOXO1*) [26] as well as the *PAX3-WWTR1* fusion transcript (forward: 5'-AGCACCAGGCATGGATTT-3', reverse: 5'-TTCGAGGTCTGTGTCTAGGT-5', product size: 192 bp). Expression levels of *DES*, *MYOG*, *MYOD1*, and *PAX-FOXO1* were normalized to *G6PD* (housekeeping gene) and referenced to the corresponding expression levels in the HREF using the ΔΔCq method (for the fusion transcript only normalization to *G6PD* as the lack of a fusion expression in HREF did not permit a further reference step).

Immunohistochemistry (IHC) and H&E stainings

To perform IHC, tumoroid models were grown as floating 3D spheres. For this, 1-3x10E6 viable cells were put into an ultra-low attachment culture flask (Corning Ultra-Low Attachment 75 cm^2 U-Flask, Corning, cat no. 3814) in BM1* but without BME supplementation. Establishment of spheres of sufficient size took between 7 and 12 days, depending on the growth characteristics of the respective tumoroid model. Spheres were harvested by carefully transferring the sphere-containing medium from the flask to a 15 ml tube and sedimenting on ice for 10 minutes. Thereafter, the supernatant was removed, and the sphere-containing pellet was resuspended in cold PBS to wash off any remaining medium. The mixture was again sedimented (see above), and PBS was aspirated. Spheres were now fixed using formalin 10% (v/v), (= 4% (w/v) HISTO GRADE, neutralized (pH 7.0 ± 0.2), J.T. Baker, 3933.9020 VWR) for 96 hours at 4 °C after carefully transferring them to a glass vial. The fixed spheres were then washed twice with PBS and dehydration was performed by adding ethanol solutions with increasing percentages (25% EtOH for 15

min, 50% EtOH for 15 min, 70% EtOH for 15 min - after this step, spheres were stored at 4 °C and further processed in batches). Now, spheres were stained with 0.8 g/l Eosin Y dissolved in 96% EtOH (Sigma, E4009) for 30 min and subsequently incubated three times with 100% EtOH for 30 min each. Thereafter, spheres were incubated in n-Butanol (three times 30 min) and melted paraffin (three times) before they were Paraffin-embedded using the HistoCore Arcadia H (Leica Biosystems) following the manufacturer's protocol in a medium size mold. Hardened paraffin blocks were cut into 4 µm slices using a microtome (HM 355S Automatic Microtome, Thermo Scientific). Slides were further processed by deparaffinization (incubation with xylene three times for 3 min, then 100% EtOH two times for 3 min, 95% EtOH two times for 1 min, 70% EtOH once for 1 min, and 50% EtOH once for 1 min) and rehydration (tap water). Thereafter, antigen retrieval was performed by boiling samples for 20 min in with citrate buffer (pH 6, for Desmin staining) or Tris-EDTA-Tween buffer (pH 9, for Myogenin and MYOD1). After washing (in TBS-0.025% Triton, twice 5 min) and blocking (1.5 h in TBS-1%BSA), slides were incubated with primary antibody (α-Desmin 1:400, Abcam ab15200 rabbit antibody; α-Myogenin 1:400, Santa Cruz 5FD mouse antibody; α-MYOD1 1:200, Cell Marque EP212 rabbit antibody) overnight at 4 °C. The next day, slides were washed twice with PBS and incubated with secondary antibodies (Desmin and MYOD1: anti-rabbit-HRP, BioRad 170-6515; Myogenin: anti-mouse HRP, BioRad 170-6516) 1:500 in PBS-1% BSA. Stainings were visualized using Liquid DAB+ 2-component system (3,3'-diaminobenzidine, DAKO, Agilent K3467) following the manufacturer's protocol and washed three times with TBS. Counter-staining was performed by incubation with thionine (0.05% for 20 min). After subsequent incubation with 96% EtOH, 100% EtOH and xylene, slides were mounted using Permount mounting medium (Fisher Scientific SP15-100) and visualized using a Leica DMi6 microscope.

H&E stainings were performed manually (steps: xylene three times for 5 min, 100% EtOH twice for 1 min, 95% EtOH twice for 30 sec, 70% EtOH for 30 sec, washed in demi-water, incubation with hematoxylin (Hematox 7211) for 2:45 min, washed with demi-water, brief incubations with acidic EtOH, washed with demi-water, 95% EtOH for 30 sec, eosin incubation for 2:45 min, EtOH 70% for 30 sec, EtOH 95% for 30 sec, EtOH 100% twice for 30 sec, xylene three times for 1 min) or were performed at the in-house pathology

department following standard protocols. Visualization was performed as described above.

The quality of stainings was evaluated by an in-house pathologist. Representative images of stained spheres are shown and were compared to H&E as well as IHC stainings obtained in pathology for the RMS tumor sample the tumoroid was derived from (representative images chosen by the pathologist).

Single-cell mRNA sequencing of RMS tumoroid models

Sample processing

For each tumoroid model (RMS127 and RMS444), viably frozen cells were thawed and resuspended in BM1* medium. Prior to sorting, 4′,6-diamidino-2-phenylindole (DAPI, Sigma-Aldrich, #D9542) and DRAQ5 (Thermo Fisher, #65-0880-92) were added to the single-cell suspensions to achieve final concentrations of 1 µM and 5 µM, respectively. Viable single-cells (DAPI-, DRAQ5+, FSC/SSC) were then sorted into 384-well plates (BioRad, #HSP3801) containing 10 µl of mineral oil (Sigma, #M5310) and 50 nl of barcoded RT primers using a SONY SH800S Cell Sorter. Libraries were prepared according to the SORT-seq protocol [72] and sequenced on the Illumina NextSeq500 (paired-end, 75bp).

Analysis of single-cell mRNA-sequencing data

Sequencing reads were demultiplexed, mapped to the Genome Reference Consortium human build 38 genome and transcript counts were generated using a custom implementation of the zUMIs pipeline [73]. Count tables from each plate were read into *R* (v4.1.0), merged and metadata fields were compiled. The merged count and metadata tables were used to initialize a Seurat (v4.0.3) object [74], and cells with < 500 expressed genes, < 800 or > 50,000 unique transcripts, a percentage of mitochondrial transcripts > 50%, a percentage of hemoglobin genes > 1% or a ratio of intergenic to genic transcripts > 2 were excluded from further analysis. The filtered object was then log-normalized, using a scaling factor of 10,000, and the top 2,000 most variable genes in the dataset were defined by calling the *FindVariableFeatures* Seurat function (default parameters). These genes were scaled, centered,

5

and used as input for running principal component analysis (PCA). The top five principal components were then used to project the data in 2-dimensions using t-distributed stochastic neighbor embedding (t-SNE). Single-cell CNV profiles were constructed using the InferCNV R package (v1.8.0) [75]. In addition to the default parameters, an average expression threshold per gene of 0.3 and a standard deviation filter of 2 was used to denoise the results. A dataset of cord blood mononuclear cells (CBMCs) generated in-house was used as the "normal" reference sample.

RNA and DNA isolation from tumor and derived tumoroid samples for whole-genome sequencing (WGS) and bulk mRNA sequencing (RNA-seq)
Tumoroid models

To isolate RNA and DNA for WGS and RNA-seq, tumoroid cells were collected as a pellet, snap frozen and stored at minus 80 °C. Isolation of RNA and DNA from the same pellet was performed using the AllPrep DNA/RNA/miRNA Universal Kit (Qiagen # 80224) according to the manufacturer's protocol. Lysis in RLT buffer was followed by homogenization using a Qiashredder column as described. The flowthrough fraction in RLT buffer was used for the Allprep DNA and RNA isolations. Quality and quantity of isolated RNA and DNA were measured by using the NanoDrop OneC (Thermo Fisher Scientific), Bioanalyzer 2100 (Agilent), Qubit Fluorometer (Thermo Fisher Scientific), and marker-checks using RT-qPCR (as above).

Tumor samples and germline control samples (EDTA blood)

Resected tissue and/or biopsies were processed within 10 min after removal from the patient. DNA and RNA were isolated from the same piece of fresh frozen tissue using the AllPrep DNA/RNA/miRNA Universal Kit (Qiagen # 80224) using the QIAcube Connect (Qiagen). Reference DNA was isolated from peripheral white blood cells (EDTA blood) using the same method.

Whole-genome sequencing (WGS) of tumor and tumoroid samples
Sequencing

150 ng of total DNA was used for library preparation using the KAPA HyperPlus kit (Roche), according to manufacturer's instructions. Libraries from tumor

and normal tissue were pooled in a 3:1 ratio, with a total of 7 tumor/normal pairs per S4 sequencing kit. Libraries were sequenced using 2x150 cycles on a NovaSeq 6000 (Illumina).

Pre-processing, alignment, and annotation

The WGS sequencing data were processed as per the GATK 4.0 best practices workflow for variant calling, using a wdl and cromwell based workflow. Reads were aligned to GRCh38 using bwamem (v0.7.13), and quality control (QC) was performed using FastQC (v0.11.5) and picardTools (v2.20.1). Somatic variants were identified using Mutect2 from GATK v4.1 and annotated using Vep (v92). Likewise, copy-number alterations (CNAs) were identified using GATK v4.1.

Identification of non-synonymous single nucleotide variants (SNVs)

Raw VCF files from germline, tumor and tumoroid samples were processed with vcftools (v0.1.13) [76]. Only variants that met the criteria (passed all quality filters in addition to PHRED quality score 100 (250 for indels) and minimum read depth of 10) were kept for further analyses. Indels were also filtered out if the minimum mapping quality (MQ) was below 60. Bcftools (https://github.com/samtools/bcftools) was used to remove all common snps (VAF $\geq$ 1%) present in dbSNP (https://www.ncbi.nlm.nih.gov/snp/, v151 downloaded in August 2020). Filtered files were then loaded into *R* (v4.0.2) and processed with the package VariantAnnotation [77] and packages from the tidyverse. Variants in tumor and tumoroid models also present in the germline sample were removed from further analyses; remaining variants were filtered for VAFs > 0.3 and those tagged as missense variant, stop gained, stop lost, start lost, inframe insertion, inframe deletion, and frameshift variant were selected as non-synonymous somatic mutations. Figures were generated with ggplot2 (v.3.3.2).

Signature analysis

Somatic signature analysis was performed using the *R* programming language (v3.6.3) and the *R* packages MutationalPatterns (v3.2.0) and VariantAnnotation (v1.32.0) [77–79]. Somatic variants were filtered on both the variant allele fraction (VAF) and depth (DP). For both the control and the tumor/tumoroid samples

we used DP $\geq$ 20. For the tumor/tumoroid samples we used VAF > 0.3, while in control samples the VAF had to be 0. Samples with 50 or less mutations would have been excluded, but this was not the case for any samples in our cohort. A mutation matrix was generated that shows how often each of the 96 types of base substitutions occurred in each sample. A variational Bayesian non-negative matrix factorization (NMF) was performed on this matrix to extract four *de novo* mutational signatures for base substitutions. The cosine similarities were then calculated between these *de novo* signatures and a set of signatures consisting of both the COSMIC signatures (v3.2, GRCh38) and the SIGNAL exposure signatures [32,34]. The four signatures most similar to the *de novo* signatures (SBS1, SBS5, SBS18, and Temozolomide..200.uM..1 [TMZ]) were then used for signature refitting. Signature refitting was performed using the *fit_to_signatures_strict* function using the best_subset method with a max_delta of 0.004. Our approach of first performing *de novo* signature extraction followed by refitting is similar to the approach suggested by Maura *et al.* [80].

To determine the similarity between the samples, the cosine similarities of their base substitution profiles were calculated. This resulted in a cosine similarity matrix that was used to calculate the distance between samples, which was then used for hierarchical clustering.

Evaluation of clonal heterogeneity using WGS data

To evaluate clonal heterogeneity in our RMS tumoroid models, two approaches were used based on the WGS data from each tumor/tumoroid pair. First, we compared the VAFs of somatic mutations in both tumor and tumoroid models by selecting variants from coding regions with a VAF of at least 0.1 in either tumor or tumoroid model. To ensure the VAFs were representative of the ratio of cell populations in the culture, we removed all SNVs from non-copy number neutral regions or tagged as sites with loss of heterozygosity (LOH) as detected by the GATK pipeline. VAFs of SNVs matching those criteria were plotted a in correlogram using *R*.

Secondly, we investigated the alternate allele (B-allele) fractions as they can indicate the presence of clonal and/or subclonal populations based on estimated allelic ratios. To this end, we extracted the median alternate allele fraction from the modeled segments from each sample; to ensure

comparability across region segments, a consensus region .bed file was generated prior to generating the density plots. Frequencies were then plotted per tumor/tumoroid pair as density plots using *R*.

For both analyses, RMS127 was excluded due the low tumor cell percentage of the tumor sample.

Bulk mRNA (RNA-seq) of tumor and tumoroid samples: transcriptional profile and gene fusions
Sequencing

300 ng of total RNA was used for library preparation using the KAPA RNA HyperPrep kit with RiboErase (Roche), according to manufacturer's instructions. The protocol was optimized to achieve an insert size of ~300-400 nt.

RNA libraries were pooled with a total of 25 samples per S1 kit or 60 samples per S2 kit. Libraries were sequenced using 2x150 cycles on a NovaSeq 6000 (Illumina).

Pre-processing: alignment, annotation, and detection of gene fusions

The RNA sequencing data were processed as per the GATK 4.0 best practices workflow for variant calling, using a wdl and cromwell based workflow (https://gatk.broadinstitute.org/hc/en-us/sections/360007226651-Best-Practices-Workflows). This included performing quality control with Fastqc (v0.11.5) to calculate the number of sequencing reads and the insert size (Andrews S., 2010. FastQC: a quality control tool for high throughput sequence data, http://www.bioinformatics.babraham.ac.uk/projects/fastqc). Picard (v2.20.1) for RNA metrics output and MarkDuplicates ("Picard Tools." Broad Institute. http://broadinstitute.github.io/picard/). The raw sequencing reads were aligned using Star (v2.7.0f) to GRCh38 and gencode version 31. Gene fusion detection was performed using Star fusion (v1.6.0) [81]. Finally, expression counts were determined at exon and gene level using Subread Counts [82].

Processing of transcriptome data

Raw count tables were loaded into *R* (v4.0.2) and processed with the packages from the tidyverse. Count matrices were transformed into log2-

5

scale transcripts per million (log2 TPM) tables and genes annotated with the same gene symbol merged.

Comparison of transcriptional profiles across samples (kidney and rhabdomyosarcomas) was performed via correlation performed in *R* using the base package.

Growth curve experiments

Growth behavior in 3D sphere cultures prior to drug screenings (see below) was tested via performing growth curve experiments. Tumoroid cells were plated at different densities (typically between 250 and 4.000 viable cells per well) in 384-well round bottom ultra-low attachment spheroid microplates (Corning, cat no. 3830). To facilitate 3D sphere formation, cells were grown in BM1* medium without BME and after dispensing them into the plates, plates were spun (1.500 rpm, 5 min, slow break) to concentrate cells in the center of the wells. Plates were incubated at standard conditions and cells were granted a recovery period of 48 hours. Thereafter, readouts were performed using CellTiter-Glo 3D Cell Viability Assay (CTG3D, Promega, cat no. G9683) according to the manufacturer's protocol at three time points: immediately (T0), 48 hours or 72 hours (T48 or T72), and 120 hours (T120). Measured luminescence (via FLUOstar Omega, BMG Labtech) was averaged per readout per cell density and the corresponding background signal from medium was subtracted. Obtained measurements from T48/T72 and T120 were normalized to T0 to calculate the relative growth over the period of 120 hours. For the following drug screening experiments (see below), a cell density was chosen that showed logarithmic growth behavior in growth curve experiments. Defined starting number of cells facilitated the establishment of a sphere and were optimized for intrinsic growth factor levels and space depletion in the well over the course of the experiment. Growth curve experiments were performed once per model but with at least ten technical replicates per number of cells plated.

Drug screenings

For drug screenings, tumoroid models were processed according to the same protocol as for the growth curve experiments, with a number of cells seeded that was determined in those experiments (see above). Drugs, dissolved in

DMSO or water, were added 48 hours after seeding of the tumoroid spheres fully automated via a robotics system: Up until 2019, this was facilitated via a Caliper Sciclone-Robotic Liquid Handler using a dilution of the drugs in medium and transferring this dilution to the cells by pipetting. From 2020 onwards, screenings were performed at the high-throughput screening (HTS) facility of the Princess Máxima Center with a Biomek i7 liquid handler, using the acoustic liquid handler Echo550 for direct drug transfers. Before the screening, the 384-well working plates containing the dissolved drugs are shaken (30 min, RT) and centrifuged (1 min, 1.500 rpm). Tumoroid spheres were treated with a ten-fold dilution series of the drugs on the library plate (0.1 nM to 10 μM). Positive control samples were treated with DMSO, negative control samples with staurosporine (final concentration of 10 μM). Readouts were performed using CellTiter-Glo 3D Cell Viability Assay (CTG3D, Promega, cat no. G9683) according to the manufacturer's protocol at T0 (before addition of drugs – control) and at T120 (120 hours after addition of drugs – readout). Dose-response was estimated per drug and concentration in relation to the DMSO-treated cells (set to 100%) and empty controls (set to 0%). Quality of the screenings was approved after assessment of the cell growth (absorbance signal of T120 over T0), the negative, positive, and empty controls and, if applicable, the amount of variability between the duplicates.

Depending on the available number of cells at drug screening, a subset of models (RMS007, RMS109, RMS110, RMS000EEC, RMS000ETY, RMS000FLV, RMS000HQC, RMS000HWO, RMS000HWQ) could be screened in technical duplicates while for the other models (RMS006, RMS012, RMS013, RMS102, RMS108, RMS127, RMS335, RMS410, RMS444, RMS000CPU) only screening without technical duplicates was feasible. To test reproducibility, we analyzed the correlation between the technical duplicates in the tumoroid models for which those were available (Appendix Figure S1). As we observed a very high correlation there ($R = 0.91$), indicating a high reproducibility, we deemed it appropriate to combine the analysis of samples tested in duplicate and those not tested in duplicate given the scope of the assay was to assess whether we could obtain biologically meaningful results (any "hit" should have been further validated). RMS tumoroid models RMS000ETY and RMS000HWO were excluded from the analysis as they did not show an increase of CTG3D signal between T0 and T120 (Table EV1), indicating that these two models did not

5

grow sufficiently under the screening conditions (while they displayed a minor increase in signal during the growth curve experiments).

Further data analysis was performed using *R* (v3.6.3). Area Under the Curve (AUC) values were calculated for every drug per tumoroid model and replicate (in the case of the tumoroid models with technical replicates) using the *auc* function of the MESS package (v0.5.6). In the case of RMS tumoroid models with technical duplicates, the two resulting AUC values per drug were correlated (using the *cor* function of base *R*) to calculate the correlation between replicates and plotted using the *plot* function of base *R* (see above). For the further downstream analysis, these replicate AUC values were averaged, resulting in a matrix with one AUC value per drug per RMS tumoroid model. On this matrix, unsupervised clustering was performed using the *get_dist* function from the factoextra package (v1.0.7) using the arguments "pearson" for RMS tumoroid models and "euclidean" for drugs to measure dissimilarity with further clustering using the *hclust* function from base *R* using the "average" argument for linkage. Data were visualized using the *heatmap.2* function from the gplots package (v3.0.3) using dendrograms generated from the established clustering. Principal component analysis (PCA) was performed using the *prcomp* function from base *R* with exclusion of the RMS tumoroid model RMS000FLV due to its outlier behavior. PCAs were visualized using the *fviz_pca_ind* and *fviz_pca_var* functions from the above-mentioned factoextra package.

CRISPR/Cas9 knockout of *TP53* and functional evaluation

RMS012 tumoroid cells were kept under standard conditions (BM1* supplemented with 0.1% BME) prior to the experiment. Upon reaching 70% confluency, tumoroid cells were passaged as usual and seeded with high density into wells of a 24-well plate. After 24 hours of recovery, transfection was performed: Nucleic acid–Lipofectamine 2000 complexes were prepared according to the standard Lipofectamine 2000 protocol (Invitrogen). Four μl of Lipofectamine 2000 reagent in 50 μl Opti-MEM medium (Gibco) and 1.5 μg of DNA (pSpCas9(BB)-2A-GFP control or sgRNA *TP53* plasmid in 50 μl Opti-MEM medium) were mixed, incubated for 5 min, and added to the cells. Plasmids were kindly shared by Jarno Drost (PMC, NL). For the plasmid sequence refer to Drost *et al.* 2015 [45]. Twenty-four hours after transfection,

transfection efficiency was evaluated using fluorescence microscopy, detecting GFP positive cells. Forty-eight hours after transfection, selection with nutlin-3 (10 µM) was started. Four days after the start of selection, first nutlin-3 resistant colonies could be detected in *TP53* knockout plasmid transfected cells whereas cells transfected with control plasmids died due to nutlin-3 exposure. Putative knockout cells were further expanded.

Knockout was confirmed using Western Blotting and Sanger sequencing of genomic DNA: For Western Blotting, snap frozen tumoroid cell pellets were lysed in Phosphatase-substituted RIPA buffer and run on a 10% precast gel for P53 detection (BioRad). Protein levels of P53 (1:1.000, Santa Cruz DO-1 P53 antibody) were detected while Histone 3 (1:2.000, Abcam ab1791 Pan-H3) served as loading control. For visualization, secondary antibodies (goat anti-rabbit, BioRad 1706515 / goat anti-mouse BioRad 1706516) conjugated with horseradish peroxidase (HRP) were used together with ECL substrate (Perkin Elmer) on an imaginer (BioRad ChemiDoc). Western Blotting analysis was performed twice, and a representative blot is shown.

For Sanger sequencing of genomic DNA, a snap frozen tumoroid cell pellet was lysed using DirectPCR Lysis Reagent for Cells (Viagen) according to the manufacturer's protocol. PCR amplification was performed using Phusion High-Fidelity DNA Polymerase (New England BioLabs) using the following primers: forward 5'-CCCATCTACAGTCCCCCTTG-3', reverse 5'-CAGGAAGCCAAAGGGTGAAGA-3'. PCR products were cleaned up and concentrated using a DNA Clean-up and Concentration Kit (Zymo Research) according to the manufacturer's protocol. Gel electrophoresis indicated the presence of a specific product which was sent for Sanger sequencing using the following primers: forward 5'-TGGTTCACTGAAGACCCAGG-3', reverse 5'-GAAGTCTCATGGAAGCCAGCC-3'. Obtained sequences were aligned and inspected using the Benchling browser tool (https://www.benchling.com/). Furthermore, sequencing data was submitted for TIDE (Tracking of Indels by Decomposition, http://tide.nki.nl) analysis to infer the composition of Indels in the knockout population [83].

For detection of DNA double strand breaks, induction of γH2AX was measured using Western Blotting. Fusion-negative embryonal rhabdomyosarcoma cell line RD (kindly shared by Jan Molenaar, PMC, NL) served as a control (either

untreated or treated with 1 μM, 5 μM, or 10 μM of staurosporine (Sigma) for 24 h). RD cells (ATCC identifier CCL-136, species human) were cultured under conventional conditions as detailed by the American Type Culture Collection (ATCC) with regular testing for mycoplasma contamination. For Western Blotting, snap frozen tumoroid (RMS012 *TP53* KO) or tumor (RD) cell pellets were lysed in Phosphatase-substituted RIPA buffer and run on a 15% self-cast gel for γH2AX (p.S139) detection. Protein levels of γH2AX (p.S139, 1:2.000, Abcam ab26350 antibody) were detected while GAPDH (1:1.000, Abcam ab9485 antibody) served as loading control. Visualization was performed as described above for the confirmation of the knockout. As above, Western Blotting analysis was performed twice, and a representative blot is shown.

To assess differential response to prexasertib (MedchemExpress), RMS012 tumoroid models (*TP53* wildtype and *TP53* knockout) were processed according to the same protocol as for the growth curve experiments (see above), with 500 cells seeded per well. Prexasertib (dilution series from 200 nM to 0.78125 nM) was added 48 hours after seeding of the tumoroid spheres. Control samples were treated with DMSO. Readouts were performed using CellTiter-Glo 3D Cell Viability Assay (CTG3D, Promega, cat no. G9683) according to the manufacturer's protocol at T72 (72 hours after addition of drugs). Dose-response was estimated per model and concentration in relation to the DMSO-treated cells (set to 100%). The experiment was performed three times. Further data analysis was performed using *R* (v3.6.3). A sigmoidal fit for the dose-response curve was calculated per replicate for both the knockout and wildtype sample with a three-parameter log-logistics function using the drc package (v3.0-1) [84]. The statistical significance of the differences in fitted IC_{50} values between knockout and wildtype were obtained using a two-sided t-test. For visualization purposes a three-parameter sigmoidal fit per model (not per replicate) was used.

Image post-processing and figure preparation

Microscopy images from RMS tumoroid IHC and H&E stainings as well as images from Western Blotting were post-processed according to good scientific practice with Adobe Photoshop 2021 and Fiji (v2.0.0-rc-69/1.52i) [85]. Images from original RMS tumors (H&E and IHC) were not processed.

Figures were prepared using Adobe Illustrator 2021.

Data availability

Bulk sequencing data (i.e., whole-genome sequencing and bulk mRNA sequencing) have been made openly available at the European Genome-Phenome Archive (EGA) with the identifiers EGAD00001008466 ("WGS soft tissue sarcoma tumoroid biobank"), EGAD00001008467 ("RNA-Seq soft tissue sarcoma tumoroid biobank") and EGAD00001008709 ("RNA-Seq of primary pediatric kidney tumor controls for the soft tissue sarcoma tumoroid biobank"). Single-cell mRNA sequencing data of the RMS tumoroid models RMS127 and RMS444 as well as the CBMC controls are similarly available at EGA with the identifier EGAD00001009002 ("sc-RNA-Seq soft tissue sarcoma tumoroid biobank").

Code for bulk sequencing data analysis is made openly available at https://github.com/teresouza/rms2018-009.

Conflicts of Interest

The authors declare that they have no conflicts of interest.

References

1. Yang, J., Ren, Z., Du, X., Hao, M. & Zhou, W. The role of mesenchymal stem/progenitor cells in sarcoma: update and dispute. *Stem cell Investig.* **1**, 18–18 (2014).

2. Li, J., Thompson, T. D., Miller, J. W., Pollack, L. A. & Stewart, S. L. Cancer incidence among children and adolescents in the United States, 2001-2003. *Pediatrics* **121**, (2008).

3. Patton, R. B. & Horn, R. G. Rhabdomyosarcoma: Clinical and pathological features and comparison with human fetal and embryonal skeletal muscle. *Surgery* **52**, 572–584 (1962).

4. Enterline, H. T. & Horn, R. C. Alveolar rhabdomyosarcoma; a distinctive tumor type. *Am. J. Clin. Pathol.* **29**, 356–366 (1958).

5. Perez, E. A. *et al.* Rhabdomyosarcoma in children: A SEER population based study. *J. Surg. Res.* **170**, e243–e251 (2011).

6. Shern, J. F. *et al.* Comprehensive genomic analysis of rhabdomyosarcoma reveals a landscape of alterations affecting a common genetic axis in fusion-positive and fusion-negative tumors. *Cancer Discov* **4**, 216–231 (2014).

7. WHO. WHO Classification of Tumours: Soft Tissue and Bone Tumors. 5th Edition. (2020).

8. Skapek, S. X. *et al.* Rhabdomyosarcoma. *Nat Rev Dis Prim.* **5**, 1 (2019).

9. Bisogno, G. *et al.* Vinorelbine and continuous low-dose cyclophosphamide as maintenance chemotherapy in patients with high-risk rhabdomyosarcoma (RMS 2005): a multicentre, open-label, randomised, phase 3 trial. *Lancet Oncol.* (2019) doi:10.1016/s1470-2045(19)30617-5.

10. Mascarenhas, L. *et al.* Risk-based treatment for patients with first relapse or progression of rhabdomyosarcoma: A report from the Children's Oncology Group. *Cancer* **125**, 2602–2609 (2019).

11. Pappo, A. S. *et al.* Survival after relapse in children and adolescents with rhabdomyosarcoma: A report from the intergroup rhabdomyosarcoma study group. *J. Clin. Oncol.* **17**, 3487–3493 (1999).

12. Sato, T. *et al.* Single Lgr5 stem cells build crypt-villus structures in vitro without a mesenchymal niche. *Nature* **459**, 262–265 (2009).

13. Clevers, H. Modeling Development and Disease with Organoids. *Cell* vol. 165 1586–1597 (2016).

14. Yuki, K., Cheng, N., Nakano, M. & Kuo, C. J. Organoid Models of Tumor Immunology. *Trends Immunol.* **41**, 652–664 (2020).

15. Bleijs, M., Wetering, M., Clevers, H. & Drost, J. Xenograft and organoid model systems in cancer research. *EMBO J.* **38**, e101654 (2019).

16. Abdullah, K. G. *et al.* Establishment of patient-derived organoid models of lower grade glioma. *Neuro. Oncol.* (2021) doi:10.1093/neuonc/noab273.

17. Jacob, F. *et al.* A Patient-Derived Glioblastoma Organoid Model and Biobank Recapitulates Inter- and Intra-tumoral Heterogeneity. *Cell* **180**, 188-204.e22 (2020).

18. Fusco, P. *et al.* Patient-derived organoids (PDOs) as a novel in vitro model for neuroblastoma tumours. *BMC Cancer* **19**, 1–11 (2019).

19. Saltsman, J. A. *et al.* A human organoid model of aggressive hepatoblastoma for disease modeling and drug testing. *Cancers (Basel).* **12**, 1–18 (2020).

20. Yamazaki, S. *et al.* Newly established patient-derived organoid model of intracranial meningioma. *Neuro. Oncol.* **23**, 1936–1948 (2021).

21. Calandrini, C. *et al.* An organoid biobank for childhood kidney cancers that captures disease and tissue heterogeneity. *Nat. Commun.* **11**, (2020).

22. Boulay, G. *et al.* The chromatin landscape of primary synovial sarcoma organoids is linked to specific epigenetic mechanisms and dependencies. *Life Sci. Alliance* **4**, (2021).

23. Brodin, B. A. *et al.* Drug sensitivity testing on patient-derived sarcoma cells predicts patient response to treatment and identifies c-Sarc inhibitors as active drugs for translocation sarcomas. *Br. J. Cancer* **120**, 435–443 (2019).

24. Manzella, G. *et al.* Phenotypic profiling with a living biobank of primary rhabdomyosarcoma unravels disease heterogeneity and AKT sensitivity. *Nat. Commun.* **11**, 1–15 (2020).

25. Dijkstra, K. K. *et al.* Challenges in Establishing Pure Lung Cancer Organoids Limit Their Utility for Personalized Medicine. *Cell Rep.* **31**, (2020).

26. Ponce-Castañeda, M. V. *et al.* Detection of common chromosomal translocations in small round blue cell pediatric tumors. *Arch. Med. Res.* **45**, 143–151 (2014).

27. Dias, P. *et al.* Strong immunostaining for myogenin in rhabdomyosarcoma is significantly associated with tumors of the alveolar subclass. *Am. J. Pathol.* **156**, 399–408 (2000).

28. Heerema-Mckenney, A. *et al.* Diffuse myogenin expression by immunohistochemistry is an independent marker of poor survival in pediatric rhabdomyosarcoma: A tissue microarray study of 71 primary tumors including correlation with molecular phenotype. *Am. J. Surg. Pathol.* **32**, 1513–1522 (2008).

29. Stewart, E. *et al.* Orthotopic patient-derived xenografts of paediatric solid tumours. *Nature* **549**, 96–100 (2017).

30. Loarer, F. Le *et al.* Clinicopathologic and Molecular Features of a Series of 41 Biphenotypic Sinonasal Sarcomas Expanding Their Molecular Spectrum. *Am. J. Surg. Pathol.* **43**, 747–754 (2019).

31. Weber-Hall, S. *et al.* Gains, losses, and amplification of genomic material in rhabdomyosarcoma analyzed by comparative genomic hybridization. *Cancer Res.* **56**, 3220–3224 (1996).

32. Alexandrov, L. B. *et al.* The repertoire of mutational signatures in human cancer. *Nature* **578**, 94–101 (2020).

5

33. Petljak, M. *et al.* Characterizing Mutational Signatures in Human Cancer Cell Lines Reveals Episodic APOBEC Mutagenesis. *Cell* **176**, 1282-1294.e20 (2019).

34. Kucab, J. E. *et al.* A Compendium of Mutational Signatures of Environmental Agents. *Cell* **177**, 821-836.e16 (2019).

35. Defachelles, A.-S. *et al.* Randomized Phase II Trial of Vincristine-Irinotecan With or Without Temozolomide, in Children and Adults With Relapsed or Refractory Rhabdomyosarcoma: A European Paediatric Soft Tissue Sarcoma Study Group and Innovative Therapies for Children With Cancer . *J. Clin. Oncol.* **39**, 2979–2990 (2021).

36. Casey, D. L. *et al.* Genomic determinants of clinical outcomes in rhabdomyosarcoma. *Clin. Cancer Res.* **26**, 1135–1140 (2020).

37. Greaves, M. & Maley, C. C. Clonal evolution in cancer. *Nature* **481**, 306–313 (2012).

38. Wachtel, M. *et al.* Gene expression signatures identify rhabdomyosarcoma subtypes and detect a novel t(2;2)(q35;p23) translocation fusing PAX3 to NCOA1. *Cancer Res.* **64**, 5539–5545 (2004).

39. Lu, J. *et al.* Characterization of an in vitro 3D intestinal organoid model by using massive RNAseq-based transcriptome profiling. *Sci. Rep.* **11**, 1–14 (2021).

40. Bersani, F. *et al.* Bortezomib-mediated proteasome inhibition as a potential strategy for the treatment of rhabdomyosarcoma. *Eur. J. Cancer* **44**, 876–884 (2008).

41. Yohe, M. E. *et al.* MEK inhibition induces MYOG and remodels super-enhancers in RAS-driven rhabdomyosarcoma. *Sci Transl Med* **10**, (2018).

42. Belyea, B. C., Naini, S., Bentley, R. C. & Linardic, C. M. Inhibition of the notch-hey1 axis blocks embryonal rhabdomyosarcoma tumorigenesis. *Clin. Cancer Res.* **17**, 7324–7336 (2011).

43. Jinek, M. *et al.* A programmable dual-RNA-guided DNA endonuclease in adaptive bacterial immunity. *Science (80-.).* **337**, 816–821 (2012).

44. Shern, J. F. *et al.* Genomic Classification and Clinical Outcome in Rhabdomyosarcoma: A Report From an International Consortium. *J. Clin. Oncol.* **39**, 2859–2871 (2021).

45. Drost, J. *et al.* Sequential cancer mutations in cultured human intestinal stem cells. *Nature* **521**, 43–47 (2015).

46. Yonish-Rouach, E. *et al.* Wild-type p53 induces apoptosis of myeloid leukaemic cells that is inhibited by interleukin-6. *Nature* **352**, 345–347 (1991).

47. Rogakou, E. P., Pilch, D. R., Orr, A. H., Ivanova, V. S. & Bonner, W. M. DNA double-stranded breaks induce histone H2AX phosphorylation on serine 139. *J. Biol. Chem.* **273**, 5858–5868 (1998).

48. Dobbelstein, M. & Sørensen, C. S. Exploiting replicative stress to treat cancer. *Nature Reviews Drug Discovery* vol. 14 405–423 (2015).

49. Ma, C. X. *et al.* Targeting Chk1 in p53-deficient triple-negative breast cancer is therapeutically beneficial in human-in-mouse tumor models. *J. Clin. Invest.* **122**, 1541–1552 (2012).

50. Lee, J. M. *et al.* Prexasertib, a cell cycle checkpoint kinase 1 and 2 inhibitor, in BRCA wild-type recurrent high-grade serous ovarian cancer: a first-in-class proof-of-concept phase 2 study. *Lancet Oncol.* **19**, 207–215 (2018).

51. Van De Wetering, M. *et al.* Prospective derivation of a living organoid biobank of colorectal cancer patients. *Cell* **161**, 933–945 (2015).

52. Sato, T. *et al.* Long-term expansion of epithelial organoids from human colon, adenoma, adenocarcinoma, and Barrett's epithelium. *Gastroenterology* **141**, 1762–1772 (2011).

53. Hettmer, S. & Wagers, A. J. Muscling in: Uncovering the origins of rhabdomyosarcoma. *Nature Medicine* vol. 16 171–173 (2010).

54. Burningham, Z., Hashibe, M., Spector, L. & Schiffman, J. D. The Epidemiology of Sarcoma. *Clin. Sarcoma Res.* **2**, 14 (2012).

55. Rudzinski, E. R. *et al.* The world health organization classification of skeletal muscle tumors in pediatric rhabdomyosarcoma a report from the children's oncology group. *Arch. Pathol. Lab. Med.* **139**, 1281–1287 (2015).

56. Acanda De La Rocha, A. M. *et al.* Clinical Utility of Functional Precision Medicine in the Management of Recurrent/Relapsed Childhood Rhabdomyosarcoma. *JCO Precis. Oncol.* 1659–1665 (2021) doi:10.1200/po.20.00438.

57. Glosli, H. *et al.* Non-parameningeal head and neck rhabdomyosarcoma in children, adolescents, and young adults: Experience of the European paediatric Soft tissue sarcoma Study Group (EpSSG) – RMS2005 study. *Eur. J. Cancer* **151**, 84–93 (2021).

58. Drummond, C. J. *et al.* Hedgehog Pathway Drives Fusion-Negative Rhabdomyosarcoma Initiated From Non-myogenic Endothelial Progenitors. *Cancer Cell* **33**, 108-124.e5 (2018).

59. Kashi, V. P., Hatley, M. E. & Galindo, R. L. Probing for a deeper understanding of rhabdomyosarcoma: insights from complementary model systems. *Nat Rev Cancer* **15**, 426–439 (2015).

60. Imle, R., Kommoss, F. K. F. & Banito, A. Preclinical In Vivo Modeling of Pediatric Sarcoma—Promises and Limitations. *J. Clin. Med.* **10**, 1578 (2021).

61. Kim, J., Koo, B. K. & Knoblich, J. A. Human organoids: model systems for human biology and medicine. *Nature Reviews Molecular Cell Biology* vol. 21 571–584 (2020).

62. Hinson, A. R. P. *et al.* Human rhabdomyosarcoma cell lines for rhabdomyosarcoma research: Utility and pitfalls. *Front. Oncol.* **3 JUL**, (2013).

63. Kersten, K., Visser, K. E., Miltenburg, M. H. & Jonkers, J. Genetically engineered mouse models in oncology research and cancer medicine. *EMBO Mol. Med.* **9**, 137–153 (2017).

64. Yan, C. *et al.* Visualizing Engrafted Human Cancer and Therapy Responses in Immunodeficient Zebrafish. *Cell* **177**, 1903-1914.e14 (2019).

65. Gao, H. *et al.* High-throughput screening using patient-derived tumor xenografts to predict clinical trial drug response. *Nat. Med.* **21**, 1318–1325 (2015).

66. Pompili, L., Porru, M., Caruso, C., Biroccio, A. & Leonetti, C. Patient-derived xenografts: A relevant preclinical model for drug development. *Journal of Experimental and Clinical Cancer Research* vol. 35 (2016).

67. Fumagalli, A. *et al.* A surgical orthotopic organoid transplantation approach in mice to visualize and study colorectal cancer progression. *Nat. Protoc.* **13**, 235–247 (2018).

68. Dekkers, J. F. *et al.* Long-term culture, genetic manipulation and xenotransplantation of human normal and breast cancer organoids. *Nat. Protoc.* **16**, 1936–1965 (2021).

69. Grassi, L. *et al.* Organoids as a new model for improving regenerative medicine and cancer personalized therapy in renal diseases. *Cell Death Dis.* **10**, (2019).

70. Custers, L. *et al.* Somatic mutations and single-cell transcriptomes reveal the root of malignant rhabdoid tumours. *Nat. Commun.* **12**, 1–11 (2021).

71. Amary, M. F. C. *et al.* Detection of SS18-SSX fusion transcripts in formalin-fixed paraffin-embedded neoplasms: analysis of conventional RT-PCR, qRT-PCR and dual color FISH as diagnostic tools for synovial sarcoma. *Mod. Pathol. 2007 204* **20**, 482–496 (2007).

72. Muraro, M. J. *et al.* A Single-Cell Transcriptome Atlas of the Human Pancreas. *Cell Syst.* **3**, 385-394.e3 (2016).

73. Parekh, S., Ziegenhain, C., Vieth, B., Enard, W. & Hellmann, I. zUMIs - A fast and flexible pipeline to process RNA sequencing data with UMIs. *GigaScience* vol. 7 (2018).

74. Hao, Y. *et al.* Integrated analysis of multimodal single-cell data. *Cell* **184**, 3573-3587.e29 (2021).

75. Tickle, T., Tirosh, I., Georgescu, C., Brown, M. & Haas, B. inferCNV of the Trinity CTAT Project. Klarman Cell Observatory, Broad Institute of MIT and Harvard, Cambridge, MA, USA. (2019).

76. Danecek, P. *et al.* The variant call format and VCFtools. *Bioinformatics* **27**, 2156–2158 (2011).

77. Obenchain, V. *et al.* VariantAnnotation: A Bioconductor package for exploration and annotation of genetic variants. *Bioinformatics* **30**, 2076–2078 (2014).

78. Blokzijl, F., Janssen, R., van Boxtel, R. & Cuppen, E. MutationalPatterns: Comprehensive genome-wide analysis of mutational processes. *Genome Med.* **10**, (2018).

79. Manders, F. *et al.* MutationalPatterns: The one stop shop for the analysis of mutational processes. *bioRxiv* 2021.11.01.466730 (2021) doi:10.1101/2021.11.01.466730.

80. Maura, F. *et al.* A practical guide for mutational signature analysis in hematological malignancies. *Nat. Commun.* **10**, (2019).

81. Haas, B. J. *et al.* Accuracy assessment of fusion transcript detection via read-mapping and de novo fusion transcript assembly-based methods. *Genome Biol.* **20**, (2019).

82. Liao, Y., Smyth, G. K. & Shi, W. The R package Rsubread is easier, faster, cheaper and better for alignment and quantification of RNA sequencing reads. *Nucleic Acids Res.* **47**, e47–e47 (2019).

83. Brinkman, E. K., Chen, T., Amendola, M. & Van Steensel, B. Easy quantitative assessment of genome editing by sequence trace decomposition. *Nucleic Acids Res.* **42**, e168–e168 (2014).

84. Ritz, C., Baty, F., Streibig, J. C. & Gerhard, D. Dose-response analysis using R. *PLoS One* **10**, (2015).

85. Schindelin, J. *et al.* Fiji: An open-source platform for biological-image analysis. *Nature Methods* vol. 9 676–682 (2012).

5

Expanded View data

Table EV1, Dataset EV1, the Appendix as well as Source Data can be downloaded at https://www.embopress.org/doi/full/10.15252/emmm.202216001 (open access).
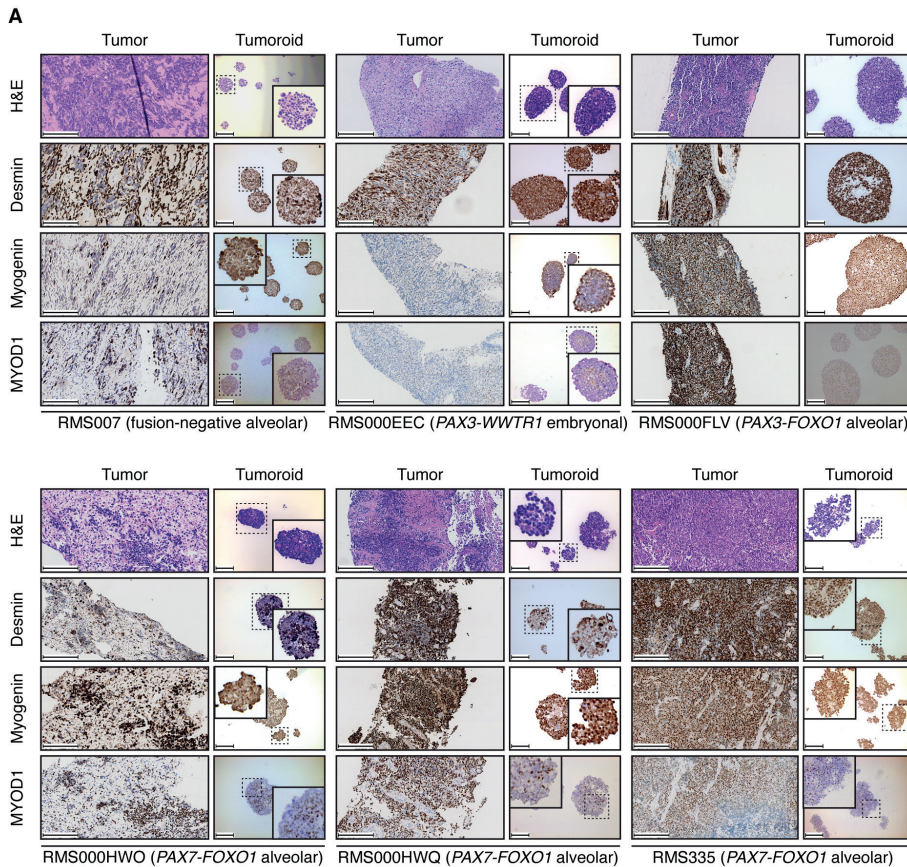
A

Fig. EV1. Morphological (via H&E) and immunohistochemical (IHC) comparison of RMS tumors and derived RMS tumoroid models shows retained marker protein (Desmin, Myogenin, and MYOD1) expression and cellular morphology. Scale bars equal 200 µm (RMS007, RMS000HWO, RMS335) or 100 µm (RMS000EEC, RMS000FLV, RMS000HWQ). For RMS tumoroid models that form small spheres a zoom-in image of a sphere was inserted.
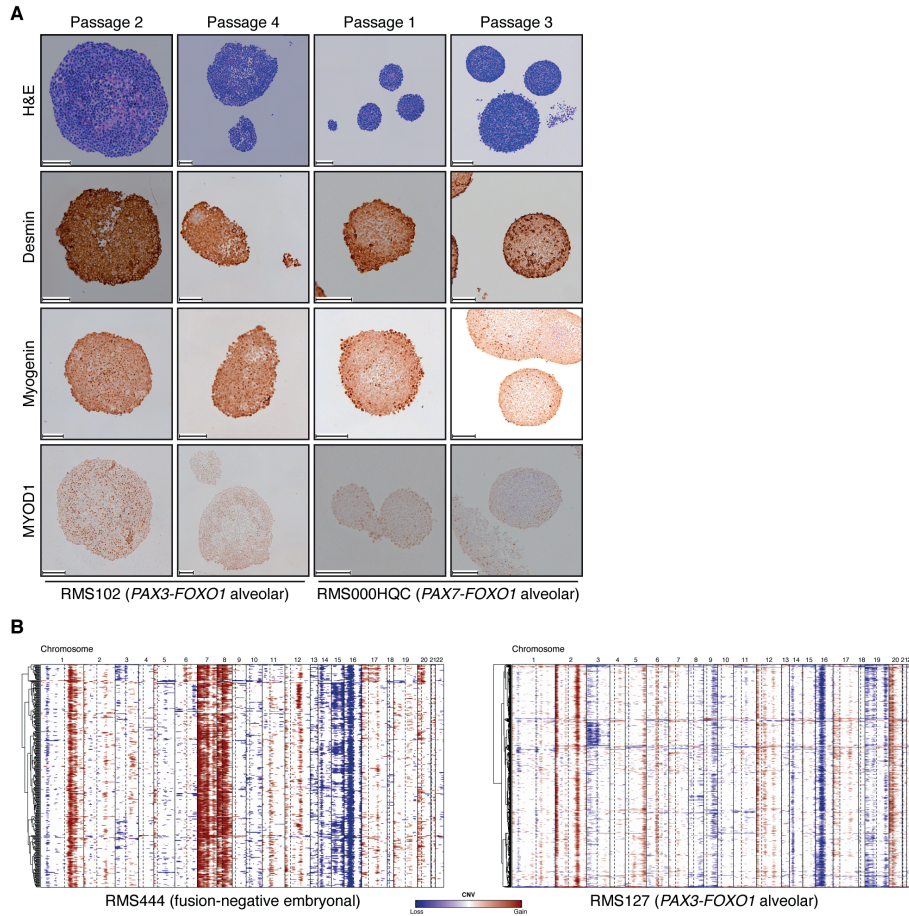
Fig. EV2. (**A**) H&E and immunohistochemistry (IHC) stainings of early passage RMS102 (passage 2 and passage 4 – passage 6 used for drug screening) and RMS000HQC (passage 1 and passage 3 – passage 5 used for drug screening). Scale bars equal 100 µm. (**B**) Heatmaps showing the inferred CNV profiles of single cells (y-axis) from the RMS127 and RMS444 tumoroid models, respectively. Chromosome arms are delineated by dotted lines where applicable.
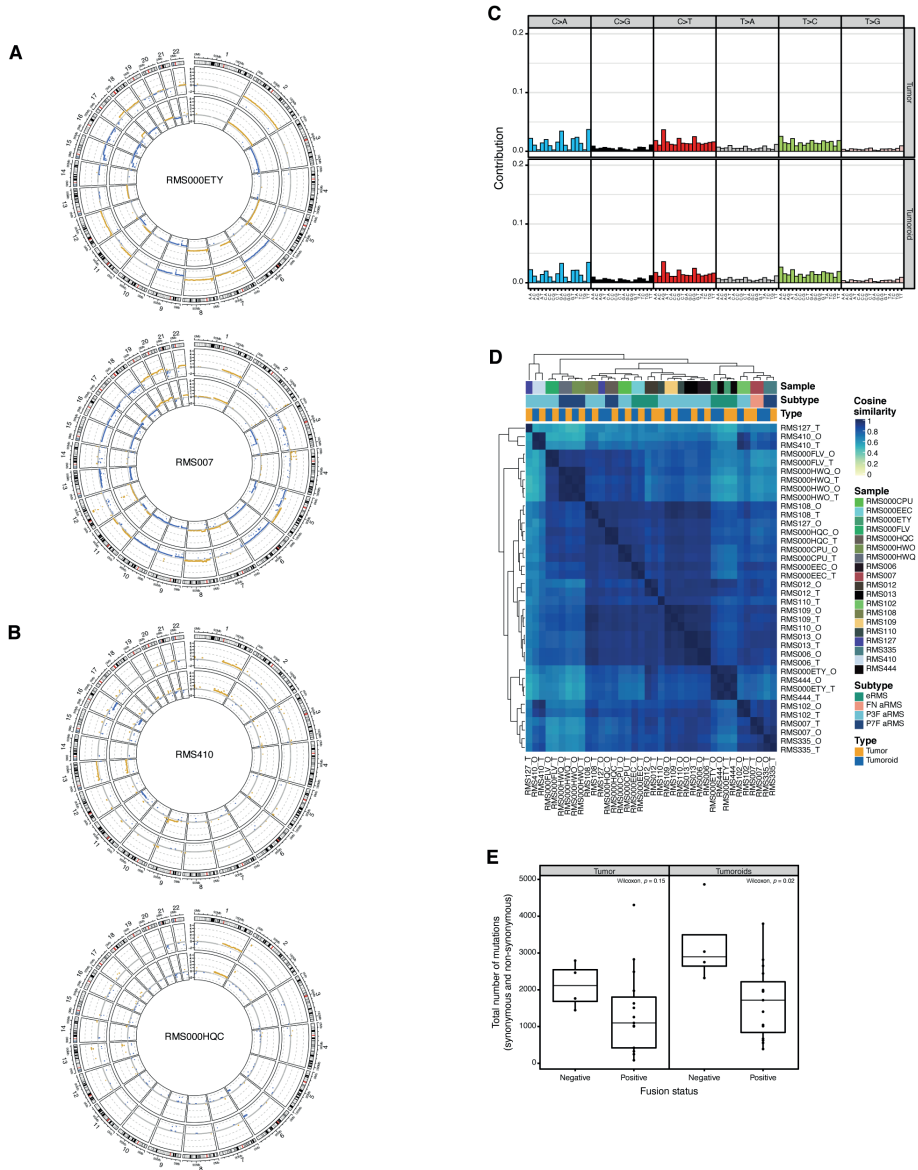
Fig. EV3. (**A**) Examples of circular copy number plots of fusion-negative RMS with embryonal (RMS000ETY) or alveolar (RMS007) histology. Outer circle depicts the tumoroid model, inner circle depicts the tumor. (**B**) Examples of circular copy number plots of fusion-positive RMS with alveolar histology and *PAX3-FOXO1* fusion (RMS410) or *PAX7-FOXO1* fusion (RMS000HQC). Outer circle depicts the tumoroid model, inner circle depicts the tumor. (**C**) Contribution of averaged single base substitution (SBS)

Fig. EV3. Continued

profiles for RMS tumors (upper row) and tumoroid models (lower row). (**D**) Clustered correlogram of SBS profiles detected in RMS tumors (T) and tumoroid models (O). (**E**) Comparison of total number of mutations (synonymous and non-synonymous) in RMS tumors and tumoroid models per fusion-type (fusion-negative n = 4, fusion-positive = 15, Wilcoxon test, p = 0.15 for tumors, p = 0.02 for tumoroid models). Data are shown as boxplots: The central line in the box represents the median; the upper and lower limits of the box represent the third and first quartile, respectively; the whiskers represent the minimum (bottom) and maximum (top) values excluding outliers, which are plotted as individual points.
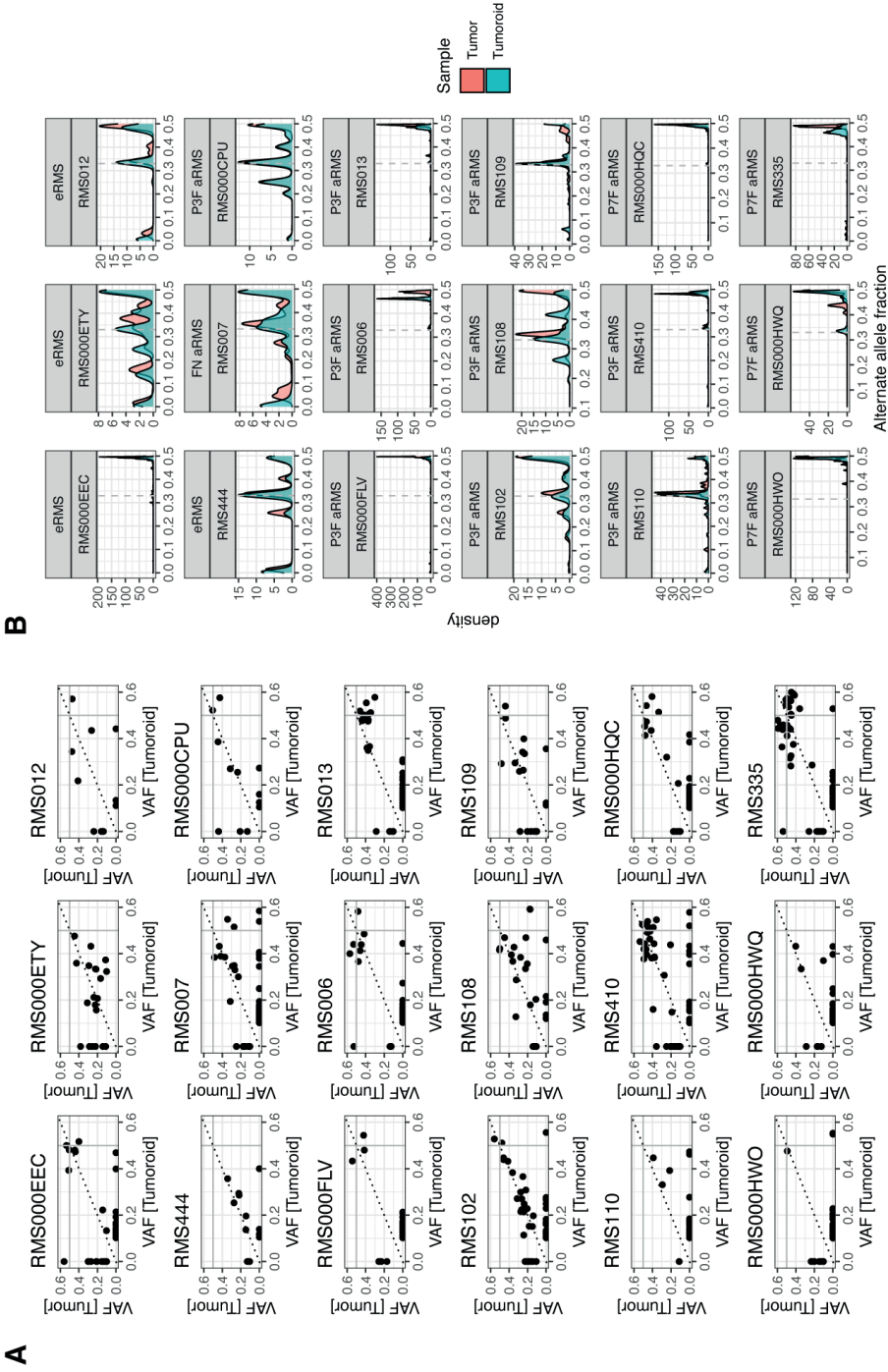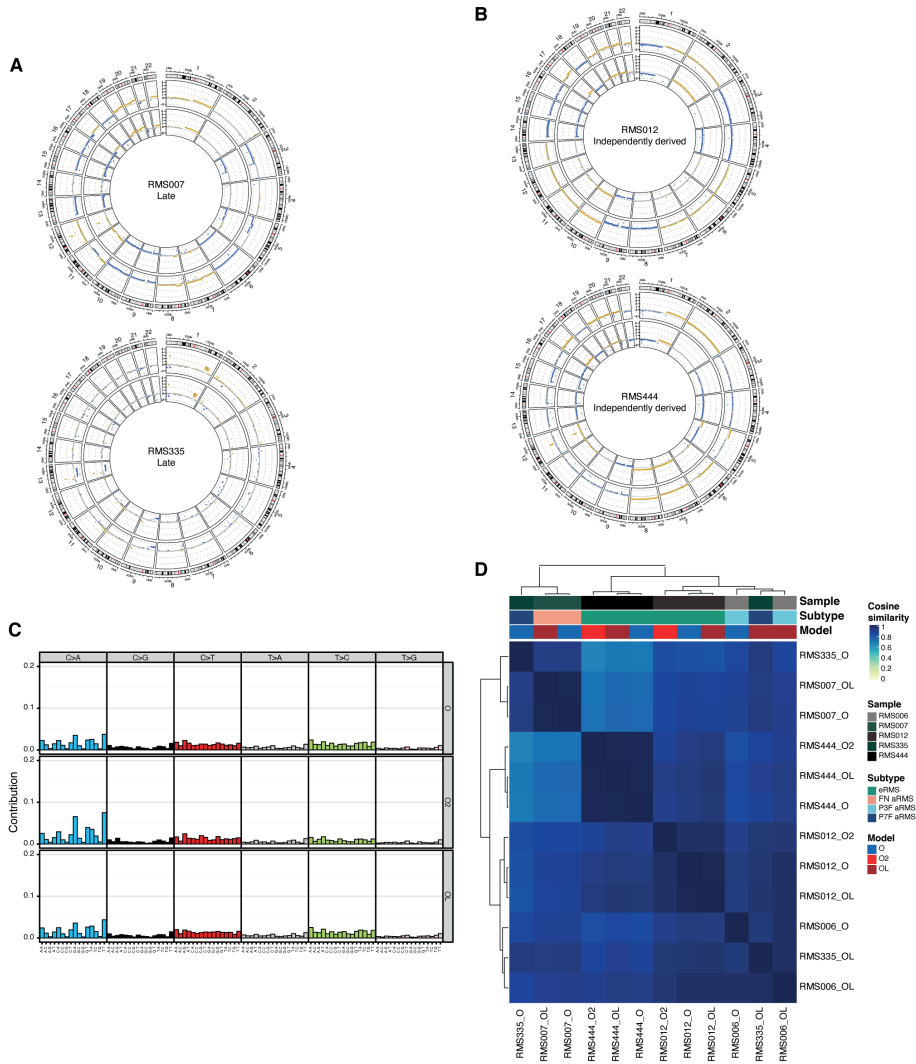
5

Fig. EV4. (A) Correlogram of variant allele fraction (VAF) of single-nucleotide variants (SNVs) detected in RMS tumors and derived tumoroid models per pair. **(B)** Density plots of alternate allele (B-allele) fraction over the entire genome per RMS tumor (red) and derived RMS tumoroid model (blue) per pair.

Fig. EV5. (**A**) Circular copy number plots of standard and late passage RMS tumoroid models of a fusion-negative alveolar (RMS007) and a *PAX7-FOXO1* positive alveolar (RMS335) RMS. Outer circle depicts the standard passage tumoroid, inner circle depicts the late passage tumoroid model. (**B**) Circular copy number plots of standard passage and independently derived RMS tumoroid models of two fusion-negative embryonal RMS (RMS012 and RMS444). Outer circle depicts the standard passage tumoroid, inner circle depicts the independently derived tumoroid model. (**C**) Contribution of averaged single base substitution (SBS) profiles for standard (O), independently derived (O2), and late passage (OL) RMS tumoroid models. (**D**) Clustered correlogram of SBS profiles detected in standard (O), independently derived (O2), and late passage (OL) RMS tumoroid models.
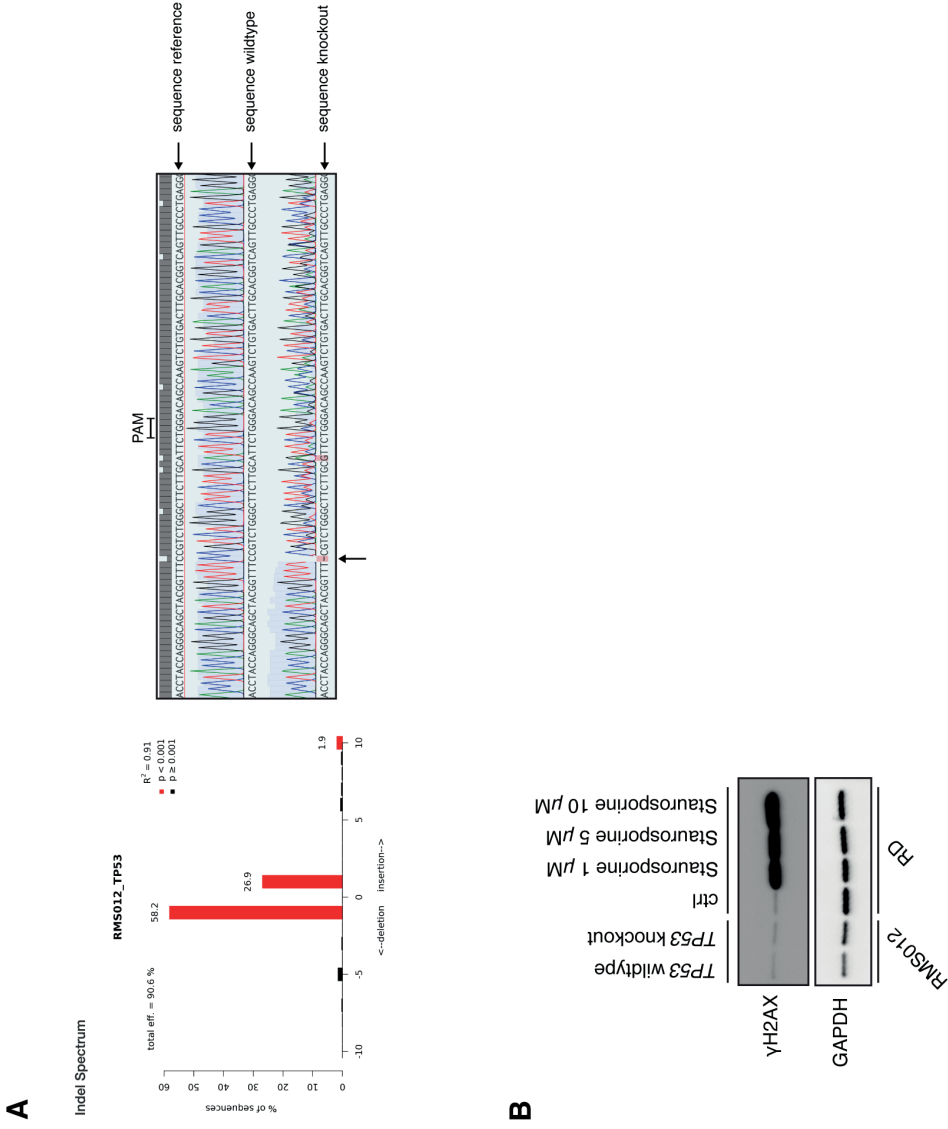
Fig. EV6. (A) Left panel: Inferred Indel Spectrum from Sanger sequencing using the TIDE tool (https://tide.nki.nl). Right panel: Sanger sequencing around Cas9 cut site (arrow at the bottom) in *TP53* gene. Protospacer Adjacent Motif (PAM) sequence indicated. (**B**) Western Blotting analysis of γH2AX (Ser-139) as proxy for DNA double-strand breaks in untreated RMS012 tumoroid cells (*TP53* wildtype and TP53 knockout). RMS cell line RD treated with staurosporine served as positive control while GAPDH served as loading control.
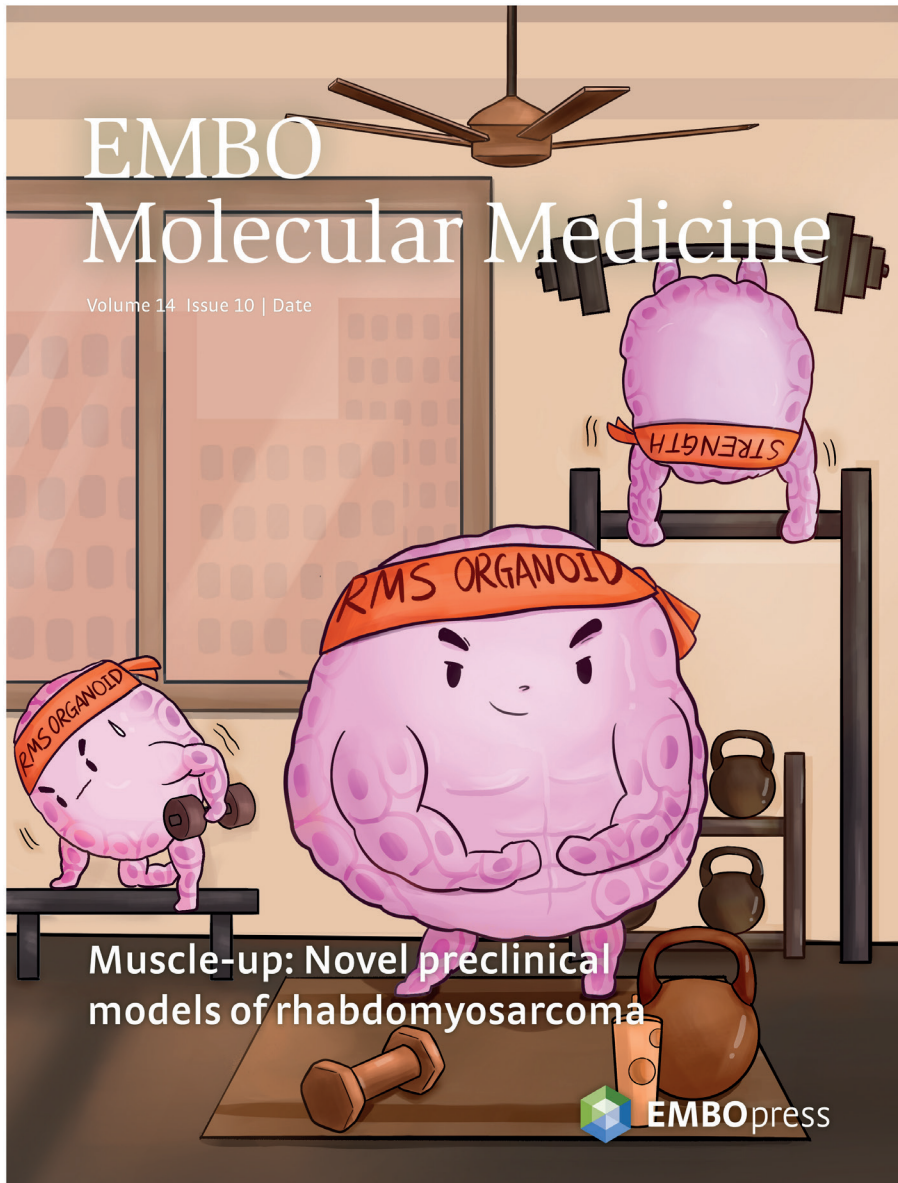
5

Muscle-up: Novel preclinical
models of rhabdomyosarcoma

EMBOpress

Single-cell transcriptomics reveals immune suppression and cell states predictive of patient outcomes in rhabdomyosarcoma

Jeff DeMartino[1,2,*], Michael T. Meister[1,2,*], Lindy Visser[1,*], Mariël Brok[1,2],
Marian J. A. Groot Koerkamp[1,2], Laura S. Hiemcke-Jiwa[1,3], Terezinha de Souza[1,2],
Johannes H. M. Merks[1], Frank C. P. Holstege[1], Thanasis Margaritis[1,#], Jarno Drost[1,2,#]

[1] Princess Máxima Center for Pediatric Oncology, Heidelberglaan 25, 3584 CS Utrecht,
The Netherlands.
[2] Oncode Institute, Heidelberglaan 25, 3584 CS Utrecht, The Netherlands.
[3] Department of Pathology, University Medical Center Utrecht, Utrecht, The Netherlands
* Equal contribution
# Co-correspondence

Abstract

Pediatric rhabdomyosarcoma (RMS) is a soft tissue malignancy of mesenchymal origin which is thought to arise as a consequence of derailed myogenic differentiation. Despite intensive treatment regimens, the prognosis for high-risk patients remains dismal. The cellular differentiation states underlying RMS and how these relate to patient outcomes remain largely elusive. Here, we used single-cell mRNA-sequencing to generate a transcriptomic atlas of RMS. Analysis of the RMS tumor niche revealed evidence of an immunosuppressive microenvironment. We also identified an interaction between NECTIN3 and TIGIT, specific to the more aggressive fusion-positive (FP) RMS subtype, as a putative cause of tumor-induced T-cell dysfunction. In malignant RMS cells we defined transcriptional programs reflective of normal myogenic differentiation. Furthermore, we showed that these cellular differentiation states are predictive of patient outcomes in both FP RMS and the more clinically homogeneous fusion-negative subtype. Our study reveals the potential of therapies targeting the immune microenvironment of RMS and suggests that assessing tumor differentiation states may enable a more refined risk stratification.

Introduction

Rhabdomyosarcoma (RMS) is the most commonly diagnosed soft tissue sarcoma (STS) in children and adolescents, accounting for approximately 3.5% of all pediatric malignancies [1]. Several characteristics, including expression of the myogenic regulatory transcription factors MYOD1 and MYOG [2] and the presence of rhabdomyoblasts [3] (cells reminiscent of terminally differentiating myocytes) point to RMS being the result of impaired skeletal muscle myogenesis. However, the disease may also arise at body sites devoid of skeletal muscle, and RMS models of non-myogenic origin have been described [4]. Despite intense, multimodal treatment strategies, outcomes remain dismal for patients with high-risk or metastatic disease, the latter of which exhibits a long-term overall survival rate (OS) of approximately 30% [5]. This emphasizes the need to improve our understanding of RMS tumor biology to enable the development of novel therapeutic approaches.

Historically, RMS has been divided into two main subtypes, alveolar and embryonal, based on histological features of tumors [6]. However, recent work has shown that the molecular classification as either fusion positive (FP) or fusion negative (FN) is a more powerful prognostic indicator [7,8]. FP RMS is characterized by recurrent chromosomal translocations resulting in the expression of a chimeric fusion protein containing the DNA binding domains of either PAX3 or PAX7, both key transcriptional regulators of normal myogenesis [9], coupled to a strong transactivation domain, most often that of FOXO1[10,11]. The genetic lesions driving FN RMS, on the other hand, are diverse and may include mutations in signal transduction pathways (especially RAS and PI3K), cell cycle regulators and the P53 pathway, among others [12]. Notably, FP RMS carries a significantly worse prognosis than FN RMS, and is more often metastatic at diagnosis [8].

Beyond the inter-tumoral genetic heterogeneity characteristic of RMS, it has been recognized that there exists a degree of heterogeneity within tumors, as exemplified by the diversity in cellular morphology [13] and variation in immunohistochemical staining for myogenic markers [14]. However, the characteristics and clinical implications of this heterogeneity remain unclear. Additionally, the composition of the tumor microenvironment (TME) and the

6

interplay between malignant cells and the TME have not been comprehensively profiled. Here, we compile a single-cell transcriptomic atlas comprising both FN and FP RMS and find distinct differences in cellular composition and single-cell differentiation states between and within subtypes that relate to clinical outcomes and suggest potential immunotherapeutic interventions.

Results

A single-cell atlas of pediatric RMS tumors

We implemented a protocol for performing plate-based single-cell mRNA-sequencing [15] (SORT-seq) on viably frozen RMS tumor samples (Fig. 1a and Extended Data Fig. 1a). Opting for a plate-based method allowed for the generation of high-quality single-cell transcriptomes from samples with low viability (including pre-treated samples) or where limited material was available (e.g., small needle biopsies). From our cohort of 19 RMS samples, encompassing the major molecular and histological subtypes (FP, FN, alveolar and embryonal, Fig. 1b,c and Supplementary Table S1), we obtained 7,364 high quality single-cell transcriptomes (median of 420 per sample) which passed quality thresholds.

To distinguish RMS cells from non-malignant cell types comprising the TME, two complementary approaches were employed. First, the similarity between each single-cell transcriptome and a reference collection of bulk transcriptomes derived from healthy cell types and RMS tumors was assessed using *SingleR* [16] (see Methods). Clustering of the resulting similarity scores revealed a clear distinction between cells with a high correspondence to bulk RMS tumors (malignant cells) and those which resembled one of several immune or stromal cell types (Extended Data Fig. 1b). Second, single-cell copy number variation (CNV) profiles were inferred and clustered on a per tumor basis. In all tumors, cells harboring coherent whole and sub-chromosomal CNVs (malignant cells) could be distinguished from those which appear to be copy neutral (Extended Data Fig. 2). In general, single-cell derived CNV profiles were highly similar to those defined by DNA sequencing of bulk tumor samples (Extended Data Fig. 2). Cells classified as "malignant" or "normal" using both methods were retained, while divergently classified cells were excluded from further analysis. The

Single-cell transcriptomics reveals immune suppression
and cell states predictive of patient outcomes in rhabdomyosarcoma

6

median percentage of malignant cells per sample was 56%, though this varied widely (2 to 97%), and did not differ significantly between molecular subtypes (Fig. 1f and Extended Data Fig. 1c). Putative malignant cells expressed high levels of classical RMS marker genes *DES*, *MYOD1* and *MYOG*, as expected (Fig. 1e). *SingleR* cell-type similarity scores and the expression of known marker genes were used to discern the identities of non-malignant cells (Fig. 1e and Extended Data Fig. 1b). As with the overall percentage of malignant cells, the proportion of each non-malignant cell type varied extensively between tumors but did not differ significantly based on fusion status (Fig. 1f and Extended Data Fig. 1c). Projecting the classified single-cell transcriptomes in Uniform Manifold Approximation and Projection (UMAP) space revealed that inter-tumoral heterogeneity and molecular subtype classification (FN or FP) drove the clustering of malignant cells, while non-malignant cells clustered by cell type (Fig. 1d), as has previously been described for other tumor entities [17–20].

Characterization of the RMS microenvironment reveals general and subtype-specific immune dysfunction

To explore the composition and functional characteristics of tumor-infiltrating immune cells, graph-based clustering was performed on the myeloid and T/NK compartments (Fig. 2b,d). Examination of marker gene expression in the myeloid clusters revealed the presence of undifferentiated (M0) and differentiated (Mq) macrophages, as well as conventional (cDC) and plasmacytoid (pDC) dendritic cells (Fig. 2b and Extended Data Fig. 3a). Scoring differentiated macrophages for M1/M2-specific gene signatures [21] indicated that they existed predominantly in the M2 state (Fig. 2c), which has been associated with several pro-tumorigenic functions including the suppression of inflammation and promotion of angiogenesis [22]. Among the T/NK cell clusters, several subtypes could be discerned including naïve and gamma delta (gd) T cells, regulatory T cells (Tregs), cytotoxic (CD8+) T cells and multiple subtypes of CD4+ T helper cells (IL7R+ and ISG+) (Fig. 2d and Extended Data Fig. 3b). IHC for immune cell markers confirmed the presence of infiltrating T cells in RMS tissues (Extended Data Fig. 1d). Interestingly, interferon-stimulated T helper cells (ISG+) were found almost exclusively in FN tumors, which may reflect a higher degree of immunogenicity (Extended Data Fig. 3b).
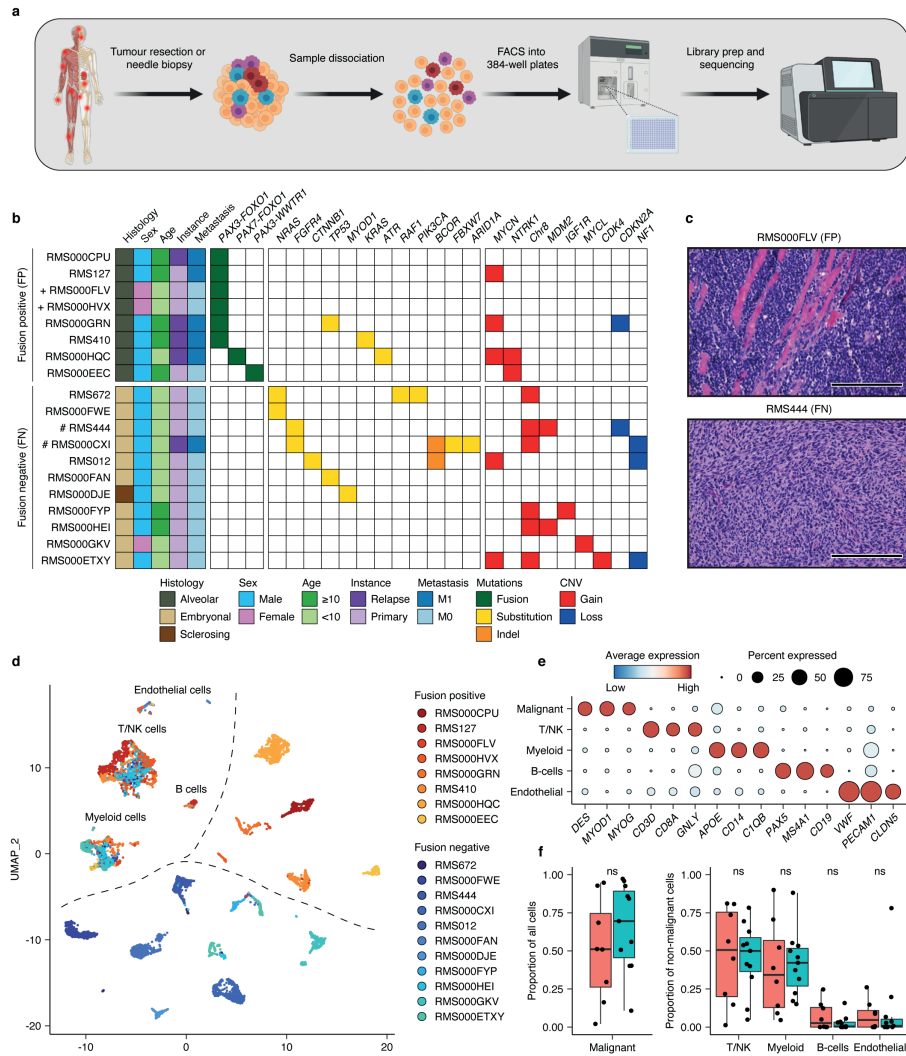
Fig. 1. Single-cell transcriptomic atlas of RMS tumors. **a,** Schematic representation of the sample processing workflow used to generate scRNA-seq data. Created with BioRender. **b**, Overview of RMS sample cohort, including patient clinical characteristics, as well as a summary of relevant mutations and copy number variants (CNV) in tumors, defined using bulk DNA sequencing. (+) and (#) indicate independent samples derived from the same patient. **c**, Representative hematoxylin and eosin (H&E) stained tumor sections depicting the two major RMS histological subtypes (alveolar and embryonal) in this cohort. Scale bars are equivalent to 200 μm. **d**, UMAP projection of single-cell RMS transcriptomes (n = 7,364) coloured by sample. **e**, Dot plot depicting the average scaled gene expression of selected marker genes for each annotated cell type (dot colour). Dot size corresponds to the percentage of cells expressing each gene. **f**, Boxplots

Fig. 1. Continued

comparing the proportion of malignant cells (left panel) and of each non-malignant cell type (right panel) between molecular subtypes. ns = not significant ($p > 0.05$, Student's t-test).

Within T cell subgroups, the expression of several genes encoding molecules associated with immune dysfunction and the suppression of immune responses [23] was observed, including *LAG3* and *PDCD1* (PD1) in CD8+ T cells, *CTLA4* and *TIGIT* in Tregs and *HAVCR2* in Tregs and NK cells (Fig. 2f). Strikingly, gene set enrichment analysis (GSEA) comparing CD8+ T cells between RMS subtypes indicated that dysfunction was more prevalent in FP samples, which were enriched for gene sets related to PD-1 signaling, oxidative phosphorylation and T cell exhaustion, while cells from FN tumors were enriched for interferon response and stimulation signatures (Fig. 2g). To define putative cell-cell interactions regulating immune dysfunction, we used *CellChat* [24] to model ligand-receptor interactions between malignant cells, per subtype, and cell types within the TME. This analysis highlighted a putative interaction specific to FP tumors between NECTIN3 expressed on malignant cells, and the TIGIT receptor on Tregs and CD8+ T cells (Extended Data Fig. 3c). The specificity of this interaction was due to the significantly higher expression of *NECTIN3* in FP tumor cells, while the expression of *TIGIT* in Tregs and CD8+ T cells was comparable between subtypes (Fig. 2h). Supporting this finding, immunofluorescence microscopy (IF) of tumor tissues revealed the presence of TIGIT-positive cells in both subtypes, while a more prevalent staining pattern of NECTIN3 was observed in FP RMS (Fig. 2i). Taken together, analysis of the TME in RMS highlighted evidence of general immune dysfunction, indicated by the prevalence of M2 macrophages, as well as a putative FP-specific T-cell exhaustion phenotype which may be partly regulated, by the interaction between NECTIN3 and TIGIT.
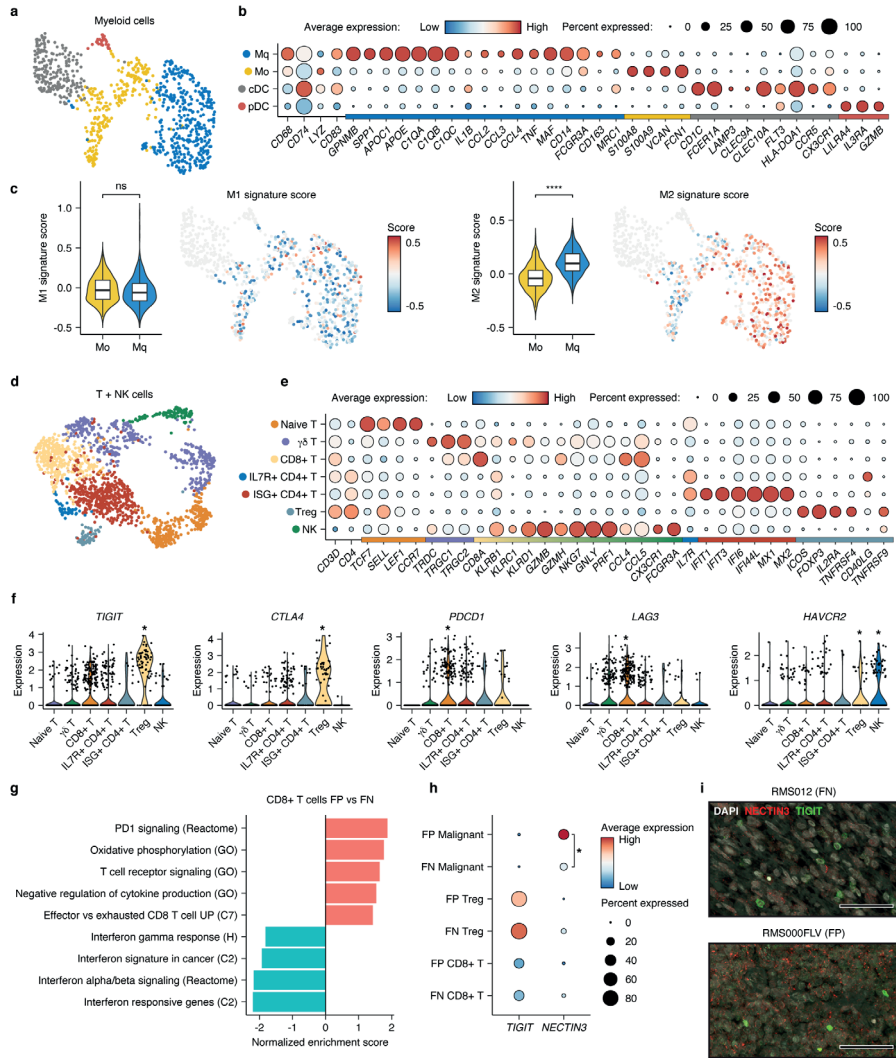
6

Fig. 2. Characterization of the RMS immune microenvironment. a, UMAP projection of myeloid cells, coloured by cluster assignment. **b**, Dot plot depicting the average expression of selected cell type-specific genes. Dot size corresponds to the percentage of cells expressing each marker. Colour bar on the x-axis indicates for which cluster each gene is specific to. **c**, Violin and UMAP plots showing the distribution of M1 (left panel) and M2 (right panel) signature scores in undifferentiated (M0) and differentiated (MF) macrophages. ns = not significant ($p > 0.05$, Student's t-test), **** indicates $p < 0.0001$ (Student's t-test). Non-macrophage cells are coloured grey on UMAP plots. **d**, UMAP projection of T and NK cells, coloured by cluster assignment. **e**, Dot plot depicting the average expression of selected cell type-

Fig. 2. Continued

specific genes. Dot size corresponds to the percentage of cells expressing each marker. Colour bar on the x-axis indicates the cluster specificity for each gene. **f**, Violin plots showing the expression of selected immune checkpoint molecules within T/NK subsets. * Indicates differential expression (Log2 FC > 0.25 and $p < 0.05$, Wilcoxon rank sum test). **g**, Normalized enrichment scores (NES) of selected gene sets, as determined by gene set enrichment analysis (GSEA) comparing CD8+ T cells between RMS subtypes. Codes in parenthesis indicate the database from which the gene set derives (H, C2 and C7 correspond to MSigDB collections). **h**, Dot plot depicting the average expression of the TIGIT and NECTIN3 genes in selected cell types (per RMS subtype). Dot size corresponds to the percentage of cells expressing each marker. * Indicates differential expression (LogFC > 0.25 and $p < 0.05$, Wilcoxon rank sum test). i, Representative immunofluorescence (IF) microscopy images depicting the expression of *TIGIT* (green) and *NECTIN3* (red), along with DAPI counterstaining (grey), in RMS tissue sections from FN and FP tumors. Scale bars equivalent to 50 μm.

Malignant cell states in RMS mirror normal myogenic differentiation

While it has been proposed that RMS tumors arise as a result of myogenic differentiation gone awry, the identification of the precise developmental origin(s) of RMS remains an active area of investigation [25]. To place RMS tumor cells within the context of normal myogenic differentiation, a series of logistic regression models were trained, as previously described [26], to predict the similarity of malignant single-cell transcriptomes to the main cell types defined by a recently published single-cell atlas of human pre- and post-natal myogenesis [27]. This analysis showed that, on average, FN RMS cells resembled both myogenic progenitors and myogenic mesenchymal cells, while FP cells most closely corresponded to committed myoblasts (Extended Data Fig. 4a). This is in line with the notion that FN tumors often exhibit an undifferentiated "embryonal" histology, while FP more widely express the key myogenic regulatory factors *MYOD1* and *MYOG* [6] (Fig. 1b,c and Extended Data Fig. 4b). However, when analyzing at single-cell resolution we found that individual cells from each subtype and tumor spanned the spectrum of myogenic differentiation, indicating that there exists large-scale intra-, as well as inter-tumoral heterogeneity in cellular differentiation states (Extended Data Fig. 4a).

NMF-defined differentiation trajectories in FN RMS reflect early myogenesis

To probe the prospective sources of heterogeneity, non-negative matrix factorization (NMF) was applied, independently per molecular subtype, to define the underlying transcriptional programs active in malignant cells from each of the tumors in our RMS scRNA-seq cohort (see Methods). In FN RMS samples, this analysis revealed three clusters of highly correlated transcriptional programs, which we merged into three meta-programs (Fig. 3a-left panel). Notably, the constituent programs underlying each meta-program were derived from several tumor samples, indicating that clustering was not driven by inter-tumoral heterogeneity. To interpret the biological relevance of each meta-program, we assessed the expression of their top weighted genes (Fig. 3a-right panel and Supplementary Table S2). The first program, which we termed "mesenchymal", was enriched for genes related to extracellular matrix (ECM) organization, including *FN1*, *TGFBI* and several collagen-encoding genes, among others (Extended Data Fig. 5a). The second program, referred to as the "progenitor-like" program included genes expressed during early myogenesis [27], such as *FGFR4* and *GPC3*, as well as markers of proliferation, including *MKI67* and *TOP2A*. Finally, the "myogenic" program, was characterized by genes involved in the regulation of myogenic differentiation, including *MYOD1*, *MYOG*, *MEF2C* and *CDH15* as well as genes encoding structural and functional components of terminally differentiated striated muscle, such as *TTN* and *CKM*. Scoring FN cells for each meta-program revealed that expression of the myogenic and mesenchymal programs was mutually exclusive, while expression of the highly proliferative progenitor-like state was restricted to cells which scored low for the mesenchymal as well as the myogenic programs (Fig. 3b). These patterns were corroborated using a dataset from a recently published independent single-nucleus RNA-seq cohort of RMS tumors [28] (Extended Data Fig. 5b).

Meta-program scores were then used to define the discrete "state" of each cell. This analysis revealed a high degree of variation between tumors in the distribution of cell states (Fig. 3c). Interestingly, some tumors (e.g., RMS012 and RMS000HEI) were dominated by mesenchymal-state cells, while others (e.g., RMS444 and RMS000FWE) almost exclusively contained progenitor-like-state cells. RNA fluorescence *in-situ* hybridization (RNA-FISH) was

used to validate the presence of each cell-state and the distribution of the progenitor-like and mesenchymal states within individual tumors (Fig. 3d and Extended Data Fig. 5c). To investigate the hierarchy of cell states in FN RMS, the data were modelled as a differentiation trajectory by projecting single-cell transcriptomes in diffusion maps space and using pseudotime and RNA velocity to assess directionality (Fig. 3e and Methods). This analysis suggested that cells transition from the highly proliferative progenitor-like state into the more differentiated mesenchymal or myogenic states. Variation in differentiation status was also evident when comparing the malignant cell-state scores with the similarity scores to normal myogenic cell types. This showed that the progenitor-like score correlated strongly with undifferentiated myogenic progenitors, while the mesenchymal and myogenic scores with more differentiated cell types, namely myogenic mesenchymal cells, and myoblasts/myocytes, respectively (Fig. 3f). Together, these data show that transcriptional cell-states in FN RMS cells can be organized in a differentiation trajectory mirroring that of early myogenic differentiation, where progenitor-like cells can give rise to terminally differentiating myoblasts, or those progressing toward myogenic mesenchymal cells.

Differentiation states in FP RMS mirror skeletal muscle regeneration

Extending the NMF analysis to FP RMS also revealed three meta-programs, as defined by correlating transcriptional programs across tumor samples (Fig. 4a-left panel). The proliferative program consisted almost entirely of genes involved in mitotic cell processes, including *MKI67*, *TOP2A* and *CENPE*, among others (Extended Data Fig. 6a). As expected, nearly all cells inferred to be in S or G2/M phases scored high for this meta-program (Fig. 4a-right panel and Supplementary Table S3). The myogenic program was marked by expression of terminal myogenic differentiation genes, such as *MYOG*, *TTN* and *CKB*. Finally, the program termed "satellite cell-like" (SC-like) was characterized by expression of the *NOTCH3* receptor gene, Notch pathway targets, including *HEY1* and *HES1*, and genes encoding type V and VI collagens. These genes are known to play roles in the context-specific regulation of quiescence, self-renewal, and activation in muscle-resident satellite cells [29,30]. Scoring single-cells for each meta-program revealed a

mutually exclusive relationship between the myogenic and SC-like programs, while the proliferative program did not correlate with either and was, in general, restricted to cells scoring low for the two former programs (Fig. 4b). Again, the relationship between meta-program scores was confirmed in an independent dataset (Extended Data Fig 6b).
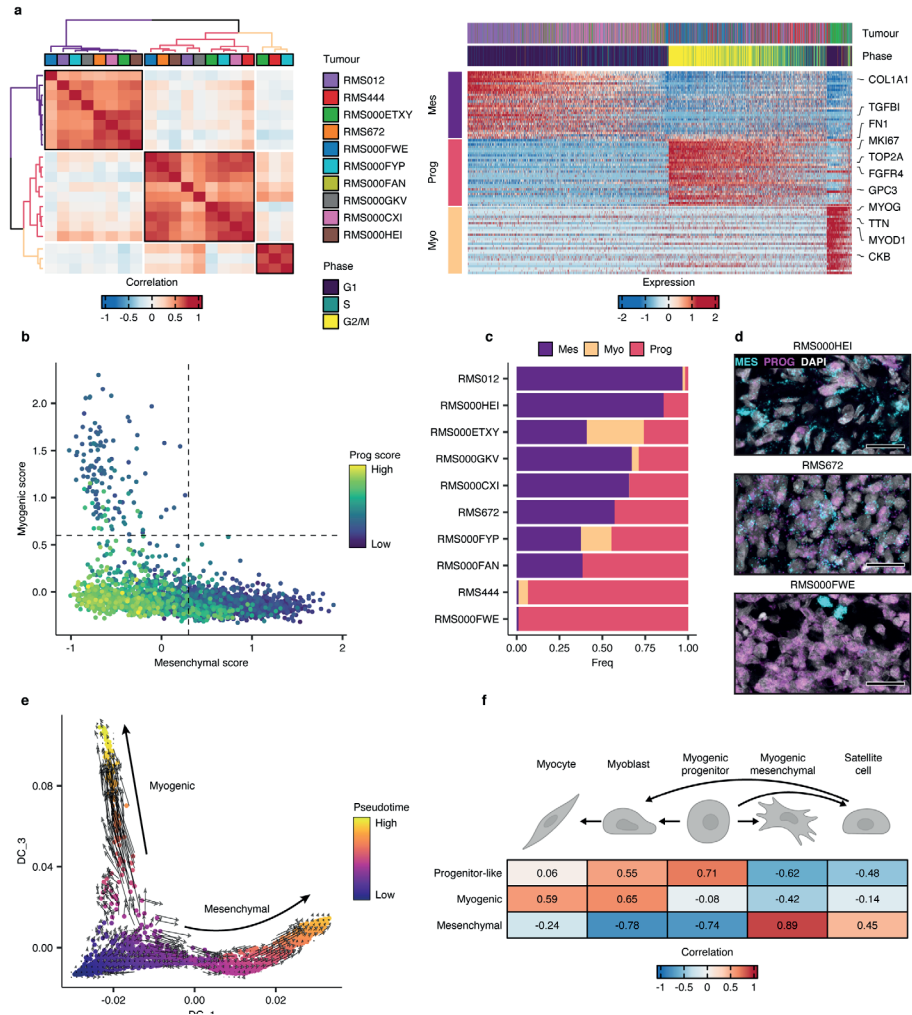

Fig. 3. NMF defines malignant cell states in FN RMS tumors. a, Left panel: Heatmap showing the pairwise Pearson correlations between all NMF-defined transcriptional programs in FN samples. The tumor sample from which each transcriptional program derived is shown in the colour bar. Meta-program clusters are delineated by black boxes

Fig. 3. Continued

and colouring of the dendrograms. Right panel: Scaled expression of the top 30 genes per meta-program across all FN cells. The corresponding tumor sample and inferred cell cycle phase of each cell are displayed in the top annotation track. Representative genes from each meta-program are labelled. **b**, Scatterplot depicting the mesenchymal (x-axis), myogenic (y-axis) and proliferative (point colour) meta-program scores. Dotted lines correspond to the cut-offs used to define discrete cell states. **c**, Proportion of cells within each discrete state, per FN tumor. **d**, Representative RNA fluorescence in-situ hybridization (RNA-FISH) images depicting the expression of mesenchymal (MES = *TGFBI*) and progenitor-like (PROG = *FGFR4*) cell state marker genes in FN tissue samples. DAPI counterstaining shown in grey. Scale bars equivalent to 25 µm. **e**, Diffusion maps projection of FN RMS single cells, coloured by pseudotime value, overlaid with the RNA velocity vector field. **f**, Heatmap depicting the Pearson correlations between cell-state scores, and the logistic regression-defined similarity scores (logits) for each normal myogenic cell type. Myogenic differentiation schematic was created with BioRender.

As with the FN samples, there was a high degree of variation in discrete cell-state proportions between tumors, particularly among the proliferative and SC-like states (Fig. 4c). The expression of each meta-program, as well as the mutual exclusivity of the myogenic and SC-like programs was validated using RNA-FISH (Fig. 4d). Comparisons between meta-program scores and the logistic regression-defined cell similarity scores showed that the myogenic program correlated strongly with cell types along the terminal differentiation trajectory (myoblasts and myocytes) while the SC-like program was comparable to post-natal satellite-cells (Fig. 4e). Though the proliferative program score did not strongly correlate with any of the normal myogenic cell types, supporting the notion that this program was indicative only of cell cycle activity, most cells within the proliferative state most closely resembled myoblasts (Extended Data Fig. 6c). Trajectory inference indicated that cells scoring high for the myogenic or SC-like programs lay at opposite ends of the differentiation continuum, while the proliferative cells appeared as an undifferentiated intermediate state (Fig. 4f). In this case, however, the RNA velocity results did not definitively imply a strict directionality of the trajectory (Fig. 4e). Altogether, these data showed that the shared cell-state heterogeneity in FP RMS forms a differentiation trajectory reminiscent of that underlying skeletal muscle regeneration, where SC-like cells connect to cells resembling proliferative, undifferentiated myoblasts, which may give rise to (or derive from) cell bearing similarity to terminally differentiating myoblasts/myocytes.

Malignant cell states are predictive of patient outcomes

Taken together, results from the analysis of NMF-defined transcriptional programs allowed us to propose a unified model of cell states and differentiation trajectories in FN and FP RMS tumors (Fig. 5a). In FN tumors,
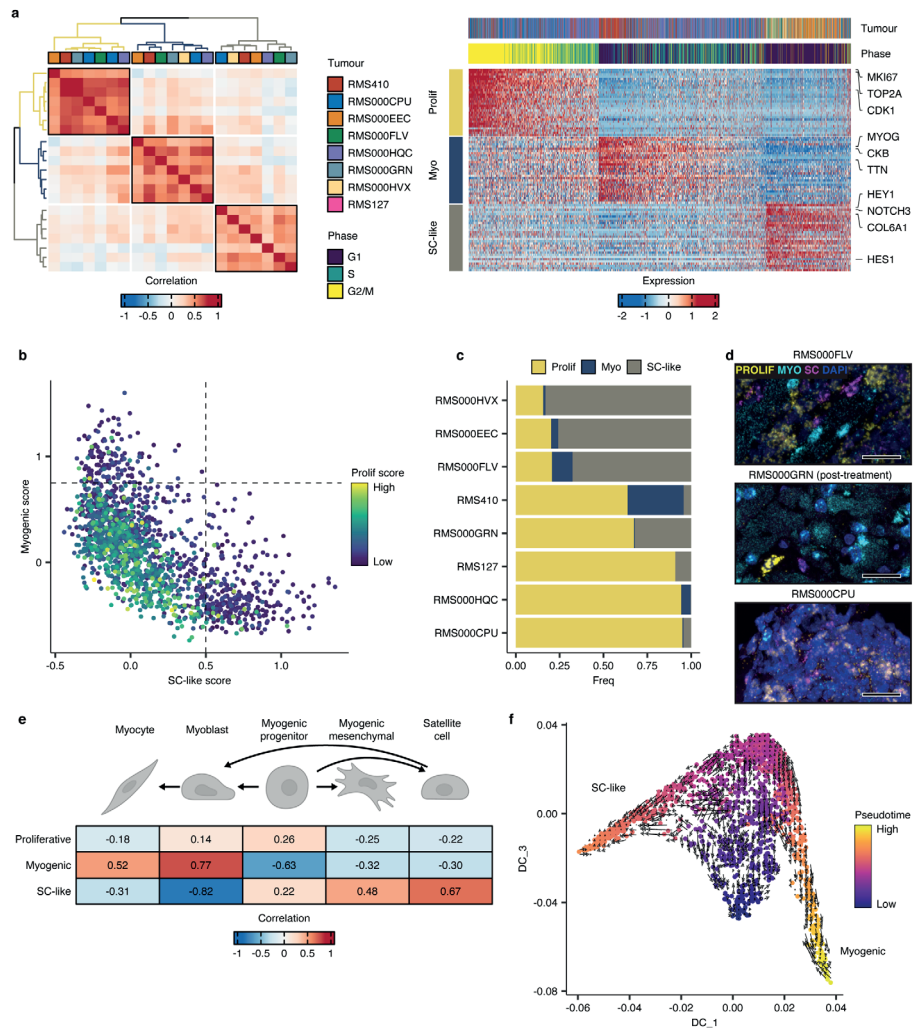

Fig. 4. Cell states in FP RMS tumors mirror skeletal muscle myogenic differentiation.
a, Left panel: Heatmap showing the pairwise Pearson correlations between all NMF-defined transcriptional programs in FP samples. The tumor sample from which each transcriptional program derived is shown in the colour bar. Meta-program clusters are delineated by black boxes and colouring of the dendrograms. Right panel: Scaled

Fig. 4. Continued

expression of the top 30 genes per meta-program across all FP cells. The corresponding tumor sample and inferred cell cycle phase of each cell are displayed in the top annotation bar. Representative genes from each meta-program are labelled. **b**, Scatterplot depicting per cell meta-program scores. Dotted lines correspond to the cut-offs used to define discrete cell states. **c**, Proportion of cells within each discrete state, per FP tumor. **d**, Representative RNA fluorescence *in-situ* hybridization (RNA-FISH) images depicting the expression of satellite cell-like (magenta, SC = *NOTCH3*), myogenic (cyan, MYO = *TTN*) and proliferative (yellow, PROLIF = *MKI67*) cell state marker genes in FP tissue samples. DAPI counterstaining shown in blue. Scale bars equivalent to 25 μm. **e**, Heatmap depicting the Pearson correlations between FP cell-state scores, and the logistic regression-defined similarity scores (logits) for each normal myogenic cell type. **f**, Diffusion maps projection of FP RMS single cells, coloured by pseudotime value, overlaid with the RNA velocity vector field. Myogenic differentiation schematic was created with BioRender.

6

highly proliferative cells with characteristics of early myogenic progenitors (progenitor-like) seem to give rise to cells which resemble either of two more differentiated types: myogenic mesenchymal cells (mesenchymal) or terminally differentiating myoblasts/myocytes (myogenic). On the other hand, in FP tumors, highly proliferative cells resembling committed myoblasts (proliferative) are an intermediate between cells closely resembling differentiating myocytes (myogenic), or post-natal muscle resident satellite cells (SC-like). To investigate whether the differentiation state of RMS tumors affects their clinical behavior, a published cohort of bulk tumor gene expression profiles [8] was scored for each meta-program. Strikingly, FN RMS patients whose tumors had a high differentiation score (mesenchymal + myogenic) exhibited a significantly better OS probability than those with a low score ($p = 0.00069$, Fig. 5b-left panel). This result was particularly intriguing, as neither cell-state program was predictive of outcomes on its own (Extended Data Fig. 7a,b). Conversely, a high score for the undifferentiated progenitor-like program was indicative of significantly worse OS than FN tumors with a low score ($p = 0.035$, Fig. 5b-right panel). In FP RMS patients, high expression of the SC-like program was associated with extended OS ($p = 0.017$), while a high proliferative score was indicative of shorter OS ($p = 0.029$, Fig. 5c). Differential expression of the myogenic program in FP tumors was not predictive of patient survival (Extended Data Fig. 7c). These data show for the first time that, in both RMS subtypes, tumors with higher proportions of cells in more differentiated states exhibit better outcomes than those with high levels of proliferative, less well differentiated cells.
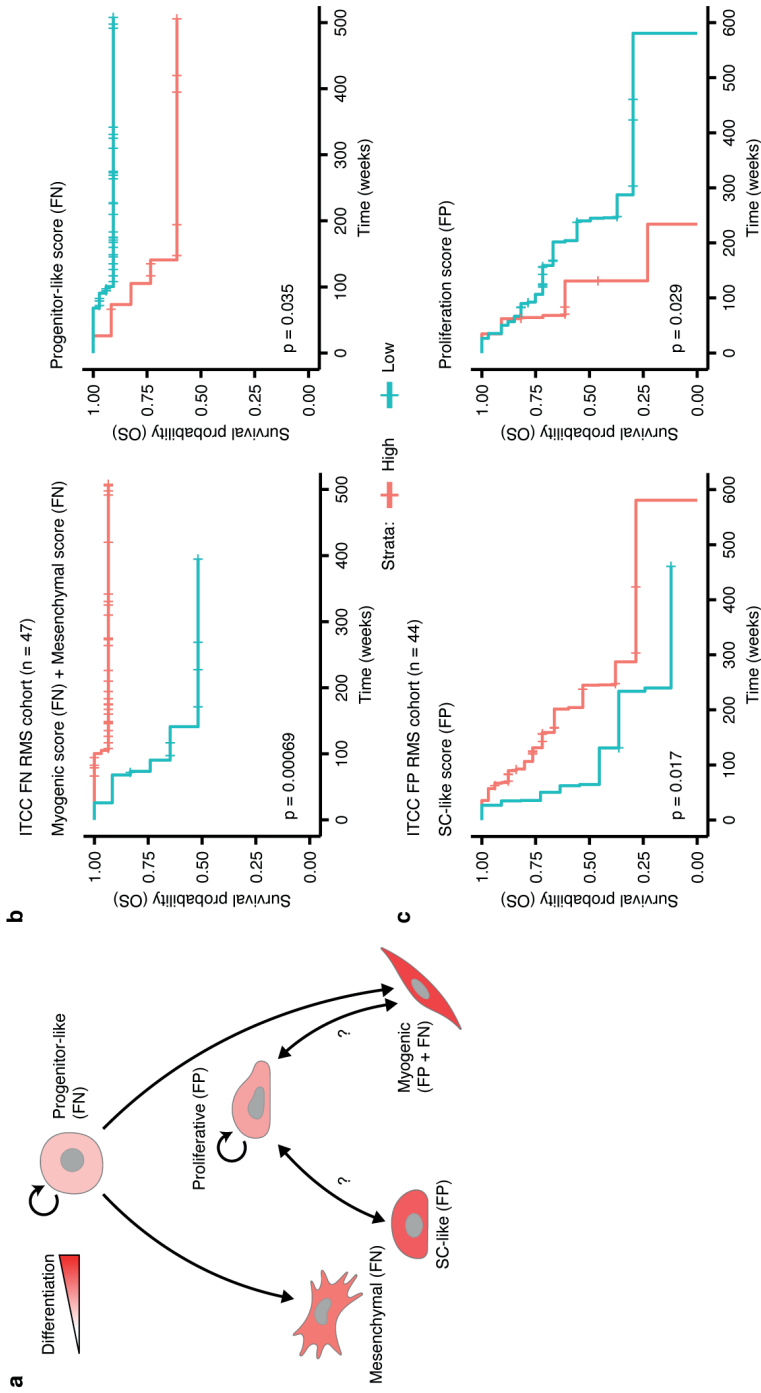
Fig. 5. Malignant cell states are predictive of patient outcomes. a, Schematic representation of differentiation trajectories in RMS. Created with BioRender. **b,c**, Kaplan-Meier plots showing the overall survival probabilities of (**b**) FN or (**c**) FP patients divided into high (red strata) or low (blue strata) groups based on their cell state scores (stated in the title of each plot panels). Log rank test was used to calculate p values between high and low scoring groups.

Discussion

We generated a single-cell transcriptomic atlas of RMS tumors, detailing cell states of both malignant cells and those constituting the TME. In our investigation of the TME, we found that among differentiated macrophages in both RMS subtypes, the immunosuppressive, pro-tumor M2-type was predominant. This result differs from the findings in two recent publications, which found a roughly balanced proportion of M1 and M2 macrophages in both RMS subtypes [31,32]. This deviation may be due to the fact that in both studies, single markers were used to delineate M1 and M2-type macrophages (CD68 and CD163, respectively), while the analysis presented here relied on multi-gene signatures which may be more robust in characterizing cell states. We also described, for the first time, a putative interaction between FP tumor cells expressing NECTIN3 and the TIGIT receptor on Tregs and NK cells, which we validated using immunofluorescence staining of patient tissue samples. This interaction may result in the suppression of anti-tumor immune responses through several mechanisms, as has been described in other malignancies [33]. As such, targeting this interaction could represent an opportunity to sensitize FP RMS tumors to immune-mediated killing through blocking of the TIGIT receptor, an approach which is currently being clinically evaluated for other tumor types [33]. Overall, we observed a higher proportion of T/NK cells, relative to myeloid cells (~1:1), than has been previously described in studies utilizing immunohistochemistry [31,32] or scRNA-seq [28]. Additionally, beyond endothelial cells, we were unable to detect any other non-immune cell types in the TME, such as cancer associated fibroblasts (CAFs) or non-malignant skeletal muscle cells. We ascribe these inconsistencies to either biases introduced by the SORT-seq protocol (multi-nucleated myotubes would be gated out during FACS sorting, for instance), or the freeze/thaw cycle tumor samples were subjected to. However, including a larger number of T and NK cells had the benefit of allowing us to resolve and characterize functional subtypes not previously identified in RMS tumors.

In analyzing NMF-defined transcriptional meta-programs and the similarity of RMS single-cells to normal myogenic differentiation, we defined subtype-specific hierarchies of malignant cell states. While myogenic differentiation of RMS cells into rhabdomyoblasts has long been appreciated [3], the presence of cells resembling myogenic mesenchymal cells or satellite cells has, to our

6

knowledge, not been previously described. Our model of RMS differentiation trajectories (Fig. 5a) has several clinical and biological implications. First, the observation that high levels of cells in more differentiated states is associated with better patient outcomes suggests the use of "differentiation therapy", where tumor cells are pharmacologically induced to undergo differentiation [34], would be a useful treatment strategy for RMS. In support of this, several studies using pre-clinical models of RMS have demonstrated that inhibiting critical pathways or regulators of tumorigenesis, including MEK in mutant RAS-driven FN RMS [35] and BAF complexes in FP tumors [36], leads to the induction of terminal myogenic differentiation. This approach could be expanded upon in future studies through the systematic elucidation of key regulators of RMS cell states which could be targeted to induce differentiation. It was notable that in both RMS subtypes, high levels of cells in states with mesenchymal characteristics (FN mesenchymal and FP SC-like) were associated with better outcomes, as mesenchymal-like cell states have been associated with drug resistance and increased metastatic potential in tumors of epithelial origin [37] as well as other sarcoma types [38]. On the other hand, the observation that high levels of proliferation are associated with worse outcomes supports the potential utility of compounds targeting key cell cycle regulators, including WEE1, PLK1 or CDK4/6 inhibitors, all of which are being investigated as therapeutic additions to RMS treatment regimens [39]. In addition to informing future treatment strategies, our results suggest that the differentiation state of RMS tumors could be a valuable metric for patient stratification, particularly in FN RMS. The translation of this finding could help advance a key goal of RMS clinical research: the de-intensification of treatment, where possible, to reduce toxicity and treatment-induced late effects [40]. However, these results first need to be validated using independent patient cohorts, an effort which is complicated by the overall lack of publicly available data sets combining gene expression of RMS tumors with clinical follow-up information. Finally, while RNA velocity analysis suggested that the myogenic, mesenchymal, and SC-like states derive from the more proliferative cell states, it does not definitively rule out the possibility of de-differentiation from more to less-well differentiated cell states. It will be important, therefore, in future studies to examine the dynamic relationships between cell states using, for instance, phylogenetic analyses [41] or functional assays in pre-clinical RMS models.

Notably, our proposed model of differentiation trajectories in RMS differs from that recently put forth by Patel *et al* [28]. In their analysis, a single trajectory explains both FN and FP RMS, whereby cells resembling paraxial mesoderm (*MEOX2*+, found mainly in FN tumors) connect to highly proliferative myoblast-like cells which in turn may give rise to (or derive from) a more differentiated myocyte-like state. This difference in interpretation could stem from the fact that Patel *et al* jointly analyzed FN and FP samples, which may have obscured subtype-specific differences. For example, while highly proliferative myoblast-like cells were observed in our FP samples, the highly proliferative state in FN tumors more closely resembled early myogenic progenitors. However, as we have shown in Extended Data Figs. 5b and 6b, the data from Patel *et al* was consistent with our subtype-specific models of RMS differentiation trajectories.

In our comprehensive analysis of single-cell transcriptomes from pediatric RMS, we characterized the immune component of the TME and defined cell-states mirroring normal myogenic differentiation trajectories. Based on these findings, we propose that targeting immune checkpoint molecules is a promising therapeutic approach for RMS that merits further investigation. Furthermore, the validation and clinical implementation of differentiation state as a prognostic indicator should be a priority, given its potential to improve patient risk stratification.

Materials & Methods

Tumor sample acquisition

Tumor samples of RMS were obtained via an established sample acquisition route as part of the biobank initiative of the Princess Máxima Center for Pediatric Oncology, Utrecht, Netherlands (remaining tumor samples). Ethics approval was granted for the biobanking initiative by the Medical Research Ethics Committee (METC) of the University Medical Center Utrecht, and the Máxima biobank committee granted approval for the present project. All patients and/or their legal representatives signed informed consent to have tumor samples taken for biobank usage. Experiments conformed to the principles set out in the WMA Declaration of Helsinki and the Department of Health and Human Services Belmont Report.

Sample processing and single-cell RNA-sequencing

Viably frozen tumor samples were rapidly thawed in a water bath, minced using a scalpel and then transferred to a tube containing 4.5 ml of BM1* medium (Advanced DMEM/F12 [Gibco, cat no. 12634010] supplemented with 1% Glutamax [Gibco, cat no. 35050061], 1% Penicillin/Streptomycin [Gibco, cat no. 15140122], 2% B27 minus vitamin A [Gibco, cat no. 12587010], 1% N2 [Gibco, cat no. 17502048], 0.25% N-acetylcysteine [500 mM, Sigma, cat no. A9165], 1% MEM non-essential amino acids [Gibco, cat no. 11140035], 1% sodium pyruvate [100 mM, Gibco, cat no. 11360070], 0.01% heparin [5,000 U/ml, Sigma, cat no. H3149-10KU], 1% hEGF [2 µg/ml, Peprotech, cat no. AF-100-15], 0.1% hFGF-basic [40 µg/ml, Peprotech, cat no. 100-18B], 0.02% hIGF1 [100 µg/ml, Peprotech, cat no. 100-11], 0.01% Rho kinase inhibitor [Y-27632, 100 mM, AbMole Bioscience, cat no. M1817] and 0.1% A83-01 [5 mM, Tocris Bioscience, cat no. 2939]). To this, 0.5 ml of Collagenase D (Roche, #11088866001, 1:10 dilution) and DNAseI (Stemcell #07900, stock diluted 1:40 in PBS, further 1:100 diluted in the BM1* mixture) were added, and samples were allowed to dissociate in a shaker set to 250 rpm for 30 minutes at 37 °C. Following digestion, samples were passed through a 70 µm strainer which was subsequently flushed with an additional 5 ml of BM1* (supplemented with DNAseI) to increase the yield. Samples were then washed twice with 5 ml of washing medium (Advanced DMEM/F12 supplemented with 1% Glutamax, 1% Penicilin/Streptomycin and 1% HEPES [1 M, Gibco, cat no. 15630049]), centrifuging at 300 g for 5 minutes (at 4 °C) in between steps. After the final washing step samples were resuspended in BM1* (supplemented with DNAseI) to a final concentration of < 1 x 10E6 cells per ml. Prior to sorting, 4′,6-diamidino-2-phenylindole (DAPI, Sigma-Aldrich, #D9542) and DRAQ5 (Thermo Fisher, #65-0880-92) were added to single-cell suspensions up to final concentrations of 1 µM and 5 µM, respectively. Viable single-cells (DAPI-, DRAQ+) were then sorted into 384-well plates containing 10 µl of mineral oil (Sigma, #M5310) and 50 nl of barcoded RT primers using a SONY SH800S Cell Sorter. Libraries were prepared according to the SORT-seq [15] protocol and sequenced on an Illumina NextSeq500 (paired-end, 75 bp read chemistry) by Single Cell Discoveries B.V.

Immunohistochemistry and H&E staining

Immunohistochemistry (IHC) and hematoxylin and eosin (H&E) staining experiments were performed on 4 μm thick formalin fixed and paraffin embedded (FFPE) tissue sections using a Ventana automated tissue staining system (BenchMark Ultra, Roche). For IHC, the antibodies used were anti-CD3 clone LN10 (Leica, PA0533), anti-CD8 4B11 (Leica, PA0183) and anti-CD68 514H12 (Leica, PA0273).

Immunofluorescence microscopy

Mounted tumor sections (5 μm thick FFPE) were baked at 60 °C for 1 hour and then deparaffinized and rehydrated using sequential washes of Xylene (2 x 100%), Ethanol (2 x 100%, 2 x 95%, 1 x 75%, 1 x 50% and 1 x 25%) and demineralized H2O (2 x 1 min, 1 x 5 min). Antigen retrieval was then performed by boiling slides in Tris-EDTA (pH 9) for 20 min in a benchtop autoclave. Slides were then washed 3 x 5 min in PBST (PBS + 0.1% Tween 20) and incubated with blocking solution (PBST + 1% BSA) for 1 h at RT. After blocking slides were incubated with primary antibody diluted in blocking solution overnight at 4 °C. The following day, slides were washed 3 x 5 min with PBS and then incubated with secondary antibody, diluted in PBST, in the dark for 1 h at RT. Slides were washed an additional 3 x 5 min with PBS before adding mounting medium containing DAPI counterstain (Vector labs, H-1200) and applying glass coverslips. Images were acquired on a Leica SP8 confocal microscope (40x/1.3NA oil immersion objective), and maximum projections of Z-stacks were obtained using the FIJI software (v2.0.0-rc-69/1.52i) [42]. Primary antibodies used: anti-TIGIT (Cell Signaling, #99567, 1:500 dilution) and anti-NECTIN3 (R&D systems, AF3064, 1:200 dilution of a 0.2 μg/μl solution in PBS). Secondary antibodies used: Donkey anti-Goat Alexa 647 (Abcam, ab150131, diluted 1:.1.000) and Donkey anti-Rabbit Alexa 568 (Abcam, ab175470, diluted 1:1.000).

RNA Fluorescence *in-situ* hybridization (RNAscope)

RNA-FISH experiments were performed on 5 μm FFPE tissue sections using the RNAscope™ Multiplex Fluorescent v2 kit (ACD bio), according to the manufacturer's instructions. The following probes were used for hybridization:

Hs-MKI67-C3 (591771-C3), Hs-TTN (550361), Hs-NOTCH3-C2 (558991-C2), Hs-FGFR4-no-XMm-C2 (443431-C2) and Hs-TGFBI (478491). Additionally, the following fluorescent dyes were used for detection (diluted 1:1.500): Opal 520 (FP1487001KT), Opal 570 (FP1488001KT) and Opal 690 (FP1497001KT). Images were acquired on a Leica SP8 confocal microscope (40x/1.3NA oil immersion objective), and maximum projections of Z-stacks were obtained using the FIJI software (v2.0.0-rc-69/1.52i).

Data processing and quality control

Sequencing reads were demultiplexed, mapped to the GRCh38v2020-A genome, available from 10X genomics (https://support.10xgenomics.com/single-cell-gene-expression/software/release-notes/build), and transcript counts were generated using the zUMIs pipeline (v5.6) [43]. Using the Seurat toolkit (v4.1.0) [44], count tables (per plate) were then loaded in *R* (v4.1.0), merged and metadata fields were compiled. Single cells excluded if they had < 500 expressed genes, < 800 or > 50.000 unique transcripts, a percentage of mitochondrial transcripts > 50%, > 1% hemoglobin gene transcripts or a ratio of intergenic to genic transcripts > 2. The data were then log normalized to 10.000 transcripts, scaled and centered. The top 2.000 most variably expressed genes were defined with the *FindVariableFeatures* function in Seurat (default parameters), and their expression was used as input for principal component analysis (PCA). Finally, the first 50 principal components were used to project single-cell transcriptomes in 2-dimensional space using uniform manifold approximation and projection (UMAP). The cell cycle phase of each single-cell was inferred using the *CellCycleScoring* function implemented in Seurat, using the built-in gene lists.

Module scoring

Module scores were calculated as previously described in ref. [20] and implemented in the Seurat function *AddModuleScore*, taking into account 25 expression bins and 100 control genes per query gene.

Cell type classification

To discriminate between malignant and healthy cells, we first used the *SingleR R* package (v1.6.1) [16] to annotate single cells based on their similarity

to reference bulk transcriptomes of healthy cells (Human Primary Cell Atlas data [45]) and RMS tumors (EGAD00001008467). We then used the InferCNV *R* package (v1.8.0) [46] to define and cluster single-cell copy number variant profiles per tumor sample (default parameters, average expression threshold of 0.3 and standard deviation filter of 2). A SORT-seq dataset of cord blood mononuclear cells (CBMCs) and other normal cell types was used as reference. CNV profiles derived from bulk DNA sequencing were plotted for comparison (see Extended Data Fig. 2), and single-cell clusters containing CNVs were manually selected and annotated "malignant". Cells were called malignant when they were classified as such using both approaches and excluded cells which were divergently classified (labelled ambiguous). The broad cell-type of non-malignant cells was inferred from the hierarchical clustering of the similarity scores.

Analysis of the immune microenvironment

To reach sharper biological distinctions between immune cell subsets, *SCTransform* [47] normalization was performed on the full dataset to normalize and scale the data for unbiased clustering. To further improve detailed immune cell sub-clustering, sample-specific gene expression was removed to reduce technical effects and enhance biological variation. Sample-specific genes were identified by differential gene expression analyses among tumor cells and immune cells separately and comparing the individual samples. Genes that were differentially expressed in both the tumor cells and immune cells of a specific samples were considered sample-specific noise and were removed from the variable gene list. To avoid clustering of cells based on specific cell processes, genes associated with sex (*XIST*, *TSIX*, and Y chromosome-specific genes), cell cycle phase, dissociation stress (heat shock proteins; GO:0006986), and activity (ribosomal protein genes; GO:0022626), were also removed from the variable gene list as described previously [48].

Healthy clusters were subset and clustered using 40 principal components and a resolution of 0.3 (Louvain algorithm) was used to define clusters of the main cell types. For in-depth analysis of the T and NK cells, the respective clusters were subset, and UMAP was re-run using 40 PCs and a resolution of 0.5 was used to define subclusters. For in-depth analysis of the myeloid

6

compartment, *SCTransfrom* normalization was re-run, sample-specific and cell process-specific genes were removed from the variable gene list and 6 PCs and a resolution of 0.3 was used to define subclusters.

Immune cell type identification

Cluster annotation was performed using *SingleR*, using the Human Primary Cell Atlas reference dataset to annotate main cell types, and additionally using the Novershtern Hematopoietic Data [49] and Monaco Immune Data [50] reference datasets to annotate the immune cell (sub)clusters. Cell annotations were further refined by consulting cluster-specific (up-regulated) differentially expressed marker genes using Seurat's *FindAllMarkers* function. The outputted genes were compared to known cell-type specific marker genes from previous studies [51–54].

Gene set enrichment analysis (GSEA)

For GSEA, differential expression analysis between two groups was performed using the *FindMarkers* Seurat function, using the following adjusted parameters: logfc.threshold = 0, min.pct = 0, min.cells.feature = 0, min.cells.group = 0. Genes were pre-ranked by their Fold Change and GSEA was performed using the *R* package fgsea (version 1.20.0). Gene sets with an FDR < 0.25 were considered significantly enriched. Gene sets were obtained from MSigDB version 7.2.

Ligand-receptor interaction analysis

The *CellChat* [24] algorithm was applied to perform an unbiased ligand-receptor interaction analysis, using the curated ligand-receptor database of CellPhoneDB (RRID: SCR_017054) [55].

Logistic regression analysis

Determination of the similarity between RMS single-cells and normal myogenic cells types (given as a probability value) was estimated as previously described in ref. [26]. We obtained the data from ref. [27] from the gene expression omnibus (GSE147457) and trained logistic regression models using the main

myogenic cell type labels. Correlations between meta-program scores and normal myogenic cell types used the logit-transformed probability values.

Non-negative matrix factorization

Non-negative matrix factorization (NMF) was carried out using the NMF *R* package (v0.23) [56]. For each RMS subtype (FN or FP), a list of shared variable features (n = 2.000) was compiled using the *SelectIntegrationFeatures* function in Seurat. The expression of these genes was then scaled, per tumor, and used as input to determine the appropriate NMF rank, by running 50 iterations (Brunet algorithm) for ranks between 2 and 10 (default settings). The optimal rank was determined, per tumor, by manually assessing in cophenetic coefficients, dispersion values and silhouette scores between rank values. We then re-performed NMF at 250 iterations using the optimal rank value. Per subtype, pairwise Pearson correlation coefficients were calculated between NMF-defined transcriptional programs (across all tumors) and hierarchical clustering was used to determine groups. Highly correlated groups of programs were merged into meta-programs by averaging gene weights. Cell-state scores were by using the top 30 weighted genes per meta-program to calculate module scores. Discrete cell-states were determined through manual inspection of the distribution of cell-state module scores.

Gene list enrichment analysis

Functional enrichment of gene lists was performed by the *enrichR R* package (v3.0) [57] (default settings) using the Reactome 2016 database.

Comparison with data from Patel *et al*

Single-nucleus RNA-seq data from the manuscript of Patel *et al* were downloaded from the Single-Cell Pediatric Cancer Atlas Portal (https://scpca. alexslemonade.org/) and loaded into Seurat. We inferred malignant cells using *SingleR*, as described for the data presented in this paper and applied an additional cutoff of > 800 unique transcripts for a cell to be considered valid. Data were then split by molecular subtype and module scores were calculated, as described above, using the top 30 genes per meta-program.

Differentiation trajectory modelling

Modelling of differentiation trajectories was done, per subtype, by projecting cells in DiffusionMaps space using expression of the top 30 meta-program-specific genes (*destiny R* package v3.1.1) [58]. The top 3 diffusion components were then used as input for trajectory modelling and cell lineage inference using Slingshot (v2.0.0) [59]. RNA velocity analysis was performed using the *scVelo* python package (v0.2.2, python v3.7) [60]. Briefly, input data per subtype, were filtered to include only genes with 20 shared (spliced and un-spliced) counts and log normalized. First and second order moments were calculated per cell using expression of the top 30 meta-program-specific genes and 30 nearest neighbors. RNA velocity was then estimated using the stochastic model and vectors were overlaid on the DiffusionMaps projections.

Survival analysis

Microarray gene expression profiles and the accompanying clinical follow-up information for the ITCC RMS cohort [8] was downloaded from the R2 genomics platform (R2: Genomics Analysis and Visualization Platform (http://r2.amc.nl)). Samples which did not exhibit either of the two main RMS histological classifications (alveolar or embryonal) were excluded. The data were divided based on fusion transcript status and Z-scores were calculated per gene. To generate meta-program scores, the average Z-score of the top 30 genes per meta-program (in the appropriate dataset) was calculated per tumor. Based on the distribution of scores, the "high" scoring groups (and *vice versa*) were defined as either the top 25% or 75% of tumors. Survival models were generated using the *survival R* package (v3.2-11) and *p* values were calculated using a Log Rank test.

Data availability

Raw single-cell RNA sequencing data have been deposited in the European genome-phenome archive. Accession numbers are pending.

Code availability

All data analysis code will be made available without restriction upon request.

Acknowledgements

Competing interests

The authors declare no competing interests.

6

References

1. Li, J., Thompson, T. D., Miller, J. W., Pollack, L. A. & Stewart, S. L. Cancer incidence among children and adolescents in the United States, 2001-2003. *Pediatrics* **121**, (2008).

2. Sebire, N. J. & Malone, M. Myogenin and MyoD1 expression in paediatric rhabdomyosarcomas. *Journal of Clinical Pathology* vol. 56 412–416 (2003).

3. Stiller, D. & Holzhausen, H. J. Ultrastructural organization of cell characteristics relevant to diagnosis in rhabdomyosarcomas. *Zentralbl. Allg. Pathol.* **134**, 449–466 (1988).

4. Drummond, C. J. *et al.* Hedgehog Pathway Drives Fusion-Negative Rhabdomyosarcoma Initiated From Non-myogenic Endothelial Progenitors. *Cancer Cell* **33**, 108-124.e5 (2018).

5. Oberlin, O. *et al.* Prognostic factors in metastatic rhabdomyosarcomas: results of a pooled analysis from United States and European cooperative groups. *J Clin Oncol* **26**, 2384–2389 (2008).

6. WHO. WHO Classification of Tumors: Soft Tissue and Bone Tumours. 5th Edition. (2020).

7. Missiaglia, E. *et al.* PAX3/FOXO1 fusion gene status is the key prognostic molecular marker in rhabdomyosarcoma and significantly improves current risk stratification. *J. Clin. Oncol.* **30**, 1670–1677 (2012).

8. Williamson, D. *et al.* Fusion gene-negative alveolar rhabdomyosarcoma is clinically and molecularly indistinguishable from embryonal rhabdomyosarcoma. *J Clin Oncol* **28**, 2151–2158 (2010).

9. Buckingham, M. & Relaix, F. The Role of Pax Genes in the Development of Tissues and Organs: Pax3 and Pax7 Regulate Muscle Progenitor Cell Functions. *Annu. Rev. Cell Dev. Biol.* **23**, 645–673 (2007).

10. Galili, N. *et al.* Fusion of a fork head domain gene to PAX3 in the solid tumour alveolar rhabdomyosarcoma. *Nat. Genet.* **5**, 230–235 (1993).

11. Barr, F. G. *et al.* In Vivo Amplification of the PAX3-FKHR and PAX7-FKHR Fusion Genes in Alveolar Rhabdomyosarcoma. *Hum. Mol. Genet.* **5**, 15–21 (1996).

12. Shern, J. F. *et al.* Comprehensive genomic analysis of rhabdomyosarcoma reveals a landscape of alterations affecting a common genetic axis in fusion-positive and fusion-negative tumors. *Cancer Discov* **4**, 216–231 (2014).

13. Patton, R. B. & Horn, R. G. Rhabdomyosarcoma: Clinical and pathological features and comparison with human fetal and embryonal skeletal muscle. *Surgery* **52**, 572–584 (1962).

14. Morotti, R. A. *et al.* An Immunohistochemical Algorithm to Facilitate Diagnosis and Subtyping of Rhabdomyosarcoma: The Children's Oncology Group Experience. *Am. J. Surg. Pathol.* **30**, 962–968 (2006).

15. Muraro, M. J. *et al.* A Single-Cell Transcriptome Atlas of the Human Pancreas. *Cell Syst.* **3**, 385-394.e3 (2016).

16. Aran, D. *et al.* Reference-based analysis of lung single-cell sequencing reveals a transitional profibrotic macrophage. *Nat. Immunol.* **20**, 163–172 (2019).

17. Venteicher, A. S. *et al.* Decoupling genetics, lineages, and microenvironment in IDH-mutant gliomas by single-cell RNA-seq. *Science (80-.).* **355**, (2017).

18. Puram, S. V. *et al.* Single-Cell Transcriptomic Analysis of Primary and Metastatic Tumor Ecosystems in Head and Neck Cancer. *Cell* **171**, 1611-1624.e24 (2017).

19. Tirosh, I. *et al.* Single-cell RNA-seq supports a developmental hierarchy in human oligodendroglioma. *Nature* **539**, 309–313 (2016).

20. Tirosh, I. *et al.* Dissecting the multicellular ecosystem of metastatic melanoma by single-cell RNA-seq. *Science (80-.).* **352**, 189–196 (2016).

21. Cheng, S. *et al.* A pan-cancer single-cell transcriptional atlas of tumor infiltrating myeloid cells. *Cell* **184**, 792-809.e23 (2021).

22. Liu, J., Geng, X., Hou, J. & Wu, G. New insights into M1/M2 macrophages: key modulators in cancer progression. *Cancer Cell Int.* **21**, 389 (2021).

23. Li, H. *et al.* Dysfunctional CD8 T Cells Form a Proliferative, Dynamically Regulated Compartment within Human Melanoma. *Cell* **176**, 775-789.e18 (2019).

24. Jin, S. *et al.* Inference and analysis of cell-cell communication using CellChat. *Nat. Commun.* **12**, 1–20 (2021).

25. Kashi, V. P., Hatley, M. E. & Galindo, R. L. Probing for a deeper understanding of rhabdomyosarcoma: insights from complementary model systems. *Nat Rev Cancer* **15**, 426–439 (2015).

26. Young, M. D. *et al.* Single-cell transcriptomes from human kidneys reveal the cellular identity of renal tumors. *Science (80-.).* **361**, 594–599 (2018).

27. Xi, H. *et al.* A Human Skeletal Muscle Atlas Identifies the Trajectories of Stem and Progenitor Cells across Development and from Human Pluripotent Stem Cells. *Cell Stem Cell* **27**, 158-176.e10 (2020).

28. Patel, A. G. *et al.* The myogenesis program drives clonal selection and drug resistance in rhabdomyosarcoma. *Dev. Cell* **57**, 1226-1240.e8 (2022).

29. Gioftsidi, S., Relaix, F. & Mourikis, P. The Notch signaling network in muscle stem cells during development, homeostasis, and disease. *Skelet. Muscle* **12**, 9 (2022).

30. Urciuolo, A. *et al.* Collagen VI regulates satellite cell self-renewal and muscle regeneration. *Nat. Commun.* **4**, 1964 (2013).

31. Kather, J. N. *et al.* CD163+ immune cell infiltrates and presence of CD54+ microvessels are prognostic markers for patients with embryonal rhabdomyosarcoma. *Sci. Rep.* **9**, 9211 (2019).

32. Dancsok, A. R. *et al.* Tumor-associated macrophages and macrophage-related immune checkpoint expression in sarcomas. *Oncoimmunology* **9**, (2020).

33. Harjunpää, H. & Guillerey, C. TIGIT as an emerging immune checkpoint. *Clin. Exp. Immunol.* **200**, 108–119 (2020).

6

34. de Thé, H. Differentiation therapy revisited. *Nat. Rev. Cancer* **18**, 117–127 (2018).

35. Yohe, M. E. *et al.* MEK inhibition induces MYOG and remodels super-enhancers in RAS-driven rhabdomyosarcoma. *Sci Transl Med* **10**, (2018).

36. Laubscher, D. *et al.* BAF complexes drive proliferation and block myogenic differentiation in fusion-positive rhabdomyosarcoma. *Nat. Commun.* **12**, 6924 (2021).

37. Lu, W. & Kang, Y. Epithelial-Mesenchymal Plasticity in Cancer Progression and Metastasis. *Dev. Cell* **49**, 361–374 (2019).

38. Sannino, G., Marchetto, A., Kirchner, T. & Grünewald, T. G. P. Epithelial-to-Mesenchymal and Mesenchymal-to-Epithelial Transition in Mesenchymal Tumors: A Paradox in Sarcomas? *Cancer Res.* **77**, 4556–4561 (2017).

39. van Erp, A. E. M., Versleijen-Jonkers, Y. M. H., van der Graaf, W. T. A. & Fleuren, E. D. G. Targeted Therapy-based Combination Treatment in Rhabdomyosarcoma. *Mol Cancer Ther* **17**, 1365–1380 (2018).

40. Chen, C., Dorado Garcia, H., Scheer, M. & Henssen, A. G. Current and Future Treatment Strategies for Rhabdomyosarcoma. *Frontiers in Oncology* vol. 9 1458 (2019).

41. Coorens, T. H. H. *et al.* Lineage-Independent Tumors in Bilateral Neuroblastoma. *N. Engl. J. Med.* **383**, 1860–1865 (2020).

42. Schindelin, J. *et al.* Fiji: An open-source platform for biological-image analysis. *Nature Methods* vol. 9 676–682 (2012).

43. Parekh, S., Ziegenhain, C., Vieth, B., Enard, W. & Hellmann, I. zUMIs - A fast and flexible pipeline to process RNA sequencing data with UMIs. *GigaScience* vol. 7 (2018).

44. Hao, Y. *et al.* Integrated analysis of multimodal single-cell data. *Cell* **184**, 3573-3587.e29 (2021).

45. Mabbott, N. A., Baillie, J., Brown, H., Freeman, T. C. & Hume, D. A. An expression atlas of human primary cells: inference of gene function from coexpression networks. *BMC Genomics* **14**, 632 (2013).

46. Tickle, T., Tirosh, I., Georgescu, C., Brown, M. & Haas, B. inferCNV of the Trinity CTAT Project. Klarman Cell Observatory, Broad Institute of MIT and Harvard, Cambridge, MA, USA. (2019).

47. Hafemeister, C. & Satija, R. Normalization and variance stabilization of single-cell RNA-seq data using regularized negative binomial regression. *Genome Biol.* **20**, 296 (2019).

48. Calandrini, C. *et al.* An organoid biobank for childhood kidney cancers that captures disease and tissue heterogeneity. *Nat. Commun.* **11**, (2020).

49. Novershtern, N. *et al.* Densely Interconnected Transcriptional Circuits Control Cell States in Human Hematopoiesis. *Cell* **144**, 296–309 (2011).

50. Monaco, G. *et al.* RNA-Seq Signatures Normalized by mRNA Abundance Allow Absolute Deconvolution of Human Immune Cell Types. *Cell Rep.* **26**, 1627-1640. e7 (2019).

51. Tang-Huau, T.-L. *et al.* Human in vivo-generated monocyte-derived dendritic cells and macrophages cross-present antigens through a vacuolar pathway. *Nat. Commun.* **9**, 2570 (2018).

52. Szabo, P. A. *et al.* Single-cell transcriptomics of human T cells reveals tissue and activation signatures in health and disease. *Nat. Commun.* **10**, 4706 (2019).

53. Zavidij, O. *et al.* Single-cell RNA sequencing reveals compromised immune microenvironment in precursor stages of multiple myeloma. *Nat. Cancer* **1**, 493–506 (2020).

54. Zhao, J. *et al.* Single cell RNA-seq reveals the landscape of tumor and infiltrating immune cells in nasopharyngeal carcinoma. *Cancer Lett.* **477**, 131–143 (2020).

55. Efremova, M., Vento-Tormo, M., Teichmann, S. A. & Vento-Tormo, R. CellPhoneDB: inferring cell–cell communication from combined expression of multi-subunit ligand–receptor complexes. *Nat. Protoc.* **15**, 1484–1506 (2020).

56. Gaujoux, R. & Seoighe, C. A flexible R package for nonnegative matrix factorization. *BMC Bioinformatics* **11**, 367 (2010).

57. Chen, E. Y. *et al.* Enrichr: interactive and collaborative HTML5 gene list enrichment analysis tool. *BMC Bioinformatics* **14**, 128 (2013).

58. Angerer, P. *et al.* destiny : diffusion maps for large-scale single-cell data in R. *Bioinformatics* **32**, 1241–1243 (2016).

59. Street, K. *et al.* Slingshot: cell lineage and pseudotime inference for single-cell transcriptomics. *BMC Genomics* **19**, 477 (2018).

60. Bergen, V., Lange, M., Peidli, S., Wolf, F. A. & Theis, F. J. Generalizing RNA velocity to transient cell states through dynamical modeling. *Nat. Biotechnol.* **38**, 1408–1414 (2020).

6

Extended data

Supplementary Tables S1 to S3 can be downloaded at https://www.biorxiv. org/content/10.1101/2022.07.15.497944v1.supplementary-material
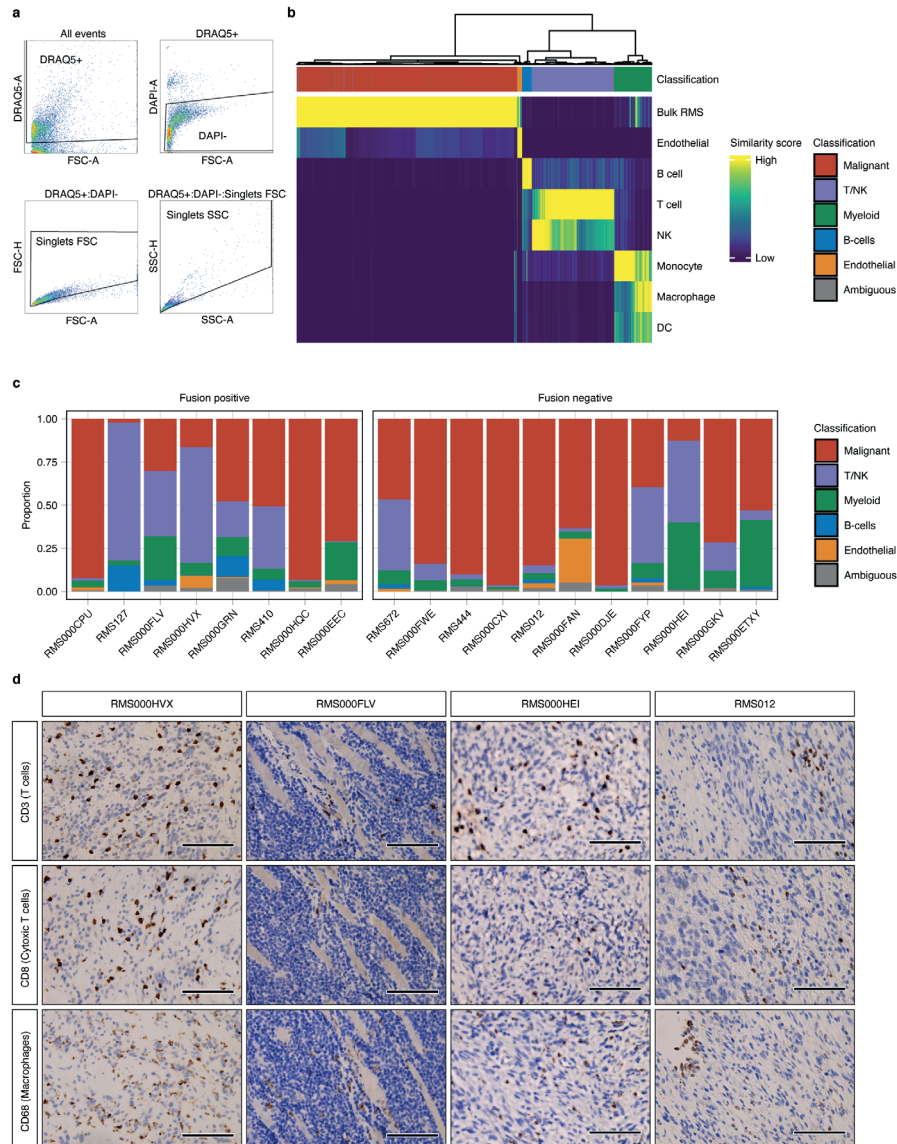
Extended data Fig. 1. a, Representative scatter plots showing the gating strategy used for SORT-seq FACS. Titles indicate the events shown in each plot (FSC = forward

Extended data Fig. 1. Continued

scatter, SSC = side scatter, -A = signal area and -H = signal height). **b**, Heatmap showing the clustered similarity scores (per cell) to each reference cell type (y-axis labels) as determined by SingleR. Cell classifications are shown in the top annotation bar (as in Fig. 1). **c**, Bar graph depicting the distribution of annotated cell types per tumor. **d**, Representative microscopy images showing IHC staining of three immune population markers (y-axis) across tissue samples from four tumors (x-axis). Positive staining indicated by brown colouring, hematoxylin counterstained nuclei in blue. Scale bars equivalent to 100 µm.

6
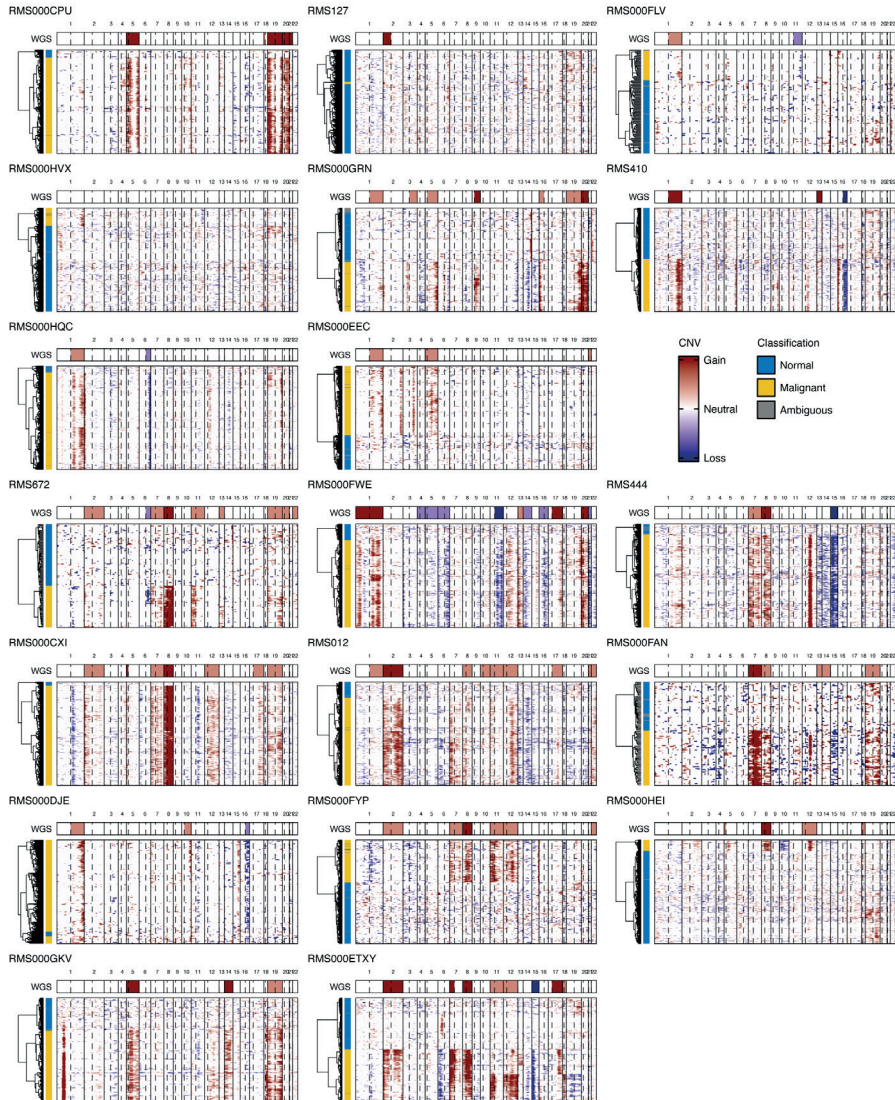
Extended data Fig. 2. Heatmaps showing the clustered single-cell inferred CNV profiles per tumor. Solid vertical lines denote chromosome boundaries and dotted vertical lines represent the locations of centromeres. Cell classifications are shown on the left annotation bars. Top annotation bars show CNVs (summarized per chromosome arm) defined by DNA-sequencing of bulk tumor samples, for comparison.
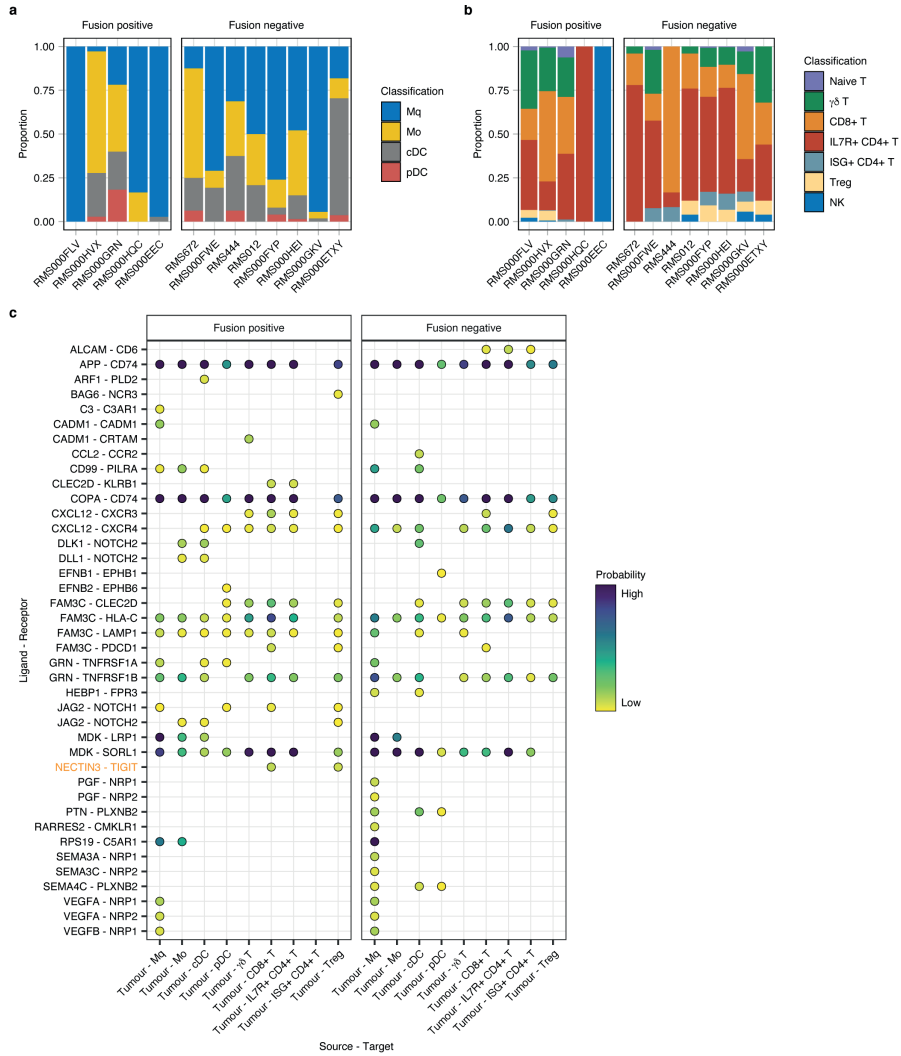
Extended data Fig. 3. Bar plots showing the proportion of cell types within the (**a**) myeloid or (**b**) T/NK compartments per tumor. **c**, Dot plot summarizing the results of ligand-receptor interaction analysis, split by molecular subtype. Dots indicate an inferred ligand-receptor interaction (y-axis) between a source-target cell type pair (x-axis). Dots are coloured by the interaction probability, as determined by *CellChat*. The NECTIN3-TIGIT interaction is highlighted in orange on the y-axis.

6
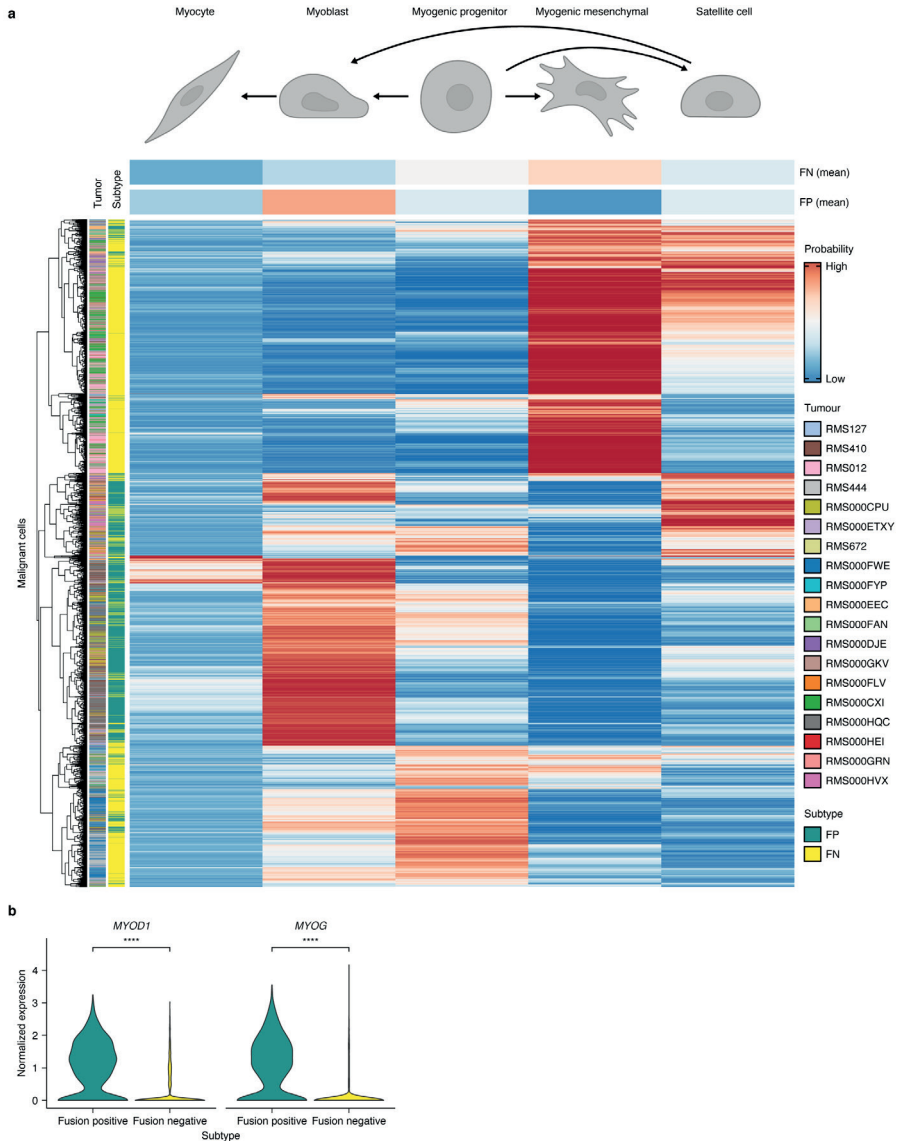
**Extended data Fig. 4. a**, Heatmap showing the comparison between RMS single cells (rows) and normal myogenic cell types (columns). Colour values represent the predicted similarity (probability) as determined by logistic regression analysis. Annotation tracks (left) indicate the tumor and molecular subtype of each cell. The top two columns show the predicted similarity aggregated per molecular subtype. Myogenic differentiation schematic was created with BioRender. **b**, Violin plots depicting the normalized expression of *MYOD1* (left panel) and *MYOG* (right panel) in malignant cells from each RMS subtype. **** indicates differential expression ($p <$ 0.00001, Wilcoxon Rank Sum test).

6
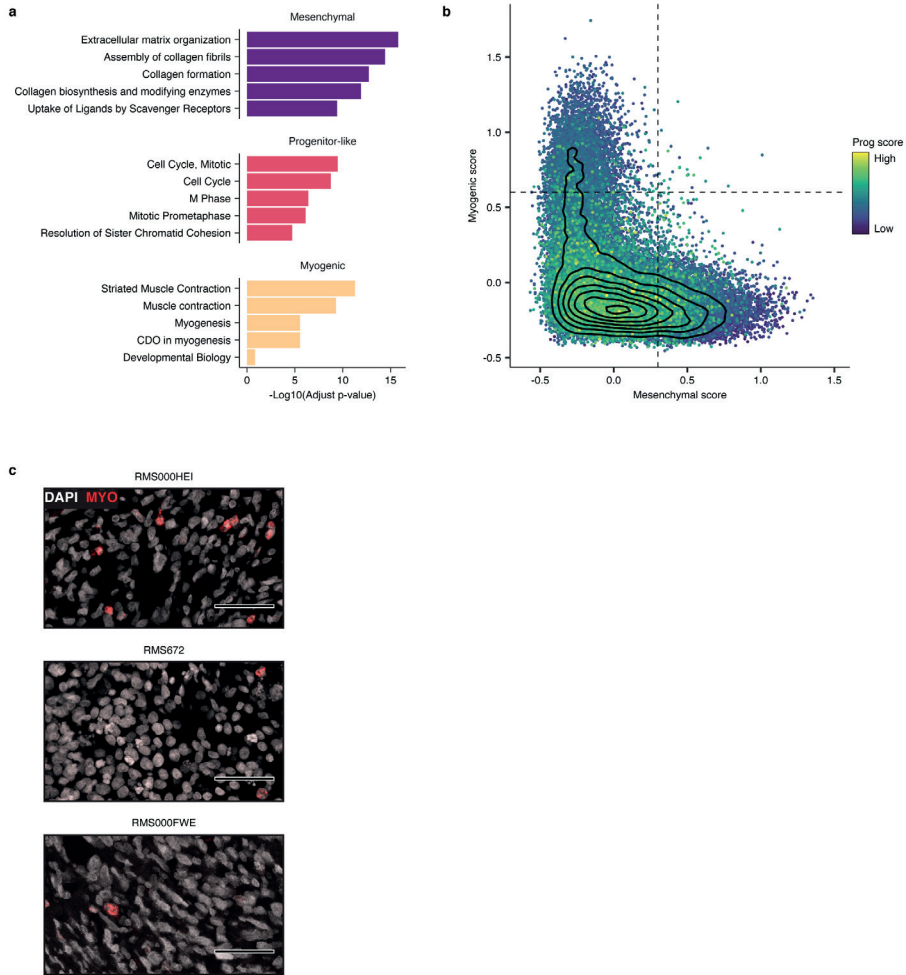
Extended data Fig. 5. a, Reactome pathway enrichment of the top 30 genes per FN meta-program. The top 5 terms per meta-program are labelled on the y-axis and the -Log10-transformed adjusted p-values (Fisher's exact test, B-H adjusted), are depicted by horizontal bars (coloured per meta-program). **b**, Scatter plot depicting the mesenchymal (x-axis), myogenic (y-axis) and progenitor-like (colour) meta-program scores calculated in the dataset from Patel et al (malignant FN cells) [28]. Vertical and horizontal lines depict the discrete cell-state cut-offs used in Fig. 3b. Density contours are overlaid in black. **c**, Representative RNA-FISH images depicting the expression a myogenic cell-state marker gene in red (MYO = *TTN*) in FN tissue samples. DAPI counterstaining shown in grey. Scale bars equivalent to 50 μm.
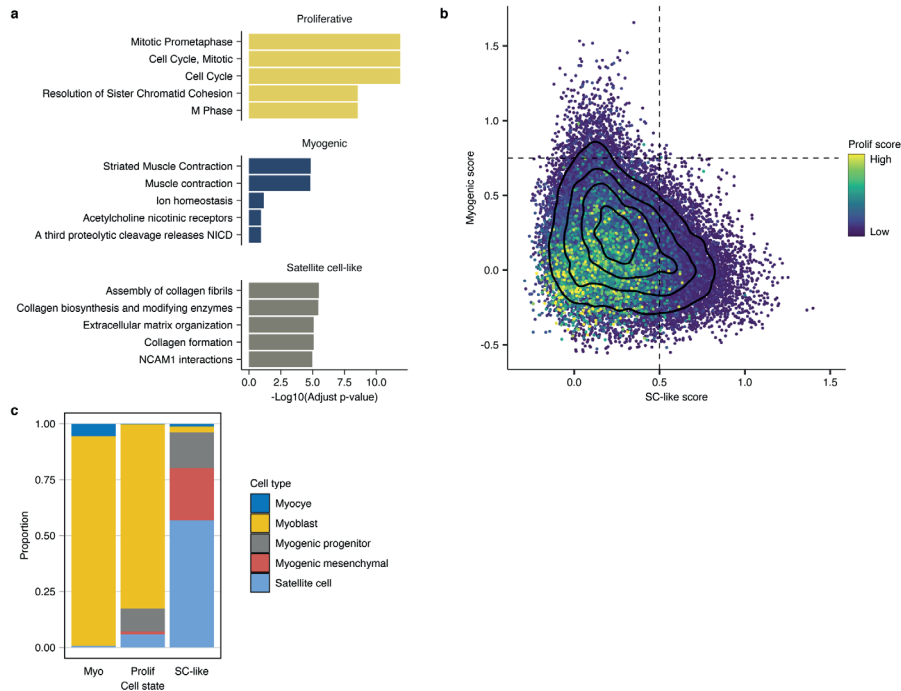
Extended data Fig. 6. a, Reactome pathway enrichment of the top 30 genes per FP meta-program. The top 5 terms per meta-program are labelled on the y-axis and the -Log10-transformed adjusted p-values (Fisher's exact test, B-H adjusted) are depicted by horizontal bars (coloured per meta-program). b, Scatter plot depicting the satellite cell-like (x-axis), myogenic (y-axis) and proliferative (colour) meta-program scores calculated in the data from Patel et al (malignant FP cells) [28]. Vertical and horizontal lines depict the discrete cell-state cut-offs used in Fig. 4b. Density contours are overlaid in black. c, Bar graph showing the distribution of normal myogenic cell-type classifications (max probability score) for cells in each FP cell state (x-axis).
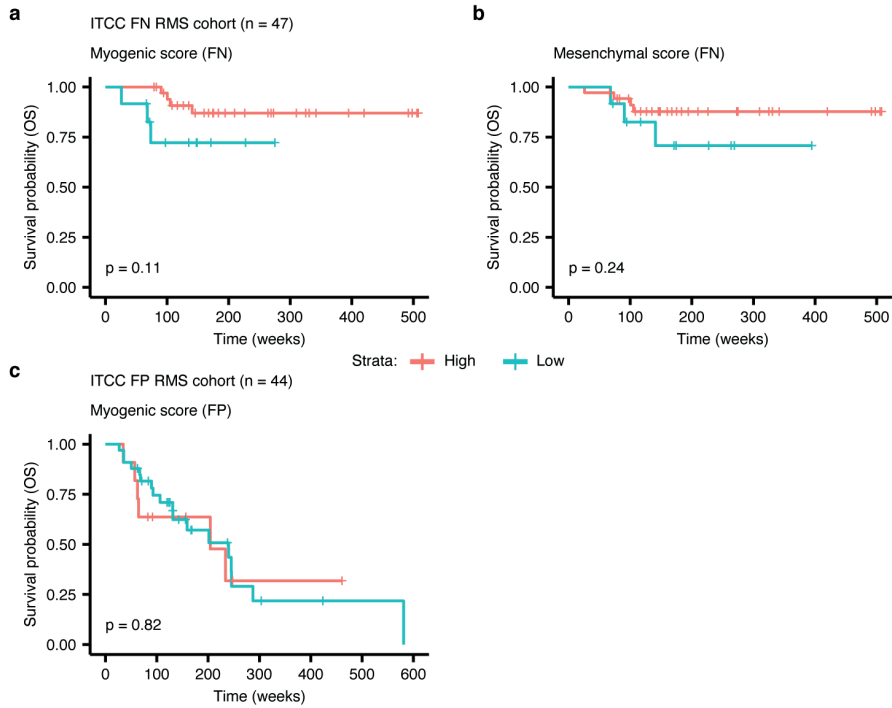
Extended data Fig. 7. Kaplan-Meier plots showing the overall survival probabilities of (**a**,**b**) FN or (**c**) FP patients divided into high (red strata) or low (blue strata) groups based on their cell state scores (stated in the title of each plot panels). Log rank test was used to calculate *p* values between high and low scoring groups.

7

General Discussion

Michael Torsten Meister

Mesenchymal tumor organoid models: a valuable asset

Organoid technology has revolutionized many aspects of life sciences and has brought major benefits for preclinical cancer research. Organoid models of cancer (i.e., tumoroid models) have proven their value as powerful tools to study mutational processes in cancer [1], predicting response to anti-cancer treatment in patients [2] and to perform cell of origin studies [3].

At the onset of this thesis, we considered the advantages and disadvantages of tumoroid models compared to the existing preclinical models of RMS (as reviewed in chapter 1) and decided to start developing RMS tumoroid models. This approach proved feasible and resulted in the generation of new preclinical models of RMS that faithfully recapitulate the patient tumors they were derived from and are usable for various preclinical applications such as high-throughput drug screening or disease modelling by CRISPR/Cas9 genetic editing. Table 1 below summarizes our current view on the characteristics and (dis)advantages of available preclinical models of RMS. As the table illustrates, conventional cell lines and the more recently described patient-derived xenograft (PDX) models of RMS can be used as complementary systems. While the ease of maintenance, the low costs involved and the potential to genetically manipulate cell lines to perform genome-wide screening was unmatched in the existing models of RMS [4], PDX models showed a higher establishment efficiency while closely recapitulating the tumors they were derived from [5]. Genetically engineered models (GEMs) of RMS filled the niche for studies on the onset of RMS tumors and inferring the potential cell of origin [6], which is to-date, however, still under debate as discussed in more detail in chapter 1. Importantly, the tumoroid models of RMS established in our studies broadly combine all important aspects of other tumor models and are not limited to one major advantage (see also Discussion section of chapter 5).

A more general aspect emerging from collaborations with other research groups is that tumoroid models are easy to share, transport and maintain. This seems to increase the possibilities for a larger community to perform preclinical and translational research in RMS. Maintenance of RMS tumoroid models is comparable to that of conventional cell lines, thus vastly easier than

that of PDX models (i.e., no need for an animal facility). Still, RMS tumoroid models enable studies on research questions which are usually outside of the capabilities of conventional cell lines (e.g., genome-wide screening in RMS models closely resembling the patient tumors they were derived from). As an example, one of our collaborators successfully performed combination high-throughput screenings of drugs with external beam radiotherapy (EBRT) (personal correspondence, data not published yet). Importantly, the group could identify drugs that potentiate the efficacy of EBRT, as well as identify an unusual susceptibility of one of our lines (i.e., RMS335) to EBRT in general.

Table 1. Comparison of preclinical RMS models. Adapted from [7] with additions from [4,6] and chapter 5 (updated for number of RMS tumoroid models available at the time of drafting this thesis). Number of available RMS PDX models derived from [8] and [9]. Zebrafish RMS PDX models are not discussed here. Abbreviations: GEMs (genetically engineered models), PDX (patient-derived xenograft), *D. melanogaster* (*Drosophila melanogaster*, fruit fly), *D. rerio* (*Danio rerio, zebrafish*), *M. musculus* (*Mus musculus*, house mouse).

Rhabdomyosarcoma	Cell lines	GEMs		PDX	Tumoroid
		D. melanogaster / D. rerio	*M. musculus*	*M. musculus*	
Availability	> 20 lines	1 / 4 lines	> 10 lines	> 30 lines	> 20 lines
Establishment efficiency	+	++ / ++	++	+++	+++
Ease of maintenance	+++	++ / ++	+	+	+++
Scalability	+++	++ / +	+	+	+++
Genetic manipulation	+++	++ / ++	+	+	+++
Genome-wide screening	+++	+ / +	+	+	+++
Retaining physiological 3D growth behavior	+	++ / ++	+++	+++	++
Relative cost	+++	++ / +	+	+	++
Recapitulation of patient tumor genetics	+	++ / ++	++	+++	+++
Studies on cancer onset and the cell of origin	+	+++ / +++	+++	+	++

7

233

We hypothesized that this may be due to this RMS tumoroid line (and the tumor it was derived from) harboring a possibly damaging missense single-nucleotide variant (SNV) in the *ATR* gene. *ATR* is critical for the maintenance of DNA integrity [10] and pharmacological inhibition of *ATR* was reported to potentiate the effects of radiotherapy [11]. It may therefore be important to screen RMS tumors for such mutations to assess which patients could especially benefit from EBRT. This finding was enabled by the ability to efficiently share and distribute our models, which can be readily used for such high-throughput approaches.

Interestingly, the ITCC-P4 study consortium [9], which aims at generating a plethora of PDX models of various pediatric tumor entities, has recently launched a sub-study to investigate the feasibility of establishing tumoroid models of pediatric solid tumors from established PDX models, thereby facilitating high-throughput drug screening approaches, which is not feasible with the PDX models themselves. Indeed, successful short-term cultures of RMS tumor cells derived from established PDX models have recently been reported [12], indicating the feasibility of generating long-term stable organoid models from PDX models. However, given the long establishment time of RMS PDX models compared to that of RMS tumoroid models, it would be more straightforward to first establish the tumoroid model and then transplant those cells onto host mice to generate an *in vivo* model, which has been shown for several tumoroid model systems [13–15]. In summary, tumoroid models of RMS are valuable assets and the establishment of RMS tumoroid models has yielded a novel preclinical system that not only complements existing systems but has its own niche, enabling efficient preclinical RMS research.

An increase in resolution or just more confusion: Applicability of single-cell genomic technologies in risk stratification for RMS

In this thesis we used single-cell RNA-sequencing to analyze primary pediatric RMS tumors and study their cellular composition and intra-tumoral tumor cell heterogeneity (chapter 6). One of the novel insights from using this technique was that we were able to define the recurrent transcriptional programs that

can be linked to normal muscle development and the prognosis of patients with RMS. Here, we will more broadly discuss the potential role of single-cell sequencing technologies in cancer risk stratification.

While single-cell genomic technologies are not yet routinely being used for risk stratification, bulk transcriptomic techniques are used in some cancer entities for risk stratification [16,17]. The most frequently used technique for bulk transcriptome analysis is bulk mRNA-sequencing (RNA-seq), which can not only be used to detect the overexpression (and thereby likely increased activity) of oncogenes but also to detect expressed single-nucleotide variants (SNVs) in regions which are poorly covered by DNA sequencing methods [18], infer copy-number alterations (CNAs) [19], and detect fusion transcripts [20]. While there have been attempts to infer the cellular composition of tumor samples from bulk transcriptomic data (i.e., deconvoluting the data [21]), these can never elucidate the true heterogeneity within a tumor sample. To study this, single-cell mRNA-sequencing (scRNA-seq) techniques can be used.

Importantly, the ongoing developments in scRNA-seq techniques have resulted in the ability to infer all of the information provided by RNA-seq (i.e., inferring SNVs [18], CNAs [22], and detect fusion transcripts [23]) on a single cell level, vastly increasing the resolution at which we can examine tumors. As an illustration of this, we showed in chapter 6 the heterogeneity within a given RMS tumor sample not only between cell types (i.e., tumor cells *versus* normal cells), but also between cells of the same type (i.e., transcriptional meta-programs of RMS tumor cells and different activation states of immune cells). Importantly, we show that the relative contribution of tumor cells within a tumor exhibiting certain meta-programs is predictive for outcome, which we validated in an independent, bulk transcriptome cohort [24]. A similar approach to use scRNA-seq on tumor cells to improve risk stratification in the field of pediatric oncology has recently been described for infant leukemias [25], further highlighting the power of this technology for the refinement of risk stratification.

As an additional benefit, scRNA-seq can be used to measure the degree of immune cell infiltration of a tumor and help assess immune cell activation states [26]. Knowledge of immune cell infiltration in RMS is sparse with only

7

a few histology-based studies [27,28], one of which showed an association between immune cell infiltration and prognosis. Due to the heterogeneity of the RMS tumor samples enrolled in our study (chapter 6), we cannot make definitive conclusions as to what the potential reasons for distinct immune cell profiles in the different RMS tumor samples are. Nevertheless, the fact that we detect these cells and that there is an association between immune cell infiltration and prognosis in RMS patients as reported by the study mentioned above, justifies further investigation using scRNA-seq.

Another potential clinical application for scRNA-seq is the pathological assessment of tumor response after (neoadjuvant) chemotherapy, which is an important risk stratification parameter for many solid tumors, e.g., osteosarcomas [29]. There are no systematic analyses available as to whether histological response to therapy has a predictive value in RMS. Interestingly however, one study found no difference in survival between pediatric RMS patients with initially unresectable tumors with or without a residual mass at the end of chemotherapeutic treatment [30]. In a small subset of patients with residual tumor mass at the end of treatment, this mass was resected and histologically analyzed. It showed viable tumor cells in 50% of cases, despite intensive chemotherapeutic treatment. The authors speculated that these may represent matured cells without malignant potential, in line with the notion that FN-RMS show maturation upon treatment [31]. However, the true malignant potential of those cells remaining after chemotherapy has not been studied, ignoring a potential cause of relapsed disease and RMS-related mortality [32]. Another clinical implication of scRNA-seq could be the study of mechanisms resulting in therapy resistance [25,33]. It is reasonable to assume that subjecting post-treatment RMS samples to scRNA-seq could elucidate mechanisms of drug insensitivity development. In fact, a recent scRNA-seq study on RMS tumors, showed a specific vulnerability to inhibitors of the epidermal growth factor receptor (EGFR) in a subset of FN-RMS cells which transcriptionally resembled mesoderm tissue and possessed tumor-propagating potential [34]. In addition, scRNA-seq would also allow the assessment of the tumor-infiltrating immune cells in post-treatment samples. Importantly, such infiltration can change after (neoadjuvant) chemotherapy and be of predictive value [35]. Taken together, analysis of post-treatment RMS tumors via scRNA-seq could further help refine risk stratification.

Lastly, scRNA-seq can be combined with single-cell epigenomic analyses to, for example, understand the interplay of chromatin accessibility and transcription. One of the techniques enabling this is the "Assay for Transposase-Accessible Chromatin using sequencing" (ATAC-seq). Since most pediatric tumors (including RMS) are considered to be driven by aberrantly active developmental arrest mechanisms, the understanding of the epigenetic regulation of such mechanisms in individual cells could be extremely valuable. The integrated analysis of both techniques can further help resolve developmental cell states and identify previously undetected cell populations [36]. Strikingly, one study on bulk DNA methylation (DNA-meth) sequencing in RMS found that especially in FN-RMS, DNA-meth could efficiently discriminate between patients with excellent and those with dismal outcomes [37]. This indicates that there are biologically relevant epigenetic differences between otherwise similar RMS samples that are strong prognostic predictors and could therefore be useful also in single-cell technologies. In summary, scRNA-seq and related technologies can help refine risk stratification for patients with RMS, potentially sparing patients with low-risk disease from unnecessary treatment, while ensuring that patients with high-risk disease receive sufficient treatment.

In this light, one question that remains is whether it is feasible to integrate single-cell analysis technologies into the diagnostic workflow for the processing of RMS tumor samples. Most diagnostic tumor samples are derived from core needle-biopsies. Plate-based scRNA-seq techniques (e.g., SORT-seq [38]) can be used for such smaller samples given the typically limited material loss involved. This technique then provides a better yield than other, more high-throughput techniques like droplet-based scRNA-seq [39,40]. As we show in chapter 6, even a relatively low number of cells (i.e., < 1.000) per tumor sample can be informative. The sample processing established in our study is straightforward and feasible. It can be performed on viably frozen tumor tissues, which is a standard procedure for all diagnostic core needle biopsies. Furthermore, this allows processing of samples in batches, increasing efficiency.

There are currently three aspects limiting the applicability of scRNA-seq for the standard of care risk stratification of RMS. First, the costs for analyzing

7

one 384-well plate (excluding the materials for the sample processing and sorting) are around 1.500 Euros, resulting in costs of ca. 3.000 Euros per sample when using two plates per tumor sample to achieve a sufficient cell number. These costs, however, will likely decrease as single-cell genomic technologies become more widely available and further developed, just as was the case with bulk sequencing of human genomes [41]. Secondly, the expertise and computational power necessary to analyze scRNA-seq data efficiently are not yet available in all treating centers [42]. While the number of algorithms allowing for the automatization of scRNA-seq data analysis are growing every day [43], to-date scRNA-seq data still have to be manually curated and evaluated by skilled bioinformatics teams. Thirdly, scRNA-seq cannot yet be viewed as a "stable" platform as it is still very much in development with frequent assay improvements and updates. To assess the clinical benefit of introducing scRNA-seq into the standard of care risk stratification of RMS however, a stable platform that allows for uniform sequencing and analysis of data to make them comparable is required [44]. Early investment into the infrastructure required to generate and analyze scRNA-seq data is important for future standard implementation.

In summary, scRNA-seq and other single-cell genomic technologies offer an exciting prospect for the refinement of risk stratification of RMS. While costs associated with this technology are currently still high and procedures require specific infrastructure, the further development of single-cell genomics will potentially result in the introduction of scRNA-seq into routine cancer diagnostics.

Are Pediatric Precision Medicine programs favorable for children and adolescents with RMS?

Precision medicine is a form of medicine that uses molecular information about a patient's own expression and alterations of genes or proteins to prevent, diagnose, or treat a disease. In the context of cancer, precision medicine implies anti-tumor treatment tailored to the specifics of the patient and his/her tumor (adapted from the definition by the National Institutes of Health of the US). Defining these specifics usually involves comprehensive molecular profiling of a patient's tumor using technologies such as whole-

genome sequencing (WGS) and RNA-seq. Detected genetic alterations are then discussed in molecular tumor boards to define their relevance for the tumor's biology and whether this alteration can be targeted using specific inhibitors.

The advent of affordable, comprehensive sequencing technologies with sufficient depth resulted in a breadth of precision medicine programs for adult (reviewed in [45]) but also pediatric cancer patients (reviewed in [46]). Hypothetically, by identifying and targeting the driving mutation of a tumor, treatment should be more efficacious with less side-effects compared to conventional chemotherapy. Unfortunately, numerous studies to-date have shown that our current understanding of, in particular, relapsed, heterogeneous tumors may be too simplistic, resulting in monotherapeutic targeted approaches that ultimately fail despite the identification of a clear driving alteration (e.g., in *RAS*-mutated high-risk pediatric cancers [47]).

The main expectations that patients have from enrollment in a precision medicine trial is the identification of a targetable mutation. Recently published data by the German pediatric precision medicine study INFORM [48], the French MAPPYACTS study [49], and the Australian Zero Childhood Cancer Program [50] include 64, 70 and 17 enrolled patients with RMS, respectively. In the INFORM trial, only patients with a "very high" priority molecular alteration who received a matching targeted drug showed an improved progression-free survival (PFS). However, no improvement in overall survival (OS) was observed. Three of the 64 patients with RMS had such a "very high" priority alteration (all activating *RAS* mutations) with one receiving a matched treatment (i.e., the MEKi inhibitor Trametinib). The MAPPYACTS study mainly reported on the identification of molecular alterations that enabled the enrollment of a patient in a Phase I/II trial with a matching drug (i.e., E-SMART study, clinicaltrials identifier NCT02813135). While these "ready-to-use" alterations were found in 10% of all tumors, no such alterations were found in RMS. Lastly, the Zero Childhood Cancer Program study reported on 17 RMS patients in which similar alterations were found as in the other studies (e.g., *CDK4* amplifications in FP-RMS). Unfortunately, reported outcome data only differentiated between tumor classes (i.e., "CNS", "Sarcoma", "Solid other") so that it is not clear whether any of the enrolled patients with RMS

received and benefitted from a matching targeted drug. Taken together, the results of these three pediatric precision medicine trials indicate that the present approach to detect actionable targets in RMS may be too limited and that studies need "to go deeper". The three studies employed whole exome and/or whole genome sequencing, a form of transcriptome analysis (microarray and/or mRNA-sequencing) and DNA methylation analysis, with the MAPPYACTS study also investigating the role of cell-free and circulating tumor DNA as biomarkers. With additional assays, further actionable targets might be identified, which could not faithfully be detected with the currently used techniques. For example, the INFORM study is currently investigating the added value of drug screening in short-term 3D spheroid cultures as well as zebrafish PDX models [51] in addition to the already established molecular analyses to (a) strengthen the rationale of using a drug matching a molecular alteration (i.e., if this drug shows efficacy in the drug screening) and to (b) identify efficacious drugs regardless of the molecular background of the tumor. Furthermore, patient tumors within the INFORM study are now also probed for their proteome to identify activated pathways as well as potential cell-surface proteins that can be targeted by immuno-therapeutic approaches (data unpublished). Case studies in high-risk RMS patients have shown that the latter can result in prolonged clinical responses (e.g., using HER2-targeting CAR T cells [52]).

Besides identifying targetable mutations, the comprehensive molecular characterization performed within precision medicine trials can potentially result in diagnosis refinement. For example, sarcomas that lack characteristics of differentiated cell lineages (e.g., bone, muscle, adipose, or cartilage tissue) are collectively termed "undifferentiated sarcomas" (UDS) [53]. Comprehensive molecular analyses can help to refine the diagnosis in such cases by identifying mutations characteristic for a specific lineage or sarcoma type, e.g., *NTRK*-fusion transcripts in *NTRK*-rearranged spindle cell neoplasms [54]. The importance of molecular diagnostics for pediatric cancers has recently been further underlined by the first WHO classification of Pediatric Tumors which is heavily reliant on molecular findings as a basis for diagnosis [55]. While RMS may be easily identifiable using conventional diagnostics, molecular characterization as part of a precision medicine trial may still result

in diagnostic refinement by the identification of mutations associated with poor prognosis in RMS. These include mutations in *TP53* in fusion-negative RMS (FN-RMS), *MYOD1* mutations in sclerosing/spindle-cell RMS (scRMS) [56] and *CDK4* amplifications in fusion-positive RMS (FP-RMS) [57]. While these findings may not have a direct therapeutic implication for the enrolled patient, they may at least explain an unusually aggressive clinical course.

Lastly, most precision medicine programs involve the analysis of the patient's germline DNA (as a control for mutation calling in genomic sequencing techniques). In most programs, patients can decide whether they want to be informed about pathological germline findings related to their tumor. As pediatric cancer can be attributed, in as much as 16% of cases, to a germline predisposition [49,50,58], information on this can be important also for other members of the patient's family, resulting in enrolling family members in a surveillance program, for instance [59]. As illustrated in Table 1 in chapter 1, FN-RMS can be attributed to various tumor predisposition syndromes, thus indicating the benefit especially for this patient group.

In summary, pediatric precision medicine studies have certainly improved our knowledge on the molecular biology of high-risk RMS, which will likely benefit future generations of patients. For patients with RMS currently enrolled in the trials, the immediate impact is limited with the main benefits being the potential identification of germline mutations and refinement of the diagnosis. The encouraging reports of single patients with RMS within these studies show, however, that pediatric precision medicine programs can have an immediate impact on the treatment of enrolled patients. To increase the number of patients with RMS benefitting in this manner, additional assays (such as complementary drug screening, proteomics, or the afore-mentioned single-cell technologies) may be needed.

Centralizing pediatric oncology care and research in comprehensive cancer centers: Numbers make a difference!

Comprehensive cancer centers (CCCs) are high-capacity centers that combine cancer research (preclinical and clinical) and direct patient care

(definition by the National Institutes of Health of the US). By assembling experts from all fields related to research on and the treatment of cancer, CCCs act as hubs of integrated expertise resulting in optimized treatment as well as translation of research findings to the clinical care of cancer patients. Depending on their size and location, CCCs can govern cancer patient care and research for a region or even an entire country.

CCCs provide several benefits compared to decentralized patient care and research with smaller local treatment centers and research centers not connected to a hospital. Firstly, certain patient groups can particularly benefit from the assembled expertise and availability of clinical trials in a CCC, such as patients suffering from so-called "rare cancers". A useful definition for rare cancers has been given by the RARECAREnet working group with rare cancers being cancer entities with an incidence of less than 6 in 100.000 in the population [60]. Importantly, while each individual subtype of these cancers is rare, as a whole, they pose a considerable burden, accounting for 24% of all cancer diagnoses [60]. Due to their general rarity, a high proportion of pediatric cancer entities also falls under this definition, including RMS. An overview of all considered cancer entities is given on the homepage of the US Surveillance, Epidemiology, and End Results (SEER) program [61]. The importance of improving our understanding and, consequently, the treatment of patients with rare cancers was addressed by the establishment of the International Rare Cancers Initiative (IRCI) in 2011 [62] that aims at connecting experts for a given rare cancer subtype and to set up clinical trials for these patients [63]. Given their nature of concentrating expertise from multiple research and clinical disciplines, CCCs align with this international approach on the national level by, for example, aggregating and describing large sets of patients with rare cancer types [64–66].

Another patient group that can benefit from being treated at a CCC are adolescents and young adults (AYAs) with cancer whose specific therapeutic needs and special attention for psychological support are well-documented [67]. Despite these needs being recognized, survival and quality of life (QoL) over the last years has improved less in AYAs compared to other patient groups [68]. The availability of experts from multiple disciplines in a CCC can enable the establishment of efficient treatment teams for AYAs [69], facilitate

the establishment of supportive care clinical trials tailored for this patient group [70,71] and potentially increase access to early phase clinical trials for adolescents below the age of 18 in this group who are often not eligible for such trials in conventional treatment centers [72]. Furthermore, by connecting AYA cancer patients at a CCC, patients can benefit from sharing their experience with their peers, which can be an important coping mechanism [73]. Therefore, CCCs can prove invaluable for AYA cancer patients who often find themselves torn between the pediatric and adult cancer world, neither of those specialties fully appreciating their specific needs.

Besides such benefits for certain patient groups, CCCs provide advantages for the researchers affiliated with them. The sheer size of the research departments of CCCs can, for instance, often justify the establishment of specialized core facilities within the CCC that can provide easy access to state-of-the-art technical equipment and the necessary expertise to handle this equipment, which would otherwise require a collaboration with an external partner [74]. Examples for this include core facilities dedicated to advanced microscopy techniques ("imaging facilities") and those dedicated to sequencing and analyzing large-scale genomic data ("genomic facilities").

Next to the availability of advanced technologies, centralizing patient treatment in one center also results in an increased number of fresh tumor samples, which are pivotal for cancer research. To streamline this process, CCCs usually establish dedicated biobanking initiatives to facilitate patient enrollment with supervisory committees overseeing access to patient materials [75]. Together, centralization and streamlining can result in the accrual of a high number of tumor samples, including from rare cancers such as pediatric cancer entities. In the few years of its existence, the Princess Máxima Center for Pediatric Oncology (Utrecht, NL) has, for example, enrolled 2.500 pediatric patients in its biobanking program, with an enrollment rate of 96%. The resulting availability of samples has already contributed to over 300 research projects since the start of the center [76].

Lastly, as with the availability of core facilities, the high patient volume at a CCC enables the use of techniques in diagnostics which are otherwise too expensive and/or intricate if used only sporadically. A good example

7

illustrating this, is the detection of fusion gene transcripts in pediatric cancer: As discussed in chapter 1, pediatric cancers usually show less mutations and simpler genomes than adult cancers [77], but are often characterized by the presence of aberrant fusion gene transcripts as the result of a chromosomal translocation event [78,79]. Conventional diagnostic techniques used to detect such fusion gene transcripts are fluorescence in-situ hybridization (FISH) or PCR-based assays, both of which require prior knowledge of the expected fusion partners. Besides these techniques, a number of commercially available targeted sequencing approaches have been developed which do not require prior knowledge of the involved fusion partners but are limited to the fusion gene transcripts they can detect [80]. Bulk mRNA-sequencing (RNA-seq) can efficiently detect fusion transcripts in an unbiased manner with more than 20 algorithms for fusion gene transcript detection described to-date [81]. However, RNA-seq is usually too expensive and intricate for smaller centers to introduce into routine diagnostics. CCCs, on the other hand, can make efficient use of RNA-seq for fusion gene transcript detection as a high sample throughput can reduce costs on a per patient basis. Given that RNA-seq is an unbiased technique, previously unknown fusion gene transcripts can be detected, which may result in a change of treatment for a given patient [82].

Besides these advantages, several disadvantages are associated with CCCs. Firstly, by centralizing patient care and research in one large center, competition between independent clinical and preclinical research centers in the region or even an entire country is diminished. While the role of competition on the overall quality of science may be debatable, with indications that rather collaboration, instead, can facilitate better science [83], the reality is that science is a competitive field when it comes to grant applications and funding. The latter is, for instance, illustrated by the fact that federal research funding in the US via the National Science Foundation is still only awarded to 28% of applicants despite a decline in applications over the last decade [84]. It may therefore be advisable to implement a system to assess the scientific quality and output of research groups within a CCC to ensure that researchers do not "rest on their laurels" once they have been recruited to a CCC.

Due to the broad availability of experts from various specialties, CCCs are also prime locations for the training of future specialists in cancer patient

care and research. The main advantage of having all necessary specialists for training in-house (i.e., not having to follow training in an external center), is also a clear disadvantage: studying abroad provides numerous benefits for the person going there (as summarized in [85]). Furthermore, mobility to conduct studies is viewed as key to a successful scientific career (as illustrated by these reports about performing a postdoctoral fellowship in the US or as someone from the US in Europe [86,87]). Lastly, returning specialists can implement acquired knowledge in their home CCC, thereby broadening the local expertise. Taken together, while it is convenient to have experts from all fields available in-house to train future generations of experts in cancer patient care and research, sending young staff members to other institutes to acquire new skills and broaden their horizon and perspective, is key to not falling into the trap of developing a too narrow view and portfolio (or, as a saying in German has it: "Um nicht nur im eigenen Saft zu schmoren.").

In summary, the establishment of CCCs has certainly improved cancer patient care and research by bundling resources and expertise. CCCs provide a number of advantages but come with challenges that require special attention and specific actions. The benefits CCCs provide on a regional or national level are similarly desirable on a multi-national level. For pediatric cancer, multi-national study groups have shown the potential of treatment studies enrolling patients in multiple countries. While such studies are intricate, they prove invaluable for sufficient patient accrual which ultimately enables addressing randomized study questions.

Concluding remarks

A thorough understanding of the molecular biology of RMS is crucial for improving treatment. In this light, our studies on signaling pathways and the single-cell landscape of RMS presented in this thesis have already expanded this understanding. Translating knowledge on the molecular biology of cancer to a clinical application needs good preclinical models, and we think that our RMS tumoroid models can facilitate this translation efficiently. I therefore hope that the studies presented in this thesis will contribute to improving the treatment and prognosis of patients suffering from RMS.

References

1.	Drost, J. *et al.* Use of CRISPR-modified human stem cell organoids to study the origin of mutational signatures in cancer. *Science (80-.).* **358**, 234–238 (2017).

2.	Vlachogiannis, G. *et al.* Patient-derived organoids model treatment response of metastatic gastrointestinal cancers. *Science (80-.).* **359**, 920–926 (2018).

3.	Custers, L. *et al.* Somatic mutations and single-cell transcriptomes reveal the root of malignant rhabdoid tumours. *Nat. Commun.* **12**, 1–11 (2021).

4.	Hinson, A. R. P. *et al.* Human rhabdomyosarcoma cell lines for rhabdomyosarcoma research: Utility and pitfalls. *Front. Oncol.* **3 JUL**, (2013).

5.	Stewart, E. *et al.* Orthotopic patient-derived xenografts of paediatric solid tumours. *Nature* **549**, 96–100 (2017).

6.	Kashi, V. P., Hatley, M. E. & Galindo, R. L. Probing for a deeper understanding of rhabdomyosarcoma: insights from complementary model systems. *Nat Rev Cancer* **15**, 426–439 (2015).

7.	Kim, J., Koo, B. K. & Knoblich, J. A. Human organoids: model systems for human biology and medicine. *Nature Reviews Molecular Cell Biology* vol. 21 571–584 (2020).

8.	Available Resources from the Childhood Solid Tumor Network | St. Jude Research. https://www.stjude.org/research/why-st-jude/data-tools/childhood-solid-tumor-network/available-resources.html.

9.	ITCC P4 - Paediatric Preclinical Proof Of Concept Platform. https://www.itccp4.eu/ (2022).

10.	Saldivar, J. C., Cortez, D. & Cimprich, K. A. The essential kinase ATR: ensuring faithful duplication of a challenging genome. *Nat. Rev. Mol. Cell Biol.* **18**, 622–636 (2017).

11.	Feng, X. *et al.* ATR inhibition potentiates ionizing radiation-induced interferon response via cytosolic nucleic acid-sensing pathways. *EMBO J.* **39**, (2020).

12.	Manzella, G. *et al.* Phenotypic profiling with a living biobank of primary rhabdomyosarcoma unravels disease heterogeneity and AKT sensitivity. *Nat. Commun.* **11**, 1–15 (2020).

13.	Fumagalli, A. *et al.* A surgical orthotopic organoid transplantation approach in mice to visualize and study colorectal cancer progression. *Nat. Protoc.* **13**, 235–247 (2018).

14.	Dekkers, J. F. *et al.* Long-term culture, genetic manipulation and xenotransplantation of human normal and breast cancer organoids. *Nat. Protoc.* **16**, 1936–1965 (2021).

15.	Grassi, L. *et al.* Organoids as a new model for improving regenerative medicine and cancer personalized therapy in renal diseases. *Cell Death Dis.* **10**, (2019).

16.	van de Vijver, M. J. *et al.* A Gene-Expression Signature as a Predictor of Survival in Breast Cancer. *N. Engl. J. Med.* **347**, 1999–2009 (2002).

17. Wang, M. *et al.* Validation of risk stratification models in acute myeloid leukemia using sequencing-based molecular profiling. *Leukemia* **31**, 2029–2036 (2017).

18. Liu, F. *et al.* Systematic comparative analysis of single-nucleotide variant detection methods from single-cell RNA sequencing data. *Genome Biol.* **20**, 242 (2019).

19. Serin Harmanci, A., Harmanci, A. O. & Zhou, X. CaSpER identifies and visualizes CNV events by integrative analysis of single-cell or bulk RNA-sequencing data. *Nat. Commun.* **11**, 89 (2020).

20. Haas, B. J. *et al.* Accuracy assessment of fusion transcript detection via read-mapping and de novo fusion transcript assembly-based methods. *Genome Biol.* **20**, 213 (2019).

21. Avila Cobos, F., Alquicira-Hernandez, J., Powell, J. E., Mestdagh, P. & De Preter, K. Benchmarking of cell type deconvolution pipelines for transcriptomics data. *Nat. Commun. 2020 111* **11**, 1–14 (2020).

22. Tickle, T., Tirosh, I., Georgescu, C., Brown, M. & Haas, B. inferCNV of the Trinity CTAT Project. Klarman Cell Observatory, Broad Institute of MIT and Harvard, Cambridge, MA, USA. (2019).

23. Jin, Z. *et al.* Single-cell gene fusion detection by scFusion. *Nat. Commun.* **13**, 1084 (2022).

24. Williamson, D. *et al.* Fusion gene-negative alveolar rhabdomyosarcoma is clinically and molecularly indistinguishable from embryonal rhabdomyosarcoma. *J Clin Oncol* **28**, 2151–2158 (2010).

25. Candelli, T. *et al.* Identification and characterization of relapse-initiating cells in MLL-rearranged infant ALL by single-cell transcriptomics. *Leukemia* **36**, 58–67 (2022).

26. Papalexi, E. & Satija, R. Single-cell RNA sequencing to explore immune cell heterogeneity. *Nat. Rev. Immunol.* **18**, 35–45 (2018).

27. Kather, J. N. *et al.* CD163+ immune cell infiltrates and presence of CD54+ microvessels are prognostic markers for patients with embryonal rhabdomyosarcoma. *Sci Rep* **9**, 9211 (2019).

28. Chen, L. *et al.* The Immunosuppressive Niche of Soft-Tissue Sarcomas is Sustained by Tumor-Associated Macrophages and Characterized by Intratumoral Tertiary Lymphoid Structures. *Clin. Cancer Res.* **26**, 4018–4030 (2020).

29. Bielack, S. S. *et al.* Prognostic Factors in High-Grade Osteosarcoma of the Extremities or Trunk: An Analysis of 1,702 Patients Treated on Neoadjuvant Cooperative Osteosarcoma Study Group Protocols. *J. Clin. Oncol.* **20**, 776–790 (2002).

30. Rodeberg, D. A. *et al.* Prognostic Significance of Tumor Response at the End of Therapy in Group III Rhabdomyosarcoma: A Report From the Children's Oncology Group. *J. Clin. Oncol.* **27**, 3705–3711 (2009).

7

31. Arndt, C. A. S., Hammond, S., Rodeberg, D. & Qualman, S. Significance of persistent mature rhabdomyoblasts in bladder/prostate rhabdomyosarcoma: Results from IRS IV. *J. Pediatr. Hematol. Oncol.* **28**, 563–567 (2006).

32. Heske, C. M. & Mascarenhas, L. Relapsed Rhabdomyosarcoma. *J. Clin. Med.* **10**, 804 (2021).

33. Aissa, A. F. *et al.* Single-cell transcriptional changes associated with drug tolerance and response to combination therapies in cancer. *Nat. Commun.* **12**, (2021).

34. Patel, A. G. *et al.* The myogenesis program drives clonal selection and drug resistance in rhabdomyosarcoma. *Dev. Cell* **57**, 1226-1240.e8 (2022).

35. García-Martínez, E. *et al.* Tumor-infiltrating immune cell profiles and their change after neoadjuvant chemotherapy predict response and prognosis of breast cancer. *Breast Cancer Res.* **16**, 488 (2014).

36. Hao, Y. *et al.* Integrated analysis of multimodal single-cell data. *Cell* **184**, 3573-3587.e29 (2021).

37. Seki, M. *et al.* Integrated genetic and epigenetic analysis defines novel molecular subgroups in rhabdomyosarcoma. *Nat Commun* **6**, 7557 (2015).

38. Muraro, M. J. *et al.* A Single-Cell Transcriptome Atlas of the Human Pancreas. *Cell Syst.* **3**, 385-394.e3 (2016).

39. Klein, A. M. *et al.* Droplet Barcoding for Single-Cell Transcriptomics Applied to Embryonic Stem Cells. *Cell* **161**, 1187–1201 (2015).

40. Macosko, E. Z. *et al.* Highly Parallel Genome-wide Expression Profiling of Individual Cells Using Nanoliter Droplets. *Cell* **161**, 1202–1214 (2015).

41. National Human Genome Research Institute (NHGRI). The Cost of Sequencing a Human Genome. *National Human Genome Research Institute (NHGRI)* 1 https://www.genome.gov/about-genomics/fact-sheets/Sequencing-Human-Genome-cost (2017).

42. Muir, P. *et al.* The real cost of sequencing: scaling computation to keep pace with data generation. *Genome Biol.* **17**, 53 (2016).

43. Abdelaal, T. *et al.* A comparison of automatic cell identification methods for single-cell RNA sequencing data. *Genome Biol.* **20**, 194 (2019).

44. Chen, W. *et al.* A multicenter study benchmarking single-cell RNA sequencing technologies using reference samples. *Nat. Biotechnol.* **39**, 1103–1114 (2021).

45. Tsimberidou, A. M., Fountzilas, E., Nikanjam, M. & Kurzrock, R. Review of precision cancer medicine: Evolution of the treatment paradigm. *Cancer Treat. Rev.* **86**, 102019 (2020).

46. Langenberg, K. P. S., Looze, E. J. & Molenaar, J. J. The Landscape of Pediatric Precision Oncology: Program Design, Actionable Alterations, and Clinical Trial Development. *Cancers (Basel).* **13**, 4324 (2021).

47. Eckstein, O. S. *et al.* Phase II Study of Selumetinib in Children and Young Adults With Tumors Harboring Activating Mitogen-Activated Protein Kinase Pathway Genetic Alterations: Arm E of the NCI-COG Pediatric MATCH Trial. *J. Clin. Oncol.* (2022) doi:10.1200/JCO.21.02840.

48. van Tilburg, C. M. *et al.* The Pediatric Precision Oncology INFORM Registry: Clinical Outcome and Benefit for Patients with Very High-Evidence Targets. *Cancer Discov.* **11**, 2764–2779 (2021).

49. Berlanga, P. *et al.* The European MAPPYACTS Trial: Precision Medicine Program in Pediatric and Adolescent Patients with Recurrent Malignancies. *Cancer Discov.* **12**, 1266–1281 (2022).

50. Wong, M. *et al.* Whole genome, transcriptome and methylome profiling enhances actionable target discovery in high-risk pediatric cancer. *Nat. Med.* **26**, 1742–1753 (2020).

51. Gatzweiler, C. *et al.* Functional Therapeutic Target Validation Using Pediatric Zebrafish Xenograft Models. *Cancers (Basel).* **14**, (2022).

52. Hegde, M. *et al.* Tumor response and endogenous immune reactivity after administration of HER2 CAR T cells in a child with metastatic rhabdomyosarcoma. *Nat. Commun.* **11**, 3549 (2020).

53. WHO. WHO Classification of Tumours: Soft Tissue and Bone Tumors. 5th Edition. (2020).

54. Wu, L. W. *et al.* Durable Clinical Response to Larotrectinib in an Adolescent Patient With an Undifferentiated Sarcoma Harboring an STRN - NTRK2 Fusion. *JCO Precis. Oncol.* 1–8 (2018) doi:10.1200/PO.18.00101.

55. Pfister, S. M. *et al.* A Summary of the Inaugural WHO Classification of Pediatric Tumors: Transitioning from the Optical into the Molecular Era. *Cancer Discov.* **12**, 331–355 (2022).

56. Shern, J. F. *et al.* Genomic Classification and Clinical Outcome in Rhabdomyosarcoma: A Report From an International Consortium. *J. Clin. Oncol.* **39**, 2859–2871 (2021).

57. Barr, F. G. *et al.* Genomic and clinical analyses of 2p24 and 12q13-q14 amplification in alveolar rhabdomyosarcoma: a report from the Children's Oncology Group. *Genes Chromosom. Cancer* **48**, 661–672 (2009).

58. Zhang, J. *et al.* Germline Mutations in Predisposition Genes in Pediatric Cancer. *N. Engl. J. Med.* **373**, 2336–2346 (2015).

59. Ripperger, T. *et al.* Childhood cancer predisposition syndromes-A concise review and recommendations by the Cancer Predisposition Working Group of the Society for Pediatric Oncology and Hematology. *Am. J. Med. Genet. Part A* **173**, 1017–1037 (2017).

60. Gatta, G. *et al.* Burden and centralised treatment in Europe of rare tumours: results of RARECAREnet—a population-based study. *Lancet Oncol.* **18**, 1022–1039 (2017).

7

61. Rare Cancer Classification - SEER Recodes. https://seer.cancer.gov/seerstat/variables/seer/raresiterecode/ (2022).

62. IRCI – Aspiring to improve the lives of patients with rare cancers. https://project.eortc.org/irci/ (2022).

63. Bogaerts, J. *et al.* Clinical trial designs for rare diseases: Studies developed and discussed by the International Rare Cancers Initiative. *Eur. J. Cancer* **51**, 271–281 (2015).

64. Skinner, H. D. *et al.* Outcomes of malignant tumors of the lacrimal apparatus. *Cancer* **117**, 2801–2810 (2011).

65. Majd, N. K. *et al.* Clinical characterization of adult medulloblastoma and the effect of first-line therapies on outcome; The MD Anderson Cancer Center experience. *Neuro-Oncology Adv.* **3**, (2021).

66. Weber, D. C. *et al.* Long-term outcome of patients with spinal myxopapillary ependymoma: treatment results from the MD Anderson Cancer Center and institutions from the Rare Cancer Network. *Neuro. Oncol.* **17**, 588–595 (2015).

67. Barr, R. D., Ferrari, A., Ries, L., Whelan, J. & Bleyer, W. A. Cancer in Adolescents and Young Adults. *JAMA Pediatr.* **170**, 495 (2016).

68. Ferrari, A. *et al.* Adolescents and young adults (AYA) with cancer: a position paper from the AYA Working Group of the European Society for Medical Oncology (ESMO) and the European Society for Paediatric Oncology (SIOPE). *ESMO Open* **6**, 100096 (2021).

69. Ishiki, H. *et al.* A Support System for Adolescent and Young Adult Patients with Cancer at a Comprehensive Cancer Center. *JMA J.* **5**, 44–54 (2022).

70. Kaal, S. E. J. *et al.* Empowerment in adolescents and young adults with cancer: Relationship with health-related quality of life. *Cancer* **123**, 4039–4047 (2017).

71. Husson, O. *et al.* Health-Related Quality of Life in Adolescent and Young Adult Patients With Cancer: A Longitudinal Study. *J. Clin. Oncol.* **35**, 652–659 (2017).

72. de Rojas, T. *et al.* Access to Clinical Trials for Adolescents and Young Adults With Cancer: A Meta-Research Analysis. *JNCI Cancer Spectr.* **3**, (2019).

73. Hotchkiss, M. E., Ahmad, Z. N. & Ford, J. S. Cancer–Peer Connection in the Context of Adolescent and Young Adult Cancer: A Qualitative Exploration. *J. Adolesc. Young Adult Oncol.* (2022) doi:10.1089/jayao.2021.0170.

74. Meder, D. *et al.* Institutional core facilities: prerequisite for breakthroughs in the life sciences. *EMBO Rep.* **17**, 1088–1093 (2016).

75. Annaratone, L. *et al.* Basic principles of biobanking: from biological samples to precision medicine for patients. *Virchows Arch.* **479**, 233–246 (2021).

76. Milestone for Biobank - Prinses Máxima Centrum - Research. https://research.prinsesmaximacentrum.nl/en/news-events/news/milestone-for-biobank (2022).

77. Lawrence, M. S. *et al.* Mutational heterogeneity in cancer and the search for new cancer-associated genes. *Nature* **499**, 214–218 (2013).

78. Roosen, M., Odé, Z., Bunt, J. & Kool, M. The oncogenic fusion landscape in pediatric CNS neoplasms. *Acta Neuropathol.* **143**, 427–451 (2022).

79. Angione, S. D. A. *et al.* Fusion Oncoproteins in Childhood Cancers: Potential Role in Targeted Therapy. *J. Pediatr. Pharmacol. Ther.* **26**, 541–555 (2021).

80. Heydt, C. *et al.* Detection of gene fusions using targeted next-generation sequencing: a comparative evaluation. *BMC Med. Genomics* **14**, 62 (2021).

81. Haas, B. J. *et al.* Accuracy assessment of fusion transcript detection via read-mapping and de novo fusion transcript assembly-based methods. *Genome Biol.* **20**, (2019).

82. Hehir-Kwa, J. Y. *et al.* Improved Gene Fusion Detection in Childhood Cancer Diagnostics Using RNA Sequencing. *JCO Precis. Oncol.* (2022) doi:10.1200/po.20.00504.

83. Thompson, E. Finding levers for culture change in science—the power of glocal. *EMBO Rep.* **20**, (2019).

84. Mervis, J. Odds for winning NSF grants improve as competition eases. *Science (80-.).* **376**, 684–684 (2022).

85. Netz, N. Who benefits most from studying abroad? A conceptual and empirical overview. *High. Educ.* **82**, 1049–1069 (2021).

86. Laursen, L. Coming to America : Doing a Postdoc in the U.S. https://lucaslaursen.com/coming-to-america-doing-a-postdoc-in-the-u-s/ (2010).

87. O'Brien, E. An American Postdoc Abroad | Science | AAAS. https://www.science.org/content/article/american-postdoc-abroad (2014).

7

Addendum

Nederlandse samenvatting
English summary
Deutsche Zusammenfassung
List of publications
Author contributions per chapter
Curriculum vitae
Acknowledgements

Nederlandse samenvatting

Rhabdomyosarcomen (RMS) zijn de meest voorkomende weke delen sarcomen bij kinderen en adolescenten (ongeveer 4% van alle pediatrische kankers). Hoewel de prognose voor patiënten met lokale ziekte vaak gunstig is, hebben patiënten die lijden aan gemetastaseerde ziekte en patiënten met een terugval of bij wie de tumoren bepaalde mutaties dragen, een slechte uitkomst, ondanks een intensieve behandeling. Therapeutische protocollen bestaan uit systemische chemotherapie en lokale therapie (meestal radiotherapie, vaak in combinatie met chirurgie). Overlevenden worden geconfronteerd met een grote behandelingslast met slopende langetermijneffecten, waaronder onvruchtbaarheid en schade aan meerdere organen zoals de nieren of het hart. Nieuwe therapeutische opties zijn dus nodig voor patiënten die aan RMS lijden, niet alleen om de prognose voor patiënten met een hoog risico te verbeteren, maar ook om de behandelingslast voor overlevenden te verminderen.

Therapeutische innovaties in de behandeling van RMS worden gehinderd door verschillende factoren, waaronder onvoldoende kennis van de belangrijkste gedereguleerde signaalroutes, een gebrek aan representatieve preklinische modellen en onvoldoende kennis over de cellulaire samenstelling van deze tumoren (d.w.z. de micro-omgeving). Met het onderzoek beschreven in dit proefschrift proberen wij deze uitdagingen aan te pakken om nieuwe therapeutische wegen te vinden die uiteindelijk de prognose voor patiënten met RMS kunnen verbeteren.

In het werk beschreven in hoofdstukken **2 tot en met 4** onderzoeken wij hoe afwijkende Hedgehog (Hh)-signalering bijdraagt aan het omzeilen van geprogrammeerde celdood (PCD, d.w.z. apoptose) in RMS-cellijnen, en hoe dit te verhelpen. Hh-signalering is van cruciaal belang voor een normale embryonale ontwikkeling en komt meestal niet tot expressie in volwassen weefsels. Afwijkende re-activatie van Hh-signalering is beschreven voor verschillende kanker soorten, waaronder RMS. Het bevordert tumor ontwikkeling door proliferatie en ontwijken van apoptose te induceren. Therapie die focust op Hh-signalering door zogenaamde Hedgehog Pathway-inhibitoren (HPI) is dus een veelbelovende therapie optie voor de behandeling van patiënten met RMS.

Ten eerste laten wij in **hoofdstuk 2** zien dat het door de FDA goedgekeurde HPI arseentrioxide (ATO) Hh-signalering blokkeert in RMS-cellijnen door het remmen van de signalering route van de belangrijkste transcriptiefactor (TF) GLI1. Bovendien veroorzaakt ATO intrinsieke apoptose in deze cellijnen door het induceren van het pro-apoptotische BH3-only eiwit NOXA. Belangrijk is dat apoptose-inductie verder wordt versterkt door het combineren van ATO met anti-microtubulus geneesmiddelen zoals vincristine, die standaard zorg zijn bij de behandeling van RMS. Alles bij elkaar illustreert deze studie het potentieel van het remmen van Hh-signalering voor het optimaliseren van de behandeling van RMS.

Vervolgens onderzoeken wij in **hoofdstuk 3** het mechanisme hoe inhibitie van Hh-signalering NOXA-expressie induceert. NOXA is een *bonafide* transcriptioneel doelwit van functioneel P53 dat de RMS-cellijnen in dit onderzoek missen vanwege inactiverende mutaties in het *TP53*-gen. Door farmacologische remming en genetische uitschakeling van GLI1 te combineren en, *vice versa*, m.b.v. overexpressie van GLI1, vinden wij dat de actieve vorm van P73 (d.w.z. TAp73), die P53 kan vervangen om NOXA te induceren, een vergelijkbare regulatie door Hh-signalering getoond wordt als NOXA. Genetische silencing van TAp73 verhindert NOXA-inductie door HPI echter niet, wat aangeeft dat TAp73 slechts mede wordt gereguleerd door Hh-signalering en NOXA zelf niet rechtstreeks reguleert. Om de link tussen Hh-signalering en co-gereguleerde NOXA en TAp73 te vinden, zochten wij naar TF-en waarvan is gemeld dat ze NOXA en TAp73 reguleren en onderzochten wij hun regulatie door Hh-signalering. Wij vinden dat EGR1 wordt gereguleerd door GLI1 en dat genetische uitschakeling van EGR1 inderdaad de NOXA- en TAp73-niveaus tegelijkertijd in RMS-cellen verlaagt. In conclusie, stellen wij met deze studie een model vast waarin afwijkende Hh-signalering bijdraagt aan het ontwijken van apoptose door EGR1 expressie te verlagen, wat op zijn beurt NOXA en TAp73 naar beneden reguleert.

In **hoofdstuk 4** vragen wij ons vervolgens af hoe de werkzaamheid van HPI verder kan worden verbeterd, rekening houdend met het werkingsmechanisme dat wij hierboven hebben geïdentificeerd (d.w.z. het induceren van NOXA-expressie). NOXA bindt het anti-apoptotische eiwit MCL-1 en leidt daardoor tot zijn proteasomale afbraak, waardoor cellen naar apoptose worden

A

geduwd. Aangezien HPI-monotherapie niet altijd voldoende is om celdood in RMS-cellen te induceren, veronderstellen wij dat NOXA-inductie door HPI's onvoldoende is om alle MCL-1-moleculen in deze cellen te remmen en dat het combineren van HPI-behandeling met aanvullende directe farmacologische blokkade van MCL-1 synergistisch kan werken om apoptose te induceren, wat inderdaad het geval is. Door farmacologische remming van GLI1 en genetische uitschakeling van MCL-1 en *vice versa* te combineren, laten wij zien dat synergisme inderdaad specifiek afhankelijk is van gecombineerde GLI1/MCL-1-blokkade. Belangrijk is dat wij met behulp van co-immunoprecipitatie laten zien dat synergetische celdood inductie niet alleen afhangt van de inductie van NOXA, maar ook van het verplaatsen van het pro-apoptotisch eiwit BIM van MCL-1 naar het anti-apoptotisch eiwit BCL-x_L, waardoor het evenwicht in de cel naar apoptose wordt geduwd. Concluderend verfijnt deze studie ons mechanistische model van hoe HPI's apoptose kunnen induceren en wordt het potentieel benadrukt voor behandeling van RMS patiënten in combinatie met andere middelen.

Aangezien de studies in hoofdstuk 2 tot en met 4 zich beperkten tot RMS-cellijnen, begonnen wij de ontwikkeling van nieuwe preklinische *in vitro* modellen die de eigenschappen van tumoren beter weerspiegelen, waardoor ze mogelijk een voorspellende waarde hebben voor de respons op geneesmiddelen. Hiertoe hebben wij in **hoofdstuk 5** protocollen ontwikkeld en beschreven voor het opzetten van tumor-organoïde (tumoroïde) modellen van RMS vanuit patiënten materiaal. Tumoroïde modellen zijn ontwikkeld voor verschillende, voornamelijk epitheliale kanker soorten en worden veel toegepast in kankeronderzoek. In onze studie tonen uitgebreide karakteriseringsexperimenten met behulp van RT-qPCR, histologie, bulk mRNA-seq, whole-exome sequencing en single cell mRNA-seq (scRNA-seq) aan dat RMS-tumoroïde modellen patiënten tumoren in hoge mate weerspiegelen met *in vitro* behouden genexpressie heterogeniteit evenals behouden klonale samenstelling. Geneesmiddelenscreening op de tumoröide modellen identificeert bekende gevoeligheden van RMS, wat de voorspellende waarde van deze modellen aangeeft. Ten slotte laten wij zien dat door gebruik te maken van genomische bewerking door CRISPR/Cas9, RMS-tumoroïde modellen kunnen worden aangepast om mutatieachtergronden met een hoog risico (d.w.z. verlies van P53) na te maken. Samenvattend, beschrijven

wij de eerste grondig gekarakteriseerde tumoroïde modellen collectie van RMS tot nu toe, die, gezien hun sterke gelijkenis met tumoren van patiënten, voorspellende studies mogelijk maakt om uiteindelijk nieuwe therapeutische wegen voor patiënten met RMS te ontwikkelen. De resultaten laten ook voor het eerst zien dat het mogelijk is om tumoroïde modellen te genereren uit tumoren met een mesenchymale oorsprong.

Geïntrigeerd door de indicaties van behouden cellulaire heterogeniteit van RMS-tumoren *in vitro* in onze tumoroïde modellen, hebben wij ten slotte besloten de cellulaire samenstelling van primaire RMS-tumoren te analyseren met behulp van scRNA-seq. Dit staat beschrijven in **hoofdstuk 6**. Hier identificeren wij verschillende transcriptionele programma's die onderscheid maken tussen de twee belangrijkste RMS-subtypen (d.w.z. fusie-negatief, FN en fusie-positief, FP) zoals verwacht en al eerder beschreven. Interessant is dat FN- en FP-RMS-cellen, wanneer vergeleken met celtypen die optreden tijdens normale spierontwikkeling, gelijkenis laten zien met cellen in verschillende stadia van deze ontwikkeling, wat mogelijk wijst op verschillende oorsprongscellen van deze twee RMS-subtypen. Verder identificeren wij transcriptionele subprogramma's binnen de twee belangrijkste RMS-subtypes die niet alleen indicatief kunnen zijn voor het biologische gedrag van de cellen (bijv. cellen die "stemness" markers vertonen zoals spierstamcellen, d.w.z. satellietcellen), maar ook voorspellend zijn voor de uitkomst van de behandeling van de patiënt, zoals gevalideerd wordt in een onafhankelijk bulk sequencing cohort van RMS. Ten slotte beschrijven wij niet alleen kanker, maar ook gezonde cellen in het tumor materiaal. Wij identificeren met name verschillende clusters van immuun cellen die verschillen tussen FN- en FP-RMS wat betreft hun activeringsstatus. Wij beschrijven hierbij een mogelijke interactie tussen FP-RMS-tumor en immuun cellen die kan resulteren in een immuun onderdrukkende micro-omgeving, waardoor de werkzaamheid van bepaalde immuuntherapieën mogelijk wordt gehinderd. Samenvattend bieden wij een diepgaande analyse van de cellulaire samenstelling van primaire RMS met indicaties van een immuun onderdrukkende micro-omgeving die therapeutisch kan worden gebruikt.

Concluderend presenteert dit proefschrift mechanistische inzichten in ontwikkelingspaden die verkeerd zijn gegaan in RMS en hoe deze kunnen

A

worden gebruikt om nieuwe combinatietherapieën te ontwikkelen. Met behulp van scRNA-seq werpen wij bovendien licht op de tumor-micro-omgeving van RMS, die mogelijk kan worden gebruikt om nieuwe immuun-therapeutische wegen te ontwikkelen voor behandeling van deze tumoren. Ten slotte beschrijven wij, om de vertaling van deze moleculaire inzichten te vergemakkelijken, nieuwe preklinische modellen van RMS die meer lijken op tumoren van patiënten, waardoor ze een hogere voorspellende waarde hebben dan conventionele preklinische modellen zoals cellijnen. Wij hopen dat deze onderzoeken samen nieuwe, minder toxische en effectievere therapieën mogelijk maken voor patiënten die lijden aan RMS om uiteindelijk de prognose te verbeteren en de toxiciteit op lange termijn te verminderen.

English summary

Rhabdomyosarcomas (RMS) are the most common soft tissue sarcomas in children and adolescents, comprising 4% of all pediatric cancers. While the prognosis for patients with local disease is often favorable, patients suffering from metastatic disease, relapse or whose tumors bear certain mutations face poor outcomes despite intense treatment. Therapeutic regimens consist of systemic chemotherapy and local therapy which is most often radiotherapy but can also comprise surgery. Survivors face a considerable treatment burden with debilitating long-term effects including infertility and damage to multiple organs such as the kidneys or the heart. Novel therapeutic options are therefore necessary for patients suffering from RMS to not only improve the prognosis for patients at high-risk but also to reduce the treatment burden for survivors.

Therapeutic innovations in the treatment of RMS have been hampered by several factors including an insufficient understanding of the key deregulated signaling pathways, a lack of representative preclinical models, as well as insufficient knowledge on the cellular composition of these tumors (i.e., the microenvironment). Through the work described in this thesis, we aimed to address these challenges and to provide rationales for novel therapeutic avenues which might ultimately improve prognosis for patients suffering from RMS.

In the work described in **chapters 2 to 4**, we investigated how aberrant Hedgehog (Hh) signaling contributes to the evasion of programmed cell death (PCD, i.e., apoptosis) in RMS cell lines and how to overcome this. Hh signaling is critical for normal embryonal development and is usually silenced in mature tissues. Aberrant reactivation of Hh signaling has been reported for several cancer entities including RMS. Here, it promotes tumorigenesis by inducing proliferation and evasion from apoptosis. Thus, targeting Hh signaling by so-called Hedgehog pathway inhibitors (HPI) is a promising avenue for the treatment of patients with RMS.

First, we show in **chapter 2** that the FDA-approved HPI arsenic trioxide (ATO) blocks Hh signaling in RMS cell lines downstream, at the level of the key transcription factor (TF) GLI1 by abrogating its transcriptional activity.

A

Furthermore, ATO triggers intrinsic apoptosis in these cell lines by inducing the pro-apoptotic BH3-only protein NOXA. Importantly, apoptosis induction is further amplified by combining ATO with anti-microtubule drugs such as vincristine which are standard of care in the treatment of RMS. Taken together, this study illustrates the potential that targeting Hh signaling may hold in optimizing the treatment of RMS.

Next, we explore in **chapter 3** how abrogation of Hh signaling mechanistically induces NOXA expression. NOXA is a *bona fide* transcriptional target of functional P53 which the RMS cell lines in the study lack due to inactivating mutations in the *TP53* gene. By combining pharmacological inhibition and genetic silencing of GLI1 and, *vice versa*, overexpressing GLI1, we find that the active form of P73 (i.e., TAp73), which can substitute for P53 to induce NOXA, shows a similar regulation by Hh signaling as NOXA. However, genetic silencing of TAp73 does not prevent NOXA induction by HPI, indicating that TAp73 is merely co-regulated by Hh signaling and does not directly regulate NOXA itself. To find the link between Hh signaling and co-regulation of NOXA and TAp73, we searched for TFs that were reported to regulate NOXA and TAp73 and tested their regulation by Hh signaling. We find that EGR1 is regulated by GLI1 and that genetic silencing of EGR1 indeed reduces NOXA and TAp73 levels simultaneously in RMS cells. Taken together, we establish with this study a model in which aberrant Hh signaling contributes to evasion of apoptosis by downregulating EGR1 which, in turn, downregulates NOXA and TAp73.

In **chapter 4** we next ask how the efficacy of HPI could be further enhanced considering the mechanism of action we identified above (i.e., inducing NOXA expression). NOXA binds the anti-apoptotic protein MCL-1 and thereby leads to its proteasomal degradation, pushing cells towards apoptosis. As HPI monotherapy is not always sufficient to induce cell death in RMS cells, we hypothesize that NOXA induction by HPIs is insufficient to occupy all MCL-1 molecules in these cells and that combining HPI treatment with additional direct pharmacological blockade of MCL-1 may synergize to induce apoptosis, which is indeed the case. By combining pharmacological inhibition of GLI1 and genetic silencing of MCL-1 and *vice versa*, we show that synergism is indeed specifically dependent on the combined GLI1/MCL-1 blockade.

Importantly, using co-immunoprecipitation, we find that synergistic cell death induction depends not only on the induction of NOXA but also on the shuttling of pro-apoptotic protein BIM from MCL-1 to anti-apoptotic protein BCL-x$_L$, thereby further shifting the balance towards apoptosis. In conclusion, this study refines our mechanistic model of how HPI can induce apoptosis and underscores its potential for treating RMS when used in combination.

As the studies in chapters 2 to 4 were limited to RMS cell lines, we sought to generate novel preclinical *in vitro* models that better reflect the characteristics of patient tumors, thereby potentially possessing predictive value for drug response. To this end, we developed and describe protocols on how to establish patient-derived tumor organoid (tumoroid) models of RMS in **chapter 5**. Tumoroid models have been established for various, predominantly epithelial cancer entities and are proving to be very useful for cancer research. In our study, extensive characterization using RT-qPCR, histology, bulk mRNA-seq, whole-exome sequencing and single cell mRNA-seq (scRNA-seq) show that RMS tumoroid models reflect patient tumors to a high extent with indications of *in vitro* retained transcriptional and clonal heterogeneity. Drug screening identified established susceptibilies of RMS, indicating the predictive value that these models hold. Lastly, we show that by using CRISPR/Cas9 genomic editing, RMS tumoroid models can be modified to mimic high-risk mutational backgrounds (i.e., loss of P53). In summary, we describe the first thoroughly characterized tumoroid collection of RMS to-date which may, given their close resemblance to patient tumors, enable predictive studies to ultimately establish novel therapeutic avenues for patients with RMS. The work also thoroughly establishes for the first time that tumoroid models can be derived from tumors of mesenchymal origin.

Intrigued by the indications of retained cellular heterogeneity of RMS tumors *in vitro* in our tumoroid models, we lastly sought to analyze the cellular composition of primary RMS tumors using scRNA-seq which we describe in **chapter 6**. Here, we identify distinct transcriptional programs differentiating between the two major RMS subtypes (i.e., fusion-negative, FN, and fusion-positive, FP) as expected and previously reported. Interestingly, when compared to cell types that occur during normal muscle development, FN- and FP-RMS cells resemble cells at different stages of this development,

A

potentially indicating distinct cells of origin for those two RMS subtypes. Furthermore, we identify transcriptional subprograms within the two main RMS subtypes which may not only be indicative of the biological behavior of the cells (e.g., cells displaying stemness markers like muscle stem cells, i.e., satellite cells), but are also predictive of patient outcome as validated in an independent bulk sequencing cohort of RMS. Lastly, we describe not only tumor but also healthy cells within the tumor samples. Notably, we identify different clusters of immune cells which are distinct between FN- and FP-RMS concerning their activation state. This results in a potential interaction between FP-RMS tumor and immune cells which may cause an immune-suppressive microenvironment, thereby potentially hampering immunotherapy efficacy. In summary, we provide an in-depth analysis on the cellular composition of primary RMS with indications of an immune-suppressive microenvironment which may be therapeutically leveraged.

In conclusion, this thesis presents mechanistic insights on developmental pathways gone awry in RMS and how targeting those can be used to develop novel combination therapies. Using scRNA-seq, we furthermore shed light on the tumor microenvironment of RMS which may potentially be used to inform novel immunotherapeutic avenues in the treatment of these tumors. Lastly, to facilitate the translation of these molecular insights, we describe novel preclinical models of RMS that more closely resemble patient tumors, thereby possessing a higher predictive value than conventional preclinical models such as cell lines. We hope that together these studies enable new, less toxic, and more efficacious therapies for patients suffering from RMS to ultimately improve prognosis and reduce long-term toxicity.

Deutsche Zusammenfassung

Rhabdomyosarkome (RMS) sind die häufigsten Weichteilsarkome bei Kindern und Jugendlichen und machen 4 % aller pädiatrischen Krebserkrankungen aus. Während die Prognose für Patienten mit lokalisierter Tumorerkrankung oft günstig ist, haben Patienten mit metastasierter Erkrankung, Rezidiven oder deren Tumoren bestimmte Mutationen aufweisen trotz intensiver Behandlung eine schlechte Prognose. Diese Behandlung besteht aus systemischer Chemotherapie und Lokaltherapie, meist in Form von Strahlentherapie, oder einem zusätzlichen chirurgischen Eingriff. Patienten, die die Erkrankung überleben, sind schwerwiegenden Langzeitfolgen wie Unfruchtbarkeit und Schäden an Organen wie den Nieren oder dem Herzen ausgesetzt. Daher sind neue therapeutische Behandlungsmöglichkeiten für Patienten mit RMS erforderlich, um nicht nur die Prognose für Patienten mit erhöhtem Risiko zu verbessern, sondern auch die Behandlungsbelastung für Überlebende zu verringern.

Therapeutische Innovationen bei der Behandlung von RMS werden durch mehrere Faktoren behindert, darunter einem eingeschränkten Verständnis der wichtigsten deregulierten Signalwege, einem Mangel an repräsentativen präklinischen Modellen sowie einem unzureichenden Wissen über die zelluläre Zusammensetzung dieser Tumoren (die sog. Mikroumgebung). Mit den in dieser Dissertation beschriebenen Studien wollten wir diese Herausforderungen angehen, um eine Rationale für neue therapeutische Optionen zu etablieren, die letztendlich die Prognose für Patienten mit RMS verbessern könnten.

In den in **Kapiteln 2 bis 4** beschriebenen Studien untersuchten wir, wie ein fehlgesteuerter Hedgehog (Hh) Signalweg zur Umgehung von programmiertem Zelltod (PCD, d.h., Apoptose) in RMS-Zelllinien beiträgt und wie dies überwunden werden kann. Der Hh Signalweg ist entscheidend für eine normale embryonale Entwicklung und wird normalerweise in reifen Geweben unterdrückt. Eine abnormale Reaktivierung des Hh Signalweges wurde für mehrere Krebsarten einschließlich RMS berichtet. Hier fördert der Signalweg die Tumorentstehung, indem er die Proliferation und die Umgehung von Apoptose induziert. Daher ist das Blockieren eines fehlgesteuerten Hh

A

Signalweges durch sogenannte Hedgehog-Pathway-Inhibitoren (HPI) ein vielversprechender Ansatz in der Behandlung von Patienten mit RMS.

Zunächst zeigen wir in **Kapitel 2**, dass der von der FDA zugelassene HPI Arsentrioxid (ATO) den Hh Signalweg in RMS-Zelllinien stromabwärts auf der Ebene des Schlüsseltranskriptionsfaktors (TF) GLI1 blockiert, indem er dessen transkriptionelle Aktivität aufhebt. Darüber hinaus löst ATO in diesen Zelllinien intrinsische Apoptose aus, indem es das pro-apoptotische BH3-only-Protein NOXA induziert. Bedeutend ist, dass die Induktion von Apoptose durch die Kombination von ATO mit Anti-Mikrotubuli-Medikamenten wie Vincristin, die bei der Behandlung von RMS eine Standardmedikation darstellen, weiter verstärkt wird. Zusammengefasst veranschaulicht diese Studie das Potenzial, welches das Blockieren eines fehlgesteuerten Hh Signalweges bei der Optimierung der Behandlung von RMS haben kann.

Als Nächstes untersuchen wir in **Kapitel 3**, wie das Blockieren des Hh Signalweges mechanistisch die Expression von NOXA induziert. NOXA ist ein transkriptionelles *bona fide* Ziel von aktivem P53, das den RMS-Zelllinien in dieser Studie aufgrund von inaktivierenden Mutationen im *TP53*-Gen fehlt. Durch die Kombination von pharmakologischer Hemmung und konnnten wir beobachten, dass die aktive Form von P73 (i.e., TAp73), die P53 ersetzen kann und ebenfalls die Expression von NOXA induziert, eine ähnliche Regulation durch den Hh Signalweg wie NOXA aufweist. Das genetische Silencing von TAp73 verhindert jedoch nicht die Induktion von NOXA durch HPI, was darauf hindeutet, dass TAp73 lediglich durch den Hh Signalweg co-reguliert wird und NOXA selbst nicht direkt reguliert. Um die Verbindung zwischen dem Hh Signalweg und co-reguliertem NOXA und TAp73 zu identifizieren, untersuchten wir TFs, von denen bekannt ist, dass sie NOXA und TAp73 regulieren, und testeten deren Regulation durch den Hh Signalweg. Hier beobachteten wir, dass EGR1 durch GLI1 reguliert wird und dass die genetische Stummschaltung von EGR1 tatsächlich gleichzeitig die Spiegel von NOXA und TAp73 in RMS-Zellen reduziert. Zusammengefast etablieren wir mit dieser Studie ein Modell, in dem ein fehlgesteuerter Hh Signalweg zur Umgehung von Apoptose beiträgt, indem EGR1 herunterreguliert wird, was wiederum NOXA und TAp73 herunterreguliert.

In **Kapitel 4** untersuchen wir als Nächstes, wie die Wirksamkeit von HPI unter Berücksichtigung des oben identifizierten Wirkmechanismus (i.e., der Induktion von NOXA) weiter verbessert werden könnte. NOXA bindet das anti-apoptotische Protein MCL-1 und führt dadurch zu dessen proteasomalem Abbau, wodurch Zellen in Richtung Apoptose getrieben werden. Da eine HPI-Monotherapie nicht immer ausreicht, um Zelltod in RMS-Zellen zu induzieren, nehmen wir an, dass die Induktion von NOXA durch HPIs nicht ausreicht, um alle MCL-1-Moleküle in diesen Zellen zu besetzen. Wir nehmen ferner an, dass eine Kombination aus einer HPI-Behandlung mit einer zusätzlichen, direkten pharmakologischen Hemmung von MCL-1 synergetisch wirkt, um Apoptose zu induzieren, was tatsächlich der Fall ist. Durch die Kombination einer pharmakologischen Hemmung von GLI1 und einer genetischen Stummschaltung von MCL-1 (und umgekehrt) zeigen wir, dass der beschriebene Synergismus tatsächlich spezifisch von einer kombinierten GLI1/MCL-1-Blockade abhängt. Mithilfe von Co-Immunpräzipitations-Experimenten stellten wir fest, dass die synergistische Zelltod-Induktion nicht nur von der Induktion von NOXA abhängt, sondern auch vom Shuttlen des pro-apoptotischen Proteins BIM von MCL-1 zum anti-apoptotischen Protein BCL-x$_L$, wodurch das Gleichgewicht der Zellen weiter in Richtung Apoptose verschoben wird. Zusammenfassend verfeinert diese Studie unser mechanistisches Modell, wie HPI Apoptose induzieren können, und unterstreicht das Potenzial einer Kombinationstherapie zur Behandlung von RMS.

Da die Studien in den Kapiteln 2 bis 4 auf RMS-Zelllinien beschränkt waren, versuchten wir, neue präklinische *In-vitro*-Modelle zu generieren, die die Eigenschaften von Patiententumoren besser widerspiegeln und dadurch möglicherweise das Ansprechen auf Medikamente besser vorhersagen. Zu diesem Zweck haben wir in **Kapitel 5** Protokolle zur Etablierung von Tumor-Organoid-Modellen aus frischem Tumormaterial (Tumoroid-Modelle) von RMS Patienten entwickelt und beschrieben. Tumoroid-Modelle wurden bereits für verschiedene, überwiegend epitheliale Krebsarten etabliert und erweisen sich als sehr nützlich in der Krebsforschung. In unserer Studie zeigen wir mittels umfangreicher Charakterisierung in Form von RT-qPCR, Histologie, bulk mRNA-seq, whole exome sequencing und single cell

A

mRNA-seq (scRNA-seq), dass RMS-Tumoroid-Modelle Patiententumoren in hohem Maße widerspiegeln, mit Hinweisen auf die Erhaltung von transkriptioneller und klonaler Heterogenität *in vitro*. Mittels drug screening konnten wir ein Ansprechen auf die Standardmedikation von RMS Tumoren nachweisen, was darauf hinweist, dass diese Modelle repräsentativ sind und Therapieansprechen vorhersagen können. Zuletzt zeigen wir, dass RMS-Tumoroid-Modelle mittels CRISPR/Cas9 auf Genomebene modifiziert werden können, um Hochrisiko-Mutationen (i.e., der Verlust von P53) nachzuahmen. Zusammenfassend beschreiben wir die bisher erste, ausführlich charakterisierte Tumoroid-Modell Sammlung von RMS, die aufgrund ihrer großen Ähnlichkeit mit Patiententumoren prädiktive Studien ermöglichen könnten, um letztendlich neue therapeutische Ansätze für Patienten mit RMS zu etablieren. Die Studie zeigt auch zum ersten Mal, dass Tumoroid-Modelle von Tumoren mesenchymalen Ursprungs etabliert werden können.

Fasziniert von den Hinweisen auf eine erhaltene zelluläre Heterogenität von RMS-Tumoren in unseren Tumoroid-Modellen, versuchten wir schließlich, die zelluläre Zusammensetzung von primären RMS-Tumoren unter Verwendung von scRNA-seq zu analysieren, was wir in **Kapitel 6** beschreiben. Hier identifizieren wir verschiedene Transkriptionsprogramme, die sich bei den beiden Haupt-RMS-Subtypen (i.e., Fusions-negativ, FN, und Fusions-positiv, FP) wie erwartet und zuvor berichtet unterscheiden. Interessanterweise ähneln FN- und FP-RMS-Zellen unterschiedlichen Zelltypen, die während der normalen Entwicklung von Muskeln auftreten. Dies weist möglicherweise auf unterschiedliche Ursprungszellen für diese beiden RMS-Subtypen hin. Darüber hinaus identifizieren wir transkriptionelle Unterprogramme innerhalb der beiden Haupt-RMS-Subtypen, die möglicherweise nicht nur auf das biologische Verhalten der Zellen hinweisen (z.B. Zellen, die Stammzellmarker wie Muskelstammzellen, i.e., Satellitenzellen aufweisen), sondern auch das Überleben eines Patienten vorhersagen können, was wir in einer unabhängigen bulk sequencing Kohorte von RMS validieren konnten. Schließlich charakterisieren wir nicht nur Krebs-, sondern auch gesunde Zellen in den Tumorproben. Insbesondere identifizieren wir verschiedene Cluster von Immunzellen, die sich hinsichtlich ihres Aktivierungszustands zwischen FN- und FP-RMS unterscheiden. Hierdurch konnten wir eine

potenzielle Wechselwirkung zwischen FP-RMS-Tumor- und Immunzellen beschreiben, die eine immunsuppressive Mikroumgebung verursachet und dadurch möglicherweise die Wirksamkeit von Immuntherapien beeinträchtigen kann. In Summe umfasst unsere Studie eine eingehende Analyse der zellulären Zusammensetzung von primären RMS mit Hinweisen auf eine immunsuppressive Mikroumgebung, was therapeutisch genutzt werden könnte.

Zusammenfassend präsentiert diese Dissertation mechanistische Einblicke in entwicklungsbiologische Signalwege, die bei RMS fehlgesteuert sind, und wie deren Blockade zur Entwicklung neuartiger Kombinationstherapien genutzt werden kann. Unter Verwendung von scRNA-seq beleuchten wir außerdem die Tumormikroumgebung von RMS, die möglicherweise Hinweise darauf geben kann, wie neue immuntherapeutische Ansätze in der Behandlung dieser Tumoren zu gestalten sind. Um die Translation dieser molekularen Erkenntnisse zu erleichtern, beschreiben wir schließlich neuartige präklinische Modelle von RMS, die Patiententumoren ähnlicher sind und dadurch einen höheren Vorhersagewert besitzen als herkömmliche präklinische Modelle wie Zelllinien. Wir hoffen, dass diese Studien zusammen neue, weniger toxische und wirksamere Therapien für Patienten mit RMS ermöglichen, um letztendlich deren Prognose zu verbessern und Langzeitfolgen zu reduzieren.

A

List of publications

Publications described in this thesis:

Chapter 2:   <u>Meister, M. T.</u> *et al.* Arsenic trioxide induces NOXA-dependent apoptosis in rhabdomyosarcoma cells and synergizes with antimicrotubule drugs. *Cancer Lett* **381**, 287–295 (2016).

Chapter 3:   <u>Meister, M. T.</u>, Boedicker, C., Klingebiel, T. & Fulda, S. Hedgehog signaling negatively co-regulates BH3-only protein NOXA and TAp73 in *TP53*-mutated cells. *Cancer Lett* **429**, 19–28 (2018).

Chapter 4:   <u>Meister, M. T.</u> *et al.* Concomitant targeting of Hedgehog signaling and MCL-1 synergistically induces cell death in Hedgehog-driven cancer cells. *Cancer Lett.* **465**, 1–11 (2019).

Chapter 5:   <u>Meister, M. T.</u> *et al.* Mesenchymal tumor organoid models recapitulate rhabdomyosarcoma subtypes. *EMBO Mol. Med.* **14**, (2022).

Chapter 6:   DeMartino, J.*, <u>Meister, M. T.</u>*, Visser L.* *et al*. Single-cell transcriptomics reveals immune suppression and cell states predictive of patient outcomes in rhabdomyosarcoma. *Under review. Preprint available at bioRxiv: https://doi.org/10.1101/2022.07.15.497944.*

* These authors contributed equally to this work.

Other publications in chronological order:

1. Meister, M. T., Voss, S. & Schwabe, D. Treatment of EBV-associated nodular sclerosing Hodgkin lymphoma in a patient with ataxia telangiectasia with brentuximab vedotin and reduced COPP plus rituximab. *Pediatr. Blood Cancer* **62**, 2018–2020 (2015).

2. Faqar-Uz-Zaman, S. F., Heinicke, U., Meister, M. T., Vogler, M. & Fulda, S. BCL-x$_L$-selective BH3 mimetic sensitizes rhabdomyosarcoma cells to chemotherapeutics by activation of the mitochondrial pathway of apoptosis. *Cancer Lett.* **412**, 131–142 (2018).

3. Merker, M.*, Meister M. T.* *et al.* Haploidentical allogeneic hematopoietic stem cell transplantation in patients with high-risk soft tissue sarcomas: results of a single-center prospective trial. *Bone Marrow Transplant.* **53**, 891–894 (2018).

4. Merker, M., Meister M. T., *et al.* Adoptive cellular immunotherapy for refractory childhood cancers: a single center experience. *Oncotarget* **10**, 6138–6151 (2019).

5. Boedicker, C., […], Meister M. T. *et al.* Co-inhibition of BET proteins and PI3Kα triggers mitochondrial apoptosis in rhabdomyosarcoma cells. *Oncogene* **39**, 3837–3852 (2020).

6. Meister, M. T. *et al.* Malignant peripheral nerve sheath tumors in children, adolescents, and young adults: Treatment results of five Cooperative Weichteilsarkom Studiengruppe (CWS) trials and one registry. *J. Surg. Oncol.* **122**, 1337–1347 (2020).

7. van Tilburg, C. M., […], Meister M. T. *et al.* The Pediatric Precision Oncology INFORM Registry: Clinical Outcome and Benefit for Patients with Very High-Evidence Targets. *Cancer Discov.* **11**, 2764–2779 (2021).

8. Erdogdu, U., […], Meister M. T. *et al.* Selective BH3 mimetics synergize with BET inhibition to induce mitochondrial apoptosis in rhabdomyosarcoma cells. *Neoplasia* **24**, 109–119 (2022).

A

9. van Spronsen, R., […], <u>Meister M. T.</u> *et al.* Infantile fibrosarcoma with an *EGFR* kinase domain duplication: Underlining a close relationship with congenital mesoblastic nephroma and highlighting a similar morphological spectrum. *Ann. Diagn. Pathol.* **57**, 151885 (2022).

10. Langenberg, K. P. S., <u>Meister M. T.*, Bakhuizen J. J.*, Boer J. M.*</u> *et al.* Implementation of paediatric precision oncology into clinical practice: The Individualized Therapies for Children with cancer program 'iTHER'. *Eur. J. Cancer* **175**, 311–325 (2022).

11. Hiemcke-Jiwa, L. S.*, <u>Meister M. T.</u>*, *et al. NTRK* rearrangements in a subset of NF1-related malignant peripheral nerve sheath tumors as novel actionable target. *Acta Neuropathol.* (2022) doi:10.1007/s00401-022-02515-3.

* These authors contributed equally to this work.

Author contributions per chapter

Chapter 1: M.M. wrote the chapter, supervised by F.H. and M.v.N.

Chapter 2: Conceptualization, M.M., S.F.; Methodology, M.M., C.B., U.G., M.H.; Investigation, M.M.; Resources, H.H., T.K.; Data curation, M.M.; Writing – Original Draft, M.M., S.F.; Writing – Review and Editing, M.M., S.F.; Visualization, M.M.; Funding Acquisition, M.M., S.F.; Supervision, S.F.

Chapter 3: Conceptualization, M.M., S.F.; Methodology, M.M., C.B.; Investigation, M.M.; Resources, T.K.; Data curation, M.M.; Writing – Original Draft, M.M., S.F.; Writing – Review and Editing, M.M., S.F.; Visualization, M.M.; Funding Acquisition, M.M., S.F.; Supervision, S.F.

Chapter 4: Conceptualization, M.M., S.F.; Methodology, M.M., C.B., B.L.; Investigation, M.M., B.L., C.B.; Resources, D.K., T.K.; Data curation, M.M.; Writing – Original Draft, M.M., B.L., S.F.; Writing – Review and Editing, M.M., S.F.; Visualization, M.M., C.B.; Funding Acquisition, M.M., S.F.; Supervision, S.F.

Chapter 5: Conceptualization, M.M. and F.H.; Methodology, M.M., M.G.K. and W.B.; Investigation, M.M., M.G.K., T.d.S., W.B., E.F-M., M.B., J.De., C.C. and F.M., M.v.T.; Resources, M.D., S.E., K.L., R.K., S.T.v.S., L.H-J., U.F., J.Me., M.v.N., B.T., J.H-K., P.K., J.Mo., M.v.d.W., R.v.B. and J.Dr..; Data curation, M.G.K., T.d.S., A.J. and H.K.; Writing – Original Draft, M.M. and F.H.; Writing – Review and Editing, M.M. and J.Dr.; Visualization, M.M., T.d.S., J.De. and F.M.; Funding Acquisition, F.H.; Supervision, M.M. and F.H.

Chapter 6: J.De., M.M., L.V., F.H., J. Dr. and T.M. conceived and designed the experiments and analyses. J.De. and L.V. analysed the data with contributions from J.Dr., T.S. and T.M. J.De., M.M. and M.G.K. processed tumor samples and performed FACS sorting for SORT-seq with contributions from T.M. L.H-J. provided detailed technical advice and acquired samples for the imaging experiments. J.De. and M.B performed the imaging experiments. J.De. wrote the manuscript with contributions from L.V., J.Dr., T.M., J.M. and F.H. J.Dr., T.M. and F.H. supervised the work. All authors read and approved the manuscript.

Chapter 7: M.M. wrote the chapter, supervised by F.H. and M.v.N.

Curriculum vitae

Michael Torsten Meister was born on November 27th, 1985, in Bad Soden am Taunus, Germany. He studied medicine at the Goethe University (Frankfurt am Main, Germany) from October 2006 to November 2012 to become an MD. He worked as a resident in the pediatric department of the University Hospital of the Goethe University Frankfurt from February 2013 to May 2018. In parallel to his studies and residency, Michael performed preclinical laboratory studies. First, he joined the lab of prof. Thomas A. Wichelhaus (Institute for Medical Microbiology and Infection Control, University Hospital Frankfurt) to study the *"In vitro and in vivo evaluation of the antimicrobial efficacy of folate antagonists and nucleoside-analogues against Staphylococcus aureus"* (October 2009 to August 2013). He finished this study with obtaining a "Dr. med." degree. In August 2014, he joined the lab of prof. Simone Fulda at the Institute for Experimental Cancer Research in Paediatrics (Department of Paediatric Oncology and Haematology, University Hospital Frankfurt) as a Clinician Scientist. Here, he performed the research described in Chapters 2 to 4. As a member of the German pediatric soft tissue sarcoma study group (CWS – Cooperative Weichteilsarkom Studiengruppe) he analyzed a large cohort of patients suffering from so-called peripheral nerve sheath tumors and was involved in the molecular characterization of soft tissue sarcomas in children and adolescents as part of the German precision medicine INFORM study.

In June 2018, he joined the group of prof. Frank C. P. Holstege at the Princess Máxima Center for Pediatric Oncology (Utrecht, Netherlands) to perform the studies described in Chapters 5 and 6 with the last experiments performed in the group of Jarno Drost. He is actively involved in all major soft tissue sarcoma initiatives of the Princess Máxima Center including the institute's precision medicine program and the institute's Sarcoma Research Meeting of which he is the chair. In addition, he became a member of the European paediatric Soft Tissue Sarcoma Study Group (EpSSG) and the EpSSG biology committee.

In July 2022, Michael started the completion of his clinical training in pediatrics, in combination with his preclinical research in soft tissue sarcomas in the group of Jarno Drost. He has received several prestigious research grants to support the research described in this thesis.

Acknowledgements

I guess that normally, one must put some philosophical quote here, comparing one's PhD to some mythical journey to acquire all-encompassing wisdom, a journey that has now come to an end. Honestly, however, I think while this PhD has come to an end, I definitely have not yet obtained all wisdom there is to obtain and that there will be many more years of exciting science in my life to come! Nevertheless, obtaining a PhD is not a small feat and it is certainly impossible without the right people to be there with and for you. This section is dedicated to these people.

First, I want to thank you, **Frank**. Not only did you agree to take me as a PhD student under your supervision, but you also helped me acquire the funding that allowed me to come to the Máxima in the first place. Through your mentorship, I have become a better scientist and have (almost) always appreciated your honest feedback. You gave me the room to develop my own ideas but also suggested directions to aim for. Unfortunately, your transition to research management, which, for sure, would have substantially improved the quality of research at the Máxima, was torpedoed by your illness. I still remember vividly the moment that you told us that you were "very sick" which struck me hard then and still does. However, despite that life-threatening disease, you kept doing what you love (i.e., science) which was, in my case, mentoring me by supervising our manuscript and this thesis. Frank, I appreciate you as a scientist, as a mentor, and as a friend. I wish you all the best for those years to come which will hopefully be many!

Thank you, **Max**, for becoming my doctoral advisor halfway-through this PhD after Frank became ill! Taking over such a task during a PhD after the "big lines" have already been laid out, is certainly a daring endeavor. However, I could not have been luckier than to have you in this position. I deeply value your guidance and mentorship not only in scientific matters, but also regarding my career path to become a pediatric oncologist that combines (pre)clinical research and clinical work. I am looking forward to the years to come with new exciting preclinical and clinical studies on pediatric soft tissue sarcomas here at the Máxima!

Many thanks to you, **Jarno**! As a member of my PhD supervisory committee, your scientific input and your expertise on organoid technology proved

A

invaluable for our manuscript on RMS tumoroid models. After the merge of Frank's and your group a bit more than a year ago, you fully supported the continuation of our work on pediatric soft tissue sarcomas and helped us develop them further. I am looking forward to cool future projects on pediatric soft tissue sarcomas!

Thank you, **Marc** and **Jacco** for joining my PhD supervisory committee! Your input both scientifically but also personally greatly helped. Furthermore, thank you, Jacco, for also being a member of my thesis assessment committee. And Marc, man, what can I say – this PhD and the work in the ML-I would have been pretty lousy without your "philosophical" input on proper music taste and improper jokes (see you at HR, buddy!).

Thank you to **Paul C.**, **Winette**, **Paul v. D.** and **Josef** for being members of my thesis assessment committee! And thank you **Judith** for agreeing to join the PhD defense committee!

Jeff, this was one hell of a ride! Thanks for being my PhD buddy throughout this time which certainly had its ups and downs. Over these years, there was not a single moment where I could not reach out to you to get advice on how to get around in Utrecht as a foreigner or anything lab related. Your kindness and helpfulness are unmatched, and you make sure that everyone feels welcomed. While you can be a drama-queen occasionally, I know that this only stems from your strong sense of justice when you think that someone has not been treated fairly. I am more than happy and proud that you accepted to be one of my paranymphs! Buddy, I hope that everything in your life will go as planned and people will always be as kind and welcoming to you as you are to everyone else! You deserve this.

Irene, how can one keep up with you (literally and figuratively)? I truly admire your ambition and enthusiasm, be it in the lab, on the track, or in all your extra-curricular commitments (socks, anyone?). I know that whatever you will do after your PhD, you will excel in it. Next to this, I think that everyone will testify that the childlike joy you find in the small things is truly contagious. Or, to put it simply: Working with you is fun! Thank you so much for agreeing to become one of my paranymphs, it is a true honor for me! I am sure that I will read about your future endeavors in no less than *Science*, *Runner's World*, and *Time Magazine*!

I want to furthermore thank all former and current members of the former **Holstege** as well as the **Drost** group!

Thank you, **Marian** for your unmatched efforts in all projects that you were and are involved in. I truly respect how you take ownership of projects and ensure that things get done. Without your countless hours in the ML-I and your vast experience in molecular techniques, our study on RMS tumoroid models would not have been feasible. In a similar vein, thank you, **Ewa**, for joining our efforts on growing tumoroid models of pediatric soft tissue sarcomas under exceptional circumstances! On the *in-silico* side of things, thank you, **Terezinha**, for your bioinformatic support! Given that you had not been working in cancer research before joining our group, I think that you underwent a tremendous development. Thank you, **Mariël**, for your help characterizing our RMS tumoroid models but also helping me organizing our last Holstege group retreat (and in general, organizing the whole group as our "good spirit")! Thank you to **Thanasis**, **Tito**, **Lindy**, and **Philip** from the now Single Cell Genomics facility for your excellent scientific input during our former Holstege group meetings! Also, thanks Philip for your help practicing Dutch before my language exam. Thank you, **Sofia, Aleksandra,** and **Yvonne**, for the support in the lab!

Thanks to you, **Kim**, **Maroussia**, **Jiayou**, **Marjolein**, **Carla**, and **Charlotte** and all other current and future members of the "Drosties PhD gang" for the fun get-togethers that totally did not spiral out of control even without alcohol. Gotta' fasten those seatbelts for the next meeting!

Thank you, **Wim**, for being a good sport and competing at the "First at the office" trophy! Really hope that after your appendix, no more of your internal organs decide to explode. Thank you, **Eduard**, for keeping me company during the COVID-19 lockdown as the only two members of the group physically at the lab! Grazie, **Camilla**, for your help in the RMS tumoroid project and with all your valuable insights in organizing one's PhD defense! Many thanks, **Arianna, Jolanda**, and **Francisco** for your valuable input before leaving the group!

Thanks to all other **Máxima (ex-)PhD students** who journeyed alongside me! Thank you, **Freek**, for your fantastic help with our RMS tumoroid manuscript! Thanks to **Axel** and **Lars** for the great time in the lab and on the football field at Olympos! Thank you, **Margit**, for being there in the very beginning, getting

A

Vielen Dank und viele Grüße auch an meine „**Zock-Bro's**" in Deutschland! Danke für die ganzen tollen Erinnerungen an Konsole, Brettspiel-Tisch, bei RPG-Abenden sowie natürlich unseren Bro-Wochenenden. Auch während meiner Zeit hier in den Niederlanden habe ich mit euch tolle Erinnerungen gesammelt, die ich nicht missen möchte. Hier vor allem ein besonderer Dank an **Simon** für eine Freundschaft, die inzwischen 20 Jahre währt!

Marit, **Tito** and **Thomas** – starting a D&D group with you guys was certainly a "Nat 20" on my persuasion check! Thanks for keeping our funky adventures in "The Pearl Archipelago" and any future shenanigans alive and strong. Also shout outs to you **Francisco** and **Jurrian** as members of "The bestest D&D group" here in Utrecht!

Zuletzt möchte ich meiner Familie in Deutschland danken! Lieber **Harry**, lieber **Steven**, liebe **Marie** und liebe **Petra**: Vielen Dank, dass ihr nunmehr seit vielen Jahren Teil meiner Familie seid!

Liebe **Mama**, vielen Dank, dass du immer für mich da warst und mich unterstützt hast! Ohne dich wäre ich sicher nicht derjenige, der ich heute bin. Auch wenn uns die Entfernung trennt, weiß ich doch, dass wir nah bei dir sind, weil du uns in deinem Herzen trägst.

Ha, Bro, du dachtest doch nicht ernsthaft, dass ich dich vergesse? Natürlich gehörst du zu meiner Familie in Deutschland! Alter, **Gaetano**, dieses Jahr werden es sage und schreibe 30 Jahre Freundschaft bei uns! Wir haben Perlenhochzeit! Auch wenn es Zeiten gab, in denen wir nicht so viel miteinander gesprochen haben, war es doch immer klar, dass wir Freunde sind – und hey, wenn wir uns dann gesehen haben, hat es nicht mehr als fünf Sekunden gedauert und alles war wieder wie früher. Mit dir habe ich wirklich alles mitgemacht und ich könnte mir echt keinen besseren „partner in crime" vorstellen. Von ungezählten Spielnachmittagen als Kinder, zu noch ungezählteren (ist das ein Wort?) Stunden in Diablo II als Jugendliche, hin zu seltsamen „kulinarischen Abenteuern" und diversen Exzessen im Studienalter, bis ins Hier und Jetzt als Familienväter verbinde ich fantastische Erinnerungen mit dir. Es hätte nie einen anderen oder besseren Trauzeugen für mich geben können als dich. Und die Tatsache, dass du mich zum Patenonkel von deinem Erstgeborenen Romano gemacht hast, erfüllt mich mit Freude und

A

Stolz. Gaetano, ich hoffe, dass ich mit dir noch die Eichenhochzeit unserer Freundschaft feiern kann!

Und zu guter Letzt: **Jenny** – ohne dich hätte ich dieses ganze Abenteuer „Niederlande" und „PhD" niemals geschafft! Ich weiß, wieviel Überwindung es dich gekostet hat, mit mir ins Ausland zu ziehen, gerade weil wir im Begriff waren, eine Familie zu gründen. Während mich nicht viel in Deutschland hielt, war es für dich doch dein Lebensmittelpunkt. Umso mehr beeindruckt mich, mit wie viel Entschlossenheit du dieses Abenteuer mit mir angegangen bist. Gleich zu Beginn bist du mit mir mit dem „fiets" zum Sprachkurs nach Utrecht gefahren, und das am Ende sogar hochschwanger. Und noch in unserem ersten gemeinsamen Jahr hier in den Niederlanden haben wir unseren **Finn** bekommen, der uns direkt und noch bis heute ordentlich auf Trab hält. Du hast mir in dieser Zeit und bis heute immer den Freiraum gegeben, den ich nötig hatte, um an meiner Forschung zu arbeiten – ein Luxus, von dem ich weiß, dass er nicht selbstverständlich ist. Dann gingen wir zu dritt in die COVID-19 Pandemie und sind zu Hause fast wahnsinnig geworden, vor allem auch, weil wir nicht nach Deutschland zu unserer Familie dort fahren konnten. Und genau zu diesem Zeitpunkt dann bekam ich mein Traumangebot: Am Máxima meine Ausbildung zum Kinderonkologen abzuschließen, um dann hier als ein solcher arbeiten zu können. Zu Beginn hatte ich nicht mit dem Versprechen in die Niederlande gelockt, dass wir hier nur zwei Jahre bleiben würden, nur um es nach drei Monaten hier direkt auf vier Jahre auszuweiten (was du klaglos angenommen hast). Und was nun mit diesem Angebot? Ich weiß noch, wir waren gerade mit Finn in der „kinderboerderij" in Zeist, da fragte ich dich. Und deine Antwort? „Na gut, dann will ich aber, dass wir uns ein Haus kaufen." Tja, so wie schon zuvor warst du bereit, für mich hier zu bleiben. Und so verging noch etwas Zeit und wir zogen in ein Haus in Bilthoven, in dem wir wenig später dann auch unsere **Hanna** bekamen, die nun mit noch nicht einmal zwei Jahren schon ganz genau weiß, was sie will (und was nicht). Und während ich im Labor fleißig war und nunmehr in der Klinik fleißig bin, hast du das Unmögliche möglich gemacht und gleichzeitig deine Arbeit, einen Haushalt und die Erziehung zweier Kinder jongliert. Trotzdem hast du mir immer das Gefühl gegeben, dass das alles hier unsere gemeinsame Entscheidung ist und du vollkommen an meiner Seite stehst und meinen

Traum unterstützt. Ich weiß, was ich von dir in den letzten Jahren mit diesem Abenteuer abverlangt habe. Und ich danke dir von ganzem Herzen, dass du dich auf dieses Abenteuer eingelassen hast. **Jenny**, du bist die Liebe meines Lebens und ohne dich, hätte das alles hier niemals geschafft. Ich liebe dich!

A